TERTIARY ALKYL PRIMARY AMINES AS STABILIZERS FOR MIDDLE DISTILLATE FUELS

Rajiv Banavali and Bharati Chheda,
Rohm and Haas Company,
Deer Park, Texas 77536

ABSTRACT

Degradation of middle distillate fuels under both the prolonged storage and high-temperature thermal stress is of concern. There is a continued challenge in developing stabilizers that are increasingly cost-effective, do not degrade the performance of fuel, and are environmentally acceptable. We are interested in developing branched tertiary alkyl primary amines (TAPA) as multi-functional fuel additives. They are ashless, combustible, and nonextractable stabilizers. The results of stability experiments for thermal and oxidative degradation of various middle distillate fuels (diesel, jet fuel, fuel oil) are presented. The TAPA, individually and in combination with other additives, are evaluated in these stability tests. An attempt is made to form a general interpretation of stabilization mechanisms of TAPA as radical chain breakers, peroxide decomposers, metal deactivators, solubilizers, dispersants, and as acid scavengers.

INTRODUCTION

The useful life of fuel is a function of its quality and of storage conditions. Depending on the crude source and amount of cracked fraction, middle distillate fuels can contain very different amounts of gum and color precursors, waxes, aromatics, and other products. Estimated useful life[1] of good quality middle distillate fuels, under normal storage conditions, varies from about 1 year for Diesel and Heating fuel to 3-4 years for Jet fuels. However, fuels are often stored for much longer periods because of logistical and economic necessities. This is particularly so for military use where it is necessary that the fuel quality remains fit for use throughout the storage period. Both the low-temperature storage and high-temperature thermal degradation, are of concern. There may be a relationship between the chemistry of deposit formation during normal long term storage and the deposits obtained by thermal stressing of jet fuel.

Fuels containing higher amounts of olefins, certain nitrogen and sulfur compounds, organic acids, or dissolved metals are likely to degrade more and faster. Sediments and gums which result from the oxidation reactions act to block filters and deposit on surfaces. The progressive lowering of sulfur levels has greatly reduced the instability of diesel. On the other hand, potential new problems resulting from increased processing and the resultant removal of natural antioxidants has occurred. Additionally, to meet increasing demands for fuels, refiners have turned to blending significant proportions of cracked stock as middle distillate fuel extenders. The cracking process produces components of lower stability than straight-run distillates.

Hydrotreating is generally considered the most effective means of improving the stability. However, often the cost of stability improvement by additives doping can be less than the hydrotreatment costs. Demand for additives in these markets is projected (The Freedonia Group estimate) to increase nearly 15% a year to $350 million in 1998. The stability enhancing additives for middle distillate fuels include hindered phenols (jet fuels), phenylenediamines, tertiary amines, metal deactivators and dispersants. Tertiary amines are generally considered[2] better than secondary or primary amines as fuel antioxidants.

Phenylenediamine type antioxidants are more effective than hindered phenols in neutralizing peroxides. Research[3] on peroxide formation in several diesel fuels found that low sulfur and aromatics content fuels (Swedish fuels) are likely to form more peroxides upon aging. It was found that traditional amine stabilizers fail to control peroxide formation adequately. Also, these amines, while being more effective than hindered phenols in gasoline, are not being used in diesel because they degrade distillate fuel stability.[3b] Phenylenediamines have been shown to participate in side reactions forming sediments[3a] and increasing color body formation.[3c]

Primary amines have not received much attention as fuel stabilizers because they are not considered as good radical/peroxide quenchers as secondary or tertiary amines. This is true for typical straight-chain fatty amines. However, we are mainly interested in a special class of primary amines that possess branched alkyl chains with the primary amino group attached to a tertiary carbon. We will refer to these as tertiary alkyl primary amines (TAPA).[4] This feature of having a tertiary carbon attached to nitrogen is very beneficial because it imparts important

characteristics[5] to these amines. The structural differences between fatty and TAPA amines are illustrated in the following figure.

Branched tertiary alkyl primary amines possess[6] excellent oil solubility, thermal and oxidative stability, strong basicity, and fluidity over a wide temperature range. These properties make them well suited for enhancing the performance of petroleum fluids[7] as well as lubricants.[8] The fact that there are no α-hydrogens attached to nitrogen gives TAPA better oxidative stability because this weak C-H bond is most prone to oxidation. The lack of α-hydrogens also ensures that unstable imines are not formed which can deaminate in the presence of water. This makes TAPA oxidatively more stable than their corresponding linear amines. The fact that TAPA can be used as fuel stabilizers, and are better than normal primary amines, was first shown in 1960.[9] We will describe the work carried out at Rohm and Haas research laboratories with TAPA, individually and in combination with other additives, for their ability to stabilize middle distillates.

EXPERIMENTAL

Fresh test fuels without any additives were obtained from commercial sources. The fuel samples were analyzed to ensure conformace with specifications and stored under ambient temperature, in dark, and under nitrogen atmosphere. All tests were started within a month of obtaining the fresh samples. All commercial additives used were as received without further purifications. All the C8, C12, and C18 TAPA samples were commercial products sold under the trademark Primene by Rohm and Haas company. The details of the stability test methods are given below.

I. Furnace Oil Stability Test: Fuel samples of 500 mL were stored in 600 mL beakers covered with watch glasses in oven at 40°C. At arbitrary intervals, optical density measurements were made on samples before and after filtering a small portion of vigorously shaken sample through a CORNING 30 F fritted glass crucible. The unused portion was immediately returned to the oven for further aging. The failure time was determined by three methods: 1) the number of days to a stated level of optical density difference (Δ OD) of 0.12 between unfiltered portions, 2) days to reach an OD value of 1.00 for the unfiltered sample, and 3) days to reach a residue level of 2.0 mg/100 mL as determined by filtration. The data is given in Table I.

II. Fuel Oil No. 2 Stability Test: A 50 mL sample of fuel oil in a test tube is stored in a 300°C bath for 90 minutes. After removal from the bath it is allowed to cool to room temperature (about 2 hr.). The aged fuel is then filtered through 4.25 cm Whatman No 1 filter paper. The paper is then washed with heptane and the color of the filter paper is compared to a set of standards (1 = No color, 20 = dark brown). A color of 7 or less is considered acceptable. The data is given in Table II.

III. Modified ASTM 2274 Diesel Oxidation Stability: A 350 mL sample of fuel is heated at 95°C for 16 hr. (or 40 hr.) while oxygen is bubbled through at the rate of 3 liters per hour. After aging, the sample is cooled to room temperature and filtered to obtain the filterable insoluble quantity. Adherent insolubles are then removed from the associated glassware with trisolvent (TAM). The TAM is then evaporated to obtain the adherent insolubles. The sum of filterable and adherent insolubles, expressed as milligrams per 100 mL, is reported as total insolubles. The data is given in Table III.

IV. Thermal Oxidation Stability of Jet Fuels (JFTOT): 600 mL of test fuel is pumped at a rate of 3 mL/min through an aluminum heater tube(JFTOT apparatus) at 260°C (or 325°C) for 150 minutes, and passed through a 17 μm SS filter. The essential data derived is the amount of deposits on the heater tube, and the rate of plugging of the filter(pressure drop). The deposits on the heater tube are rated by the ASTM Color Standard. The data is given in Table IV.

RESULTS AND DISCUSSION

The results of the various stability tests as measured by color, sediments and gum formation show clearly that addition of TAPA, at few ppm levels, significantly improves the stability of fuel oils and diesel. Table I shows that the stability of catalytically cracked furnace oil can be improved by C_{12} TAPA doping at 30 ppm. Several commercial fuel stabilizers at the same dosage level show similar or worse performance. Similar behavior is noted for the No. 2 fuel oil stability. The data

that TAPA are equal or better stabilizers is also seen in comparative experiments with two commercial additives. The fuel oil stability results using the C_{12} TAPA in combination with a dispersant and/or a metal deactivator show that the performance over the TAPA alone is not significantly improved. Oxidative stability of diesel fuel was studied on fuel samples collected from three major regions around the world; namely, North America, Latin America, and Asia. Once again, improvement in the oxidative stability is obvious with the addition of 30 ppm of TAPA. The diesel data, in addition, shows the differences in activity of various TAPA additives. This data allows both dosage and structure-activity relationships establishment. Furthermore, JFTOT tests with TAPA show improvement in thermal stability benefit. Particularly noteworthy is the effect seen at 325 °C heat exposure. This is significantly higher exposure than the traditional 260 °C tests. This result is not only supportive of TAPA benefit, but important in light of the current need to develop aircraft fuels which can operate under supercritical conditions.

Several chemistries may contribute to fuel stabilization. Antioxidants act to inhibit the reactions that form sediment. Most additives control peroxide formation, but do not curb formation of polymerized gum products. Dispersants act to suspend any sediment particles that form and prevent them from agglomerating and becoming a problem. The sediment and gum formation mechanisms have been studied in great details[2,10] and can be summarized[3] as: acid-base reactions involving N, O, and S species, free radical induced polymerization reactions involving unsaturated hydrocarbons, and esterification reactions involving aromatic and heterocyclic species. The mechanism by which TAPA act as antioxidants is not completely understood, but an attempt is made here to form a general interpretation of their stabilization mechanisms. The additive concentration and structure effect suggest that the stabilization properties of TAPA result from factors such as radical scavenging, acid scavenging, hydroperoxide decomposition, metal deactivation, dispersing of gums and particulates, or any combination of these factors.

CHAIN BREAKING MECHANISMS

Hindered phenols and aromatic amines are considered radical chain breakers. The chain carrying peroxy radical is scavenged by the phenol or amine by hydrogen atom donation. The resulting radicals are resonance stabilized and are eventually destroyed by reaction with another peroxy radical. Hindered amines can also react with free radicals to form stable intermediates that do not readily take part in chain reactions. Although they are not as resonance stabilized, they can regenerate by scavenging another hydrogen radical.

REDUCTION OF PEROXIDES AND HYDROPEROXIDES

Amines in general, and tertiary amines in particular, are well known peroxide decomposers. The catalytic efficiency of the amines generally correlate with their ionization potentials. This correlation supports the mechanistic interpretation that a charge transfer complex between the amine and the peroxide weakens the O-O bond. Quenching by amines is also subject to steric effects.

METAL DEACTIVATORS

It is anticipated that middle distillates will have a higher metal content[11] than gasoline, and the content increases with increasing metal contents of the crude. Complexes of Fe, Mn, Co, and Ni, when solubilized as fuel soluble salts, are all known to be oxidation catalysts and are present in most middle distillate fuels in trace amounts. These metals will promote oxidation of the fuel with subsequent gum formation and deposit build-up. The MDA is believed to form a caged complex with dissolved metal salts(especially copper) that is generally less active as an oxidation catalyst than the free metal itself. TAPA can also effectively chelate these metal atoms. Molecular modeling shows that the resulting complexes can effectively shield the metal atoms thereby reducing their ability to catalyze degradative reactions. The TAPA also migrate to new surfaces, further inhibiting the formation of soluble metal salts. Their filming action can also lead to protection of metal surfaces and thus inhibiting metal ions solubilization.

SOLUBILIZATION AND DISPERSANCY

For a good stabilizer, it is important not only to mitigate the oxidative process, but also to help resolve problems caused by them. TAPA act by forming fuel soluble salts with acidic by-products of oxidation. Furthermore, their complexation with metals and other species allows suspension of gums and particles. The role of TAPA in minimizing gums and sediment formation by "solvating ability" of the branched alkyl chains of TAPA is also likely. By keeping the sediment particles from agglomerating they can be kept small enough to be dispersed through the fuel filters. Despite their dispersant action they are unlike many additives that cause emulsions when fuels containing them mix with water. In fact, they also act as demulsifiers and provide another benefit to the fuel storage.

ACID SCAVENGERS

Hazelett has shown[12] the correlation of carboxylic and sulfonic acids in increasing deposit formation. The reaction of certain acidic compounds, such as naphthalene sulfonic acid, with nitrogen compounds, such as indoles, quinolines, and carbazoles, appears to be one of the mechanisms for fuel insolubles formation. Dodecylbenzenesulfonic acid promotes sediment formation and also may get incorporated into the sediment. Tertiary amines were shown[12] to be effective in reducing deposits in fuel blends containing acids. For weak acids, the amines exhibit more than 1:1 action and certain amines exert favorable behavior only if they are strong organic bases. TAPA are strong bases[13] and can readily react with acidic species, sacrificing themselves to form salts that are miscible in these liquids and thus do not precipitate.

CONCLUSIONS

We have shown that Fuel deterioration is delayed, color degradation is inhibited and sludge formation is reduced by addition of TAPA to the middle distillate fuels. The tertiary alkyl primary amines are highly effective stabilizers for the prevention of sludge formation in fuel oils and diesel and their effectiveness depends on the structure of the amine. They inhibit the reactions responsible for sludge formation and also disperse the gum and sediment from depositing. They also improve the thermal stability of jet fuels. In addition, these amines are also ashless and completely combustible. They are virtually insoluble in water and are not leached from fuels by contact with water during storage and handling. Additionally, they do contribute beneficially to other fuel properties. Corrosion inhibition is another benefit that can be obtained by the use of TAPA. Water contained within fuel, or permeating from external sources, combines with air to attack iron to form rust. This can be prevented by protecting metallic surfaces with an additive film by using TAPA or their salts. The polar portion of the molecule adheres to the metal surface and forms the protective film.

ACKNOWLEDGMENTS

We would like to thank Rohm and Haas company for providing the support for this work and permission to publish the results.

REFERENCES

1) Chevron USA Inc.; *Long-Term Fuel Storage Technical Bulletin*, **1981**.

2) Beaver, B.; *Fuel Science And Technology Intl.*, **1992**, 10(1), 1.

3) a)Bart, R. J.; Henry, C. P.; Whitesmith, P. R.; *Proceedings of the 5th International Conference on Long Term Storage Stability of Liquid Fuels*, **1995**; Eds.; Giles, H. N.; National Technical Information Service, Springfield, Va, Vol. 2, 761. b)Hazlett, R. N.; Hardy, D. R.; *NRL Letter Report 6180-832*, Naval Research Laboratory, Washington, DC, **1984**. c)Henry, C.; *Proceedings of the 2nd Intl Conf on Long Term Storage Stabilities of Liquid Fuels*, Stavinova, L.L.; Ed.; SWRI, San Antonio, TX; **1986**, p 807.

4) These TAPA are commercially available from Rohm and Haas Company as Primene® Amines. The C-8 is available as Primene® TOA, C-12 as Primene® 81-R and C-18 as Primene® JM-T.

5) Banavali, R.; Ellis, M. J.; Piccolini, R. J.; *Resin Review*, Rohm and Haas, Philadelphia, Pa, **1993**, XLIII, 1, 13.

6) Banavali, R.; Chheda, B.; In *International Symposium on Production and Application of Lube Base Stocks*, Singh, H.; Prasada Rao, T.S. R.; Eds.,Tata McGraw-Hill, New Delhi, **1994**; p 318.

7) Banavali, R.; Chheda, B.; Uhran, J.; *In 2nd Brazilian Symposium on Lubricants*, Instituto Brasileiro de Petroleo, **1995**, p 1.

8) Banavali, R.; Karki, S. B.; *Prepr. Pap.- Am. chem. Soc. Div. Of Pet. Chem.*, **1997**, 42(1), p 232.

9) H. J. Andress, Jr., Mobil Oil Co., U.S. Patent # 2 945 749, **1960**.

10) Mushrush, G. W.; Speight, J. G.; In "*Petroleum Products: Instability and Incompatibility*", Taylor and Francis, Washington, DC; **1995**.11) Woodle, R. A.; Chandler, W. B.; *Ind. Eng. Chem.*, 44(11), 2591, **1952**.

12) Hazlett, R. N.; *Fuel Science and Technology*, 6(2), 185, **1988**.

13) Rohm and Haas Research Laboratory Unpublished Data.

TABLES

Table I. Fuel Oil Stability Test (Catalytically Cracked Furnace Oil)

Additive	Dosage (ppm)	Days to failure		
		Δ OD	OD = 1.00	2 mg/100 mL
None	----	38	71	60
C_{12} TAPA	30	94	120	68
Commercial AO #A	30	35	105	85
Commercial AO #B	30	36	88	58
Commercial AO #C	30	54	107	63
Commercial AO #D	30	64	104	75

Table II. Accelerated Storage Stability Tests (No. 2 Fuel Oil)

Additive	Dosage (ppm)	Louisiana Sample		Mid-West Sample	
		Filter Pad Rating	ASTM Color	Filter Pad Rating	ASTM Color
None	---	11	205	16	6
C_{12} TAPA	7.5	3	2	3	4
"	15	2	2	4	3.5
Commercial AO #1	7.5	5	2	6	4
"	15	2	2	4	4
Commercial AO #2	7.5	3	2	10	3.5
C_{12} TAPA+MDA	7.5+1.5	3	2	4	4
C_{12} TAPA+Dispersant	7.5+7.5	3	2	3	4
C_{12} TAPA+Dispersant+MDA	7.5+7.5+1.5	7	2	7	3.5

Table III. Oxidative stability Results Using ASTM 2274 Test Method(Diesel)

Additives	Dosage (ppm)	Insolubles mg/100 mL			
		Gulf Coast Sample A	LAR Sample	Asian Sample	Gulf Coast Sample B
None	---	1.1	0.5	2.2	2.3
C_{12} TAPA	100	<0.1	0.3	0.3	---
C_{18} TAPA	100	0.1	0.6	---	---
C_8 TAPA	15	---	---	---	<0.1
TAPA #A	15	---	---	---	0.9
C_{12} TAPA	15	---	---	---	1.2
TAPA #B	15	---	---	---	<0.1
C_{18} TAPA	15	---	---	---	1.4
TAPA #C	15	---	---	---	1.9

Table IV. Thermal Oxidation Stability Using (JFTOT) ASTM -D 3241(Jet Fuel)

Additives	Dosage (%)	Preheater Tube Deposit	Pressure Drop	Comments
None	---	3	30	@ 260°C
C_{12} TAPA	1	2	4	@ 260°C
C_{18} TAPA	1	2	2	@ 260°C
None	----	1	6	@ 260°C
C_{18} TAPA	0.1	1	<1	@ 260°C
None	-----	4	2	@ 325°C
C_{18} TAPA	0.1	<4	<1	@325°C

COMPUTER SIMULATION OF HIGH PRESSURE SLUDGE LIQUEFACTION REACTOR

Sung-Chul Yi[1], Sung-Yeol Bael, Ho-Tae Lee[2], and Wang-Lai Yoon[2]

1. Department of Chemical Engineering, Hanyang University, Seoul, Korea
2. Korea Institute of Energy Research, Daejun, Korea

Keywords: mathematical model, sewage/waste water sludge, high pressure liquefaction

INTRODUCTION

The increasing population of municipal area and the improved activity of the economy are causing more polluted water in streams. However, the public demand more action on the environmental protection, resulting in more than 70% treatment of total sewage/waste water in 1997. The volume of sludge from the sewage/waste water treatment plants is increasing and it is expected to be 8000 ton per day in 1997. Seventy to eighty percent of water content in the sludge makes landfill of sludge an ineffective way of treating sludge. Thus, the development of sludge treatment technologies is inevitable in the direction of reducing water content of sludge to prevent odor generation and to reduce the leaching of heavy metal in some area.

Overall objective of this research is to develop a sludge treatment technology to recover organic portion of sludge as a fuel oil using a high pressure liquefaction technique. The result would be the reduction of the volume and the weight of sludge to be land filled while generating useful energy from wastes. A bench scale liquefaction process has been operated for several months and the scale up process is underway.

The detailed understanding of the behavior of a high pressure sludge reactor during transient operation is crucial to the design of scale up process.

THEORETICAL FOUNDATION OF THE MODEL

Nature of the Analysis

The starting point of the present analysis is the set of elliptic partial-differential equations that express the conservation of mass, momentum and energy in two-dimensional transient non-Newtonian flow.

These equations are reduced to finite-difference equations exhibiting 'upwind' formulation of the coefficients over a grid that covers the domain of interest. Appropriate boundary conditions are supplied to the procedure which is incorporated into a computer program. The computation is a set of grid-node values for the velocity components, pressure, and temperature.

Differential Equations

All dependent variables such as velocity components in two dimensions and energy, with the exception of pressure, appear as the subjects of differential 'conservation' equations. Although these equations are deduced from physical principles, they are all expressed in a standard form, in which Φ stands for a generic fluid property [1,2].

$$div\{(\rho \upsilon \Phi + J_\Phi)\} = S_\Phi \qquad (1)$$

where ρ, υ, J_Φ,S_Φ are density, velocity vector, diffusive-flux vector and source rate per unit volume.

The pressure variable is associated with the continuity equation:

$$div(\rho \upsilon) = 0 \qquad (2)$$

in anticipation of the so-called pressure correction equation [1] which is deduced from the finite-difference form of the continuity equation.

The diffusive flux J_Φ is given by:

$$J_\Phi = -\Gamma_\Phi grad\Phi \qquad (3)$$

where Γ_Φ denotes the effective exchange coefficient of Φ.

DETAILS OF COMPUTATIONS PERFORMED

Outline

Because of the exploratory nature of the computations, simplifications in the modeling of the reactor have been introduced. These simplifications include the treatment of the problem as two-dimensional, axi-symmetric reactor. A coarse-grid, consisting of 84 x 18 control cells, has been chosen, and grid-spacing is such as to model the geometric features as accurately as

possible shown in Fig. 1.

Initial and Boundary Conditions

To complete the mathematical analysis, it is necessary to provide initial and boundary conditions. For the typical reactor problem illustrated in Fig. 2, these conditions are as follows:

- At the inlet to the reactor, mass flux of sludge and temperature are prescribed; the momentum flux at the inlet is computed from the prescribed mass flux and the known area. Temperature is defined with respect to incoming sludge and is therefore set equal to room temperature. Table 1 shows the inlet velocities based on the various speed of pump strokes.
- At the reactor wall, the non-slip condition is used for velocity components parallel to the wall. Thermal boundary conditions on reactor wall can be modeled with specified temperatures due to three zone heaters around the wall.

Physical Properties

Physical properties of sludge (thermal conductivity, heat capacity, density) assumed same as those of water since sludge contains 80 - 90% of water. Unreacted raw sludge behaves as a highly non-Newtonian flow. However, when heated in the reactor vessel, it quickly turns Newtonian flow. Viscosity of the sludge is assumed to be a function of temperature.

The Solution Procedure

The procedure adopted for the solution of the equations is the SIMPLE algorithm[1]. The reader is directed to the above reference for further details.

PRESENTATION OF THE RESULTS

Many results were obtained during the present study but space considerations dictate that only a part of these can be presented. Representative sample predictions for two cases are shown in Figs. 3 and 4, mainly in the form of maps of temperature distributions. Fig. 5 is the streamline contours.

DISCUSSION OF RESULS

The coarseness of the finite-difference grid used does not allow the results to be quantified in detail. It does allow, however, the description of their qualitative nature, and the study of the relative differences coming from changes to design conditions.

Table 2 shows experimental conditions such as reaction time and a temperature at each zone for runs performed.

The temperature distribution across the reactor is presented in Figs. 3 and 4 at 5, 15, and 30 minutes for Cases 1 and 8. It can be seen that first section of the reactor could serve as a preheating zone. Since the temperature development through the reactor is strongly affected by the second and third heaters as well as the sludge residence time, these variables should be optimized to minimize coking phenomena on the reactor wall. Fig. 5 is the streamlines which represent the flow field of the fluid in the reactor. Due to the highly viscous of initial sludge condition the inlet velocity to the reactor is quite slow, eddies caused by sudden expansion do not appear. This allows the simple design of reactor is feasible. The predicted average outlet temperature and the outlet temperature experimentally obtained are shown in Table 2. Predicted outlet temperatures was 15 - 20 % higher than experimental outlet temperature. This is due to the sludge cokes formed on inner reactor wall which inhibits a heat transfer from the wall.

CONCLUSIONS

A numerical modeling approach is developed for prediction of transport phenomena in the high pressure sludge reactor using the operation parameters of the laboratory scaled continuous process. The heat transfer phenomena in the reactor was reasonably predicted and will be better predicted including the sludge coking effect. The computer modeling tools are based on a computational fluid dynamics code developed in our laboratory.

Although the test cases considered in this paper are rather limited, the computer program can handle more complicated situations and serve as a useful design guide.

REFERENCES

[1] Spalding, D.B., Recent Advances in Numerical Methods of Fluids, 1 (1980).
[2] Yasuda, Y., Water Science and Technology, 23 (1991)

Table 1. Pump stroke and inlet velocity

Retention time (min)	pump stroke	volumetric flow rate (ml/hr)	inlet velocity (m/s)
16	50	1871	0.01242
20	40	1406	0.00933
30	30	1070	0.00710

Table 2. Experimental conditions for runs performed

Case No.	Retention time	heating zone 1 (°C)	heating zone 1 (°C)	heating zone 1 (°C)	outlet temp (°C)
	SET	130	250	250	
1	16	121	251	241	109
2	16	121	209	247	103
3	16	125	216	242	109
4	20	125	222	245	112
5	20	125	200	245	116
6	30	134	241	233	120
7	30	134	234	222	113
	SET	130	300	300	
8	16	115	265	304	131
9	16	119	262	304	131
10	16	131	264	295	133
11	20	133	258	262	129
12	20	132	257	263	129
13	30	140	257	300	128
14	30	140	258	298	127
15	30	141	257	299	127

Table 3. Comparison between experimental and numerical results.

	Experimental outlet temperature	Predicted outlet temperature
Case 1.	382 K deg	446.13 K deg
Case 8.	404 K deg	482.63 K deg

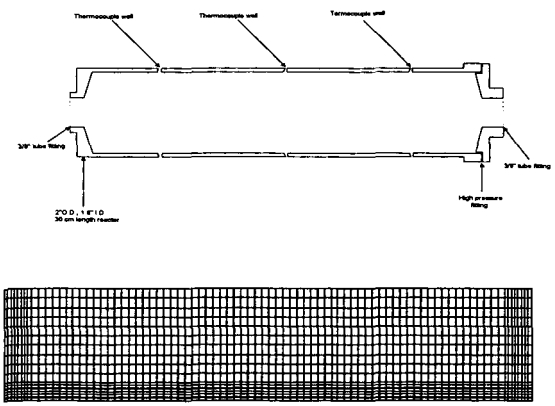

Figure 1. The sludge reactor considered and its finite difference representation

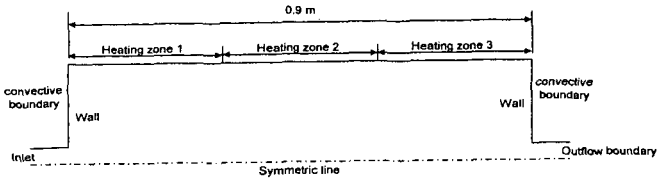

Figure 2. Schematic of sludge reactor

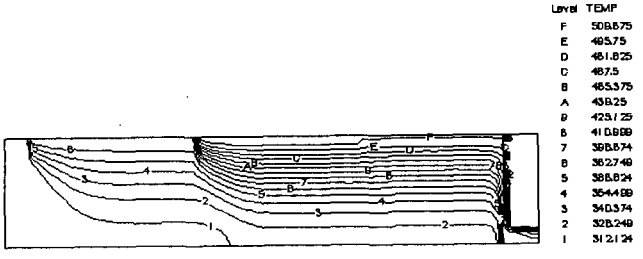

(a) Time = 5 min

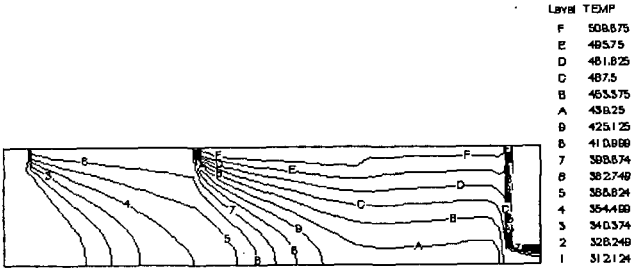

(b) Time = 15 min

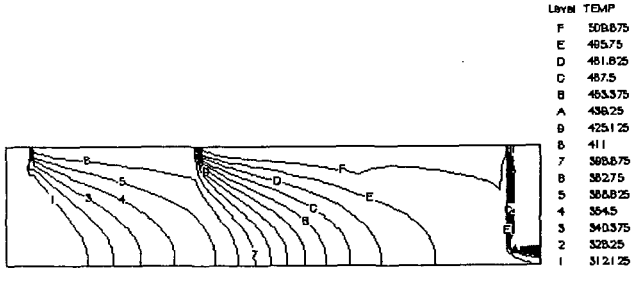

(c) Time = Steady

Figure 3. The maps of temperature for case1.

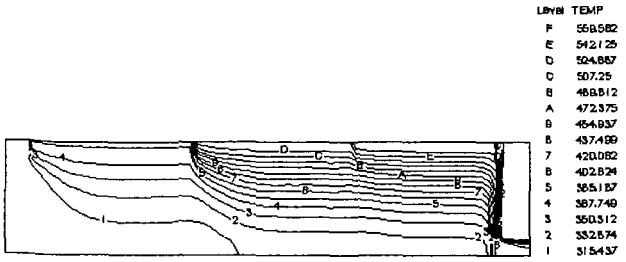

(a) Time = 5 min

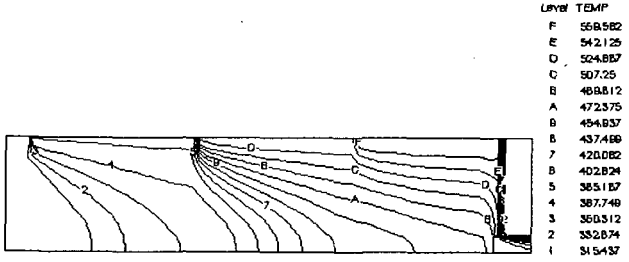

(b) Time = 15 min

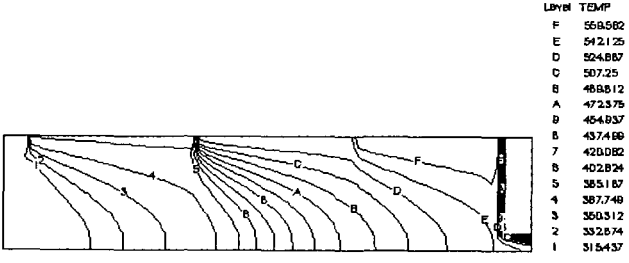

(c) Time = Steady

Figure 4. The maps of temperature for case8.

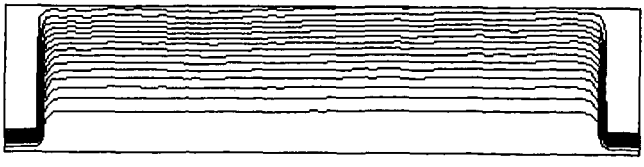

Figure 5. Streamlines in the reactor

RECOVERY RATE OF CH_4 FROM CH_4-HYDRATE IMMERSED IN CO_2-CH_4 MIXTURES

S.Hirohama, Y.Shimoyama,A Wakabayashi,
Chiyoda Corp.,Yokohama 221 Japan,
S.Tatuda, I.Norikyo, Hokuriku Electric Power Co., Toyama 930,Japan,
N.Nishida, Sugino Machine Ltd.Uozu 937,Japan.

INTRODUCTION

Occurrence of subterranean CH_4-hydrate layers is known and inferred in all over the world. A vast quantity of CH_4 contained in the hydrate layers can be one of the main energy sources in the next century (Holder et al.1984, Kvenvolden,1994). Injection of liquid CO_2 into the hydrate layers might be a promising technique to recover CH_4 simultaneously segregating CO_2 from the biosphere as CO_2-hydrate, because some portion of CH_4-hydrate is converted to CO_2-hydrate by simply immersing it in liquid phase containing CO_2(Hirohama et al. 1996). Mass-transfer in hydrate solid is presumed to determine the rate because CH_4-hydrate at the interface with the liquid phase is initially converted to CO_2-hydrate which can inhibit further conversion.

As CH_4 content in the liquid phase increases, the recovery rate can decrease because of decrease in the driving force. So that evaluation of this technique requires that the effect of the composition on the rate of the conversion is known in a wide composition range. However there has been no datum on the effect of the liquid composition. Although Hirohama et al. (1996) proposed a diffusion model to describe the mass-transfer in hydrate solid, its accuracy was not tested at altered compositions of the liquid phase.

This article proposes data on the conversion rate under varied compositions of the liquid phase. The accuracy of the model is discussed by comparing the data with the prediction.

EXPERIMENTAL

The experimental setup is the same as that used by Hirohama et al.(1996). The apparatus consists of a reactor, a feeding system for each component, a temperature controlled water bath and a back pressure regulator. The experiments were conducted by the following procedure:

Formation of CH_4-hydrate: Water and CH_4 were charged in the reactor. Quantity of consumed CH_4 was determined from the temperature, the pressure and the volume of the gas phase before and after the formation of CH_4-hydrate.

Purging CH_4 in gas phase by gaseous CO_2: Gaseous CO_2 was fed to the reactor to purge the CH_4 in the gas phase keeping the total pressure of the reactor above the dissociation pressure of CH_4-hydrate at the temperature.

Injection of CH_4 and CO_2: Liquid CO_2 and CH_4 were fed to the reactor. The change of the total pressure was monitored for about 600-1100 hours while the temperature was kept constant.

Discharge from the reactor: The total pressure of the reactor was reduced to the atmospheric pressure to vaporize all of the liquid and dissociate all the hydrate. The volume and the composition of the outlet gas were measured to determine the quantities of CH_4 and CO_2 existed in the reactor.

The experimental conditions and the results are listed in Table 1. The material balance of CH_4 and CO_2 through the procedures are between 90% and 105%. The change of the total pressure of the reactor is shown in Fig.1.

CONVERSION RATE

Quantity of recovered CH_4 can be determined from the total pressure and the temperature by solving the following material balance and volume balance simultaneously.

$$n_{CO2,i} - n_{CO2,by} = G(1 - y_{CH4}) + L(1 - y_{CH4}) \quad (1)$$

$$n_{CH4,i} - n_{CH4,by} = Gy_{CH4} + Ly_{CH4} \quad (2)$$

$$V_t - V_{hy} = G/\rho_G + L/\rho_L \tag{3}$$

Eliminating G and L from the equations above gives:

$$n_{CH4,t} - n_{CH4,hy} = \frac{\left(n_{CO2,t} - n_{CO2,hy}\right)/\rho_L + \left(x_{CH4} - 1\right)\left(V_t - V_{hy}\right)}{\left(1 - y_{CH4}\right)/\rho_L - \left(1 - x_{CH4}\right)/\rho_G} y_{CH4} + \frac{-\left(n_{CO2,t} - n_{CO2,hy}\right)/\rho_G + \left(1 - y_{CH4}\right)\left(V_t - V_{hy}\right)}{\left(1 - y_{CH4}\right)/\rho_L - \left(1 - x_{CH4}\right)/\rho_G} x_{CH4} \tag{4}$$

In Eq.(4), x_{CH4}, y_{CH4}, ρ_L and ρ_G were calculated by the Patel-Teja equation of state (Patel and Teja,1982) from the temperature and the pressure. The effects of H_2O on the vapor-liquid equilibria and the material balance were neglected because the solubility of H_2O in liquid CO_2 is less than 0.5 mol% (Wiebe and Gaddy,1941). The value of $n_{CO2,hy}$ was estimated assuming that all the free H_2O was consumed to form CO_2-hydrate shortly after the injection of CO_2. V_{hy} was estimated from the superficial density of the hydrate solid measured by Hirohama et al (1996).

Figure 2 shows the quantity of CH_4 recovered from the hydrate phase. As the initial mole fraction of CH_4 in the liquid phase increased, the rate of the conversion decreased. A rapid increase in the pressure in the first 10 hours was not taken in account, because the homogenization of the gas and the liquid in the reactor takes about 10 hours. Figure 3 shows the effect of the liquid composition on the amount of methane recovered in 600h. As the CH_4 content increased, the rate of the conversion decreased dramatically.

DISCUSSION

CH_4-hydrate at the interface with the liquid phase can be initially converted to the hydrate of CO_2-CH_4 mixture through which CO_2, CH_4 and/or H_2O permeate to continue the conversion. The following diffusion-like equation proposed by Hirohama et al.(1996) was applied to calculate the flux (N_i) of CO_2 and CH_4 in hydrate solid.

$$N_i = -\rho_{cage}\theta_i^*\omega\left(\frac{\partial \mu_i}{\partial z}\right)_t \tag{5}$$

where $$\theta_i^* = \left(\theta_{i,1}\nu_1 + \theta_{i,2}\nu_2\right)/\left(\nu_1 + \nu_2\right) \tag{6}$$

Chemical potential (μ_i) was calculated by the following empirical equation of which parameter values were determined by fitting to the rigorous solution of the solid solution theory (Waals et al., 1959, Saito et al.,1964) which gave good prediction for the initial hydrate forming pressures of CH_4-CO_2 mixtures.

$$f_i = \frac{1}{K_i^*} \times \frac{\theta_i^*}{1 - \sum_k \theta_k^*} \tag{7}$$

In Eq.(7), K^*_{CO2} and K^*_{CH4} were 21.5 MPa^{-1} and 9.98 MPa^{-1} respectively at 274K. Quantity of CH_4 recovered from the hydrate phase was calculated by solving Eqs.(4)-(7) simultaneously under the same boundary conditions as those used by Hirohama et al.(1996).

No single value of solute mobility was able to describe the effect of the CH_4 content on the decrease in the conversion rate. So that the cause of the effect of the liquid composition can not be attributed only to the decrease in the driving force if the equilibrium model is applicable at the conditions. The fact implies that the composition of the liquid phase might influence the solute mobility in the layer of initially converted hydrate at the surface of the hydrate solid.

This work tempted to correlate the solute mobility as a function of the fraction of vacant cage as follows:

$$\ln\left(RT\omega\right) = A\theta_v^* + B \tag{8}$$

where $\theta_v^* = 1 - \sum_i \theta_i^*$ (9)

A and B are empirical parameters of which values were determined so as to describe the data of all runs. The values of A and B were 610 and 10.1 respectively. Simulation was carried out by solving Eqs.(4)-(9) simultaneously. The model was capable of describing well the tendency of the experimental results as shown in Figs.2 and 3.

CONCLUSIONS

Conversion rate of CH_4-hyrate to CO_2-hydrate immersed in the liquid phase of varied compositions was determined. As the CH_4 content increased, the conversion rate decreased more rapidly than predicted from the decrease in the driving force calculated by the solid solution theory. An empirical equation was proposed to correlate the solute mobility as a function of the fraction of vacant cage.

NOMENCLUTURE

A:	empirical parameter in Eq.(8)	[-]
B:	empirical parameter in Eq.(8)	[-]
G:	quantity of gas phase	[mol]
f:	fugacity	[MPa]
K:	Langmuir constant for simplified model	[1/MPa]
L:	quantity of liquid phase	[mol]
n_i:	quantity of component i	[mol]
P:	pressure	[MPa]
R:	gas constant	[J/(mol·K)]
T:	temperature	[K]
t:	time	[s]
V:	volume	[m^3]
x:	mole fraction in liquid	[-]
y:	mole fraction in gas	[-]
Z:	depth	[m]
μ:	chemical potential	[J/mol]
v:	fraction of water of cage type j	[-]
$\theta_{i,j}$:	occupancy of component i in cage type j	[-]
θ_i^*:	average occupancy of component i	[-]
ρ:	density	[mol/m^3]
ρ_{cage}:	cage number in a unit volume of hydrate	[mol/m^3]
ω:	effective mobility of solute	[$m^2/(s \cdot J)$]

<Subscript>

G	gas phase
hy:	hydrate solid
i,k:	component identification number
j:	cage type
L:	liquid phase
t:	total
v:	vacant

LITERATURE CITED

Adisasmito, S., R. J. Frank, III, and E. D. Sloan, Jr.; J. Chem. Eng. Data, 36, p68 (1991)

Hirohama,S., Y.Shimoyama, A.Wakabayashi, S.Tatuda and N.Nishida; J. Chem. Eng. Japan, 29, p1014 (1996)

Holder, G. D., V. A. Kamath and S. P. Godbole; Ann. Rev. Energy, 9, p427 (1984)

Kvenvolden K.A.: "International Conference on Natural Gas Hydrate", Annals of the New York Acad. of Sciences, vol 715, The New York Acad. of Sciences, New York, U.S.A., p 232 (1994)

Patel, N. C. and A. S. Teja; Chem. Eng. Sci, 37, 3, p463 (1982)

Saito, S., D. R. Marshall and R. Kobayashi; A.I.Ch.E. Journal, Sep., p734 (1964)

Waals, J. H. van der, and J. C. Platteeuw; Advances in Chemical Physics, vol.2, 1st

ed., Interscience, New York,U.S.A. p1 (1959)
Wiebe,R and V.L.Gaddy;"Vapor Phase Composition of Carbon Dioxide-Water Mixtures at Various Temperatures at Pressures to 700 Atmospheres," J.Am.Chem.Soc.,63,475-477(1941)

Table 1. Experimental conditions and results

items		unit	Hirohama et al.(1996)		This work	
Formation of CH_4-hydrate						
H_2O charged		[mol]	31.29	31.71	31.10	31.97
CH_4 trapped in hydrate		[mol]	4.23	3.74	4.16	4.52
H_2O remained free		[mol]	6.95	10.23	7.18	5.98
Purging CH_4 in gas phase by CO_2						
CH_4 remained in gas phase		[mol]	0.52	0.35	0.38	0.52
CO_2 existed in gas phase		[mol]	5.12	5.35	5.34	5.25
Soaking CH_4-hydrate in CO_2-CH_4 mixture						
liquid CO_2 charged		[mol]	10.3	10.3	10.94	10.16
CH_4 charged		[mol]	0	0	2.48	5.23
temperature		[K]	274	276	274	274
Material balance	CH_4	[%]	96		91	103
	CO_2	[%]	96		96	94
Reaction time		[h]	800	800	600	1100
CH_4 recovery		[%]	13	16	8	2

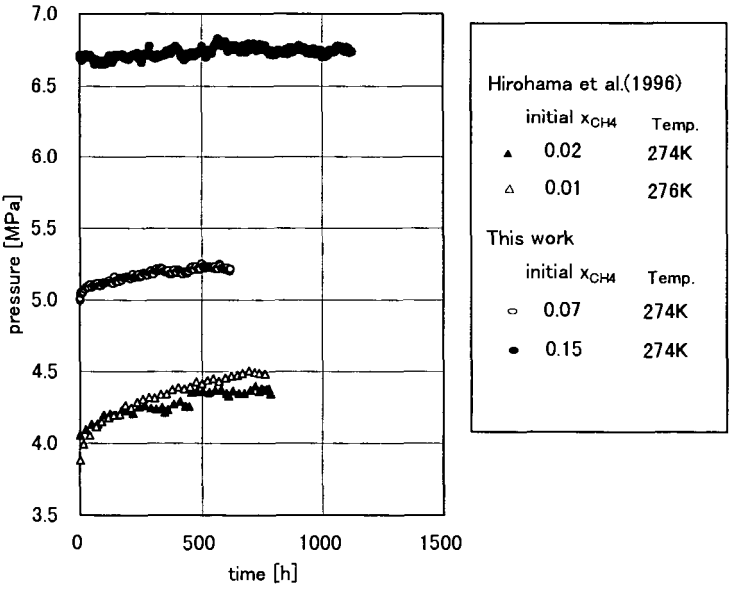

Fig.1 Change of total pressure

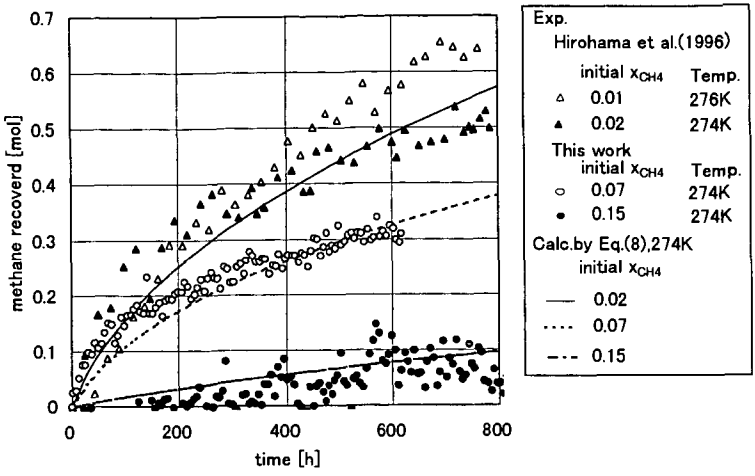

Fig.2 CH_4 recovered from the hydrate phase

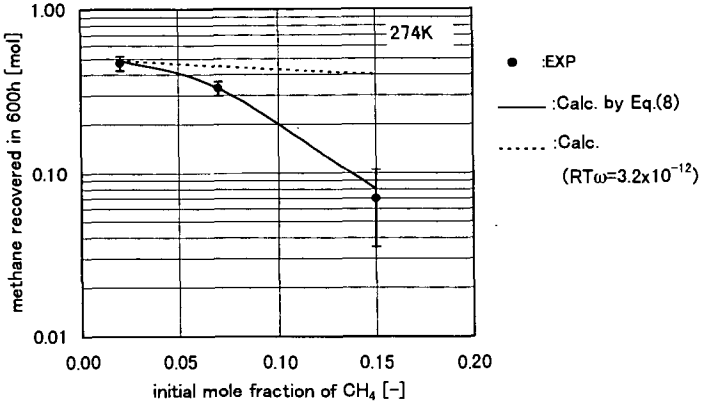

Fig.3 Effect of CH_4 content on methane recovery

SEARCHING FOR MICROBES AND OTHER BIOREMEDIATION TOOLS

Lisa Murdock
Amtrak West
The National Railroad Passenger Corporation
810 N. Alameda St.
Los Angeles, CA 90012

Charles Lin
Amtrak
The National Passenger Railroad Corporation
400 North Capitol St. NW
Washington, D. C 20001

Introduction

The National Passenger Railroad Corporation (Amtrak) is in the process of selecting bioremediation tools to enhance our waste water treatment systems. The primary contaminants of our waste water is diesel fuel, lube oil, and gear lubricants. The goal is to have a tool capable of being used at any Amtrak location in the United States. The bioremediation products are tested on a bench scale in Washington, D. C. and pilot tested in Los Angeles. Los Angeles is the chosen test site due to its mild climate and infrequent rain. The waste water treatment system in Los Angeles is a series of three settling ponds with a belt oil skimmer.

Experimental

The bench scale testing was performed using the following materials: a 10-gallon aquarium, a small air pump, a thermometer, 3 gallons of tap water, 20 drops of waste water from the Wilmington facility, a plastic teaspoon, a screen, a pipette, one 16 ounce glass bottle, and ½ mug of sea salt. Microbes are supplied for these experiments by various vendors.

1. The procedure is to aerate the aquarium filled with the tap water for approximately 1 hour.
2. Add 20 drops of the waste water to the aquarium.
3. Fill a 16 oz glass bottle with a waste water sample from the aquarium and place it in a cooler for analysis.
4. Empty the aquarium.
5. Repeat steps 1 and 2.
6. Spray ¼ teaspoon of microbes through the screen over the waste water in the aquarium.
7. Conditions: Temperature 74° F and pH 9.5.

Repeat the experiment using fertilizer and a greater concentration of waste water.

1. Aerate aquarium for 2 hours.
2. Fill 16 oz glass bottle with 100 drops of waste water and tap water. Place in the cooler for analysis.
3. Place 100 drops of waste water in a plastic tubing in the aquarium.
4. Filtered fertilizer into the tank using a mesh screen.
5. Spray ¼ teaspoon of microbes through screen over oil in the tubing.
6. Place a foam partition between tubing and air pump to eliminate over spill at the tubing.
7. Conditions: Temperature 72° F and pH 9.5.

The pilot testing was performed using the following materials: three 2lb. bags of bacteria, three 2 lb. bags of nutrients, nine 55-gallon drums of catalyst, Microbes are supplied for these experiments by various vendors. The products were introduced into three settling ponds 52 feet by 52 feet and 8 feet

deep. The three ponds were identified as S-1, S-2, and S-3. S-1 was filled to capacity, S-2 was ½ full, and S-3 was ¼ full.

1. Add three 55- gallon drums of catalyst per pond.
2. Hydrate one bag of nutrients with three gallons of water and then add one container per pond.
3. Hydrate one bag of bacteria with three gallons of water and then add one container per pond.
4. Conditions: Temperature 67° F.

No aeration or agitation was performed. All products were poured into the waste water. The waste water settling ponds had been inactive for several months prior to the pilot test (no treatment was being performed). The pilot test was performed for a period of five months. Analysis was performed monthly for the entire five months and samples were taken from the three phases of each pond top, middle, and bottom. The samples were analyzed for total petroleum hydrocarbons diesel specific EPA Method 8015 (TPH-D), metals EPA Method 6010, total recoverable petroleum hydrocarbons EPA Method 418.1, and oil and grease EPA Method 413.1. The analysis was performed by a California State ELAP certified laboratory.

Results and Discussion

The results from the first bench test showed after 24 hours oil flakes observed and a slick surface. A large amount of debris settled to the bottom of the aquarium. After 6 days the oil layer becomes thinner but the slick surface remains. More debris settles at the bottom. After 10 days the oil layer is even thinner and more debris has settled at the bottom of the aquarium. After 6 days the oil layer becomes thinner but the slick surface remains. The settled debris at the bottom of the aquarium increases. After 10 days the oil layer is even thinner and more debris has settled at the bottom of the aquarium.

The second bench test was done introducing the fertilizer to increase microbial activity. The analytical results are shown below:

Table 1 Bench Testing Results

Before	After	Analytical Method
692 mg/L	102 mg/L	8015
3.340 mg/L	1,840 mg/L	418.1

There was a color change after 24 hours from black to brown. The slick surface condition was observed again. The debris at the bottom of the aquarium was also observed again. The results listed as after above or from 48 hours of treatment with the microbes. The removal efficiency was calculated at 85% for the diesel fuel and 44% for the total petroleum hydrocarbons.

The pilot test results are very similar to what we observed in the bench test. The only real difference is that a longer period of time was allowed for the microbes to perform. See attached figures for the results for S-1, S-2, and S-3.

Month 1 Observations

S-1 appears to have a larger amount of oil rising to the surface. The oil is thicker and darker than before.

S-2 has a huge algae bloom which covers the surface of this pond.

S-3 has an algae bloom and the oil layer looks thinner.

Month 2 Observations

S-1 appears to have a larger amount of oil rising to the surface. The oil is thicker and darker than before.

S-2 still has some algae and the surface color is changing from black to brown.

S-3 has more and surface color is changing from black to brown.

Month 3 Observations

S-1 surface color is changing from black to brown.

S-2 has no algae growth and the surface appears much clearer you can see to the bottom of the pond. The sludge can be clearly seen.

S-3 has no algae growth and the surface appears much clearer you can see to the bottom of the pond. The sludge can be clearly seen.

Month 4 Observations

All ponds appear to be clear at the surface. The sludge looks darker and can be seen very clearly.

The analytical test results show a c decrease in the surface oil in all three ponds. The most oil contaminated pond S-1 showed the largest decrease in diesel and other petroleum hydrocarbons. See the attached Figures 1-6.

Conclusions

Bench testing of microbes can be correlated to pilot scale testing under industrial scale conditions. In both tests the microbes decreased the amount of surface oil in the waste water over time. The larger the amount of oil contamination the greater the activity of the microbes in degrading the oil. The efficiency of the microbes was observed in all cases to be greater than 80%. The time was controlled in these experiments and perhaps that had an impact on microbe efficiency. The additional time would probably cause this to increase.

The increased soil hydrocarbon numbers was not caused by surface oil migrating to the sludge phase. The more likely conclusion is that microbes migrated to the sludge phase after all of the surface oil was degraded. The beginning of the sludge degradation is observed with a large initial increase in petroleum concentration and then a tapering. If the pilot test had been maintained longer a decrease in the sludge petroleum concentrations should be observed. In the future, tests will be conducted with new microbes using the same methods on waste water. There will also be additional tests performed on soil and sludge under similar conditions.

The success of bioremediation tools is very important to the railroad industry. A reasonably priced treatment technology can save thousands of dollars in disposal costs. The disposal costs including treatment and transportation for fuel contaminated soil is generally between $26.00-$35.00 per ton. The price to treat soil using bioremediation methods is approximately $2-$10 per ton. Bioremediation of water has similar costs comparison that is why it is so important to have test methods that prove which products are really successful.

References

1. Disinfection of Wastewater-Task Force Report EPA-430/9-75-013, U. S. Environmental Protection Agency, Washington, D. C. 1976.
2. Yaws, C. L., H-C. Yang, J. R. Hopper, and K. C. Hansen 1990. 232 Hydrocarbons: Water Solubility Data. Chemical Engineering, April, pp. 177-182.
3. Hutchins, S. R., Sewell, G. W., Kovacs, D. A., and Smith, G.A. 1991b, Biodegradation of aromatic hydrocarbons by aquifer microorganisms under nitrifying conditions. Environ. Sci. Technol. 25, 68-76.
4. Kaufman, A. K., Krueger, C. C., Applied Bioremedial Technology: Feasibility Criteria, Proceedings of the Hazardous Materials and Environmental Management Conference West/Spring, Long Beach, CA 1993.
5. Environmental Compliance Handbook for Short Line Railroads, U. S. Environmental Protection Agency and U. S. Department of Transportation, Washington, D. C. April 1996.

Figure 1 Pond S1

S1-Top	S-1-Middle	S-1-Bottom
1800	23	8400
1300	11	49,000
11	9.4	42,000

Figure 2 Pond S2

S-2-Top	S-2-Middle	S-2-Bottom
8.9	6	2500
5.1	181	21,000
5.1	5.1	29,000

Figure 3 Pond S3

S-3-Top	S-3- Middle	S-3-Bottom
0	0	7.8
3	3	5,000
3	4	4,300

Figure 4

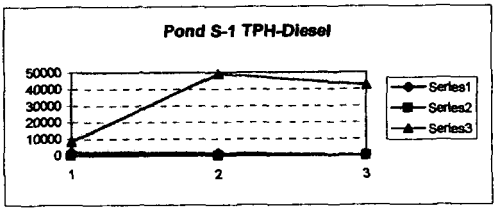

Figure 5

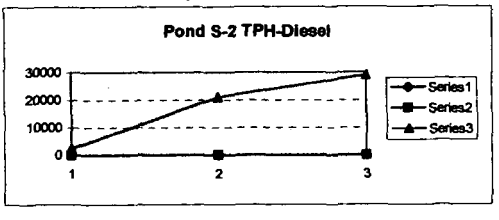

Figure 6

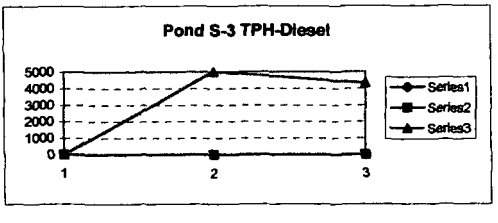

MODIFICATION OF COAL-DERIVED MATERIALS BY *RHODOCOCCUS* SPP.

D. L. Stoner,* J. G. Jolley, R. B. Wright, and K. S. Miller
Idaho National Engineering and Environmental Laboratory
Lockheed Martin Idaho Technologies Company, Inc.
P. O. Box 1625, Idaho Falls, ID 83415-2203

INTRODUCTION

The isolation and identification of microorganisms which degrade organic sulfur compounds is often considered the first step in the development of a biological process for the removal of coal organic sulfur (1-4, 7-9). Organic sulfur compounds which contain thiophene, sulfide, disulfide, or thiol groups are used as analogs of the sulfur-containing functionalities and compounds found in coal and coal-derived materials. Because the organic sulfur moieties are assumed to be an integral part of the macromolecular structure, the preferred coal beneficiation process would selectively remove the sulfur and leave the carbon matrix intact with a minimum of oxidation. Microorganisms which degrade dibenzothiophene via the excision of the thiophenic sulfur (2, 3, 5, 6, 10) are of particular interest to the biological treatment of coals containing relatively high proportions of thiophenic sulfur.

Two bacteria, UMX3 and UMX9, isolated by Purdy et al (6) are able to desulfurize dibenzothiophene or dibenzothiophene sulfone. These bacteria, tentatively identified as members of the genus *Rhodococcus* are capable of sustained growth in media in which DBT or DBT-sulfone are the only added source of sulfur. Sulfur is selectively removed leaving 2 phenylphenol. Desulfurization activity is manifested during growth and is repressed by the presence of sulfate.

In order to be effective for coal desulfurization, microorganisms must be able to mediate the desired enzymatic transformation on coal, a chemically complex and heterogeneous material. This paper describes the evaluation of microbial strains UMX3 and UMX9 for the ability to modify water-soluble coal-derived materials. Soluble coal materials (Fig. 1) have been used as substrates to assess microbial desulfurization (7-9). The soluble coal materials are chemically representative but are without the physical limitations inherent with the use of particulate coal.

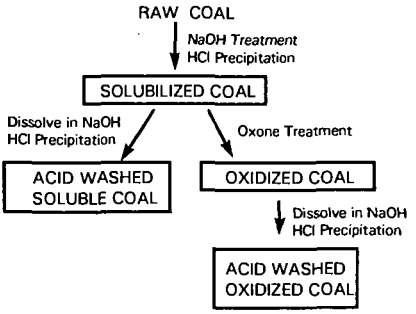

Figure 1: Schematic of the methods used to prepare water-soluble coal materials.

METHODS

Cultures UMX3 and UMX9 were provided by Bailey Ward, University of Mississippi, University, MS. Prior to their use in this study, cultures were transferred 3 times and confirmed for growth on sulfur-limited (SL) medium containing DBT-sulfone as the sole source of sulfur (6).

Cultures UMX3 and UMX9 were tested for the ability to remove sulfur from the soluble coal and oxidized soluble coal materials. Cells from starter cultures of UMX3 and UMX9 were harvested by centrifugation and washed twice with several volumes of sterile phosphate buffered saline (PBS) solution. The washed cells were resuspended in a small volume of PBS. Approximately one-half of the cells were used to inoculate the soluble coal medium and the remaining cells used to inoculate the oxidized soluble coal media. Cultures were shaken at 30°C for 7 days.

In an experiment which utilized a relatively large amount of biomass, one liter cultures of UMX3

and UMX9 were cultivated on SL medium, harvested as noted previously, and washed twice with sterile PBS. Approximately one-half of these cells were used to inoculate 1 liter of medium amended with 100 mg of oxidized soluble coal material (from a filter-sterilized 2.5% solution) while the remaining cells were used to inoculate medium which was amended with 20 mM $MgSO_4$ to inhibit desulfurization activity. There were cell-free controls for each treatment. Cultures were analyzed at 3 days.

To prepare samples for analysis, cells were removed by centrifugation followed by filtration (0.2μm pore size membrane filters). The coal material was precipitated by acidification to pH 1.5 using 6 N HCl. The precipitate was collected by centrifugation and washed twice with pH 1.5 water (acidified with HCl), then freeze-dried. Elemental composition was determined using an elemental analyzer (Model EA1108, CarloErba/Fisons Instruments, Valencia, CA). Fourier transform infrared (FTIR) spectra of coal and soluble coal materials formed into KBr pellets were obtained by using an FTIR spectrometer (model FTS-65; Digilab). For XPS spectra (PHI 5400 ESCA, Perkin Elmer, Inc.), energy corrections (downwards by 0.5 to 1 eV) were made to correct for sample charging based on the C(1s) peak position at 284.5 eV. Data in Tables 1 and 2 were obtained using the services of Huffman Laboratories, Inc., (Golden, CO).

RESULTS AND DISCUSSION

Water-soluble materials derived by alkali treatment of weathered or low-grade coals have been used to examine the mechanisms by which bacteria modify coal organic sulfur (7-9). The water-soluble characteristic of the coal products makes them an excellent and easy-to-use substrate for biodesulfurization studies. The accessibility of the organic functional groups to microbial attack may be enhanced by the water solubility, while the absence of inorganic sulfur facilitates the interpretation of data. In this study, the sulfur (Table 1) in water-soluble materials derived from Ugljevik coal was almost entirely organic sulfur (Table 2).

TABLE 1. COMPOSITION DATA FOR MATERIALS DERIVED FROM UGLJEVIK COAL

ANALYSIS %	RAW	SOLUBLE	OXIDIZED SOLUBLE	ACID WASH	ACID WASH OXIDIZED
MOISTURE*	7.1	6.5	4.7	7.2	9.6
CARBON	56.5	57.0	57.8	59.2	57.9
HYDROGEN	4.9	4.1	4.5	4.4	4.3
OXYGEN	24.1	27.5	30.6	29.9	31.1
NITROGEN	1.5	1.8	1.8	1.7	1.7
SULFUR	6.8	6.4	5.6	5.9	5.0
ASH	15.0	3.9	0.4	0.3	0.2

*Moisture is reported on an 'as received' basis. All others are reported on a 'dry weight' basis.

TABLE 2. SULFUR FORMS DATA FOR RAW, SOLUBLE AND OXIDIZED SOLUBLE COAL MATERIALS DERIVED FROM UGLJEVIK COAL.

ANALYSIS (%)	RAW	SOLUBLE	OXIDIZED SOLUBLE	ACID WASH SOLUBLE	ACID WASH OXIDIZED
TOTAL SULFUR	6.8	6.2	5.6	5.9	5.0
SULFATE SULFUR	0.3	0.7	1.3	0.1	0.1
PYRITIC SULFUR	1.1	<.2	<0.2	0.0	0.04
ORGANIC SULFUR	5.4	5.6	4.3	5.7	4.9

The cultures grew in medium amended with the water-soluble Ugljevik coal material. UMX3 increased from 4.1×10^8 cells/ml to 3.8×10^9 cells/ml, while UMX9 increased from 8.4×10^7 cells to 3.6×10^9 cells/ml. After 7 days of incubation, the cultures appeared to do little to the elemental composition of soluble coal material (Table 3).

TABLE 3. ELEMENTAL ANALYSIS OF WATER-SOLUBLE UGLJEVIK COAL MATERIAL TREATED WITH BACTERIAL CULTURES UMX3 AND UMX9

Sample	C (%)	H (%)	N (%)	S (%)	C/S	S (% control)
Day 0						
Control	57.7 ± 0.2	4.6 ± 0.2	1.9 ± 0.0	5.7 ± 0.2	10.1 ± 0.4	
UMX3	58.2 ± 0.1	4.8 ± 0.0	1.9 ± 0.0	5.9 ± 0.0	9.9 ± 0.1	103.2 ± 0.7
UMX9	57.9 ± 0.2	4.8 ± 0.1	1.9 ± 0.0	5.9 ± 0.0	9.8 ± 0.1	103.9 ± 0.3
Day 7						
Control	58.2 ± 0.2	4.9 ± 0.1	2.0 ± 0.0	5.7 ± 0.1	10.2 ± 0.1	
UMX3	58.7 ± 0.3	4.9 ± 0.2	2.1 ± 0.0	5.7 ± 0.1	10.3 ± 0.2	99.5 ± 1.8
UMX9	59.1 ± 0.2	4.7 ± 0.1	2.1 ± 0.0	5.8 ± 0.2	10.2 ± 0.4	101.8 ± 3.1

When cultivated on oxidized water-soluble coal material UMX3 increased from 7.1×10^8 cells/ml on day 0 to 4×10^9 cells/ml on day 7. UMX9 increased from 6.6×10^7 cells/ml to 2.6×10^9 cells/ml. No desulfurization activity was detected with the oxidized coal (Table 4).

TABLE 4. ELEMENTAL ANALYSIS OF OXIDIZED WATER-SOLUBLE UGLJEVIK COAL MATERIAL TREATED WITH BACTERIAL CULTURES UMX3 AND UMX9

Sample	C (%)	H (%)	N (%)	S (%)	C/S	S (% control)
Day 0						
Control	56.4 ± 0.3	4.7 ± 0.0	1.8 ± 0.0	5.2 ± 0.0	10.9 ± 0.1	
UMX3	55.2 ± 1.0	4.5 ± 0.2	1.8 ± 0.1	5.1 ± 0.0	10.9 ± 0.2	98.3 ± 0.7
UMX9	56.3 ± 0.1	4.6 ± 0.1	1.8 ± 0.0	5.3 ± 0.1	10.6 ± 0.2	102.5 ± 1.9
Day 7						
Control	57.8 ± 0.2	4.8 ± 0.1	2.0 ± 0.0	5.2 ± 0.2	11.2 ± 0.5	
UMX3	57.9 ± 0.1	4.9 ± 0.1	2.1 ± 0.0	5.1 ± 0.1	11.5 ± 0.2	97.7 ± 1.5
UMX9	56.3 ± 0.2	4.7 ± 0.1	2.0 ± 0.0	5.2 ± 0.1	10.9 ± 0.1	100.2 ± 1.2

The inability to detect changes in the sulfur content of bacterially-treated coal material may have been due to the extremely small amounts required for cell growth. The sulfur requirement for growth is only 0.2% of the wet weight of the biomass. Table 5 reports the data for an experiment in which a relatively high amount of biomass was used. Again, the bacterial cultures did not appear to desulfurize the coal material.

TABLE 5. ELEMENTAL ANALYSIS OF OXIDIZED WATER-SOLUBLE UGLJEVIK COAL MATERIAL TREATED WITH HIGH BIOMASS

	C (%)	H (%)	N (%)	S (%)	C/S	S (% CONT)
Starting Material	54.9 ± 0.6	4.3 ± 0.1	1.7 ± 0.0	5.3 ± 0.1	10.3 ± 0.1	
Sulfur "Limited"						
Control	54.6 ± 0.1	4.2 ± 0.1	1.9 ± 0.0	5.2 ± 0.1	10.4 ± 0.2	
UMX3	54.7 ± 0.1	4.3 ± 0.1	2.2 ± 0.0	5.3 ± 0.2	10.5 ± 0.4	98.3 ± 3.8
UMX9	54.5 ± 0.2	4.4 ± 0.1	2.3 ± 0.0	5.0 ± 0.3	10.9 ± 0.6	96.6 ± 5.3
Sulfate Amended						
Control	53.7 ± 0.2	4.3 ± 0.0	1.8 ± 0.0	5.3 ± 0.1	10.8 ± 0.2	
UMX3	54.5 ± 0.4	4.7 ± 0.0	2.4 ± 0.0	4.9 ± 0.1	11.2 ± 0.2	92.7± 2.4
UMX9	54.7 ± 0.2	4.5 ± 0.1	2.4 ± 0.0	5.0 ± 0.1	10.9 ± 0.1	95.1 ± 1.0

As determined by FTIR analysis, the treatment of the soluble coal materials with cultures UMX3 and UMX9 had little effect on the organic constituents of the materials (Data not shown). The microbially-treated oxidized coal material exhibited a slight depletion in the region of 3330 to 3400 cm^{-1} while the microbially-treated soluble coal material exhibited an enhanced signal in this region. This region was assigned to water and coal-OH and coal-NH functionalities. Both UMX3 and UMX9 treated oxidized coal material exhibited greater absorbances in the regions of 1780 cm^{-1}, 1630 cm^{-1}, and 1540 cm^{-1}. The increased absorbances at 1780 and 1630 cm^{-1} were attributed to highly conjugated carbonyl functionalities. The absorbance at 1630 cm^{-1} may also

have been due to primary amines or water. The peak at 1540 cm^{-1} was attributed to carboxylate anion functionalities, aromatic groups or conjugated and aromatic nitro groups.

Both UMX3 and UMX9-treated soluble coal had slight increases in absorbances in the regions of 3400, 1630, and 1030 cm^{-1}. An increase in absorbance at 1780 and 1540 cm^{-1} was observed for UMX3-treated soluble coal material while these same regions exhibited a decrease for soluble coal material treated with UMX9.

In view of the data presented here and in earlier publications (Stoner et al., 1990, 1991) the use of model compounds to select for bacteria that can desulfurize coal may be problematic. The effectiveness of such microorganisms may be dependent on the relative abundance of that organosulfur form in the coal. In this case, the ability of UMX3 and UMX9 to desulfurize the water-soluble coal materials may have been dependent on the amount of thiophenic moieties that were present. Coal and coal-derived materials are complex substrates, whose chemical structures are still undefined. The coal materials behave as complex polymers which would be quite different from the model compounds used to select the bacteria. Therefore, there is the possibility of steric hindrance interfering with enzymatic activity.

ACKNOWLEDGEMENTS

This work was supported under contracts DE-AC07-76ID01570 and DE-AC01-94-ID13223 from the U. S. Department of Energy to the Idaho National Engineering Laboratory

LITERATURE CITED

1. Constanti, M., A. Bordons, and Jaume Giralt. 1994. Degradation of dibenzothiophene by *Pseudomonas putida*. Letts. Appl. Microbiol. 18:107-111.

2. Kilbane, J. J., 1990. Microbial removal of organic sulfur from coal: Current status and research needs. p. 487-506. In Bioprocessing and Biotreatment of Coal. D. L. Wise, (ed.), Marcel Dekker, Inc., New York.

3. Kilbane, J. J., 1990. Sulfur-specific microbial metabolism of organic compounds. Res. Conserv. Recycl. 3:69-79.

4. Krawiec, S. 1990. Transformations of dibenzothiophene by axenic cultures of *Sulfolobus acidocaldarius* and other bacteria: A critique. p. 569-601. In Bioprocessing and Biotreatment of Coal. D. L. Wise, (ed.), Marcel Dekker, Inc., New York.

5. Omori, T., L. Monna, Y. Saiki, and T. Kodama. 1992. Desulfurization of dibenzothiophene by *Corynebacterium* sp. strain SY1. Appl. Environ. Microbiol. 58:911-915.

6. Purdy, R. F., B. Ward, and J. E. Lepo. 1991. Microbial extraction of sulfur from model coal organosulfur compounds. p. 63-82. In Proceedings of the Third Symposium on Biotechnology of Coal and Coal-Derived Substances. DGMK, Hamburg, Germany.

7. Stoner, D. L., 1993. Microbial transformation of organic nitrogen and sulfur in low rank coals. p. 157-169. In Microbial Transformations of Low Rank Coals. D. L. Crawford (ed.) CRC Press, Boca Raton, FL.

8. Stoner, D. L., K. S. Miller, K. B. Barrett, J. B. Tingey, R. B. Wright, and J. E. Wey. 1991. The use of water-soluble coal products to examine microbial coal desulfurization. p. 549-566. In. Processing and Utilization of High Sulfur Coals, IV. P. R. Dugan, D. R. Quigley and Y. A. Attia, (eds.) Elsevier Science Publishers, B. V. Amsterdam.

9. Stoner, D. L., J. E. Wey, K. B. Barrett, J. G. Jolley, R. B. Wright, and P. R. Dugan. 1990. Modification of water-soluble coal-derived products by dibenzothiophene-degrading microorganisms. Appl. Environ. Microbiol. 56:2667-2676.

10. van Afferden, M., S. Schacht, J. Klein, and H. G. Trüper. 1990. Degradation of dibenzothiophene by *Brevibacterium* sp. DO. Arch. Microbiol. 153:324-328.

BIOREMEDIATION OF SYNTHETIC CHEMICALS AS A CONSEQUENCE OF GROWTH ON PETROLEUM HYDROCARBONS.

Charles C. Somerville* and Erica S. K. Becvar†
USAF Armstrong Laboratory, Environics Directorate*
and Applied Research Associates†
139 Barnes Drive, Tyndall AFB, FL 32403

INTRODUCTION

The Department of Defense uses approximately 8.5 million gallons of light distillate fuels each day (1). At this level of use, spills or leaks during transport, storage, or use can lead to a large environmental burden of fuel hydrocarbons. The Air Force alone has more than 2,500 sites that are contaminated with petroleum hydrocarbons. Fortunately, the components of light fuels are naturally occurring compounds. Because of their long term presence and wide distribution in the environment, many soil microorganisms have adapted to the degradation of fuel compounds. In fact, it is likely that all natural products can be degraded by one or more microbial species under the proper conditions (2). This does not mean that spills and leaks of light fuels are unimportant or that such contamination will always be amenable to bioremediation. However, it does mean that natural or augmented biological processes are important tools in the cleanup of fuel-contaminated sites.

Unfortunately, environmental contamination is not limited to naturally occurring chemicals. Some man-made chemicals (e.g. highly substituted chloro- and nitro-compounds) are common environmental contaminants and are known to resist biodegradation. However, the presence of petroleum hydrocarbons at contaminated sites can actually aid, directly or indirectly, in the degradation of synthetic co-contaminants. In this report, we consider the biodegradation of two types of synthetic compounds influenced by the presence of petroleum hydrocarbons in the environment. The first type includes the chlorinated ethenes: tetrachloroethylene (PCE), trichloroethylene (TCE), the isomers of dichloroethylene (DCEs), and vinyl chloride (VC). The second type includes substituted aromatic compounds such as chloro- and nitroaromatics.

CHLORINATED ETHENES

PCE and TCE have been used extensively in dry cleaning, degreasing of metals, and as solvents (3). The prevalent use of these solvents has led to widespread environmental contamination. TCE has been reported to be the major volatile organic contaminant of groundwater in the United States (4). There are a growing number of reports on the degradation of chlorinated ethenes by bacterial consortia and isolated bacterial species. The biotic degradation of chlorinated ethenes appears to occur in one of two ways: (i) cometabolic attack by non-specific oxygenases, or (ii) dehalorespiration.

Cometabolic Oxidation. Several species of bacteria produce enzymes which cometabolize PCE and/or TCE. The enzymes studied in the greatest detail are methane monooxygenase, toluene dioxygenase, and toluene monooxygenase. All three types of enzymes have relaxed substrate specificity and will fortuitously degrade chlorinated ethenes. The presence of fuel hydrocarbons in the environment can lead to the establishment of conditions favoring cometabolism of chlorinated ethenes.

In the jet fuel JP-4 n-alkanes constitute 32% of the mixture by weight (5). The n-alkanes of intermediate chain length are degraded by terminal oxidation to a carboxylic acid followed by β-oxidation. The acetyl-coenzyme A produced as a result is further metabolized to carbon dioxide by the tricarboxylic acid cycle for energy production, or converted to cellular carbon via the glyoxylate cycle. The n-alkanes of odd chain length result in the formation of propionyl-coenzyme A which is further metabolized to pyruvic acid with the concomitant production of hydrogen (6). The consumption of oxygen coupled with the production of carbon dioxide and hydrogen produces conditions favorable to the biological formation of methane. Methanotrophic bacteria, in turn, utilize methane via a series of oxidations to yield carbon dioxide (6). The initial oxidation of methane to methanol is catalyzed by the enzyme methane monooxygenase (MMO). Methanotrophic bacteria characterized to date produce two forms of the enzyme: a membrane-associated particulate form (pMMO) which requires copper for activity, and a soluble form (sMMO) which is expressed under copper-limited conditions (7). Both pMMO and sMMO oxidize TCE, but sMMO degrades TCE at higher rates (8) and has been demonstrated to catalyze the transformation of DCEs (9). A series of reactions leading to methane formation and TCE transformation is outlined in Fig. 1.

Aromatic compounds account for approximately 20% of the jet fuel JP-4 by weight (5). Mineralization of aromatic substrates is usually initiated by hydroxylation of the ring by either dioxygenase or monooxygenase reactions. Many of the enzymes which initiate degradation of aromatic compounds (e.g. toluene) are also capable of attacking TCE (Fig. 2). Therefore, the contamination of a site with fuel hydrocarbons can select for a microbial population pre-adapted to the degradation of TCE. In fact, exogenous addition of aromatic hydrocarbons has been shown to stimulate the degradation of TCE *in situ* (11-13). Fortuitous oxidation of TCE has generally not been observed in the absence of inducer compounds such as phenol or toluene. Recently, however, Leahy et al. (14) confirmed that the toluene monooxygenase of some strains is induced by TCE. Still, TCE does not serve as a source of carbon or energy for these strains, and thus can

not sustain the degrader population. Unfortunately, none of the aromatic oxygenases have been demonstrated to attack PCE or VC, and only toluene dioxygenase has activity against the DCE isomers (see Fig. 2). Another drawback of toluene/TCE cometabolism is a high demand for oxygen which is required as a co-substrate in the oxidation of both TCE and the primary substrate. Oxygen is also required as a terminal electron acceptor by the host bacterium. Oxygen limitation has been shown to inhibit TCE degradation in soil (15). The addition of nitrate to contaminated soils may overcome oxygen limitation for denitrifying strains, but some of the best studied TCE-degrading isolates (e.g. *Burkholderia cepacia* G4 and *Pseudomonas putida* F1) are not denitrifiers (14).

Toluene and methane oxygenases have been most extensively studied. However, other bacterial oxygenases, including ammonia monooxygenase (16) and propane monooxygenase (17), also degrade TCE. Propane monooxygenase is notable for its ability to degrade DCEs and VC. Chloroethene degradation, however, does not appear to be a common property of bacterial oxygenases. Wackett et al. (17) showed that nitropropane dioxygenase, cyclohexanone monooxygenase, cytochrome P-450 monooxygenases, 4-methoxybenzoate monooxygenase, and hexane monooxygenase do not attack TCE.

Dehalorespiration. In the process of dehalorespiration, chlorinated compounds serve as terminal electron acceptors for anaerobic bacteria growing on an appropriate carbon source. Dehalorespiration differs from cometabolism in that the bacteria that mediate reductive dechlorination gain energy from the process. The combination of chloroethenes with a suitable electron donor can thus support growth of strains capable of coupling dechlorination to energy production. Reductive dechlorination of halogenated aliphatic compounds was first reported in the early 1980's (18). Vogel and McCarty (19) later established the pathway for reductive dechlorination of PCE to VC under methanogenic conditions. Although [^{14}C]PCE mineralization was demonstrated by the detection of labeled carbon dioxide, the major products of dechlorination were TCE and VC. The formation of VC represents an increase in toxicity over TCE or PCE, and seemed to indicate that reductive dechlorination would be deleterious at contaminated sites. It was later found that PCE and TCE could be dehalogenated to ethylene (ETH) under methanogenic conditions (20). However, the dehalogenation of VC was rate limiting, and in many situations VC was found to persist (21). A breakthrough was made when DiStefano et al. (21) tested a mixed culture of predominantly methanogenic bacteria for dehalogenation of PCE. At very high initial levels of PCE, methanogenesis was completely inhibited, and the culture gave a nearly complete conversion of PCE to ETH. Further study of the culture showed that hydrogen was the direct electron donor for reductive dechlorination and that the bulk of the hydrogen was produced by acetogenic bacteria growing on methanol. High levels of PCE selectively inhibited the methanogenic bacteria that would otherwise compete for available hydrogen (22). The organism responsible for dehalogenation of chloroethenes has recently been isolated and identified as a eubacterium tentatively named *Dehalococcoides ethenogenes* (23). Furthermore, Sharma and McCarty (24) isolated a facultative enterobacterium that dehalogenates PCE primarily to *cis*-1,2-DCE in the absence of oxygen, nitrate, and fermentable carbon sources. The ability to work with pure cultures represents a major advance in the effort to determine the conditions most favorable for complete dehalogenation of chloroethenes. The pathway for the dehalogenation of PCE to ETH is shown in Fig. 3.

SYNTHETIC SUBSTITUTED AROMATICS

Synthetic substituted aromatic compounds are common industrial chemicals and are often found as soil and groundwater contaminants. Microorganisms that mineralize synthetic aromatic compounds can be isolated from contaminated soil and groundwater but have not been isolated from uncontaminated sites. This suggests that a selection or adaptation process must occur after site contamination. One hypothesis is that the enzymes which attack synthetic aromatics are homologous to enzymes specific for naturally-occurring aromatic hydrocarbons. The isolation and sequencing of the genes encoding degradative enzymes have allowed us to test that hypothesis for chlorobenzene and nitrotoluene degradative pathways.

Chlorobenzenes. *Pseudomonas* sp. strain P51 grows on 1,2-dichlorobenzene, 1,4-dichlorobenzene, and 1,2,4-trichlorobenzene as sole sources of carbon and energy (25). The metabolic pathway for chlorobenzenes in strain P51 proceeds from an initial dioxygenase attack to yield a chloro-dihydrodiol intermediate which is rearomatized by the action of a diol dehydrogenase to form a di- or trichlorocatechol. The aromatic ring is opened in the *ortho* position by a chlorocatechol dioxygenase, and the substrate is mineralized by a series of reactions analogous to the β-ketoadipate pathway (6, 25). Removal of the chloro substituents is thought to occur after ring cleavage. The striking similarities between the metabolism of chlorobenzenes and naturally occurring aromatic hydrocarbons (e.g. benzene, phenol, toluene) strongly suggests that pre-existing enzymes have become adapted to chlorinated compounds. The genes that encode the initial chlorobenzene dioxygenase from strain P51 have been isolated and sequenced (26), and that data can be used to determine the phylogeny of the enzyme.

Fig. 4 is a phylogram of large subunits of the terminal dioxygenase (ISPLs) of ten aromatic ring dioxygenases identified by their primary substrate. The phylogenetic analysis indicates a close and statistically significant relationship between chlorobenzene dioxygenase and benzene and toluene dioxygenases. The topology of the phylogram suggests that the chlorobenzene dioxygenase of strain P51 shares a recent common ancestor with benzene and toluene dioxygenases, and that their common ancestor evolved from a biphenyl dioxygenase. The data clearly support the theory that enzymes which attack chloroaromatics arise by adaptation of

enzymes specific for aromatic petroleum hydrocarbons.

Nitrotoluenes. The metabolic pathways for both 2-nitrotoluene (2-NT) and 2,4-dinitrotoluene (2,4-DNT) are initiated by dioxygenase reactions which form diol-derivatives of the parent compounds (37, 38). The degradation of these nitroaromatic compounds differs from that of the chlorobenzenes in three respects: (i) rearomatization of the ring occurs spontaneously, (ii) rearomatization is accompanied by elimination of a substituent nitro group prior to ring cleavage, and (iii) the ring is opened by a *meta* ring cleavage. Although the initial reactions differ in these details, the overall degradation of nitrotoluenes is analogous to the *meta*-cleavage pathway of naturally-occurring aromatic compounds (6) . Sequence data are available for three oxygenases that attack nitrotoluenes (39-41), and can be used to establish the origin of these enzymes.

Fig. 5 is a phylogram of the ISPLs of ten aromatic ring dioxygenases including the three nitrotoluene dioxygenases. The nitrotoluene degrading enzymes form a statistically significant, exclusive group, and clearly share a recent common ancestor with enzymes that hydroxylate polyaromatic hydrocarbons. This relationship again implies that enzymes for naturally-occurring substrates have adapted to the degradation of synthetic compounds (although the chemical similarity between PAHs and nitrotoluenes is not immediately apparent). The fact that the three nitrotoluene dioxygenase sequences cluster together is interesting because the organism that degrades 2-NT was found at a site hundreds of miles away from the site where the 2,4-DNT degraders were found (37, 44). This observation suggests that enzymes which attack synthetic compounds do not arise *de novo* at each contaminated site; however, more data will have to be collected before the mechanisms of adaptation are clear.

CONCLUSIONS

The studies of chlorinated ethenes, chloroaromatics, and nitroaromatics clearly show that the presence of bacteria adapted to the degradation of fuel hydrocarbons can have a positive impact on the bioremediation of man-made chemicals. Cometabolic processes are clearly of interest; however, there are obstacles to relying on these processes for site remediation. Because cometabolism does not provide the bacterial community with carbon or energy, it is not a self-sustaining process. The cometabolism of TCE by methane or toluene oxygenases is oxygen intensive, and will therefore be of limited extent in unamended soil and groundwater. Also, the enzymes which catalyze the breakdown of chloroethenes are primarily limited to TCE degradation and will not be useful at sites where PCE or VC have accumulated.

Dehalorespiration is an exciting alternative to cometabolic oxidation of chloroethenes for two reasons. First, the biological degradation of light fuels is an oxygen-intensive process. Removal of oxygen inhibits cometabolic degradation but favors reductive dehalogenation. Second, reductive dehalogenation appears to function on a much wider range of chloroethenes than cometabolism indicating that the process could prove useful at many contaminated sites. Furthermore, the presence of DCEs and VC at sites known to have been contaminated with PCE or TCE indicates that reductive dehalogenation is already occurring in the environment (45-47).

We now know that enzymes which attack chlorobenzenes and nitrotoluenes are homologous to enzymes specific for naturally occurring compounds. Therefore, the presence of petroleum hydrocarbons at a site co-contaminated with one or more of these synthetic compounds may enrich for the presence of the genotypes required for bioremediation of the man-made chemicals. Research is now in progress to answer some of the basic questions regarding how bacteria adapt to the degradation of xenobiotic compounds.

Based on the information presented here, we recommend careful analysis of data from contaminated sites in order to take advantage of fortuitous interactions between co-contaminants. We encourage both industry and regulatory agencies to continue to look for opportunities to use *in situ* biological remediation strategies as alternatives, or supplements, to physical remediation of sites contaminated with synthetic compounds.

LITERATURE CITED

(1) Wells, R. *Personal communication*, **1996**.
(2) Alexander, M. *Biodegradation and Bioremediation.* Academic Press: San Diego, **1994**.
(3) Budavari, S.; O'Neil, M.J.; Smith, A.; Heckelman, P.E (eds.). *The Merck Index* (11th edition). Merck & Co.: Rahway, NJ, **1989**.
(4) Shields, M.S; Reagin, M.J. *Appl. Environ. Microbiol.*. **1992**, *58*, 3977-3983.
(5) Spain, J.C.; Somerville, C.C.; Lee, T.J.;Butler, A.C; Bourquin, A.W. *Degradation of Jet Fuel Hydrocarbons by Aquatic Microbial Communities.* (AFESC ESL-TR-83-26), **1983**.
(6) Gottschalk, G. *Bacterial Metabolism* (2nd edition). Springer-Verlag: New York, **1986**.
(7) Zahn, J.A.; DiSpirito, A.A. *J. Bacteriol.* **1996**, *178*, 1018-1029.
(8) McDonald, I.R.; Uchiyama, H; Kambe, S.; Yagi, O.; Murrell, J.C. *Appl. Environ. Microbiol.* **1997**, *63*, 1898-1904.
(9) Oldenhuis, R.; Vink, R.L.M.K.; Janssen, D.B.; Witholt, B. *Appl. Environ. Microbiol.* **1989**, *55*, 2819-2826.
(10) Little, C.D.; Palumbo, A.V.; Herbes, S.E.; Lidstrom, M.E.; Tyndall, R.L.; Gilmer, P.J. *Appl. Environ. Microbiol.* **1988**, *54*, 951-956.
(11) Gibson, S.A.; Sewell, G.W. *Appl. Environ. Microbiol.* **1992**, *58*, 1392-1393.
(12) Major, D.W.; Cox, E.E. pp. 48-56 In *In situ Bioremediation Symposium.* Niagara-on-the-Lake, Canada, **1992**.
(13) Hopkins, G.D.; McCarty, P.L. *Environ. Sci. Technol.* **1995**, 29, 1628-1637.

(14) Leahy, J.G.; Byrne, A.M.; Olsen, R.H. *Appl. Environ. Microbiol.* **1996**, *62*, 825-833.
(15) Fan, S.; Scow, K.M. *Appl. Environ. Microbiol.* **1993**, *59*, 1911-1918.
(16) Vannelli, T.; Logan, M.; Arciero, D.; Hooper, A.B. *Appl. Environ. Microbiol.* **1990**, *56*, 1169-1171.
(17) Wackett, L.P.; Brusseau, G.A.; Householder, S.R.; Hanson, R.S. *Appl. Environ. Microbiol.* **1989**, *55*, 2960-2964.
(18) Bouwer, E.J.; McCarty, P.L. *Appl. Environ. Microbiol.* **1983**, *45*, 1286-1294.
(19) Vogel, T.M.; McCarty, P.L. *Appl. Environ. Microbiol.* **1985**, *49*, 1080-1083.
(20) Freedman, D.L.; Gossett, J.M. *Appl. Environ. Microbiol.* **1989**, *55*, 2144-2151.
(21) DiStefano, T.D.; Gossett, J.M.; Zinder, S.H. *Appl. Environ. Microbiol.* **1991**, *57*, 2287-2292.
(22) Maymó-Gatell, X.; Tandoi, V.; Gossett, J.M.; Zinder, S.H. *Appl. Environ. Microbiol.* **1995**, *61*, 3928-3933.
(23) Maymó-Gatell, X.; Gossett, J.; Zinder, S.H. *Abstract no. Q-96, 97th Annual Meeting of the American Society for Microbiology.* Miami, FL, **1997**.
(24) Sharma, P.K.; McCarty, P.L. *Appl. Environ. Microbiol.* **1996**, *62*, 761-765.
(25) van der Meer, J.R.; van Neerven, A.R.W.; de Vries, E.J.; de Vos, W.M.; Zehnder, A.J.B. J. Bacteriol. **1991**, *173*, 6-15.
(26) Werlen, C.; Kohler, H.P.; van der Meer, J.R. *J. Biol. Chem.* **1996**, *271*, 4009-4016.
(27) Kurkela, S.; Lehvaeslaiho, H.; Palva, E.T.; Teeri, T.H. *Gene* **1988**, *73*, 355-362.
(28) Kimbara, K.; Hashimoto, T.; Fukuda, M.; Koana, T.; Takagi, M.; Oishi, M.; Yano, K. *J. Bacteriol.* **1989**, *171*, 2740-2747.
(29) Zylstra, G.J.; Gibson, D.T. *J. Biol. Chem.* **1989**, *264*, 14940-14946.
(30) Neidle, E.L.; Hartnett, C.; Ornston, L.N.; Bairoch, A.; Rekik, M.; Harayama, S. *Eur. J. Biochem.* **1992**, *204*, 113-120.
(31) Taira, K.; Hirose, J.; Hayashida, S.; Furukawa, K. *J. Biol. Chem.* **1992**, *267*, 4844-4853.
(32) Simon, M.J.; Osslund, T.D.; Saunders, R.; Ensley, B.D.; Suggs, S.; Harcourt, A.A.; Suen, W.-C.; Cruden, D.L.; Gibson, D.T.; Zylstra, G.J. *Gene* **1993**, *127*, 31-37.
(33) Tan, H.M.; Tang, H.Y.; Joannou, C.L.; Abdel-Wahab, N.H.; Mason, J.R. *Gene* **1993**, *130*, 33-39.
(34) Thompson, J.D.; Higgins, D.G.; Gibson, T.J. *Nucl. Acids Res.* **1994**, *22*, 4673-4680.
(35) Asturias, J.A.; Diaz, E.; Timmis, K.N. *Gene* **1995**, *156*, 11-18.
(36) Masai, E.; Yamada, A.; Healy, J.M.; Hatta, T.; Kimbara, K.; Fukuda, M.; Yano, K. *Appl. Environ. Microbiol.* **1995**, *61*, 2079-2085.
(37) Spanggord, R.J.; Spain, J.C.; Nishino, S.F.; Mortelmans, K.E. 1991. *Appl. Environ. Microbiol.* **1991**, *57*, 3200-3205.
(38) Haigler, B.E.; Wallace, W.H.; Spain, J.C. *Appl. Environ. Microbiol.* **1994**, *60*, 3466-3469.
(39) Parales, J.V.; Kumar, A.; Parales, R.E.; Gibson, D.T. *Gene* **1996**, *181*, 57-61.
(40) Suen, W.C.; Haigler, B.E.; Spain, J.C. *J. Bacteriol.* **1996**, *178*, 4926-4934.
(41) Haigler, B.E.; Somerville, C.C.; Spain, J.C.; Jain, R.K. *Abstract no. Q343, 97th Annual Meeting of the American Society for Microbiology.* Miami Beach, FL, **1997**.
(42) Denome,S.A.; Stanley, D.C.; Olson, E.S.; Young, K.D. *J. Bacteriol.* **1993**, *175* , 6890-6901.
(43) Takizawa, N.; Kaida, N.; Torigoe, S.; Moritani, T.; Sawada, T.; Satoh, S.; Kiyohara, H. *J. Bacteriol.* **1994**, *176*, 2444-2449.
(44) Haigler, B.E.; Spain, J.C. *Appl. Environ. Microbiol.* **1993**, *59*, 2239-2243.
(45) Kitanidis, P.K.; Semprini, L.; Kampbell, D.H.; Wilson, J.T. pp. 57-60 In *Symposium on Bioremediation of Hazardous Wastes: Research, Development, and Field Evaluations* (EPA/600/R-93/054), Dallas, TX, **1993**.
(46) Weaver, J.W.; Wilson, J.T.; Kampbell, D.H. *Natural Bioattenuation at the St. Joseph, Michigan Superfund Site* (EPA/600/SV-95/001), **1995**.
(47) Wilson, J.T.; Kampbell, D.; Weaver, J.; Wilson, B.; Imbriglotta, T.; Ehlke, T. *Symposium on Bioremediation of Hazardous Wastes: Research, Development, and Field Evaluations,* Rye Brook, NJ, **1995**.

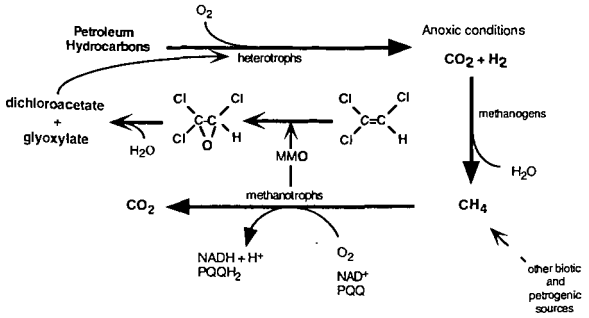

Fig.1. A proposed scheme for the involvement of petroleum hydrocarbon degradation in cometabolism of TCE. The formation of dichloroacetic acid and glyoxylic acid was proposed by Little et al. (10). The abbreviation PQQ refers to the coenzyme methoxatin which is reduced in the oxidation of methane to carbon dioxide (6).

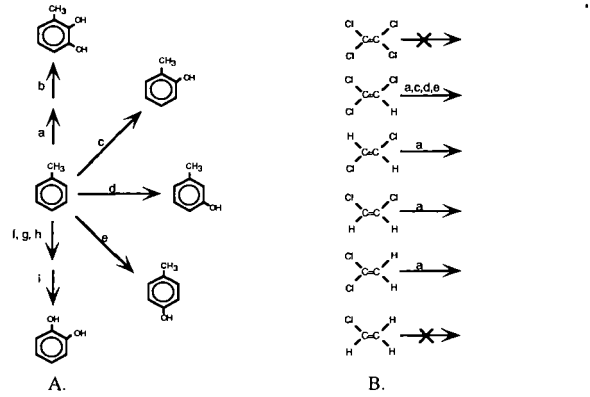

Fig. 2. (A) Enzymes involved in the degradation of toluene, and (B) their ability to cometabolize chloroethenes. Symbols: a, toluene dioxygenase; b, toluene dihydrodiol dehydrogenase;c, toluene-*ortho*-monooxygenase; d, toluene-*meta*-monooxygenase; e, toluene-*para*-monooxygenase; f, toluene oxidase; g, benzyl alcohol dehydrogenase; h, benzaldehyde dehydrogenase; i, benzoate oxidase.

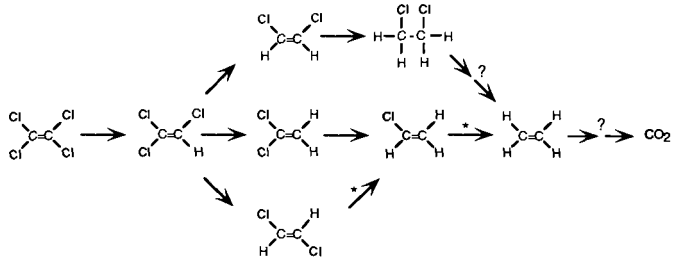

Fig. 3. Pathway for the reductive dechlorination of PCE based on the work of Vogel and McCarty (19) and Maymó-Gatell et al. (23). Question marks (?) represent transformations with unknown intermediates. Astericks (*) indicate reactions not coupled to cell growth in *Dehalococcoides ethenogenes* (23).

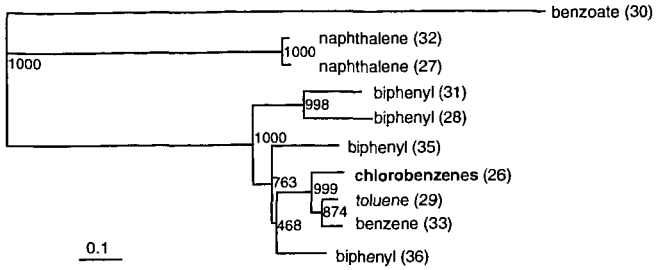

Fig. 4. Phylogram depicting the relationships between selected aromatic dioxygenases. Amino acid sequences were aligned, evolutionary distances were corrected for multiple substitutions, and bootstrap analysis was performed using the ClustalW package (34). Numbers indicate the frequency that the topology shown at each node was recovered out of 1000 bootstrap replicates.

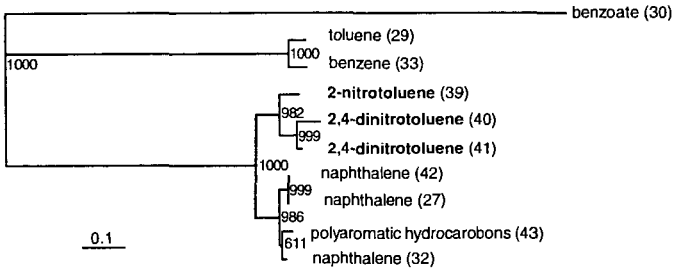

Fig. 5. Phylogram depicting the relationships between selected aromatic dioxygenases. Analyses and symbols are as described in Fig. 4.

NATURAL ATTENUATION EVALUATION AND MODELING OF GASOLINE IMPACTED GROUNDWATER

K. Brown, L. Tyner, B. Sibbett, D. Daftary, T. Perina
IT Corporation
312 Director's Drive
Knoxville, TN 37923

Denise Caron, Vandenberg AFB, CA

ABSTRACT

Natural attenuation was evaluated as a containment option for a gasoline-impacted aquifer located at the Vandenberg, AFB (VAFB) Base Exchange Service Station (BXSS). The site, which was found to have a complex geological and hydro geological profile, was impacted through releases from a leaking underground storage tank (UST). Elements of the site evaluation included records search, placement of approximately 40 Geoprobe points and 7 monitoring wells, slug testing of 18 wells, groundwater and soil sampling and analysis, development of a site conceptual model, and completion of fate and transport modeling.

INTRODUCTION

IT Corporation, contracted through the Air Force Center for Environmental Excellence, completed the evaluation of natural attenuation as a containment option at the VAFB BXSS. The VAFB BXSS was established in 1967 to provide motor vehicle fuel to residents. The BXSS currently consists of the main office building with three gasoline dispensing islands, six automobile service bays, and a four-bay car wash building. It is immediately bordered by trees to the west and south and grassy open fields to the east and north.

In 1967, four 10,000-gallon, single-walled underground fuel tanks, a 250-gallon single walled underground waste oil storage tank, and associated piping were installed at the BXSS. In 1985, two of the four 10,000-gallon USTs were replaced with two 10,000-gallon double-walled fiberglass tanks. In 1991, the two remaining 1967 USTs, along with the associated piping and the underground waste oil storage tank, were replaced with 10,000-gallon USTs.

Site contaminants of concern include benzene, toluene, ethyl benzene, and xylenes (BTEX), total petroleum hydrocarbons (TPH), and methyl tertiary butyl ether (MTBE). The majority of contamination at the site is centralized around the old pump island. Highly contaminated soil in this area extended from 4 to 12 feet bgs. Although no free product was present at the site, the impacted soil appeared to be the source of the groundwater contamination. Outside of the old pump island, soil concentrations dropped off to non detect. Groundwater concentrations of BTEX, TPH, and MTBE increased in and around the old pump island (Figures 1 and 2). Based on the biodegradability of BTEX and TPH, the lack of BTEX and MTBE migration, and the absence of human or ecological receptors in the area, natural attenuation was deemed a feasible alternative for site remediation.

Natural attenuation is most accurately viewed as an effective, natural plume containment process, whereby the intrinsic capacity of the impacted and downgradient aquifer to assimilate contaminants exceeds the contaminant migration rate. As a result, most plumes undergoing natural attenuation achieve a steady-state or stability within a moderate period of time following the release. Some of the advantages of natural attenuation include the fact that it is nonintrusive, less costly than conventional methods and that the most mobile and toxic fuel compounds are generally the most susceptible to biodegradation. The primary limitations of natural attenuation include the fact that it is affected by changes in local hydro geologic conditions, potential future releases, and aquifer heterogeneity and that time frames for completion may be relatively long.

In order to pursue natural attenuation or any technology as a remedy, evidence must be generated documenting the potential and effectiveness of the process. The objectives of the natural attenuation evaluation were to collect evidence to verify or eliminate the potential of natural attenuation as a remedy at the BXSS.

MATERIALS AND METHODS

Forty Geoprobe points were installed during the site investigation. The Geoprobe method drives a 2-inch-diameter sampler mounted on the end of 1-inch-diameter drive rods into the soil, pushing the soil aside until the desired sample depth is reached. During this process soil and groundwater sampling may be collected. Ten soil samples were collected during the direct-push investigation and analyzed by EPA Methods 6010, 8015, 8260, and 9045 for iron, TPH, VOCs, and pH, respectively. Additional analysis for ammonia as nitrogen, total phosphate, microbial

enumerations, and soil moisture was also conducted. Thirty-five groundwater samples were analyzed by an on-site, mobile laboratory for BTEX and MTBE by modified EPA Method 8020.

Geoprobe data were used to guide the placement of seven additional groundwater monitoring wells around the BXSS. The wells were installed to a depth of 20 feet with a hollow-stem auger in a 10-inch-diameter boring. The wells were completed with 4-inch-diameter polyvinyl chloride casing and 15 feet of screen. Conductivity and natural gamma logs were run in 14 monitoring wells (7 existing and 7 newly installed) and 1 soil boring to characterize the subsurface and provide another method for correlating beds between the new and existing wells.

Site monitoring wells were sampled and analyzed by a fixed-facility using EPA Methods 8260, 8015, for VOC and TPH, as well as several general water chemistry analyses. During groundwater sampling, an electronic water-level indicator was used to measure depth to groundwater and depth to the bottom in each monitoring well. Wells were purged and sampled with a 2-inch "readiflow-2" Grundfos pump at a rate of 1 L/min. Field parameters, such as pH, specific conductivity, turbidity, and dissolved oxygen, were measured with a Horiba U-10 water-quality checker. Turbidity was measured with the HACH 2100P turbidity meter. Redox potential was measured with an Orion 290A pH concentration meter. H_2S was measured with a qualitative H_2S kit, and ferrous iron (Fe II) was measured with the HACH 2000 Spectrophotometer.

Following sampling and analysis, slug testing was conducted on 18 wells to characterize the aquifer. A 2.36-inch-diameter, 5.1-foot-long slug constructed of a flush-threaded, 5-foot-long section of stainless-steel pipe with steel caps at both ends was used for the slug tests performed on 4-inch-diameter wells. A 1-inch-diameter, 5.2-foot-long slug constructed of a 5-foot-long section of steel pipe with steel cap at both ends was used for the slug tests performed in 2-inch-diameter wells.

Prior to the slug test, depth to static groundwater was measured using an electrical water level indicator. Changes in water level were digitally recorded during the test using 10-pound-per-square-inch pressure transducers, eight channel Hermit 2000, and LTM 3000 data loggers. The drawdown data were recorded in feet, with a specified reference point of zero feet. Before the tests were started, the pressure transducer constants and test numbers were verified by reviewing the input parameters in the data loggers.

Following the collection of all field data, modeling exercises were initiated. A finite-difference groundwater flow program MODFLOW was selected for the flow portion of the model. MT3D was selected for the transport portion of the model; this code offers a choice of different numerical solution schemes for the transport and can be directly linked to MODFLOW. A graphical processor MODIME for MODFLOW and MT3D was used for model input and output. The degradation of a solute in MT3D is simulated using a first order decay; both dissolved and sorbed phase can be degraded. Only the dissolved phase was allowed to degrade in the presented model. MT3D was selected because of the model's ability to link with USGS MODFLOW, simulate time-varying constant concentration at the source, and input/output portability.

RESULTS

Geologically, the BXSS sits on an uplifted late Pleistocene marine terrace covered with well-sorted, fine-grained sand and clay beds deposited in a shallow marine or lagoon setting. The sands are very well sorted with rounded and polished quartz grains. A fine-grained to silty sand is present from the surface to a depth of 19 to 28 feet. An upper clay bed 2 to 4 feet thick occurs within the sand, between depths of 12 and 16 feet. The bed consists of silty clay and clayey sand, and is highly deformed with high-angle to vertical beds or blocks of sand within the clay. The clay bed may have been deformed by large animal bioturbation, grazing animals sinking into soft sediments, or some other mechanism of soft sediment deformation. The apparent variable thickness of the upper clay bed may be due to its deformed or irregular nature.

A deep clay bed, approximately 4 to 5 feet thick, is present at a depth of 19 feet under the east side of the site, dipping to a depth of 28 feet northwest of the BXSS. The deep clay grades from a fat clay to a clayey silt and clayey sand from top to bottom. The clay bed is continuous under the site and dips to the northwest.

A perched saturated zone is present from approximately 9 feet below the surface to the deep clay bed. Both the piezometric surface and the underlying clay slope to the northwest. Sand and gravel beds below the deep clay bed are unsaturated, and a deep saturated zone was not found to a depth of 60 feet below the site. A deeper perched groundwater was not found above the clayey silt bed at 38 feet depth, which suggests that little water is migrating through the deep vadose zone. The clay bed at a depth of 15 feet is not expected to be a barrier to groundwater movement

because of the disturbed nature of the bed. The deep clay bed forms an impermeable bottom of the shallow saturated zone and prevents vertical migration of contaminants.

The shallow saturated zone water table was found to be unconfined. The saturated thickness of the shallow zone ranges from approximately 10 feet to 21 feet. Groundwater flow direction is approximately to the north with an average hydraulic conductivity of 0.52 ft/day. Flow into the aquifer beneath the site occurs predominantly from the south and west. Groundwater is also likely recharged from a car wash at the site. The evapotranspiration of Eucalyptus trees along California Avenue appears to have a significant impact on the groundwater flow budget. A groundwater flow model of the site was completed using MODFLOW and a fit within 0.66 foot of the observed water levels was achieved.

Once the site groundwater flow model was established, groundwater data were collected and evaluated to determine the occurrence of biological activity at the site and the loss of contaminants of concern. Biological activity at the site has created a reducing environment in the plume source area (i.e., in or near the old pump island). This area is dominated by anaerobic metabolic pathways such as iron and manganese respiration, sulfate reduction, and methanogensis. The plume fringe has a high capacity for aerobic metabolism with increased concentrations of nitrate/nitrite and a positive redox. Overall, the biocapacity of the aquifer to assimilate the release exceeds the sum BTEX detected during the September 1996 sampling event.

A first order decay rate for BTEX removal was calculated following correction of the BTEX concentrations for loss of a recalcitrant tracer (1,3,5-trimethylbenzene). Corrected concentrations indicated that within the plume core, 99 percent of the benzene concentrations were removed by biological reduction rather than physical attenuation. Based on these corrected concentrations, a first order decay rate for BTEX was estimated. A decay of 0.12 yr^{-1} BTEX removal was calculated. Based on the potential biological reduction of the tracer under field conditions, this rate is considered overly conservative.

Once the plumes were delineated, concentrations determined, and the groundwater flow model calibrated, MT3D was used to simulate contaminant fate and transport. The sum of BTEX components was used to represent the contaminant concentrations in the fate and transport model (MT3D). The results of groundwater sampling were used to represent the current distribution of concentrations. The sum of current maximum concentrations of BTEX components was assumed to represent the current source concentration.

It was assumed that groundwater was first impacted in 1970. The source concentration at the time of release was assumed to be 20 times higher than the current source concentration and was assumed to exponentially decrease over time. A combined aerobic/anaerobic biodegradation rate was used to predict loss due to biological activity. The model results indicate the model is in agreement with the high concentrations in the center of the plume, while concentrations higher than observed were calculated at the plume edges (a conservative result). This may be explained by a faster, aerobic degradation of the actual contaminants at the plume edges. The BTEX attenuation time to achieve 1 part per billion was estimated at less than 100 years.

An exponentially decreasing source concentration was also used to determine the fate and transport of MTBE; the rate of decrease was the same as the rate estimated for the BTEX source. No biological degradation of MTBE was assumed in the model. The MTBE concentrations persisted at the site, with the maximum concentrations occurring in the vicinity of well 1-MW-3. The concentration buildup in this area may be explained by groundwater uptake by the trees. Additional sampling rounds will facilitate the calibration of the fate and transport models.

Although contaminants may persist at the site for an extended period of time, no migration of the MTBE or BTEX plume was identified or predicted. The risk to human health and the environment is also negligible. No drinking water sources are present within 3 miles upgradient or downgradient of the site. And all near- site groundwater production wells are screened from 200 to 400 feet deep. Based on fate and transport modeling, the plume will never reach these wells.

CONCLUSION

Based on the documented occurrence of biological contaminant reduction, lack of contaminant migration, and the absence of risk that the impacted groundwater poses, natural attenuation should be considered as a means of site remediation and potential closure.

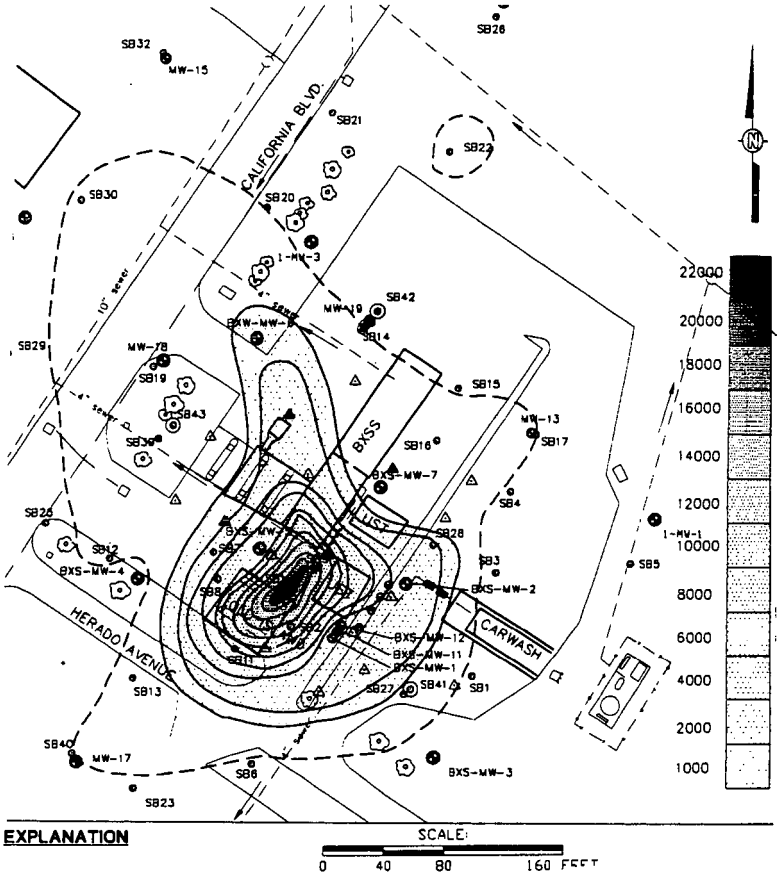

FIGURE 1

BENZENE GROUNDWATER CONCENTRATION CONTOURS SEPTEMBER 1996 BASE EXCHANGE SERVICE STATION

PREPARED FOR

U.S. AIR FORCE VANDENBERG AIR FORCE BASE CALIFORNIA

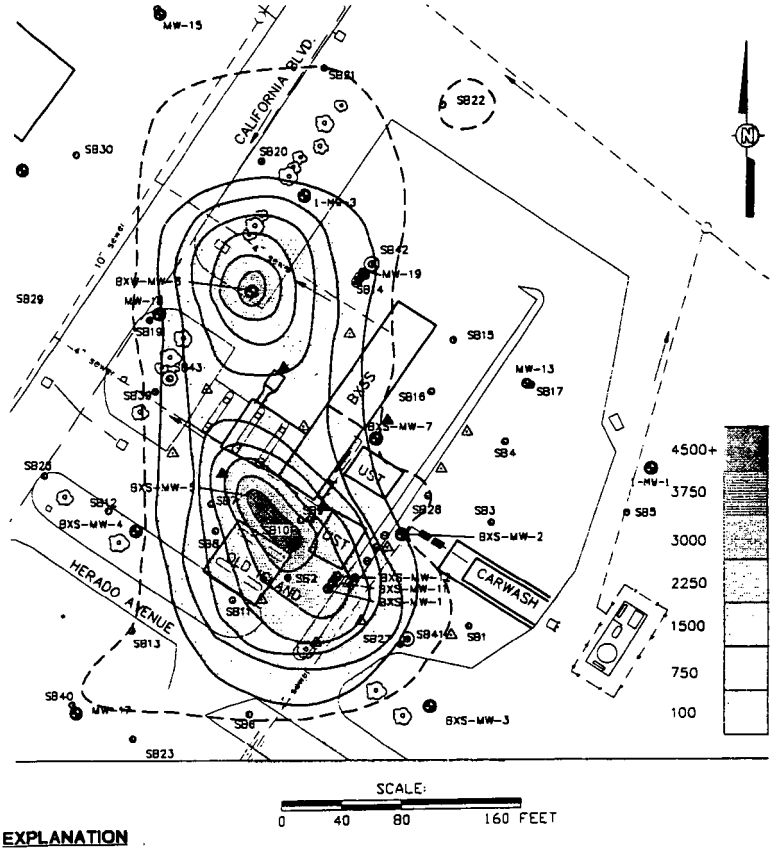

EXPLANATION

MW-13 — GROUNDWATER MONITORING WELL

SB8 — DIRECT-PUSH SOIL BORING

SB41 — AUGER SOIL BORING

MTBE CONCENTRATIONS IN ug/L

ND – NON-DETECT

FIGURE 2

MTBE GROUNDWATER CONCENTRATION CONTOURS SEPTEMBER 1996 BASE EXCHANGE SERVICE STATION

PREPARED FOR

U.S. AIR FORCE VANDENBERG AIR FORCE BASE CALIFORNIA

EX SITU BIOLOGICAL PETROLEUM REMEDIATION: LANDFARM CASE HISTORY

Kevin M. Brackney, M.S., P.G.; and R.L. Crawford, Ph.D.
Center for Hazardous Waste Remediation Research
University of Idaho, Moscow, ID 83844-1052

INTRODUCTION

In the late 1980s, the University of Idaho (UI) negotiated an option to purchase an 11-acre industrial parcel in Moscow, Idaho, for possible university expansion. Phase I and II environmental site investigations took place at three former petroleum bulk plants on this site, and at four underground storage tank sites (USTs) on the UI campus. The investigations identified ≈20,00 yd^3 of soil with weighted average total petroleum hydrocarbon (TPH) concentrations of 947 ppm oil, 465 ppm diesel, and 624 ppm gasoline. The Idaho Division of Environmental Quality (IDEQ) petroleum cleanup requirements mandated remediation levels of 40 ppm gasoline, 100 ppm diesel, and 40 ppm oil based on depth to groundwater (<25 ft) and proximity to surface water (<100 ft). The low permeability of the contaminated silt-clay-sand sediments and refractory long-chain hydrocarbons indicated that in situ remediation would be unlikely to achieve cleanup levels in an acceptable time period. Excavation was considered necessary, but the high cost of low-temperature thermal desorption ($1.3 million at $65/ton, plus trucking) and lack of a local commercial landfarm required that UI design and construct its own landfarm to bioremediate the petroleum-contaminated soil (PSC). An administrative decision was made to maintain ownership of the PCS over concerns about potential liabilities from the landfarm operation or residual contamination. Negotiations with the responsible parties were conducted on a sliding scale based on shared responsibility with a service fee of ≈$35/$yd^3$.

Idaho Division of Environmental Quality siting criteria for land application of petroleum-contaminated soils (IDEQ, 1994) specified six major landfarm siting criteria: 12% maximum slope, 100-ft minimum distance from surface water, 100-ft minimum distance to water wells, 931-ft setback from buildings (based on estimated contaminant concentrations and volumes), and >25 ft to groundwater. In addition, treated soils were not be used for food-chain agricultural purposes, regardless of the level of remediation. On the basis of these criteria, three critical questions were raised: (1) Could the landfarm be designed to prevent surface and groundwater contamination? (2) Would the contaminants be degraded in the acceptable 2-year time frame? (3) Would residual metal contamination perpetually classify the soil as hazardous waste, preventing the return of the land to agricultural use?

SITE DESCRIPTION AND EXPERIMENTAL METHODS

Hydrogeologic site investigations consisted of a literature review, consulting water well boring logs in a 2-mile radius, and drilling a total of 12 hollow-stem-auger boreholes to characterize the shallow stratigraphy. The chosen landfarm site is located on a northwesterly trending ridge ≈900 ft long, 200 to 450 ft wide, and covering ≈10 acres within the city limits of Moscow, Idaho. The average slope is about 9%, with 80 ft of elevation change from top to bottom. Previous land use at the site was pasture for the UI beef herd.

Since the landfarm was designed to be placed on an unlined parcel of agricultural land, careful consideration was given to the regional and site hydrogeology to assess probable impacts to groundwater. Detailed hydrogeologic investigations previously conducted at the UI Aquaculture Site, located ≈1600 ft to the northeast of the landfarm (Kopp, 1994), and the UI Groundwater Research Site, located 2500 ft northeast (Li, 1991), indicated that a basalt aquitard separates the shallow alluvial and upper fractured basalt sub-aquifer from the upper drinking water aquifer. This site-specific hydrological barrier, combined with a relatively thick vadose zone (135 ft) composed of silt, clay, and basalt, suggested that impacts to groundwater would be minimal at the landfarm site. Interpretation of the data indicated that the petroleum was at residual saturation in the soil, so free product migration was unlikely to be a problem. Dissolved organics were a potential problem but were considered degradable in the aerobic vadose zone beneath the landfarm, or in the shallow drainfield in the stormwater discharge zone. Absence of surface water runon, generally well-drained soils with a high soil moisture-holding capacity, and reinfiltration of the limited quantity of stormwater runoff prevented any direct surface water impacts from the landfarm. The primary concern for off-site contaminant migration was from soil erosion. The fine-grained, unconsolidated contaminated soils placed on an 8% slope were highly erodible, so considerable efforts were expended to prevent offsite soil migration.

One to two feet of topsoil was stripped from the landfarm , placed in a berm along the perimeter, and covered with straw and coconut fiber erosion control mats to stabilize the berm and to contain all contaminated soils within the landfarm area. To minimize erosion on the landfarm during the winter and spring, the soil was aerated with a subsoil ripper along contour and covered with composted manure and animal bedding, and silt fences were installed and spaced on 50-ft centers parallel to contour (Gill, et al., 1997).

A seasonal perched water table was identified on the lower third of the landfarm (Brackney, 1995). A stormwater runoff and leachate collection system was keyed into a low-permeability "B-soil" horizon. It was designed as an underdrain to prevent ponding by gathering water into two 1000-gallon sediment-settling and oil-water separator tanks. A 12-inch culvert drains the tanks and discharges to a trapezoidal flume where stormwater effluent is gauged with an ISCO 4230 bubbler flow meter and sampled with an ISCO 3700 stormwater sampler prior to discharging to a shallow drainfield. Six groundwater monitoring wells were installed, four upgradient and two downgradient from the landfarm, including three multi-point standpipe well clusters. These were sampled to characterize petroleum and inorganic impacts to the shallow groundwater.

A literature review indicated the following optimal conditions for petroleum biodegradation: Maintain soil O_2 levels at near atmospheric conditions by thin spreading the soil and tilling whenever levels are <5%; maintain soil moisture levels to 60-70% of field capacity; and balance the carbon:nitrogen:phosphorus levels to 10-20:1:0.1

The landfarm was irrigated with secondarily treated sewage effluent from the municipal wastewater treatment plant which was applied with a wheel line sprinkler irrigation system. Soil moisture was measured in the field by Soil Moisture Equipment tensiometers (model 2725AR) installed in three arrays from 6 to 36 inches deep. The contaminated soils were aerated monthly during the growing season by a subsoil ripper with 2.5 ft ripper teeth, spaced on 2.5 ft. centers, with an attached ripper shoe to increase soil fracturing. Soil O_2 levels were sampled with an AMS soil vapor probe and analyzed with a hand held combustible gas/O_2 meter.

Because of the heterogeneity of the petroleum concentrations from seven sites in various stages of weathering, three 30-ft-diameter grids were installed across the site. Although the contaminated soil had been placed on the site in fall 1994, change in TPH concentrations over time were measured in each grid in May and October 1995 to estimate the progress of degradation over the entire site. Three different treatments were designed for the grids: Grid 1 was planted in perennial ryegrass and irrigated, Grid 2 was tilled and irrigated, and Grid 3 was tilled without irrigation. Most probable number (MPN) bacterial counts, with hexadecane as a sole-carbon source, were measured from soil samples collected during the May and October 1995 sampling periods. A random number radial-coordinate system was generated to select sample locations within each grid. At the end of the first season, a crop of rapeseed and perennial ryegrass was planted for erosion control. At the beginning of the second season (June 1996) the entire site was sampled, establishing uniform gridlines across the site. On each gridline random numbers were generated to select sample locations along the line. Because the oil fraction was considered to be the slowest to degrade, EPA Method 418.1, TPH-Oil, was selected to monitor remediation progress. In June 1997 another round of soil samples will be collected to measure residual contamination.

RESULTS

Very little dissolved or miscible petroleum products were transported offsite from stormwater runoff (Figure 1). Ethylbenzene and xylene were detected only on November 1, 1994, with total concentrations of 0.036 mg/L. Maximum TPH-diesel was 1 mg/L in December 1994, while the maximum TPH-oil of 2.6 mg/L was measured in March 1995. The low levels of TPH-diesel and oil may reflect interference from the high organic concentrations leached from the composted animal manure. The erosion controls at the site worked remarkably well, and no contaminated soil left the landfarm, largely as a result of the compost covering the site.

Leachate from the compost contributed high nitrogen concentrations (NH_3, NO_3, and organic N), chemical oxygen demand (COD), and total dissolved solids (TDS) to stormwater runoff (Figure 2). Maximum concentrations of total nitrogen (400 mg/L), COD (1,800 mg/L), and TDS (2,800 mg/L) occurred in December 1994. Dissolved lead concentrations were also elevated during this period, peaking at 22 µg/L (data not shown). These dissolved inorganic constituents declined during the first year and stabilized by March 1996, with lead concentrations dropping to below detection limit (1 µg/L).

The downgradient monitor well network showed elevated nitrate during spring 1995, with maximum concentrations of 61 mg/L NO_3-N in the perched aquifer, as compared to a back-

ground of 1-2 mg/L NO_3-N in the upgradient wells (Figure 3). COD increases in shallow groundwater is more difficult to assess, since several of the of the upgradient wells apparently have COD concentrations similar to those of the downgradient compliance wells.

During the first season, changes in TPH-oil concentrations were most significant in Grid 1, seeded with ryegrass (Figure 4). Mean TPH changed from 203 ±452 to 32 ±79 mg/kg (error band = 1 SD). Grid 2, tilled and irrigated, changed from 230 ±268 to 165 ±295 mg/kg. Grid 3, tilled but not irrigated, was essentially unchanged from 55±47 to 54±28 mg/kg. MPN bacterial counts measured from the samples ranged from 3.0×10^5 to 2.7×10^6 colony forming units per gram of soil (Table 1). When the entire landfarm was sampled at the onset of the second season, mean TPH-oil was estimated at 131±38 mg/kg ($p = 0.95$); 45% of the samples were below the remediation criteria of 100 mg/kg TPH. The maximum concentration from the June 1996 sampling was 620 mg/kg, compared to the May 1995 maximum of 2,004 mg/kg.

Spot checks of soil O_2 analysis indicate that at both 1- and 2-ft depths, O_2 concentrations were >5% (data not shown). Soil moisture was maintained at 60 to 70% of field capacity on all areas of the landfarm except for the upper 6 inches of Grid 1 which were seeded to ryegrass (data not shown). Though the ryegrass was green throughout the season, evapotranspiration from this plot exceeded our ability to maintain the desired soil moisture levels.

Metal concentrations were determined to be the greatest potential impediment to returning the landfarm to pasture once degradation was completed. IDEQ conservatively interprets all TPH-oil concentrations as used engine oil with potentially toxic levels of heavy metals, particularly lead. Lead analyses, made routinely during the environmental site investigation, showed 149 soil samples to have a mean lead concentration of 57±57 mg/kg (error band = 1 SD) with maximum concentrations of 640 mg/kg. TCLP (toxicity leaching control procedure) analysis, conducted on two of the most contaminated samples, showed <5 mg/L lead in the resulting leachate, indicating that these soils did not test positive for the toxicity characteristic of hazardous waste. It was determined that 74% of samples with lead concentrations greater than the mean came from depths <2.5 ft below ground surface. Of these, 40% had petroleum concentrations less than detection limit. Since background soil lead concentrations for native/undisturbed Palouse soils range from 10-20 mg/kg, mean lead concentrations for the contaminated soil are 3 to 6 times background.

DISCUSSION

The highly erodible soil at the landfarm was stabilized primarily by the high residue content of the composted manure, available at no charge and in unlimited quantities adjacent to the landfarm site. The unconsolidated and saturated contaminated soils were largely inaccessible to heavy equipment until they froze during the winter. Lack of adequate manure-spreading capability and a relatively short window of opportunity required that manure be spread with a dump truck and bulldozer, resulting in overapplication of compost. The unintended consequences were excessive nitrogen, COD, and TDS concentrations. The high organic content of the leachate apparently may have caused chelation of lead and other ions from the soil. These relatively short-lived problems had limited environmental consequences due to the minimal volumes of stormwater runoff from the site (data not shown). The high organic content of the compost may have helped limit the mobility of the petroleum by sorbing it onto the compost. Heavy fall rains brought earthworm populations to the surface through the contaminated soil, causing near-total earthworm mortality. However, by the next spring earthworms began to recolonize the site. The growth of healthy ryegrass and rapeseed crops indicates that the present soil toxicity is minimal.

Landfarm management was capable of maintaining O_2, soil moisture, and nutrient levels at near optimum conditions for petroleum degradation. Precipitation during the first season was sufficient to prevent Grid 3 from receiving enough moisture stress to differentiate its treatment from that of Grid 2. Since the initial TPH concentrations of Grid 3 were lower than the remediation criteria of 100 mg/kg, the lack of significant change in TPH concentration in Grid 3 is inconclusive. Experience at the site showed that tillage was required less frequently than originally considered necessary. Tilling only when soil moisture levels were at near-optimum conditions prevented compaction of too-wet soils, and avoided pulverizing soils that were too dry. The subsoil tillage was highly effective at fracturing the soils, and O_2 stress was never detected. However, this was true even for the soil planted in ryegrass. This area, Grid 1, had the greatest total change in TPH concentration, possibly due to an enhanced microbial environment in the rooting zone of the ryegrass. Additional controlled research is needed to confirm this possibility.

Residual metal concentration in landfarm soils represents a potential long-term detriment to the site. The bioavailability of the lead is unknown. Even if the lead is not absorbed by forage crops,

some may be ingested in soil by grazing animals. The absorption characteristics of lead in the gut of an animal is beyond the scope of this research. However, it is planned to cover the treated soil with the stockpiled topsoil, reducing the potential for ingestion of lead-contaminated soil by cattle. Additional metal analysis planned for June 1997 will better assess the actual metal concentrations of the landfarm soils. Though the soils exceed the background concentrations for lead, preliminary data indicates that the values are still relatively low, and we are optimistic that the landfarm can be returned to productive agricultural use.

ACKNOWLEDGMENTS

We would like to thank Ken Gill for his assistance in managing the field operations at the landfarm and Jennifer Meehan for microbiological work. We are grateful to the University of Idaho College of Agriculture for lending us some highly productive grazing land for use in landfarming petroleum-contaminated soil. We are optimistic that it will soon be returned, no worse for the wear it has taken during the course of our research.

REFERENCES CITED

Brackney, K. M., J. Lee, and T. Bourque, 1995. Stormwater pollution prevention plan, petroleum contaminated soil landfarm. Center for Hazardous Waste Remediation Research, University of Idaho, p. 59.

Gill, K. W., S. M. Miller, and R. L. Crawford, 1997. Erosion control and water-quality monitoring at a petroleum landfarm, p. 137-141. *In* Proceedings of Conference 28, International Erosion Control Association, Feb. 25-28, 1997, Nashville, Tennessee.

IDEQ, 1994. Idaho Division of Environmental Quality, Boise. UST Information Series no. 7.

Kopp, W.P., 1994. Hydrogeology of the upper aquifer of the Pullman-Moscow Basin at the University of Idaho Aquaculture site. M.S. thesis, University of Idaho, Moscow, p. 192.

Li, T., 1991., Hydrogeologic characterization of a multiple aquifer fractured basalt system. Ph.D. dissertation, University of Idaho, Moscow.

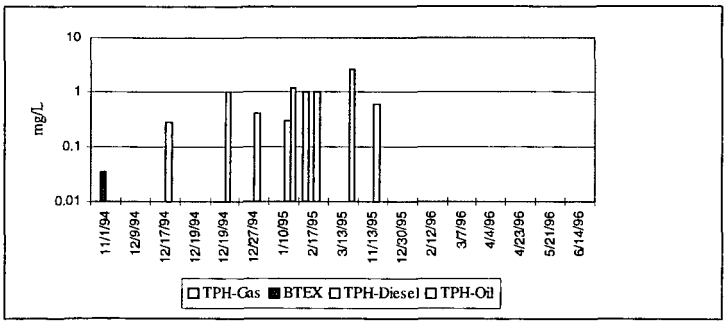

Figure 1. Petroleum concentrations of landfarm stormwater.

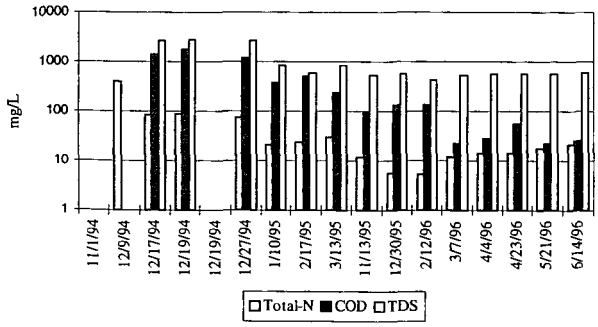

Figure 2. Stormwater analysis. Total N = NH_3-N, NO_3-N, and organic nitrogen; COD = chemical oxygen demand, TDS = total dissolved solids.

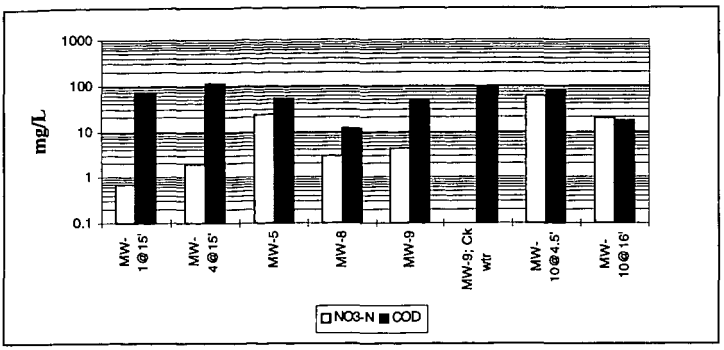

Figure 3. Groundwater concentrations of inorganic compounds, spring 1995. Monitor well cluster MW-10@4.5 ft and 16 ft is immediately downgradient from the landfarm. The 4.5 ft depth is located in the same perched water table that the stormwater collection facility is keyed into. Petroleum was not detected in any of the wells (data not shown). The 16-ft-deep well is located in a sand lens on top of the underlying basalt in a seasonal aquifer that is moderately protected by a clayey-silt aquitard. MW-9 is downgradient; the other wells are either upgradient or lateral to the landfarm. The nitrate and COD concentrations of wells, except for MW-5, probably indicate background levels on fertile pasture under range management. Elevated nitrate concentrations in MW-5 may result from lateral groundwater interflow from the landfarm, or the presence of cattle manure.

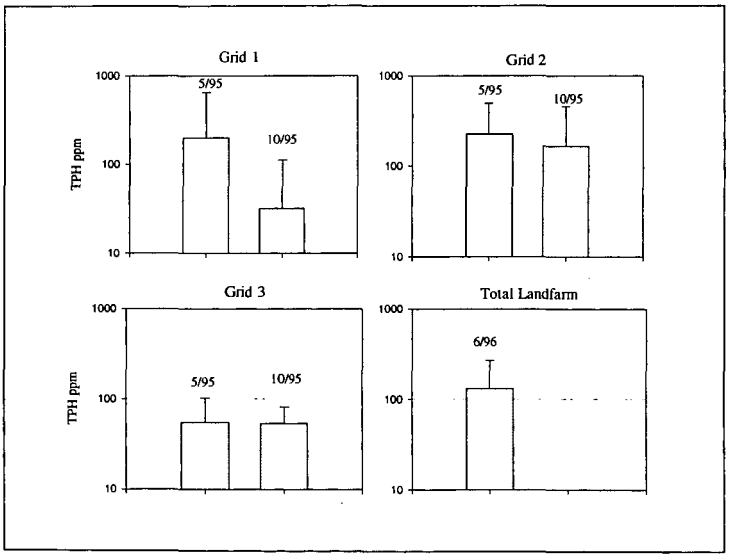

Figure 4. Total petroleum hydrocarbon (TPH) concentrations over time. Grid 1 (ryegrass and irrigation); Grid 2 (tillage and irrigation); Grid 3 (tillage only). Rapeseed and ryegrass were planted over the majority of the landfarm in October 1995. The total landfarm was sampled in June 1996, when a mature rapeseed crop covered the majority of the landfarm, except for Grid 1, which had a mature ryegrass covercrop. Error bars = 1 SD.

Date	Grid 1	Grid 2	Grid 3
May, 1995	$7.69 \pm 0.75 \times 10^5$	$1.61 \pm 0.12 \times 10^6$	$3.47 \pm 0.2 \times 10^6$
October, 1995	$2.67 \pm 0.08 \times 10^6$	$1.03 \pm 0.07 \times 10^6$	$3.01 \pm 0.0 \times 10^5$

Table 1. Most probable number bacterial counts in colony forming units per gram of soil.

POTENTIALS AND LIMITATIONS OF BIOREMEDIATION OF A DIESEL FUEL CONTAMINATED SITE

Martin Steiof [1], Matthias Meier-Löhr [2], Gerhard Battermann [2] and Wolfgang Dott [3]

[1] Institute for Environmental Microbiology and Hygiene, Technical University of Berlin, Germany
[2] Technologieberatung Grundwasser und Umwelt (TGU) GmbH, Koblenz, Germany
[3] Department of Hygiene and Environmental Medicine, RWTH Aachen, Germany

ABSTRACT

In situ bioremediation relies on the stimulation of microbial activity and enhancement of the mass transfer rate of contaminants from nonaqueous phase liquids (NAPL) into the aqueous phase. Over a period of four years, a sandy aquifer contaminated with residual constituent compounds of aged diesel fuel was infiltrated with H_2O_2 and nutrient-amended water. The release and biodegradation of the hydrocarbons was improved by a factor of about 20 - 50. However, it became apparent through soil analysis that the mass transfer kinetic was the limiting factor. The conclusion was reached that the soil clean-up levels are too far below the levels which are perceived to be technically and economically feasible. Nevertheless, GC-analysis showed that the more soluble aromatic compounds, which have been widely regarded as the primary contaminants affecting groundwater, had been completely removed. Evidence gathered while monitoring the groundwater for one year following the bioremediation process indicated that the established water clean-up levels could easily be maintained through the *in situ* treatment.

INTRODUCTION

The *in situ* bioremediation of the described diesel oil contamination started in the beginning of 1992, ended 4 years later, and was in a final monitoring phase in the beginning of 1997. In 1992, the authorities established limiting values (clean-up levels) for total petroleum hydrocarbons (TPH) of 500 mg/kg dry weight for soil and 500 µg/L for groundwater. In order to evaluate the efficiency of the remediation, an attempt was made to follow the reduction of hydrocarbons in groundwater and soil. In general, the balancing of the degradation during an *in situ* bioremediation and the demonstation of the remediation success afterwards is very difficult, due to several problems in monitoring a 'black-box' system (Madsen, 1991).

MATERIAL AND METHODS

Description of the Contaminated Site

The contamination caused by a leaking pipeline 45 to 50 years ago was assumed to be associated with diesel oil. The estimated amount of leaked diesel oil was 15,000 to 17,000 L, and most of the oil floating on the groundwater was removed at the end of the 1970s, leaving approximately 5,700 kg. The subsoil of the contaminated area is characterized as a pleistocene aquifer with fine- and medium-grained sands. The average permeability (k_f) is 10^{-4} to 5 x 10^{-4} m/s. The highest concentration of TPH was about 18,000 mg/kg dry weight (see Figure 2, at a depth of 6 to 7 m). The pollution is distributed to a depth of 4 to 9 m below ground level, thus lying in the aquifer (the groundwater level is approximately 4.5 m below ground level). Gaschromatographic profiles of water and soil extracts showed no typical *n*-alkanes, thus indicating that these compounds had already been degraded. Details concerning the chemistry of the contamination (Steiof, 1993) and the inorganic parameters of this bioremediation (Steiof & Dott, 1995) have been described previously. A top view of the contaminated area, illustrating the positions of the production and infiltration wells, all observation wells, and the distribution of the hydrocarbons is given in Fig. 1.

Remediation Design

The *in situ* remediation design included two infiltration wells, two production wells, and an on-site groundwater processing plant. This groundwater treatment-plant consisted of an iron-removal filter, an oxygenator (using technical oxygen gas), a manganese-removal filter, and an air stripping column. Before the reinfiltration of the treated groundwater, it was possible to add electron acceptors and nutrients. To meet the electron acceptor demand, hydrogen peroxide and nitrate were added to the reinfiltrated water. Phosphate was added to meet the nutrient demand. During the four years of operation, the following amounts were added to the infiltration water:
H_2O_2 : 33 t (about 15 t O_2) ; $NaNO_3$: 5 t; $(NaPO_3)_n$: 0,4 t (about 0,3 t PO_4).

The two production wells had a joint average production rate of 5-10 m^3/h and the two infiltration wells a joint average rate of 3-6 m^3/h during the four years of operation. The groundwater velocity during operation was about 2 m/d, in contrast to 0.4 m/d without operation. The average residence time of the circulated groundwater in the aquifer was about 15 days (Battermann & Meier-Löhr, 1996).

RESULTS AND DISCUSSION

Hydrocarbons in Soil

The hydrocarbon concentrations in the soil samples of ram boring S3 during the remediation are given in Figure 2. The samples '-100 days' represent the concentrations 100 days before the bioremediation was started. Afterwards samples were taken from the same location with a horizontal shifting of 10 cm each year. Some samples from later ram borings contained higher TPH concentrations than earlier samples. After 1340 days of remediation TPH concentrations higher than the limiting value remained in some samples. The soil samples of the ram borings S1, S2 and S4 showed similar results.

Because of the heterogeneity of the subsoil and the typical inhomogeneous distribution of the contaminants, soil samples can not be regarded as representative. A significant reduction of the contaminants was observed only in an advanced stage of the remediation process. Obviously, the homogeneity and the permeability of the aquifer have a decisive influence on the success or failure of an *in situ* remediation.

Hydrocarbons in Groundwater

The TPH concentrations in groundwater samples from three observation wells are given in Figure 3. During the first year of bioremediation, no effect from addition of electron acceptors and nutrients could be observed. The highest TPH concentration was about 2,100 µg/L in well B5 (in most observation wells <1,000 µg/L) and there was no significant decrease during this time. However, a decrease was not expected because a permanent re-solubilization of hydrophobic fuel oil compounds from the soil matrix into the water matrix occurred. After two years of bioremediation, the TPH concentrations in all observation wells settled down below the given limiting value of 500 µg/L.

The gaschromatographic profile of the hydrocarbons in the groundwater of observation well B5 (exemplarily for all observation wells within the contaminated zone) in the beginning of the remediation process is given in Figure 4. In contrast to the GC-MS analysis of the hydrocarbons in soil, only aromatic hydrocarbons could be identified in the groundwater extracts. Iso-alkanes could not be identified. After about 3.5 years of operation, the typical aromatic compounds (see Figure 4) were completely removed and the TPH concentrations declined below the clean-up level of 500 µg/L.

Methodical Approach to the Quantification of Hydrocarbon Degradation

Because of the lacking representativity of the soil samples and the lacking correspondence of TPH in soil and groundwater samples, a different approach to balance the success of the fuel oil degradation was made (Meier-Löhr, 1997). For this indirect attempt, the consumption of added electron acceptors (oxygen from hydrogen peroxide; nitrate) as well as the production of inorganic carbon species (free carbon acid and hydrogencarbonate) had to be determined in groundwater samples. Unfortunately, the complete quantification of these compounds is complicated (Zeyer et al., 1995) since additional sources (e.g. mobilization of mineral lime) and sinks (oxydation of inorganic compounds) are difficult to estimate. A balance applying this approach (consumption of electron acceptors and production of inorganic carbon species, measured as acid- and base-capacity) showed that about 3,500 to 3,700 kg (60 to 65% of the starting amount) of the hydrocarbons were degraded.

Registration of the Risk Potential

Experiences with different *in situ* bioremediations showed that the given limiting values often were not reached in all soil samples. Nevertheless, there is not enough knowledge to estimate the risk potential of these remaining hydrocarbons at the end of a bioremediation. On the other hand, a bioremediation usually leads to a reduction of the contaminants and the toxicity in the groundwater (Dasappa & Loehr, 1991) and, as a consequence, the risk potential will be lowered or eliminated.

It is generally accepted, that the mobility and bioavailability of contaminants have a crucial influence on the risk potential of a polluted site (Rippen et al.,1994). Therefore, it is more important to monitor the TPH concentrations in the groundwater than in the soil. In addition, the application of toxicity tests is necessary (DECHEMA, 1995). Chemical analysis of environmental samples usually does not lead to reasonable predictions of biological or ecological effects. Toxicity tests, however, integrate the effects of all mobile and bioavailable contaminants and complement

the chemical analysis of a contaminated site. We conducted the bioluminescence test assay with *Vibrio fischeri* according to the German Standard Methods (1991). The EC_{50}-values of the groundwater samples of the remediation zone and downstream of the contaminated area did not reach toxic levels (data not shown here).

CONCLUSIONS

During a final control phase, the groundwater was examined with special attention given to the TPH concentrationc and the toxicity. Although the TPH concentration in some soil samples exceeded the limiting values, the authorities agreed to bring the remediation to an end. The TPH concentration in the groundwater in combination with the results of the toxicity tests seemed to verify, that the risk potential of this contamination has been eliminated.
However, it became apparent through soil analysis that the mass transfer kinetic from the NAPL attached to the soil surface in the groundwater was the limiting factor. The conclusion was reached that the soil clean-up levels are too far below the levels which are perceived to be technically and economically feasible. Nevertheless, GC-analysis showed that the more soluble aromatic compounds, which have been widely regarded as the primary contaminants affecting groundwater, had been completely removed. Also, the dissolution of the remaining low soluble aliphatic hydrocarbons did not reach detectable levels and therefore did not affect the groundwater quality. Evidence gathered while monitoring the groundwater for one year following the bioremediation process indicated that the established water clean-up levels could easily be maintained through the *in situ* treatment. Given that the main objectives are the clean-up and protection of water resources, the application of an *in situ* remediation technology is technically and economically effective.

ACKNOWLEDGEMENTS

We thank the 'Berliner Wasser-Betriebe' (water works) for their research grant.

REFERENCES

Battermann, G. and M. Meier-Löhr. 1996. „Erfahrungen aus zwei in situ Sanierungen in der gesättigten Bodenzone". In Kreysa,G. u. Wiesner, J. (Eds.): *In-Situ Sanierung von Böden, 11. DECHEMA Fachgespräch Umweltschutz*, DECHEMA, Frankfurt a.M., 163-190.

Dasappa, S. M. and R. C. Loehr. 1991. "Toxicity Reduction in Contaminated Soil Bioremediation Process." *Wat. Res. 25*(9): 1121-1130.

DECHEMA (Dott, W. and K. Hund). 1995. "Bioassays for Soil" In G. Kreysa and J. Wiesner (Eds.), *4th Report of the Interdisciplinary DECHEMA Committee „Environmental Biotechnology - Soil"; Ad-hoc- Commitee „Methods for Toxicological / Ecotoxicological Assessment of Soils", 46 pages,* DECHEMA e.V., Frankfurt a.M..

German Standard Methods. 1991. "Testverfahren mit Wasserorganismen, Bestimmung der Hemmwirkung von Abwasser auf die Lichtemission von Photobacterium phosphoreum - Leuchtbakterien-Abwassertest mit konservierte Bakterien." *Deutsche Einheitsverfahren zur Wasser-, Abwasser- und Schlammuntersuchung* DIN 38412 Teil 34, L34.

Madsen, E. L. 1991. "Determining *in situ* Biodegradation." *Environ. Sci. Technol. 25*(10): 1663-1673.

Meier-Löhr, M. 1997. „Bilanzierung und Modellierung von biologischen und physikalisch-chemischen Prozessen bei der In-Situ Sanierung von kohlenwasserstoffverunreinigten Grundwassersystemen", PhD Thesis, Technical University of Dresden, Germany.

Morgan, P. and R.J. Watkinson. 1992. "Factors Limiting the Supply and Efficiency of Nutrient and Oxygen Supplements for the in situ Biotreatment of Contaminated Soil and Groundwater". *Wat. Res. 26*(1): 73-78.

Rippen, G., T. Held, and P. Ripper. 1994. "Microbiological Remediation of Waste-Oil Polluted Soils - Ecotoxicological and Toxicological Considerations." *Environ. Sci. Poll. Res. 1*(3): 185-189.

Steiof, M. 1993. "Biologische *in situ* Sanierung eines mit Dieselöl kontaminierten Aquifers." Ph. D. Thesis and Publication from the Department of Hygiene, Technical University of Berlin, Germany.

Steiof, M. and W. Dott. 1995. "Application of Hexametaphosphate as a Nutrient for *In Situ* Bioreclamation". In R. E. Hinchee, J. A. Kittel. and H. J. Reisinger (Eds.), *Applied Bioremediation of Petroleum Hydrocarbons*, pp.301-310. Battelle Press, Columbus, OH.

Zeyer, J., P. Höhener, D. Hunkeler and D. Hahn. 1995. "*In situ* Bioremediation of Mineral Oil Contaminated Soils and Aquifers: Quantification of Degradation Rates and Fate of Hydrocarbons." In W. J. van den Brink, R. Bosman and F. Arendt (Eds.), *Contaminated Soils '95*, pp. 319-326. Kluwer Academic Publishers, Netherlands.

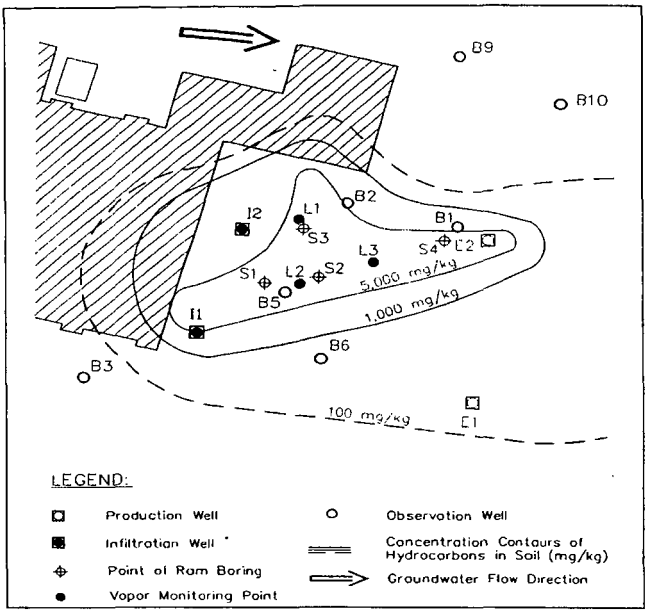

FIGURE 1. Top view of the contaminated area with TPH concentration and the position of all wells and points of ram boring with open sided tube.

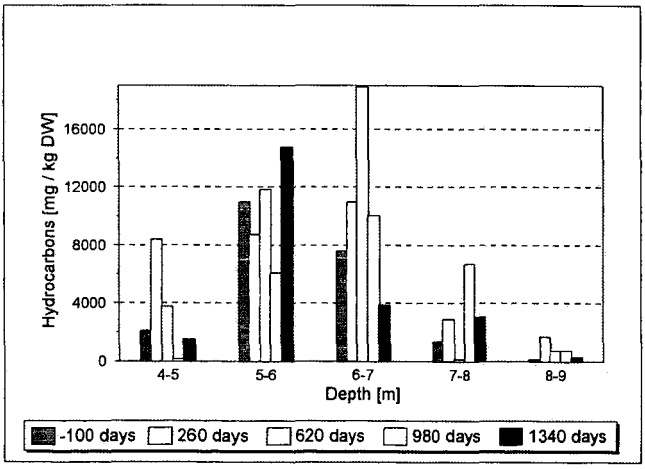

FIGURE 2. Hydrocarbon concentrations in the soil of ram boring S3.

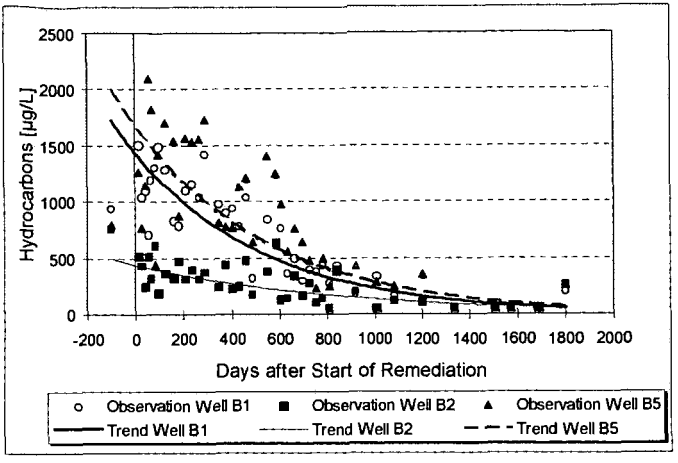

FIGURE 3. Hydrocarbon concentrations in the groundwater of the observation wells B 1, B 2 and B 5.

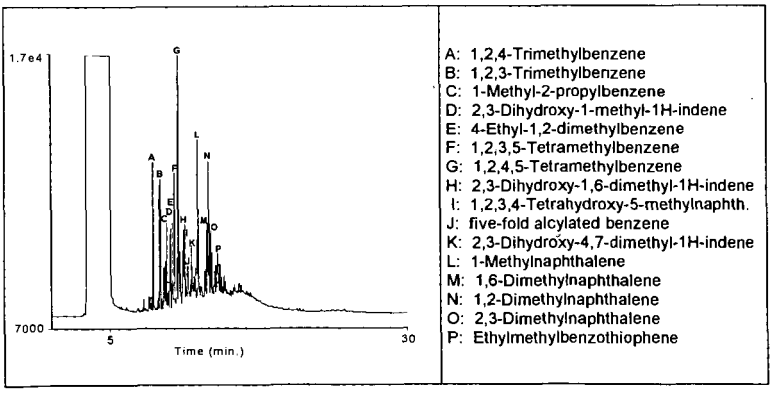

FIGURE 4. Gaschromatographic analysis of the hydrocarbons in the groundwater of observation well B 5 (TPH-concentration: 1,800 µg/L).

CHEMICAL COMPOSITION CHANGES AND BIODEGRADATION POTENTIALS OF NINE ALASKAN OILS UNDER FRESHWATER INCUBATION CONDITIONS.

Zhendi Wang, S. Blenkinsopp, M. Fingas, G. Sergy, M. Landriault, and L. Sigouin
ESD, Environment Canada, 3439 River Road, Ottawa, ON K1A 0H3
J. Foght and K. Semple
Dept. of Biological Sciences, Univ. of Alberta, Edmonton, AB T6G 2E9
D. W. S. Westlake
Westec Microbes Ltd., Victoria BC V9C 1X4

ABSTRACT

Nine representative Alaskan crude oils and oil products commonly transported in Alaska were weathered and incubated using the Environment Canada freshwater oil biodegradation protocol. A complete "total oil analysis method by GC/MS and GC/FID" was developed for monitoring and quantifying the resultant compositional changes of the biodegraded oils. All of the oils exhibited measurable hydrocarbon losses after incubation. Various indices were defined to describe the biodegradability of the oils. The Jet B Fuel and Diesel No.2 were more biodegradable than Alaska North Slope and Cook Inlet crude oils, while the Bunker C/Diesel mixture was found to be less biodegradable than these crude oils. The screening procedure developed in this work would be useful in optimizing the application of bioremediation technology for the cleanup of spilled oils in selected freshwater environments. In addition, an analytical method has been developed to differentiate oil composition changes due to weathering from those due to biodegradation.

INTRODUCTION

Bioremediation has received much attention as an option for oil spill cleanup [1-8], especially for inaccessible or sensitive environments. However, before bioremediation can be considered a realistic method for spill response, two factors must be considered. First, is the oil relatively biodegradable? Secondly, if the oil is biodegradable, to what degree does the oil composition change? These data are critical for making the least environmentally damaging and most cost-effective cleanup decisions. Oils vary greatly in their chemical composition, depending on their geological sources. There is no point in using an effective and relatively non-toxic bioremediation agent on a crude oil or oil product that is not going to degrade readily.

At present, little information exists on the biodegradation potential of crude oils and oil products in Arctic freshwater systems. The purpose of this study is to determine the biodegradation potential, under freshwater conditions, of nine crude oils and oil products commonly transported in Alaska, using a defined microbial inoculum and quantitative oil analysis, ranking the 9 oils, in terms of susceptibility to biodegradation. With this data, spill responders would be able to make judicious decisions regarding clean-up effort and the potential use of bioremediation strategies in Arctic freshwater environment.

METHODS

Weathering of Nine Oils and Oil Products

Nine oil and oil products were selected for biodegradation tests under freshwater incubation conditions based on discussions with the Alaska Department of Environmental Conservation (Camille Stephens), the Cook Inlet Regional Citizens Advisory Council (Ruth Post) and the Cook Inlet Spill Response Group (Eric Haugstaud). They are North Slope (NS) oils collected from Northern Pipeline, Middle Pipeline, and Southern Pipeline respectively, Jet B, Diesel No.2, Cook Inlet (Granite Point), Cook Inlet (Trading Bay), Cook Inlet (Swanson River), Bunker C/Diesel Mixture.

The oils were collected in uncoated one gallon (U.S.) paint cans and were weathered at the Environmental Technology Centre (ETC) by pouring them into 250 mL beakers and letting them stand for 24 hours in a fumehood. The evaporative loss by mass varied in a wide range from 0.23% for Bunker C/Diesel mixture to 22.16% for Cook Inlet (Granite Point).

Oil Biodegradation Method

The nine weathered Alaskan oils were tested for biodegradation potential in batch of three. Eight flasks were prepared for each oil (Table 1). Briefly, the tests were conducted as follows: Two hundred mL of standard freshwater medium [9] was added to a 500 mL Erlenmeyer flask and sterilized with an autoclave. After cooling, the appropriate flasks were supplemented with 4 mL of a filter-sterilized stock solution of nitrogen and phosphate (+N, P) (1 g/L of NH_4Cl; 2 g/L of KNO_3; 0.5 g/L K_2HPO_4). Six microbial strains (3 aliphatic degraders and 3 aromatic degraders) comprised the standard freshwater inoculum used in the freshwater oil biodegradation potential test. Oil was added gravimetrically (400 mg) to each flask, using a 5 mL ground glass syringe, weighed before and after each oil addition to the nearest 0.1 mg. Duplicate, uninoculated flasks served as sterile 'weathering' controls to account for abiotic oil losses through volatility and dissolution during the

incubation period. Alberta Sweet Mixed Blend (ASMB, our standard reference oil) was included with each batch of 3 Alaskan oils tested, for quality control. All flasks were incubated at 10 degree Celcius in darkness with shaking at 200 rpm for 28 days. After incubation, 1.0 mL of surrogate standard solution (*o*-terphenyl, d_{10}-phenanthrene, squalane) was added and the residual oil was extracted with spectrophotometric-grade dichloromethane and subjected to a comprehensive chemical analysis.

Table 1. Study Design for Assessing Oil Biodegradation Potential
(✔ = present; ✗ =absent)

FLASK	ALASKAN OIL OF INTEREST	FRESHWATER INOCULUM	NUTRIENTS (N,P)
Positive Controls (+N,P); n = 3	✔	✔	✔
Negative Controls (-N,P); n = 3	✔	✔	✗
Sterile Controls n = 2	✔	✗	✔

Chemical Analysis of Oil Composition Changes

Each residual oil extract was made up to 5.0 mL with hexane using a 5.0 mL volumetric flask. A 200 µL aliquot of the diluted residual oil extract (about 16 mg of oil) was quantitatively transferred onto the pre-conditioned silica-gel column for oil hydrocarbon group fractionation [10].

The following groups will be referred to when describing and discussing oil composition changes during biodegradation:

TPH or total gas chromatograph (GC) detectable petroleum hydrocarbons (GC-TPH): the sum of concentrations of all GC-resolved and unresolved hydrocarbons. The resolvable hydrocarbons appear as peaks and the unresolvable hydrocarbons appear as the area between the lower baseline and the curve defining the base of resolvable peaks;

Total aliphatics: the sum of concentrations of all resolved and unresolved aliphatic hydrocarbons including the total n-alkanes, branched alkanes, and cyclic saturates;

Total aromatics: GC-TPH minus the total saturates;

Total n-alkanes: the sum of concentrations of all resolved n-alkanes (from C_8 to C_{40} plus pristane and phytane);

Total of 5 alkylated PAH homologous series: the sum of concentrations of five target alkylated homologues of naphthalene, phenanthrene, dibenzothiophene, fluorene, and chrysene determined by GC/MS.

Analyses for *n*-alkane distribution and total petroleum hydrocarbons (TPH) were performed on a Hewlett-Packard (HP) 5890 gas chromatograph equipped with a flame-ionization detector (FID) and an HP 7673 autosampler. A 30-m x 0.32-mm id. (0.25-µm film) DB-5 fused silica capillary column (J&W, Folsom, CA, USA) was used. The carrier gas was helium (2.5 mL/min). The injector and detector temperatures were set at 290 °C and 300° C, respectively. The oven temperature program was: a 2 minute hold at 50 °C; ramp to 300 °C at 6 °C/min; and finally a 16 minute hold at 300 °C. A 1 µL aliquot was injected in splitless mode with a 1 minute purge-off.

Analyses of target polycyclic aromatic hydrocarbons (PAHs) and biomarker compounds were performed on an HP Model 5890 GC equipped with a Model HP 5972 mass selective detector (MSD). System control and data acquisition were achieved with an HP G1034C MS ChemStation (DOS series). The MSD was operated in the selected ion monitoring (SIM) mode for quantitation of target compounds. An HP-5 fused-silica column with dimensions of 30-m x 0.25-mm id. (0.25-µm film) was used. The chromatographic conditions were as follows: carrier gas, helium (1.0 mL/min); injection mode, splitless; injector and detector temperature, 290 °C and 300° C respectively. The temperature program for target PAHs was: 90 °C for 1 minute, ramp to 160 °C at 25 °C/min and then to 290 °C at 8 °C/min, and hold for 15 minutes. The temperature program for alkylated PAHs and biomarker compounds was: 50 °C for 2 minutes, ramp to 300 °C at 6 °C/min and hold 16 minutes.

For details of methodologies of fractionation, analysis quality control and quantification, please refer to references [10-14].

RESULTS AND DISCUSSIONS

Chemical Composition of the Weathered Source Oils

Figures 1 through 4 show representative GC chromatograms of sterile controls, negative controls, and positive controls, illustrating the changes in chemical composition of biodegraded oil samples. However, in order to put the biodegradation data in perspective, a brief overview of the initial composition (% by weight) of the weathered crude oils and weathered oil products is useful. All of the crude oils and oil products tested had a ratio of aromatics to saturates of about 1:3, with

the exception of the Bunker C/Diesel mixture, in which it was about 1:1 (Fig. 5). The *n*-alkanes accounted for 13 to 19% of the saturate fraction in all of the oils and oil products, with the exception of the Bunker C/Diesel mixture, in which they accounted for only 8%. The 5 PAH homologous series accounted for a very small fraction of the total aromatics in all of the oils and oil products, ranging from 4% in the Bunker C/Diesel mixture to 13% in Diesel No. 2. The distribution of 5 alkylated PAH homologous series was quite similar for all of the crude oils, with the two most dominant being naphthalenes (approx. 70%) and phenanthrenes (approx. 20%). However, the relative contribution of dibenzothiophenes was notably different between the North Slope and Cook Inlet oils. The North Slope oils had approximately 9% dibenzothiophenes, while the Cook Inlet oils had only approximately 1% dibenzothiophenes. The three oil products differed significantly from the crude oil pattern and from each other. The alkyl naphthalene series accounted for 99% of the 5 alkylated PAH homologous series for Jet B Fuel and 86% for Diesel No. 2, respectively. In the Bunker C/Diesel mixture, naphthalenes and phenanthrenes each accounted for approximately 35%, and chrysene accounted for 18%.

In addition to the features described above, the following characteristics of the oil products should be noted, since they are very different from the crude oils. The composition of Jet B Fuel (sterile controls) was as follows:

(1) The *n*-alkanes formed a narrow Gaussian distribution from n-C_8 to n-C_{17} with maxima at n-C_{12}. The sample also contain a large amount of unresolved complex mixture (UCM).

(2) The ratios of GC-resolved peaks to total GC area was much higher than for all the crude oils (~0.36 and 0.33 for F1 and F3 of the sterile control respectively).

(3) Concentrations of pristane and phytane were very low.

(4) C_4-phenanthrene, C_3-dibenzothiophene, and alkylated chrysene homologues were not detected.

(5) For other PAHs, only low molecular weight and low-number-ring PAHs such as biphenyl, acenaphthalene, and acenaphthene were detected.

(6) Biomarker compounds were not detected.

The sterile controls of Diesel No. 2 showed similar chemical composition features as Jet B Fuel sterile controls with the following exceptions:

(1) A broader distribution of *n*-alkane from n-C_8 to n-C_{23} with a maximum being around n-C_{12} to n-C_{14}.

(2) A significant amount of n-C_{17} and pristane, and n-C_{18} and phytane.

(3) Significantly higher abundances of alkylated phenanthrene (C_0-C_4), dibenzothiophene (C_0-C_3), and fluorene (C_0-C_3) series.

(4) Very low concentrations (sub-ppm levels) of C_{20}-C_{24} terpanes.

The GC traces of Bunker C sterile control revealed that the Bunker C sample was a mixture of a large portion of heavy residual fuel (so-called "old-type Bunker C") with a smaller portion of lighter diesel fuel. The *n*-alkane distribution featured two "humps", with the maxima around n-C_{13} and n-C_{24}.

Chemical Composition Changes of Hydrocarbons due to Biodegradation

General biodegradation trends of various hydrocarbon groups are summarized as follows.

Biodegradation of GC-TPH, total saturates and total n-alkanes:

For all of the crude oils and oil products, biodegradation were greatly enhanced when nutrients were present, as shown by the reductions in GC-TPH, total saturates and total *n*-alkanes (Figs. 6 and 7). When nutrients were present, GC-TPH, total saturate and total *n*-alkane losses were greater than 20%, 20%, and 90%, respectively for the crude oils, and greater than 15%, 20%, and 70%, respectively, for the oil products. In contrast, in the absence of nutrients, however, GC-TPH, total saturate and total n-alkane losses were on average ≤10%, <10% and <15%, for all crude oils and oil products except for the Bunker C/Diesel mixture, which had a total n-alkane loss of approximately 30%.

In the Bunker C/Diesel mixture, the largest losses of *n*-alkanes occurred in the lighter components of the diesel portion. The resolved aliphatics, including *n*-alkanes and isoprenoids, remained largely unchanged even when nutrients were added in both Jet B Fuel and Diesel No. 2.

Biodegradation of total aromatics and 5 alkylated PAH homologous series:

For crude oils, the degradation of total aromatics and 5 alkylated PAH homologous series was not enhanced by addition of nutrients (Figs. 8 and 9). In some cases, greater losses occurred in the absence of nutrients. It is interesting to note that the biodegradation of both Jet B Fuel and Diesel No. 2 was enhanced for the aromatics and 5 alkylated PAH homologous series when nutrients were added (Figs. 8 and 9). However, it should be noted that lower molecular weight PAHs were the dominant components in Jet B and Diesel No. 2. In contrast, the losses in the higher molecular weight Bunker C/Diesel mixture were more similar to those of the crude oils (Figs. 8 and 9).

Among the 5 alkylated PAH homologous series, the alkyl homologues of naphthalene (the most abundant, 2-rings) were the most easily degradable, followed in order, by alkyl homologues of dibenzothiophene (sulphur-containing 3 rings), fluorene (3 rings, 13 carbons) and then phenanthrene (3-rings, 14 carbons). Alkylated chrysenes (4-rings) were the most biodegradation

resistant of the target PAH homologues. No significant signs of degradation in the homologous chrysenes was observed in most samples.

The target parent PAHs such as naphthalene, dibenzothiophene, fluorene, and phenanthrene were the most significantly degraded in each alkylated PAH series. The degradation order of $C_0>C_1>C_2>C_3>C_4$ derivatives of the PAHs is pronounced, and particularly striking within the alkylated naphthalene family. It is clear that both the rate and degree of degradation decrease dramatically as the number and size of substitute alkyl groups in aromatic rings increase.

Among the 5 target alkylated PAH series, the alkylated naphthalene series, especially naphthalene and its C_1-, C_2-, and C_3- derivatives made up the largest portion of the losses of the five target alkylated PAH series. Among other target PAHs, the low-molecular-weight PAHs with lower aromatic ring numbers such as biphenyl and acenaphthalene were nearly completely lost, while the high-ring-number PAHs did not degraded to a significant degree or not degraded at all. (Note that no other high-ring PAHs were detected in the source Jet B Fuel and Diesel No. 2).

BTEX and Alkylbenzenes:

The crude oils and oil products contained significant amounts of BTEX compounds and alkylbenzenes, but the corresponding sterile controls only contained very small amounts. This indicates that evaporative loss of BTEX and alkylbenzenes occurred during the incubation period.

In the oils and oil products, two major alkylbenzene peaks eluted before the naphthalene peak (retention time, 12.65 min) in the sterile control. They were identified to be 1,2,3,4-tertramethylbenzene (RT= ~11.84 min) and 1,2,3,5-tertramethylbenzene (RT= ~11.06 min). These two C_4-benzene compounds were biodegradable, with greater losses observed when nutrients was added. The C_4-benzene compounds, especially the late-eluted 1,2,3,4- and 1,2,3,5-tertramethylbenzenes, were more biodegradation-resistant than naphthalene, and C_1 and C_2-naphthalenes.

Biomarker Compounds:

No noticeable sign of degradation of biomarker terpanes and steranes was observed in all of the crude oils and oil product samples.

Biodegradation Potential Index

All of the oils tested had measurable losses of hydrocarbons as a result of incubation with the standard microbial inoculum. Abiotic losses were accounted for through the use of sterile controls, therefore the reported losses are definitely due to biodegradation. In addition, the use of various analytical chemistry indices and loss patterns also confirmed that the reported losses are due to biodegradation [15].

In terms of ranking the tested crude oils and oil products with respect to oil biodegradation potential, the following philosophy was applied. First, the ranking index was to be kept relatively simple, so that it could be understood and used by a wide audience. Of the 5 groupings discussed in the preceding section (that is, TPH, total saturates, total n-alkanes, total aromatics, total 5 alkylated PAH homologous series), it was felt that the losses in GC-TPH and total aromatics were of the most use. An overall measure of oil biodegradation was desired, which is readily provided by the GC-TPH grouping. However, since the GC-TPH grouping is largely composed of saturates, a means of quantifying the degradation of the aromatics was also desired, since aromatics are considered to be more recalcitrant and some of their bio-oxidation products are potentially more toxic than those derived from saturate metabolism. The total aromatics grouping was chosen as being the most representative index. Note that of the remaining groupings discussed in the previous section, the n-alkane and 5 alkylated PAH homologous series groupings are but small subsets of the total saturates and total aromatics, respectively. In addition, since total saturates are generally quite degradable, and are already accounted for in the GC-TPH, this grouping was not considered a relevant addition to the biodegradation index calculations.

An important consideration is the relative weight assigned to the losses of the GC-TPH and total aromatics for creating a biodegradation potential index. In previous studies by Environment Canada and NOAA [16], two different weightings of the GC-TPH and total aromatic losses have been proposed (on a scale of 0 to 10):

Equation A: Equal weighting:

$$\text{Index Value} = [0.5(\text{mean \% GC-TPH loss}) + 0.5(\text{mean \% Total Aromatics loss})]/10$$

Equation B: A 30:70 ratio:

$$\text{Index Value} = [0.3(\text{mean \% GC-TPH loss}) + 0.7(\text{mean \% Total Aromatics loss})]/10$$

For example, given that the crude oil Cook Inlet (Granite Point) had a mean GC-TPH loss of 29.3% and a mean total aromatics loss of 7%, in the nutrient-amended flasks, the calculations for Equation A would be performed as follows:

$$\text{Granite Point Index Value} = [0.5(29.3) + 0.5\ (7)]/10 = 1.8$$

Equations A and B were used to generate index values for each crude oil/oil product tested in this study (Fig. 10A and 10B). The trends depicted are similar in both plots, i.e., the oil products Jet B Fuel and Diesel No. 2 are more biodegradable than the crude oils, while the Bunker C/ Diesel Fuel mixture is the least biodegradable.

The bottom line is that laboratory pre-screening can identify oils which should be considered for bioremediation. The Bunker C/Diesel mixture would definitely not be as amenable to bioremediation as the other tested oils/oil products. A similar conclusion was reached by Song *et al.* [17] when investigating the bioremediation potential of terrestrial fuel spills of gasoline, jet fuel, heating oil, diesel oil, and Bunker C. Bunker C was found to be the most recalcitrant, with close to 80% persisting after one year of incubation.

Interesting trends were noted with respect to nutrient addition. For both crude oils and oil products, the addition of nutrients enhanced GCD-TPH, total *n*-alkane and total saturate loss. Although nutrient addition did not enhance aromatic or PAH degradation in crude oils, enhancement due to nutrient addition was apparent for Jet B Fuel and Diesel No. 2. This phenomenon is discussed in detail by Blenkinsopp et al [9].

ACKNOWLEDGEMENTS

This project was funded by the Alaska Department of Environmental Conservation and the Emergencies Science Division of Environment Canada. The findings and conclusions presented by the authors are their own and do not necessarily reflect the views or position of the Alaska Department of Environmental Conservation or of Environment Canada. The use of the trade names or commercial products in this manuscript does not constitute endorsement for their use.

REFERENCES

1. Cooney, J. J. *The fate of petroleum pollutants in freshwater ecosystems*, in R. M. Atlas (ed.) *Petroleum Microbiology*, Macmillan, New York, NY, **1984**.
2. Leahy, J. G.; Colwell, R. R. *Microbiology Rev.*, **1990**, 54, 305-315.
3. Chaîneau, Claude-Henri. Morel, Jean-Louis. Oudot, J. *Environ. Sci. Technol.* **1995**, 29, 1615-1621.
4. Lee, K. Tremblay, G. H. Cobanli, S. E. in *Proceedings of 1995 International Oil Spill Conference*, American Petroleum Institute, Washington, D.C., **1995**, 105-113.
5. Lee, K. Levy, E. M. in *Aquatic Toxicology and Water Quality Management*, J. O. Nriagu and J. S. S. Lakshminarayana (eds.), John Wiley and Sons, Inc., New York, **1989**, 217-243.
6. Atlas, R. M. Bartha, R. in *Advance in Microbial Ecology*, K. C. Marshall (ed.), Plenum Press, New York, v12, **1992**, 287-338.
7. Bragg, J. R.; Prince, R. C.; Harner, E. J.; Atlas, R. M. *Nature*, **1994**, 368, 413-418.
8. Bragg, J. R.; Prince, R. C.; Harner, E. J.; Atlas, R. M. *Bioremediation for Shoreline Cleanup Following the 1989 Alaska Oil Spill*, EXXON Company, USA, Houston, TX, **1992**.
9. Blenkinsopp, S.; Wang, Z. D.; Foght, J.; Westlake, D. W. S.; Sergy, G.; Fingas, M.; Landriault, M.; Sigouin, L.; and Semple, K. in *Proceedings of The 20th Arctic and Marine Oil Spill Program (AMOP) Technical Seminar*, June 11-13, 1997, Vancouver, Canada; Environment Canada: Ottawa, **1997**.
10. Wang, Z. D.; Fingas, M.; Li, K. *J. Chromatogr. Sci.* **1994**, 32, 361-366, and 377-382.
11. Wang, Z. D.; Fingas, M.; Sergy, G. *Environ. Sci. Technol.* **1994**, 28, 1733-1746.
12. Wang, Z. D.; Fingas, M.; Sergy, G. *Environ. Sci. Technol.* **1995**, 29, 2622-2631.
13. Wang, Z. D.; Fingas, M. *J. Chromatography A*, **1995**, 712, 321-343.
14. Wang, Z. D.; Fingas, M.; Landriault, M.; Sigouin, L.; and Mullin, J. *J. Chromatography A*, **1997**, in press.
15. Wang, Z. D.; Fingas, M.; Blenkinsopp, S.; Sergy, G.; Landriault, M.; Sigouin, L.; Foght, J.; Westlake, D. W. S. in *Proceedings of the 19th Arctic and Marine Oil Spill Program Technical Seminar*, Environment Canada, Ottawa, Vol. 1, pp. 163-183, **1996**.
16. Hoff, R. Z.; Blenkinsopp, S.; Sergy, G.; Henry, C.; Foght, J.; Wang, Z. D.; Roberts, P.; and Westlake, D. in *Proceedings of the 18th Arctic and Marine Oilspill Program Technical Seminar*, Environment Canada, Ottawa, Vol. 2, pp. 1233-1241, **1995**.
17. Song, H.-G.; Wang, X.; Bartha, R. *Applied and Environmental Microbiology*, **1990**, 56, 652-656.

Figure 1 GC Chromatograms for TPH analysis of biodegradation North Slope (NS) oil samples. A,sterile control, B, positive control, C,negative control

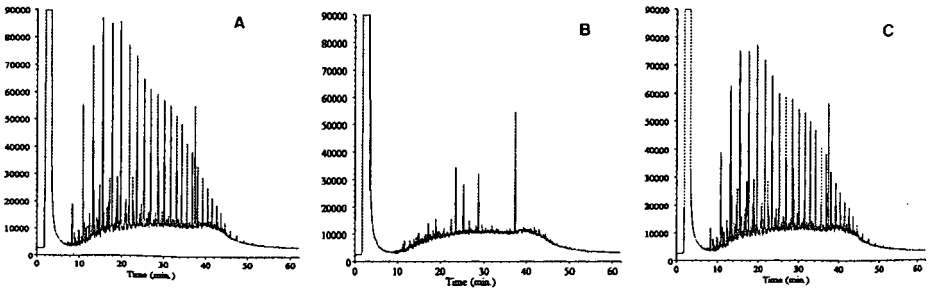

Figure 2 Changes of n-alkane distribution of NS oil samples under the standard inoculum conditions (28 days at 10 degrees C)

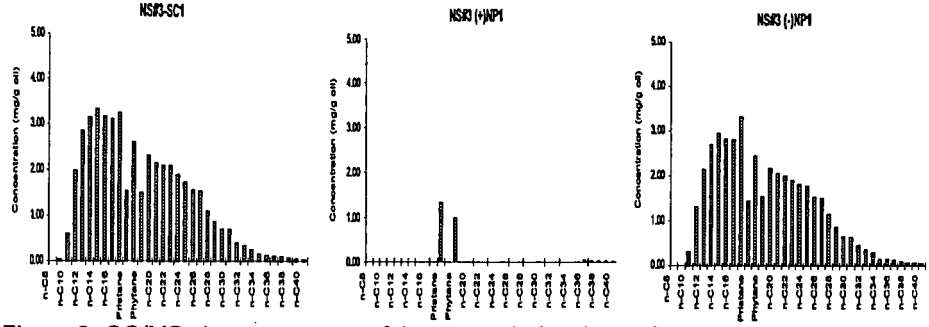

Figure 3 GC/MS chromatograms of the aromatic fractions of NS oil biodegradation series. CnB represent alkylbenzenes.

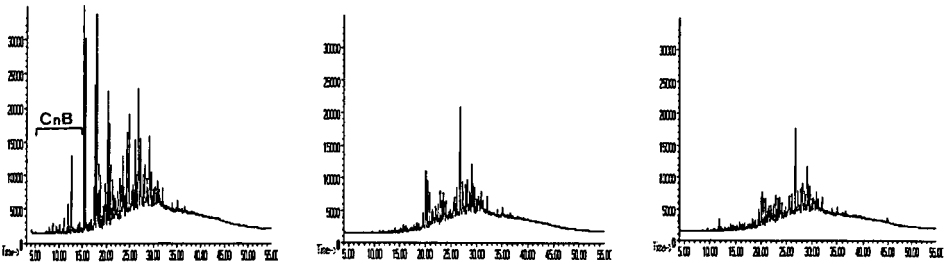

Figure 4 Distribution changes of 5 target alkylated PAH homologous series in NS oil samples due to biodegradation

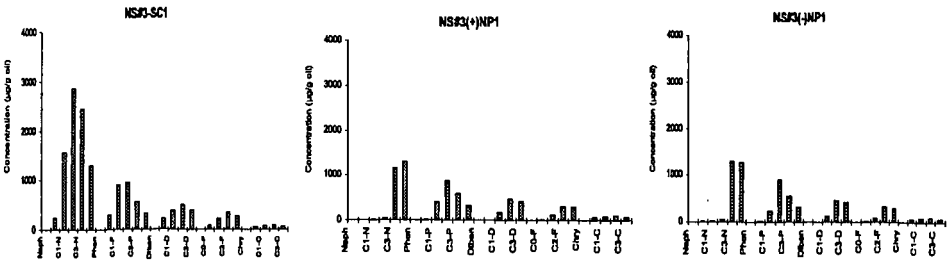

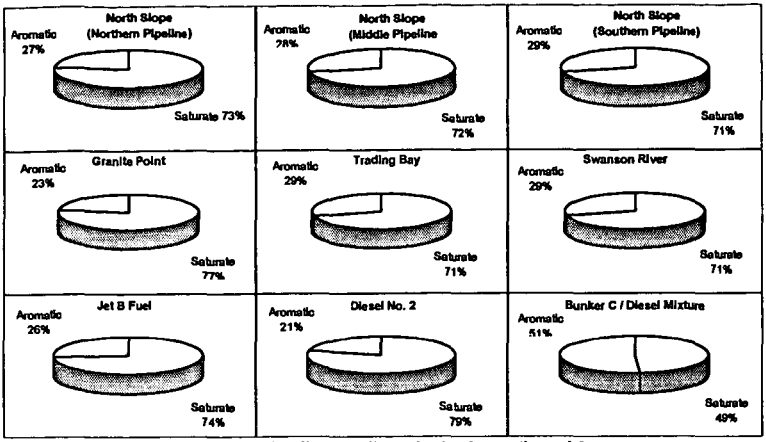

Figure 5 Weathered Alaskan crude oils and oil products: Aromatic and Saturate Comparison (% by weight).

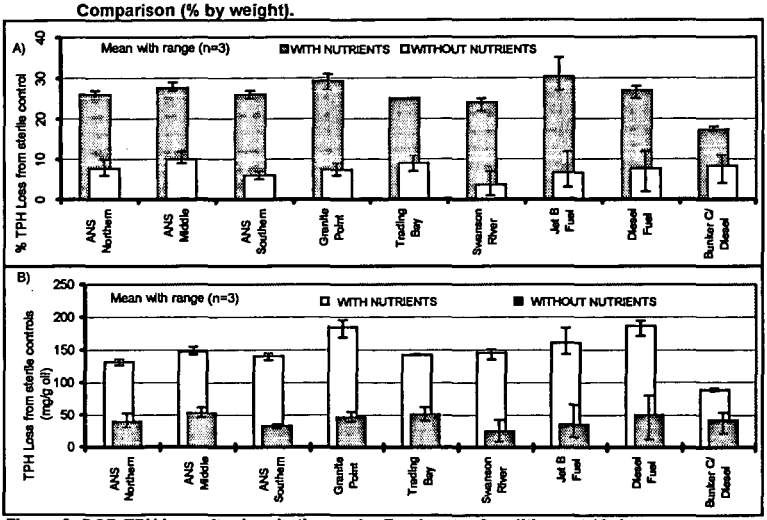

Figure 6 GCD-TPH loss after incubation under Freshwater Conditions at 10 degrees Celcius for 28 days, for all tested crude oils and oil products. A) % loss. B) Actual measured loss.

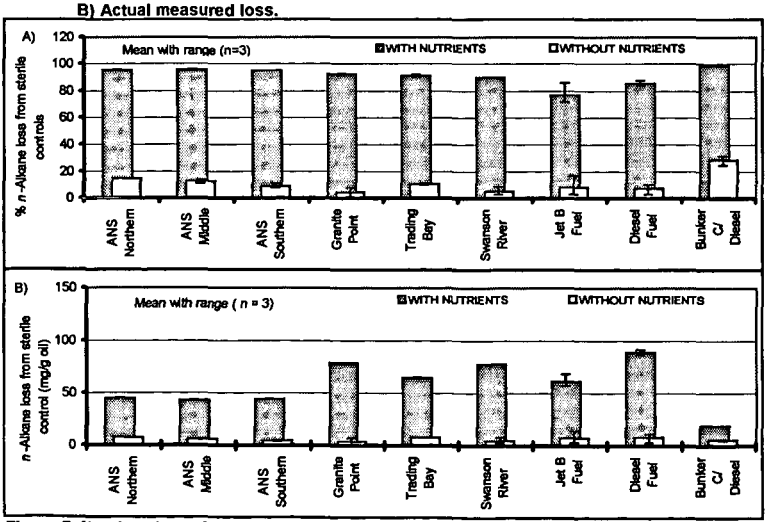

Figure 7 Total *n*-alkane loss after incubation under Freshwater conditions at 10 degrees Celcius for 28 Days, for all tested crude oils and oil products. A) % loss. B) Actual Measured Loss.

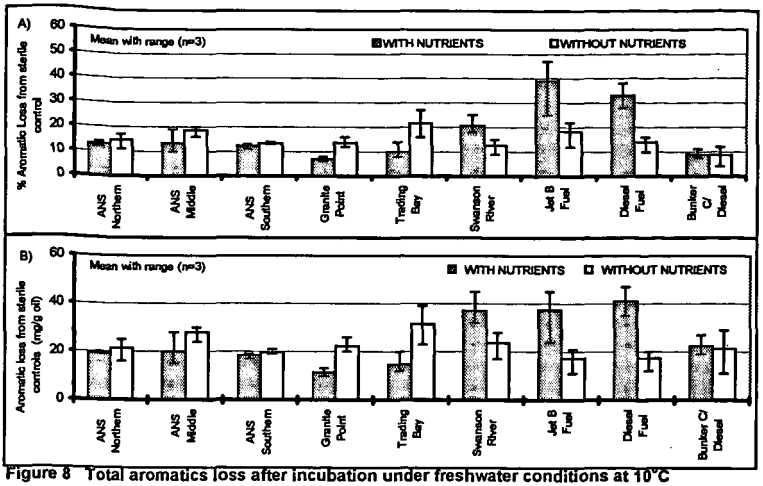

Figure 8 Total aromatics loss after incubation under freshwater conditions at 10°C for 28 Days, for all test crude oils and oil products.
A) % Loss. B) Actual Measured Loss.

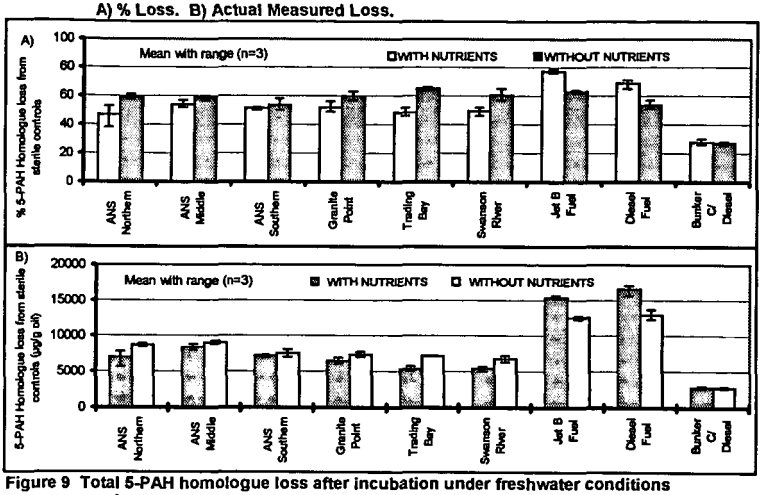

Figure 9 Total 5-PAH homologue loss after incubation under freshwater conditions at 10° C for 28 Days, for all tested crude oils and oil products.
A) % Loss. B) Actual Measured Loss.

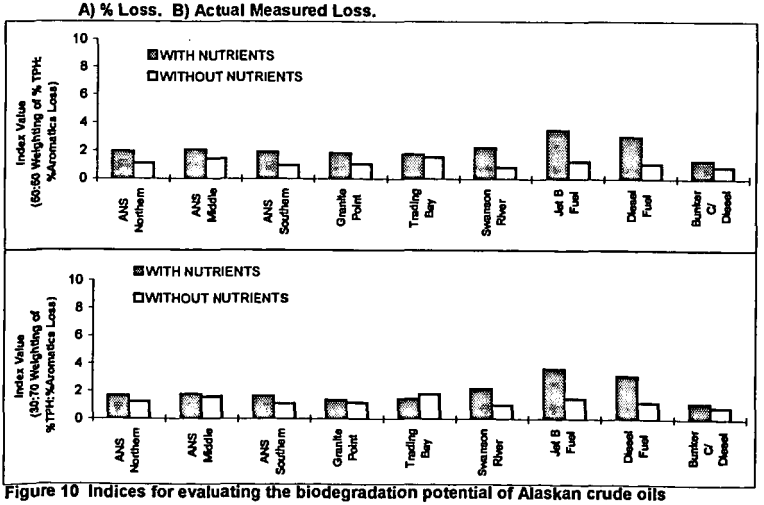

Figure 10 Indices for evaluating the biodegradation potential of Alaskan crude oils and oil products under freshwater conditions.
A) 50:50 Weighting of %TPH : % Aromatic Loss
B) 30:70 Weighting of %TPH : % Aromatics Loss

INTERACTION OF FUEL HYDROCARBONS AND CHLORINATED SOLVENTS AT AN AVIATION MAINTENANCE FACILITY

Austin I. Cooley, P.E.
W. Alan Hopkins, P.G.
Brown and Caldwell
1415 Louisiana, Suite 2500
Houston, TX 77002

Mark S. Nelson, P.E.
Transcontinental Gas Pipe Line Corporation
2800 Post Oak Boulevard
Houston, Texas 77251-1396

ABSTRACT

Releases of fuel hydrocarbons and chlorinated solvents from a former waste management unit at an aviation maintenance facility have resulted in impacts to soil and groundwater. As a result of the fuel hydrocarbon releases, strongly reducing conditions have been created in the source area. This has resulted in reductive dechlorination through dehalorespiration. Outside the source area aerobic conditions exist, resulting in biologically mediated oxidation of fuel hydrocarbons and chlorinated solvent daughter products, including vinyl chloride. The overall rate of natural attenuation in groundwater is sufficient to prevent plume migration, allowing for site closure with no active remediation. In addition to examining the interaction of the fuel hydrocarbons with the chlorinated solvents, the impact of naturally occurring inorganic electron acceptors on plume behavior is discussed.

INTRODUCTION

The site is an active aviation maintenance facility for corporate aircraft. A 500-gallon underground storage tank was used as a waste management unit to store used aviation fuel, waste oil, and spent solvents starting in 1980. The waste management unit was decommissioned and removed in 1991. During the removal, evidence of a release was observed due to visibly stained soil. Confirmation samples collected from the excavation indicated the soil was impacted with fuel hydrocarbons and chlorinated solvents.

MATERIALS AND METHODS

In response to the discovered release, soil borings were performed to collect soil samples to determine the extent of the impact. Because the impacted soils extended into the saturated zone, an array of seven monitoring wells was installed and sampled. Groundwater is encountered at a depth of 12 feet in a silty sand unit, which is overlain by a clay confining unit. Hydraulic conductivity in the saturated zone is approximately 0.5 feet per day with an effective porosity of 35%. The typical gradient of 0.005 feet per foot yields a calculated groundwater seepage velocity of 0.007 ft/day.

Benzene, toluene, ethylbenzene and xylenes (BTEX) and chlorinated aliphatic hydrocarbons (CAHs) were identified as the chemicals of concern. Industrial solvents present in the dissolved phase plume include tetrachloroethene (PCE), trichloroethene (TCE) and 1,1,1-trichloroethane (1,1,1-TCA). In addition, CAH daughter products are present in the dissolved phase, including isomers of dichloroethene (DCE), 1,1-dichloroethane (1,1-DCA), vinyl chloride and chloroethane.

To better understand the groundwater conditions and the potential for natural attenuation as a dissolved-phase plume management strategy, a groundwater geochemistry monitoring program was initiated. Samples were analyzed for common inorganic parameters that can act as electron acceptors in biologically mediated reduction/oxidation reactions. Where measurements of electron acceptor concentrations were not reliable, concentrations of reduction by-products were measured instead (Weidemeir, et al, 1995a). For example, ferric iron (Fe^{3+}) is a potential electron acceptor, but it is insoluble. Therefore, ferrous iron (Fe^{2+}), the reduction by-product of ferric iron, was instead analyzed. In addition to the inorganic analyses, concentrations of ethene and ethane were measured, as these are products of complete dechlorination of CAHs. Groundwater samples were also analyzed for other indicators of natural attenuation. Table 1 shows the suite of groundwater analyses that were performed.

RESULTS

Analysis of the data which is representative of groundwater quality at the site indicates that:

1. Fuel hydrocarbons are not migrating from source area.
2. Highly oxidized CAHs are not migrating from the source area.
3. Products of partial dechlorination are migrating from the source area.
4. The partially dechlorinated CAHs are degrading rapidly once they leave the source area.
5. Methanogenesis is occurring in the source area.
6. Depletion of nitrate, ferric iron and sulfate occur both in the methanogenic source area and the area immediately adjacent to it.
7. High dissolved oxygen is present both upgradient and downgradient of the source area.
8. Reduction/oxidation potential (E_h) is significantly lower in the source area than in the upgradient and downgradient groundwater.

DISCUSSION

Through biologically-mediated redox reactions, dissolved phase fuel hydrocarbons have created strongly reducing conditions in the source area. The fuel hydrocarbons act as the electron donor, depleting dissolved oxygen, nitrate, ferric iron and sulfate, which act as electron acceptors (Weidemeir, et al,1995b). As a result, methanogenic microbes can compete successfully in the source area, even though the rate of reaction for methanogenesis is significantly slower than reactions that utilize other common inorganic electron acceptors. Because of this differential preference, different zones have formed in groundwater at the site (Figure 1):

1. The anaerobic zone, where carbon dioxide is the primary electron acceptor, resulting in methanogenesis.
2. The anoxic zone, where sulfate, ferric iron and nitrate act as the primary electron acceptors. Dissolved oxygen is also present in this zone, but at low concentrations (<0.5 mg/L).
3. The aerobic zone, where oxygen is the primary electron acceptor.

The interaction of the fuel hydrocarbons, the CAHs and the inorganic elector acceptors at the site are fairly complex as illustrated in Figure 2.

The reduced conditions in the anaerobic zone are favorable for microbes that utilize CAHs as electron acceptors through dehalorespiration (Gosset and Zinder, 1996). As with inorganic electron acceptors, some CAHs are more favorable electron acceptors than others are. The more highly oxidized CAHs, such as PCE and 1,1,1-TCA are preferential to less oxidized species, such as vinyl chloride and chloroethane (Chapelle, 1996). This is because the rates of reaction for the more oxidized CAHs are faster than for the less oxidized CAHs. In the anaerobic source area, PCE and 1,1,1-TCA are degraded rapidly. This is evidenced by the lack of detections of these CAHs outside the anaerobic zone. Apparently, conditions are reduced enough in the anaerobic zone that even vinyl chloride is acting as an electron acceptor. This is indicated by the presence of ethene as a product of vinyl chloride dechlorination.

In the anoxic zone, degradation of the fuel hydrocarbons is completed, as evidenced by their absence in this zone. It is unclear how the less oxidized CAHs in the anoxic zone are reacting. Conditions are probably not reduced enough for vinyl chloride and chloroethane to act as electron acceptors in this zone. This is indicated by the lack of ethene detections in the anoxic zone. These less oxidized CAHs may be acting as electron acceptors in redox reactions where fuel hydrocarbons act as electron donors. Vinyl chloride may also act as electron donors in the anoxic zone. For example, microcosm studies have shown that vinyl chloride can act as an electron donor in a biologically mediated redox reaction where ferric iron is the electron acceptor (Bradley and Chapelle, 1996). 1,1-DCA and isomers of DCE may also act as electron donors under anoxic conditions through cometabolism. A possible primary substrate for this cometabolism is methane that has migrated out of the anaerobic zone. Chloroethane readily hydrolyzes abiotically under anoxic conditions (McCarty and Semprini, 1994).

In the aerobic zone, the remaining CAHs are degraded, evidenced by their absence in this zone. These less oxidized species, including DCE isomers, 1,1-DCA, vinyl chloride and chloroethane, appear to be acting as electron donors in this zone, with oxygen as the electron acceptor. 1,1-DCA, chloroethane and vinyl chloride can act as electron donors under aerobic conditions (Weidemeir et al, 1996). There is conflicting evidence as to whether or not DCE isomers can act as a carbon source under aerobic conditions (RTDF, 1996). However, aerobic cometabolism of DCE isomers is reasonably well established (Hirl and Irvine, 1997).

A spatial analysis was performed to determine natural attenuation rate constants through linear regressions (Buscheck, et al, 1993). Table 2 shows the results of this analysis. As indicated by the R^2 values, the validity of the analysis is good with the exception of PCE, 1,1-DCE and cis-1,2-DCE. The poor R^2 values for the DCE isomers is probably due to:

1. DCE being both created and destroyed through the dechlorination process.
2. DCE acting as both an electron acceptor and an electron donor within the plume.
3. Limitations of primary substrates for DCE degradation under cometabolism.

The poor R^2 value for PCE is due to destruction of PCE at a more rapid rate in MW-7, the area immediately beneath the source, which skews the curve fit. This is probably attributable to greater BTEX concentrations in the overlying source area soils. Apparently, fuel hydrocarbon electron donors are being contributed to the groundwater at a more rapid rate than in this area.

CONCLUSIONS

At this site, fuel hydrocarbons created anaerobic and anoxic conditions by depleting inorganic electron acceptors. In the absence of inorganic electron acceptors, other than carbon dioxide in the anaerobic zone, highly oxidized CAHs act as electron acceptors for fuel hydrocarbons. This dehalorespiration degradation results in partial dechlorination to less oxidized CAHs. The degradation of fuel hydrocarbons is completed in the anoxic zone, where oxidation of the partially dechlorinated hydrocarbons commences. The mineralization of the remaining CAHs is completed in the aerobic zone.

As a result of the interaction of the fuel hydrocarbons, the CAHs and the inorganic electron acceptors, the plume stabilizes at a short distance from the source. Because of this, natural attenuation is a feasible plume management strategy for this site.

REFERENCES

Buscheck, T.E., K.T. O'Reilly and S.N. Nelson, 1996, Evaluation of Intrinsic Bioremediation at Field Sites *The Proceedings of the 1995 Petroleum Hydrocarbons and Organic Chemicals in Groundwater: Prevention, Detection, and Remediation*: 367-381

Bradley, P.M. and F.H. Chapelle, 1996, Anaerobic Mineralization of Vinyl Chloride in Fe(III)-Reducing Aquifer Sediments *Environmental Science and Technology* Volume 30: 2084 - 2086

Chapelle, F.H., 1996, Identifying Redox Conditions That Favor the Natural Attenuation of Chlorinated Ethenes in Contaminated Ground-Water Systems *Symposium on Natural Attenuation of Chlorinated Organics in Ground Water* EPA/540/R-96/509: 17-20

Gosset, J.M. and S.H. Zinder, 1996, Microbiological Aspects Relevant to Natural Attenuation of Chlorinated Ethenes *Symposium on Natural Attenuation of Chlorinated Organics in Ground Water* EPA/540/R-96/509: 10-13

Hirl, P.J. and R.L. Irvine, 1997, Degradation of Perchloroethylene Using Aerobic Sequencing Batch Reactors *In Situ and On-Site Bioremediation: Volume 3*:87-92

McCarty, P.L. and L. Semprini, 1994, Ground-Water Treatment for Chlorinated Solvents *Bioremediation of Groundwater and Geological Material: A Review of In-Situ Technologies*:5-1-5-2

Remediation Technology Development Forum, 1996, Guidance Handbook on Natural Attenuation of Chlorinated Solvents

Vogel, T.M, 1994, Natural Attenuation of Chlorinated Solvents *Bioremediation of Groundwater and Geological Material: A Review of In-Situ Technologies*: 10-1-10-25

Weidemeir, T.M., J.T. Wilson, D.H. Kampbell, R.N. Miller, and J.E. Hansen, 1995a, Technical Protocol for Implementing Intrinsic Remediation for Natural Attenuation of Fuel Contamination Dissolved In Groundwater

Weidemeir, T.M., J.T. Wilson, and D.H. Kampbell, 1995b, Significance of Anaerobic Processes for the Intrinsic Bioremediation of Fuel Hydrocarbons *The Proceedings of the 1995 Petroleum Hydrocarbons and Organic Chemicals in Groundwater: Prevention, Detection, and Remediation*: 49-61

Table 1. Groundwater Analyses Performed

Analysis	Method
Volatile Organic Compounds	EPA Method 8260
Methane, Ethane, and Ethene	RSKSOP-147
Sulfate	EPA Method 375.4
Nitrate	EPA Method 353.3
Dissolved Oxygen	Field Probe in Flow Through Cell/Hach Field Kit
Ferrous Iron	Hach Field Kit
Oxidation/Reduction Potential	Field Probe in Flow Through Cell
Temperature	Field Probe in Flow Through Cell
PH	Field Probe in Flow Through Cell
Conductivity	Field Probe in Flow Through Cell

Table 2. Degradation Rate Constants

Parameter	λ/v_x	R^2 Value	Groundwater Velocity (ft/d)	Degradation Rate Constant (day^{-1})
BTEX Compounds (Non-Chlorinated VOCs)				
Benzene	0.0602	0.9427	0.007	4.30%
Toluene	0.0553	0.8038	0.007	3.95%
Ethylbenzene	0.0194	0.8038	0.007	1.39%
Xylenes	0.0429	0.8038	0.007	3.06%
PCE-Based Compounds				
Tetrachloroethene	0.0114	0.1662	0.007	0.81%
Trichloroethene	0.0379	0.8713	0.007	2.71%
cis-1,2-Dichloroethene	0.0580	0.6230	0.007	4.14%
1,1-Dichloroethene	0.0865	0.7331	0.007	6.18%
Vinyl Chloride	0.0785	0.8038	0.007	5.61%
TCA-Based Compounds				
1,1,1-Trichloroethane	0.0239	0.8958	0.007	1.71%
1,1-Dichloroethane	0.0147	0.7413	0.007	1.05%
1,2-Dichloroethane	0.0499	0.9564	0.007	3.56%
Chloroethane	0.0953	0.8038	0.007	6.81%
Vinyl Chloride	0.0785	0.8038	0.007	5.61%

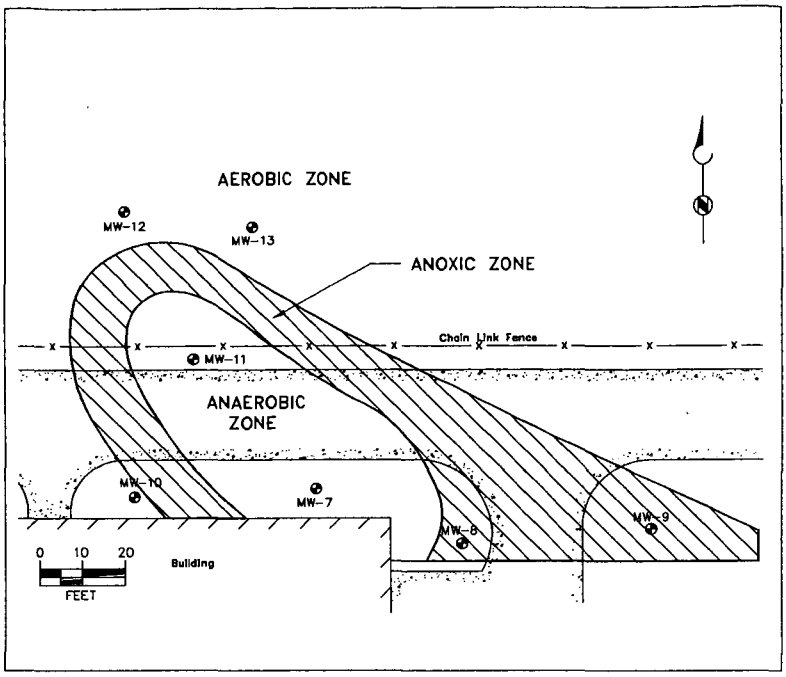

Figure 1: Groundwater Zones

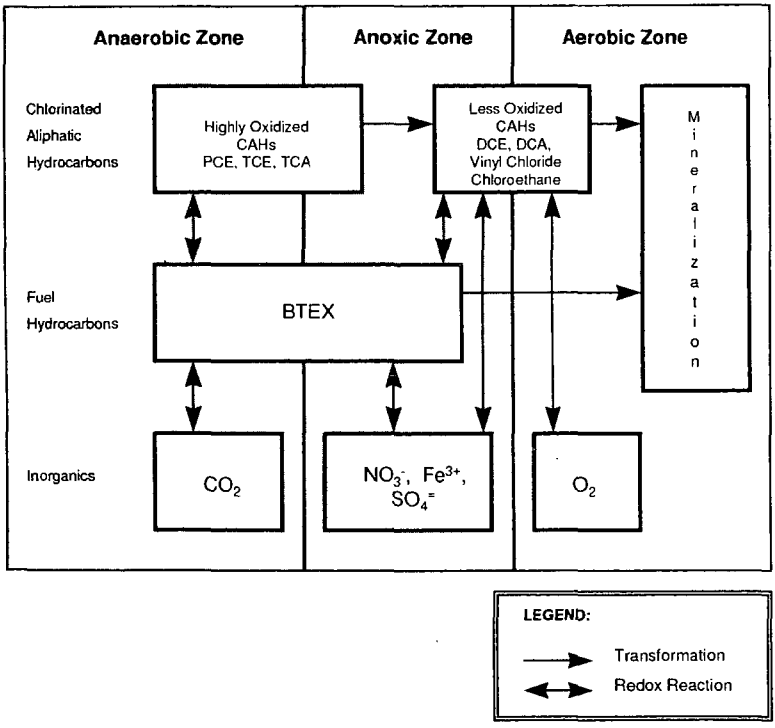

Figure 2: Chemical Interactions

Adjusting Bioremediation Expectations to the Reality of Bioavailability

Maureen E. Leavitt
Paladin International, Inc.
1946 Oak Ridge Turnpike
Oak Ridge, TN 37830-6001

ABSTRACT

Bioremediation of hydrocarbons in groundwater systems has been conducted with great success at a multitude of sites. In most cases, hydrocarbon concentrations in groundwater can be brought near or below drinking water standards. This is not hard to believe since these are biodegradable contaminants that are solubilized and available for biodegradation. Attaining these low levels in soils has been a challenge in the bioremediation industry. The true issue, bioavailability, has been clouded by vendors' eagerness to cite other limitations such as biomass or nutrients. Bioremediation of most hydrocarbon contamination is limited most by the extent of sorption of contaminants to the soil particles. Therefore contaminant properties, soil type and mixing are the primary governing factors with respect to bioremediation. This paper will illustrate the issue of bioavailability of hydrocarbons in soil, focusing on the achievable endpoints and regulatory issues.

INTRODUCTION

Biodegradation of petroleum fuels has been documented under both laboratory and field conditions (1,2). Many different matrices including groundwater, ocean water, sediment, soil and even gravel support bacterial populations capable of mineralizing various hydrocarbons into carbon dioxide and water. It is generally accepted that biodegradation can gradually mitigate most light end petroleum hydrocarbons to an extent that biodegradation can be used to "clean" contaminated soil and groundwater.

The challenge in applying accelerated biodegradation techniques is not the ability to stimulate bacteria to degrade hydrocarbons; it is judging how low the hydrocarbon concentration can go. This judgment is based more on physical/chemical properties of the soil and contaminants (and their interactions) which together are referred to as "bioavailability". The following text describes the current models regarding bioavailability and how the issue is incorporated into the practice of bioremediation.

REASONS FOR BIOAVAILABILITY CONSIDERATION

Cost - The issue of bioavailability is met with mixed opinions. Some bioremediation vendors see it as an opportunity to produce and sell "elixir" products that might alleviate the limitation and further lower cleanup endpoints. Specific surfactants, bacterial blends and nutrient packages have all been offered to address the limitation of bioavailability. In cases where side by side testing with and without the product can be compared, the product does not provide a significant benefit that would justify the added cost (3). In more cases, comparable data from a test without addition of the product are not available. When site owners are uncertain of the principles of biostimulation (the practice of using indigenous bacteria), they tend to choose these products as a tangible enhancement to their system. Subsequent results are disappointing.

Contaminant Detection - Among the array of contaminants addressed with bioremediation, hydrocarbons present one of the most difficult analytical challenges. Most hydrocarbon contamination in soil and groundwater is derived from fuel, which is composed of several hundred compounds. Analytically, these compounds are typically measured using a method that groups these compounds into a single number. Analyses that use this approach include diesel range organics (DRO), gasoline range organics (gro), total recoverable petroleum hydrocarbons (TRPH), and oil and grease (O&G). With so many components influencing a single value, significant reduction in certain components can be masked. Furthermore, there is no opportunity to incorporate weighted distinction between those components that do/don't pose health risks. The result may be more cost than is needed to protect human health and the environment.

In some cases, specific compounds have been chosen to represent the compounds of concern within a fuel blend. These compounds are typically volatiles and semivolatiles such as benzene, toluene, ethylbenzene, and xylenes (BTEX), naphthalene and methylnaphthalenes. Choosing these compounds as targets for remediation efficiency assessment is desirable since these compounds are easy to detect

and they are among the first compounds to be biodegraded in environmental systems. When these compounds are the targets, remediation systems become more predictable and more finite.

A remediation specialist may be fortunate to have contaminant that is made up of light end TRPH compounds (smaller hydrocarbons, less complexity to the compound's configuration), reaching the endpoint in a timely manner. This specialist can be unfortunate, addressing compounds that are grouped at the heavier end of the spectrum (longer hydrocarbons, more branching), which may result in extended treatment periods. Therefore, knowing the origin of the contaminant and the means by which success will be measured is critical in determining a system's treatment period.

THE MODELS

The mechanisms behind bioavailability have been explored and are still the subject of significant research efforts (4,5). From a grand scale, three explanations exist. The first is that contaminants are not available for biodegradation because they are physically occluded within the soil and do not have contact with the microorganisms, therefore they are unavailable. This is always true to some extent because contaminant migration over extended periods can result in contaminant located in areas where short-term, aqueous-based treatment supplements cannot penetrate. However, there are many techniques that provide a great degree of soil disruption prior to treatment. These techniques are generally known to produce lower endpoints, but there are occurrences where contaminants still exist at appreciable levels after treatment.

The second model is based on soil type. Sorptive properties of soils vary depending on their characteristics. Figure 1 illustrates the relative bioavailability of contaminants in different soil types. Soils that are sandy generally contain larger soil particles and less of an ionic charge. Contaminants in these soils are more likely to be bioavailable. Soils that contain clay have finer particles and more of an ionic charge.

The third model explaining persistent contamination is molecular hindrance. In this case, the contaminants are composed in such a complex manner that the molecule itself is not available for microbial attack. This model is not influenced by environmental factors. However, at sites where the original source of contamination is not known, detecting these contaminants in a TRPH measurement could be misleading, causing an extended treatment period that may not reach target endpoints. It is likely that limited bioavailability is the primary obstacle as depicted in Figure 2.

CURRENT PRACTICES

While research and development of the issues surrounding biotreatment endpoints continues, some strategies have been developed to proceed with bioremediation. Regulators have been given some degree of flexibility in determining endpoints based on Risk-Based Correction Action (RBCA) approaches. This new site-specific approach to determine how clean is clean has resulted in acceptance of higher endpoints because the risk to human health and the environment is reduced at that specific site. RBCA has been and will continue to assist in the understanding and acceptance of the limitations of bioavailability.

Stakeholders have begun to consider the grand effects bioremediation has on their site's contamination. Bioremediation certainly decreases the overall concentration of contaminants. However, bioremediation also provides important benefits that reduce the risk of contaminants that remain on-site. By removing the most available compounds, bioremediation reduces the mobility of the remaining contaminants. Similarly, it can reduce the leachability of the contamination. Therefore, even if the analytical value is still detectable, the remaining contamination poses a reduced risk to human health and the environment.

CONCLUSIONS

While all of the activity dedicated to mitigating organic contamination in the environment continues, policy-makers and scientists must complete the database that persuades cleanup target endpoints. The goals of cleanup should be determined based on the risk to human health and the environment, not on the analytical detection capabilities. Hydrocarbons are a challenge in this regard since evaluating toxicity and health hazards of hundreds of individual compounds is time-consuming and expensive. RBCA techniques have been successful at providing a degree of realism in endpoint decision-making;

however, more effort needs to focus on the benefit of remediation dollars spent to pursue very low endpoints. Further, this cost benefit should be directly related to estimated lives saved.

REFERENCES

1. Huesemann, M.H. 1995. "Predictive Model for Estimating the Extent of Petroleum Hydrocarbon Biodegradation in Contaminated Soils", Env. Science and Technol. 29:7-18.
2. Cioffi, J.C. W.R. Mahaffey and T.M. Whitlock. 1991. "Successful Solid-Phase Bioremediation of Petroleum Contaminated Soil", Remediation, Autumn, 373-389.
3. Leavitt, M.E. and K.L. Brown. 1994. "Biostimulation Versus Bioaugmentation - Three Case Studies", in R. Hinchee et al., (eds) Hydrocarbon Bioremediation p.72-79, CRC Press, Inc. Boca Raton.
4. Huesemann, M.H. 1997. "Incomplete Hydrocarbon Biodegradation in Contaminated Soils: Limitations in bioavailability or Inherent Recalcitrance?" Bioremediation Journal (1):27-39.
5. Loehr, R.C. 1996. "The Environmental Impact of Soil Contamination: Bioavailability, Risk Assessment, and Policy Implications", National Environmental Policy Institute and the Reason Foundation.

TABLES AND FIGURES

Table 1. Analytical Methodology and Fuel Molecular Weight Classes

Fuel Class or Analytical Method	Detectable Carbons Per Molecule Range
Gasoline	C5-C10
Jet Fuel	C9-C16
Diesel	C10-C22
Kerosene	C12-C18
Gas Oil	>C12
Waste Oil	>C18
EPA 8010 (volatiles)	C2-C12
EPA 8015 (TRPH)	C7-C30
EPA 418.1 (TPH)	>C14

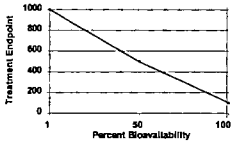

Figure 1. Relationship Between Bioavailability and Treatment Endpoints

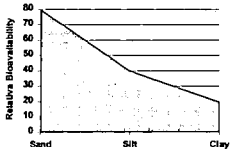

Figure 2. Soil Type Influence on Bioavailability

QUALITY ANALYSIS OF PETROLEUM COKES AND COALS FOR EXPORT SPECIFICATIONS REQUIRED IN USE OF SPECIALTY PRODUCTS AND UTILITY FUELS

Jun M. Lee, James J. Baker, Daniel Murray, Robert Llerena, Jeffrey G. Rolle
A. J. Edmond Co.
1530 West 16th Street, Long Beach, CA 90813

Keywords: petroleum coke, coal, export quality

ABSTRACT

Quality of petroleum cokes and coals has been evaluated for export specifications required in use of specialty products and utility fuels. Various green and calcined cokes, produced at refineries in California, and coals for shipment are sampled at California and national ports, and analyzed by using ASTM Methods. Quality analysis reports include: proximate and ultimate analyses, metals, Btu, density, size distribution, hardgrove grindability, and other physical, chemical and mechanical properties. Some of recent analysis results from calcined petroleum coke produced for aluminum anode grade, green (raw) coke used in calcination, petroleum coke for high- and low-Btu fuel grade, low- and high-rank coals are compared and presented. QC/QA/SQC programs have been utilized for good precision and accuracy of data generated with acceptable repeatability and reproducibility.

INTRODUCTION

The A. J. Edmond Co. bas over 30 years extensive experience specialized in analysis, testing and evaluation of petroleum cokes and coals for export specifications, which are used primarily as solid fuels in power plants and cement kilns and in other applications to produce specialty products, carbon anodes, metallurgical cokes, etc. Process development services currently provided include consulting, training, and process studies in production of calcined petroleum cokes for aluminum anode-grade. Quality of petroleum cokes was evaluated by Rolle, et. al. [1,2], investigating the effects of metal impurities (vanadium, nickel and sodium) on the properties of cokes and anodes.

The quality of petroleum cokes produced by U. S. refineries has been affected by several major governing factors during the past decade from 1984 to 1993: (1) declining quality of crude oils, (2) coke production increase, (3) market demand and supply in liquid/solid fuels and exports, (4) specifications for end-use products, and (5) coking processes and calcination technology [3]. The average API gravity of crude oils declined annually by 0.17 degree/yr from 33 to 31; and the average sulfur content of crude oils increased by 0.029 wt%/yr from 0.88 to 1.21. As a result the coke production steadily increased by 51 % expecting continuous increase in the coming years, and the sulfur content of cokes is projected to increase from current average, 4.5 wt% to 5.5 wt% in future.

The U. S. coking capacity was fully utilized in 1993 having more than 100% coke production factor. The annual production was 78,430 tons/cd, of which 66% was exports (a major market demand) to Japan, Turkey, Italy, and other countries (total 44). The price of petroleum coke varies highly dependent upon its quality estimating in the range of $19/ton for utility fuel-grade to $550/ton for calcined super-premium needle coke. Anode-grade coke can vary from $45/ton for green (raw) to $200/ton for calcined.

The objective of this study is to evaluate the petroleum coke quality for export primarily based on recent analysis results from calcined petroleum coke produced for aluminum anode grade, green (raw) coke used in calcination, petroleum coke for high- and low-Btu fuel grade, and in addition the quality of low- and high-rank coals is evaluated.

SAMPLING AND PREPARATION

Representative samples of petroleum cokes and coals have been obtained from various refineries in California and storage facilities at numerous national ports. The auto sampler installed at the Long Beach port is sometimes used upon client's request for periodic routine sampling of blends for shipment. Laboratory samples are prepared for quality analysis following the procedures and principles in handling listed in the ASTM Methods D 346, D 2013 and D 2234, which are documented in the Quality Assurance Manual. Analysis samples are designated as refinery daily, weekly, monthly, M/V ship, QC/QA round robin, special test, etc. and stored for additional week, three or six months before disposal.

QUALITY SPECIFICATIONS FOR EXPORT

Petroleum cokes are produced at refineries using three different types of coking processes: delayed, fluid, and flexicoking. The delayed coker is mostly used at forty-nine U. S. refineries processing total 1.57 mm b/sd [3]. The other fliud coker and flexicoker are less utilized at a relatively smaller capacity (seven refineries and 0.2 mm b/sd). Coke products are classified as shot, sponge, (sometimes honeycomb), or needle coke depending on their chemical and physical characteristics. Shot coke is hard, having spherical form, and physically produced through precipitating asphaltenes; sponge coke is dull and black, having porous, amorphous structure, and is considered as a mixture of shot and needle cokes; and needle coke is silver-gray, having crystalline broken needle structure, and chemically produced through cross linking of condensed aromatic hydrocarbons during coking reactions[4].

Product grades and uses of green (raw) and calcined petroleum cokes

Green petroleum cokes are mostly used as utility fuels (about 73% for fuel-grade) in power generation and cement production including future developing projects of gasification IGCC and COG, and as feedstock (about 27%) for further upgrading calcination [5]. Uses of calcined cokes are: 71% for aluminum anode-grade, 9% for graphite electrodes, needle-grade, 8% for titanium dioxide pigments, 6% for recarburization of ductile iron products, and 6% for others (chlorine, phosphorous, silicon carbide, calcium carbide, etc.). Needle-grade calcined coke has three types, super-premium (SP), premium (P) and intermediate (I) depending on properties. Calcined petroleum cokes are used as reducing agent in production of titanium dioxide pigments because of extremely low ash and volatile content (6), and are further thermally treated at 2500 deg C to lower sulfur content to 0.03 wt% to meet specifications for recarburization (7).

Fuel-grade green coke

Depending on the location of refineries in the U. S. sulfur content of fuel-grade cokes varies; 2.25-2.60 wt% produced in Kansas and Oklahoma and 4.30-4.95 wt% in California, Louisiana Gulf Coast and Texas Gulf Coast. Typical ranges of coke properties for fuel-grade specifications are listed as follows:

13,000-15,000 Btu/lb
2.5-5.5+ wt% sulfur
200-400+ ppm vanadium
9-12 wt% volatile matter
0.1-0.3 wt% ash
100 HGI

Normally cokes are blended with coals at 10-20 % before burning in boilers because of their low volatile matter and high sulfur content. In use of cement kilns the addition of cokes can constitute up to 50 % of the fuel mixture and is carefully controlled conducting test burn due to detrimental effects of high sulfur and vanadium content to concrete quality [8]. Sulfur contamination can cause cement cracking and preheater plugging, and high vanadium content above 500 ppm can cause cement to lose strength.

Aluminum anode-grade calcined coke

Calcination process basically removes volatile matter, hydrogen and some of sulfur present in green cokes as a result increasing density and electrical conductivity suitable for use of carbon anodes in aluminum production. Typical ranges of calcined coke properties for aluminum anode-grade specifications are listed as follows [5,7-9]:

Property	Green	Calcined
wt% S	2.5	2.5 (1.7-3.0)
wt% ash	0.25	0.30 (0.1-0.3)
ppm V	150	200 (165-350)
ppm Ni	150	200(120-350)
wt% Si	0.02	0.02
wt% VM	10-12	<0.25
resistivity, microomega-m		950
real density, g/cu-cm		2.06
bulk density, g/cu-cm		0.80
coefficient of thermal expansion per deg C		2 x 10 to -6

Graphite needle-grade calcined coke

Feedstocks, needle coke precursors, are characterized by low API gravity, low asphaltene content, and a high degree of aromaticity [8]. Generally hydrocarbon streams are used with low sulfur content catalytic cracker slurry oils, tars derived from the thermal cracking of refinery gas oils, hydrodesulfurized catalytic cracker slurry oils, and coal tar pitches. Operating pressure and temperature of a coker are higher than other coking operations. The most important specification has been the coefficient of thermal expansion (CTE) as an indicator of the coke's structural alignment, which is related to the current-carrying capacity and mechanical integrity of resultant graphite electrodes. Typical ranges of calcined coke properties for graphite needle-grade specifications are listed as follows [7-9]:

Property	Green	Calcined (SP/P/I)
wt% S	0.8	0.8 (0.3-0.8)
wt% ash	0.10	0.15 (0.03-0.2)
ppm V	10	10
ppm Ni		20-40
wt% Si	0.04	0.04
wt% VM	8	<0.25
resistivity, microomega-m		1100
real density, g/cu-cm		2.12 (2.12-2.15)
bulk density, g/cu-cm		0.88
coefficient of thermal expansion per deg C		0.3 x 10 to -6 (0.2-0.4 x 10 to -6)

Coal quality specifications

On-line coal quality analyzers are available for power plant monitoring and optimization resulting in lower operating costs [10]. Electric Power Research Institute (EPRI) developed coal quality impact model (CQIM) and coal quality evaluation system (C-QUEL). Coal quality is based on various complex properties such as heating value, ultimate analysis, ash content, moisture content, sulfur content, and mineral analysis. Key properties correlated for EPRI cause and effect relationships are ash, moisture, sulfur, silica, alumina, heating value, volatile matter, etc.

Typical ranges of coal properties analyzed at the A. J. Edmond Co. are listed in the following. Bituminous coal properties are obtained from M/V ship samples, and subbituminous coal properties are from western coal round robin samples.

Property	Bituminous	Subbituminous
(As-received)		
wt% moisture	6-10 (max. 10)	25-30
wt% ash	8-10	4-8
wt% volatile	36-41	30-35
wt% fixed carbon	42-47	30-35
Btu/lb	11,450-11,750	8,000-9,000
wt% sulfur	0.3-0.5	0.3-0.5
(Ultimate, dry, wt%)		
carbon	71-72.5	66-68
hydrogen	4.5-5.5	4.6-5.1
nitrogen	1.2-1.5	0.9-1.1
chlorine	0.01-0.03	
sulfur	0.4-0.5 (max. 0.7)	0.4-0.6
oxygen	10-12.5	17-20
(Mineral, wt% ash)		
silica	52-62	30-40
alumina	12-17	15-20
ferric oxide	3-7	3-6
titania	0.6-0.8	1-2
phosphorous pentoxide	0.2-0.8	
lime	7-14	15-25
manganese oxide	0.02-0.03	0.01-0.03
magnesia	1-3	3-6
barium oxide	0.04-0.11	
sodium oxide	0.5-4	1-3
potassium oxide	0.4-0.9	0.5-2

Property	Bituminous	Subbituminous
(Mineral, wt% ash)		
sulfur trioxide	5-7	10-15

Hardgrove Grindability Index 45-49

ash fusion temperature, deg C

	IDT	+1,220
	HT	+1275
	FT	+1,340
size	50 mm x 0	100%
	2 mm x 0	30% max.

ANALYTICAL METHODS USED

Laboratory test methods using various advanced analytical instruments are described in the Quality Assurance Manual of A. J. Edmond Co. Primary analytical methods are summarized in the following.

Purpose	ASTM Method		Instrument
metals	D5600	ICP-AES	PE Optima 3000
	D3682	ICP-AES, AA	
	D5056	AA	
sulfur	D4239	LECO	LECO SC 432
	D3177	PARR	PARR 1760
	D1552	Dietert/LECO	
	D5016	LECO	
CHN	D5373	LECO	LECO CHN-1000
N	D3179	KJELDAHL	
	ISO333	KJELDAHL	
Btu	D3286	PARR	PARR 1108, 1261, 1563
moisture	D3173		
ADL/RM	D3302,D4931		
volatile	ISO562,D3175,D4421		
ash	D4422,D3174		
VBD	D4292		
RD	D5004		
HGI	D5003,D409		
sieve	D5709,D293		

QC/QA/SQC PROGRAMS

Laboratory quality control (QC) program includes sample tracking and identification, sample preparation and analysis. Analytical tests are generally run within 24 hour period, however, some analyses of samples, i.e. moisture, sulfur, volatile, shot, etc. are completed in an hour, two hour or eight hour intervals in order to meet customer's requests and respond to any process changes. Information of analysis results is transferred through a Computer Data Base or simply by hand-written daily analytical reports. Statistical quality control (SQC) is performed by X and R control charts to assure good precision and accuracy of data generated with acceptable repeatability and reproducibility. Besides SQC trending or plotting of data, other notable quality assurance checks include use of calibration standards for elemental and metals analyses, daily instrument calibration, and check lists without any known standards. For quality assurance (QA) program in addition to the QC/SQC system, round robin samples of petroleum cokes and coals are analyzed routinely, monthly or as required, for further evaluation of the quality control results.

RESULTS FROM QUALITY TREND ANALYSIS

Quality of green petroleum coke (Figures 1-4)

Figure 1 shows sulfur content of green petroleum cokes obtained from fourteen refineries (designated as coke type A to N) and analyzed during the period of December 19, 1996 to February 20, 1997. Daily, weekly and monthly data are included for trend evaluation. Delayed cokes are A to L, fluid coke is M and type N is delayed coke used for calciner feedstock. A, B and C are best fuel-grade cokes with lowest sulfur content in the range of 0.8-1.6 wt% (average 1.0-1.2 wt%), while L has highest sulfur content of 4.2-6.0 wt%. Sulfur content of fluid coke M is 2.8-3.2 wt%.

In Figure 2 cokes A, B and C have highest heating values (15,500-15,800 Btu/lb), again best suited for fuel feedstock. Heating value of fluid coke M is lowest, 14,300-14,700 Btu/lb.

Figure 3 illustrates ash content varies in the range of 0.2 to 0.5 wt% except for coke N with 0.1 wt% ash, which is used for calciner feedstock.
Vanadium content of cokes significantly varies from 300 to 1600 ppm (Figure 4), depending on origin of production refinery and their usages. Good fuel-grade cokes A to E have vanadium content in the range of 300 to 600 ppm. Calciner feedstock coke N has 300-340 ppm vanadium.

Quality specifications of calcined petroleum coke (Figures 5 and 6)

Three different calcined petroleum cokes selected from M/V ship samples are compared in Figures 5 and 6. Most of our analytical data for these samples are within the specification limits for export. Sulfur content, vibrated bulk density (VBD), real density (RD), vanadium, nickel and sodium metal contents are plotted with actually measured, specification high and low values.

QC/QA/SQC programs

Figure 7 presents a SQC trend X-chart for sulfur content of green petroleum cokes (type A, B, C, L, M and N). For simplicity of presentation, only three data series show average, upper control limit (UCL) and lower control limit (LCL). All data are statistically controlled with two standard deviation interval at 95% confidence level.

SQC trend X-chart for metal contents (V, Ni and Na) of calcined cokes are plotted in Figure 8. These data were generated during the period of July, 1996 to February, 1997. Although the trend shows slightly increases in metal contents (about 20-30 ppm) in the latter part of the period, most of data are within the specification limits for export.

In January, 1997 a QA round robin sample of petroleum coke was analyzed for metal contents using PE Optima 3000 (ICP-AES). Test method was ASTM D 5600 performed with two different dissolution acids, 20% HCl and 4% HNO3, respectively. Results of six analyses are summarized below.

	Concentration, ppm		
Metal	Average	Standard Deviation	ASTM RR Ranges
Si	61.2	25.6	19-94
	83.7 w/HCl	10.0 w/HCl	
	38.7 w/HNO3	4.5 w/HNO3	
Fe	46.5	1.8	17-94
V	402.8	4.4	24-59
Ni	168.2	3.5	17-23
Al	24.3	1.5	15-40
Ca	7.2	1.3	21-36
Na	34.5	6.1	10-31
Cr	0.5	-----	-----

With 20% HCl dissolution acid, silicon content of the coke is observed to be higher by 45 ppm than that with 4% HNO3 dissolution acid. Other metal contents are similar with both acids. Good standard deviation values were obtained, and all are within ASTM repeatability and reproducibility (RR) ranges.

SUMMARY

Quality of green (raw) and calcined petroleum cokes did not significantly change during the study period. Sulfur and metal contents (V, Ni and Na) of these cokes were statistically controlled, meeting the specification limits for export. In January, 1997 a slight increasing trend in metal contents (about 20-30 ppm) was observed. This increase may be speculated due to variety of reasons such as crude oil quality, coking and calcining process conditions, etc. QC/QA round robin results showed good repeatability and reproducibility in determination of metals present in petroleum coke by ICP-AES.

Future studies of interest include: expansion of data base beyond the current study period, coal quality analysis for power plant fuels and metallurgical cokes, sampling and sample preparation, problem solving in QC/QA, and quality impacts on end-use products (aluminum anode, graphite electrode, TiO2, recarburization, etc.).

REFERENCES

1. J. G. Rolle, et. al., Light Metals 1997, 489-495, 126th TMS Annual Meeting, Orlando, FL, Feb. 9-13.
2. J. G. Rolle and Y. K. Hoang, Light Metals 1995, 124th TMS Annual Meeting, Las Vegas, Feb. 12-16.
3. E. J. Swain, Oil & Gas Journal, Jan. 2, 1995, 33-39; Jan. 9, 1995, 37-42.
4. N. P. Lieberman, Oil & Gas Journal, Mar. 27, 1989, 67-69.
5. R. E. Dymond and B. H. Spector, Light Metal Age, Feb. , 1992, 34-38.
6. W. M. Goldberger, et. al., Petroleum Derived-Carbons, ACS Symposium Series 303, 1986, Ch. 15, 200-214, (Edited by J. D. Bacha, et. al.).
7. Ullmann's Encyclopedia of Industrial Chemistry, Volume A20 and A27 (1986).
8. E. J. Swain, Oil & Gas Journal, May 20, 1991, 49-52.
9. Kerk-Othmer Encyclopedia of Chemical Technology, Volume 4, 4th Ed., Carbon, 956 (1992).
10. D. Mitas, et. al., Power Engineering, May, 1991, 29-32.

Figure 1. SULFUR CONTENT OF GREEN COKE

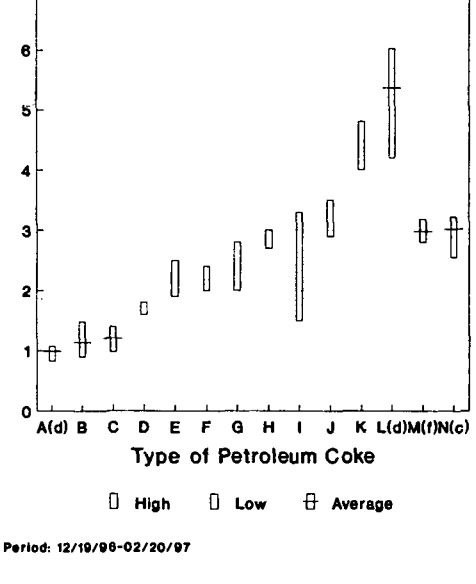

Figure 2. CALORIFIC VALUE OF GREEN COKE

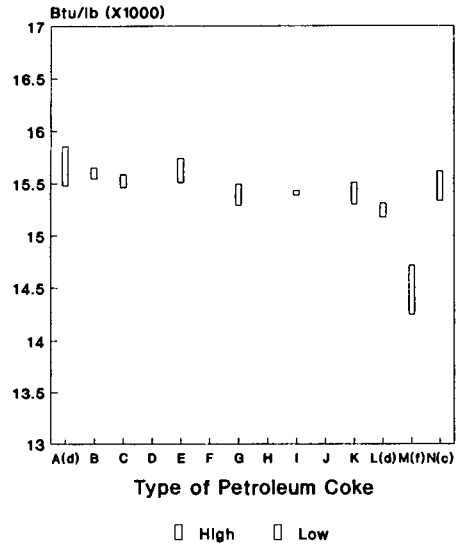

Period: 12/19/96-02/20/97

Figure 3. ASH CONTENT OF GREEN COKE

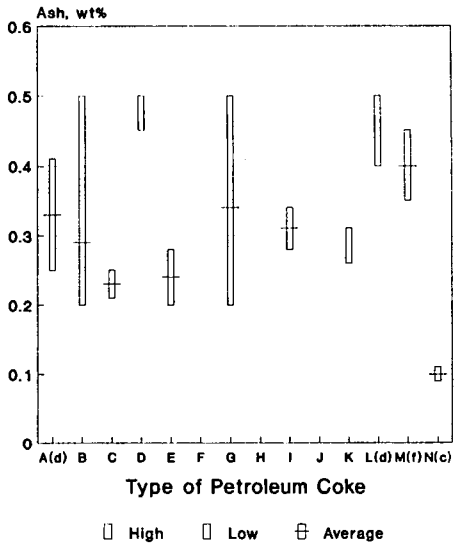

Period: 12/19/96-02/20/97

Figure 4. VANADIUM CONTENT OF GREEN COKE

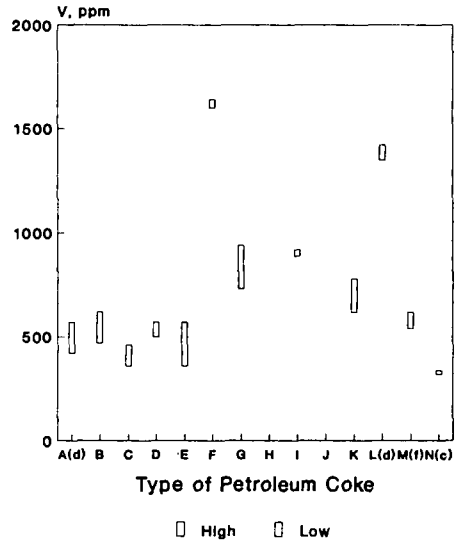

Period: 12/19/96-02/20/97

Figure 5. QUALITY SPECS OF CALCINED COKE
Aluminum Anode-Grade

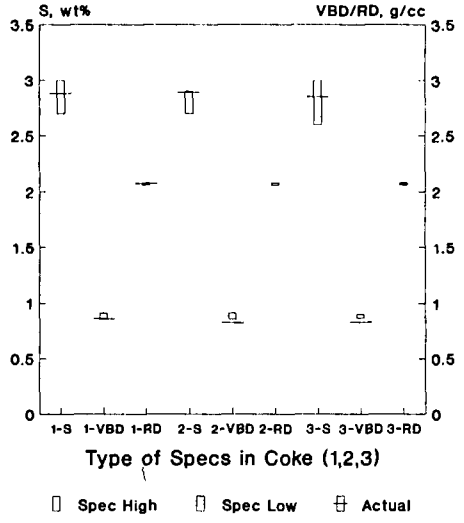

Period: 12/19/96-02/20/97

Figure 6. METAL CONTENT OF CALCINED COKE
Aluminum Anode-Grade

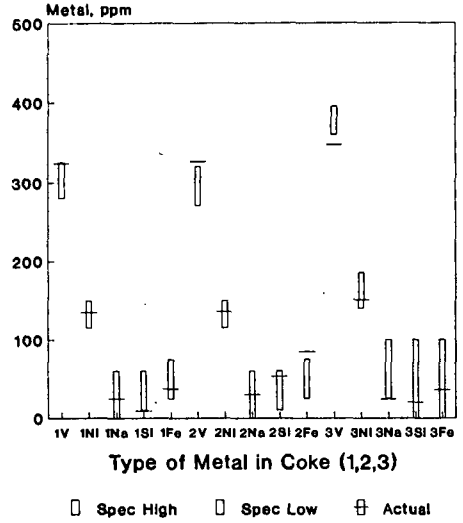

Period: 12/19/96-02/20/97

Figure 7. QC TREND CHART
Sulfur Content of Coke

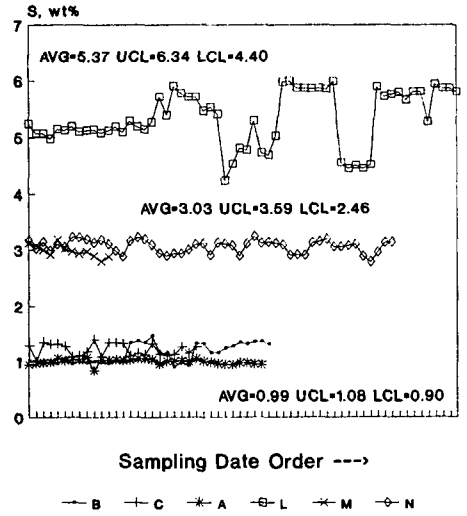

Period: 12/19/96-02/20/97

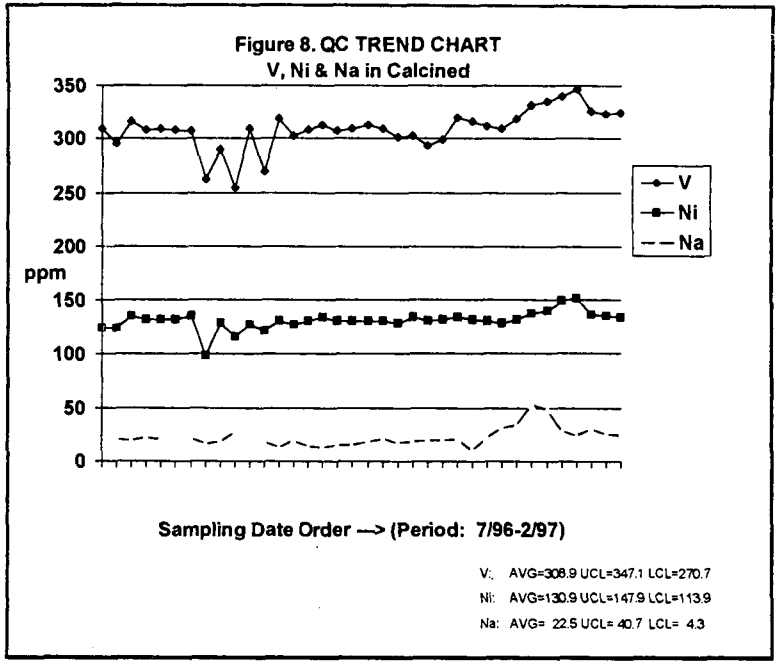
Figure 8. QC TREND CHART
V, Ni & Na in Calcined
350
300
250
200
ppm
150
100
50
0
V
Ni
Na
Sampling Date Order —> (Period: 7/96-2/97)
V: AVG=308.9 UCL=347.1 LCL=270.7
Ni: AVG=130.9 UCL=147.9 LCL=113.9
Na: AVG= 22.5 UCL= 40.7 LCL= 4.3

SMALL ANGLE NEUTRON AND X-RAY SCATTERING STUDIES OF CARBONS PREPARED USING INORGANIC TEMPLATES

Giselle Sandí, Pappannan Thiyagarajan†, Randall E. Winans, and Kathleen A. Carrado
Chemistry and † Intense Pulsed Neutron Source Divisions
Argonne National Laboratory, Argonne, IL 60439

ABSTRACT

Small angle neutron (SANS) and X-ray (SAXS) scattering analyses of carbons derived from organic-loaded inorganic template materials, used as anodes in lithium ion cells, have been performed. Two clays were used as templates to load the organic precursors, pillared montmorrillonite (PILC), a layered silicate clay whose sheets have been permanently propped open by sets of thermally stable molecular props, and sepiolite, a natural channeled clay. Five different organic precursors were used to load the PILC: pyrene, styrene, pyrene/trioxane copolymer, ethylene and propylene, whereas only propylene and ethylene were used to load sepiolite. Pyrolysis took place at 700 °C under nitrogen. Values such as hole radius, fractal dimension, cutoff length and density of the final carbons will be compared as a function of the clay and carbon precursors.

INTRODUCTION

In these studies, SANS and SAXS scattering techniques are used to obtain information concerning the hole radius, fractal dimension, cutoff length and density of carbons and their precursors, prepared using inorganic pillared templates. These carbons have been tested in electrochemical cells as anodes in lithium secondary batteries and proved to deliver high specific capacity (a measure of the power in mAh/g) and excellent performance in terms of the number of cycles runs (1,2). Preliminary results suggested that these carbons containe holes whose diameter is approximately the same as the Al_{13} pillar, thus facilitating the lithium ion diffusion. It is one of our goals to determine the distribution of the carbon within the pillared clay before and after the heating process and upon removal of the pillared clay by acid treatment.

A critical feature of SANS and SAXS scattering methods is their potential for analyzing the inner structure of disordered systems. Their application is a unique way of obtaining direct information on systems with a random arrangement of density inhomogeneities in a colloid-size range. The signal measured in SANS is the intensity of scattered neutrons as a function of the scattering angle. Since the scattering angle θ is related to the wave vector of the scattered radiation according to:

$$q = \frac{2\pi}{\lambda}|s - s_0| = \frac{4\pi}{\lambda}\sin\frac{\theta}{2} \qquad (1)$$

where $\mathbf{s}$ and $\mathbf{s}_0$ are the unit vectors in the direction of the incident and scattered radiation, it is customary to cxpress the scattering intensity as a function of the wave vector q.

The amplitude of the scattered radiation is given by:

$$A(q) = b\sum_{k,l} e^{-i q r_{kl}} \qquad (2)$$

where b is the scattering length of one atom and r_{kl} is a vector describing the distance between atom k and l. The intensity of the scattered radiation $I(q)$ is proportional to the square of this amplitude. The product of wave vector q and the distance between two scattering centers r_{kl} determines the phase difference between two scattered waves. The smaller the scattering angle, i.e., the smaller the q value, the larger the particle size can be from which emanates scattered radiation before a phase difference that leads to destructive interference is established. The total scattering signal reflects an average measure of the particle size and geometry (3). Since the high-q range of the scattering function results from the smallest features of the scattering particles, the inverse power terms describe the external surface of the particles, and the exponent depends entirely on the structure of this surface.

For porous materials, depending on the geometrical arrangement of the filled or the void space, the power law that describes the mass scaling may have an exponent of less than three. In the most general case the scaling law is given by:

$$M(r) \propto r^{d_f} \qquad (3)$$

where the d_f is called the Hausdorff dimension or fractal dimension and can assume noninteger values. It describes how the mass of the cluster increases with its linear dimension r. While a material may appear perfectly regular and three dimensional on the scale of a centimeter it may scale in a fractal way on the scale of a nanometer. Diffraction experiments probe the density correlations on length scales that correspond to the inverse momentum transfer q^{-1}, and since the intensity per particle scales with the correlated mass in the probing volume, it is expected that the intensity scales as q^{-d_f}.

SAXS probes scattered wave vectors q ranging from 10^{-4} to 10^{-1} Å, where the scattered wave vector is defined as in equation 1. Scattered intensities reflect a correlation in X-ray scattering length density on length scales between 10 and 10^4 Å. For porous materials consisting of a void and a solid phase, the difference in scattering length density is approximately equal to the scattering length density of the solid phase.

EXPERIMENTAL

The synthesis of the calcined pillared clays (PILCs) has been described in detail elsewhere (1,2). The calcined PILC was loaded with five different organic precursors using the procedures summarized as follows. For pyrene, the pillared clay is stirred in a 0.1 M solution of pyrene in benzene at room temperature overnight. Liquid styrene was heated under a nitrogen flow in a vacuum system. The styrene vapor was carried to a round bottom flask containing the PILC. The PILC was stirred as a solid phase and heated to 150°C. Trioxane was heated to 70°C. Pyrene was added to the reaction vessel once the trioxane was completely melted. PILC was then added to the solution and stirred. The reaction was catalyzed by addition of few drops of 0.1 M HCl. The excess trioxane and pyrene mixture was washed away with toluene before pyrolysis. The pyrolysis of the above samples took place in stainless steel tubes purged with nitrogen for several minutes. The tubes were sealed and heated to 700°C for 4 hours. Ethylene and propylene were loaded in the gas phase, where the loading and the pyrolysis processes were done in one step. Here, a three-zone furnace was used. Quartz boats containing PILC or sepiolite were placed within a quartz tube. The tube was initially flushed with nitrogen for about 3 hours. After that period of time, the gas was switched to propylene or ethylene and the gas flow was kept about 5 cm^3/min. The temperature of the oven was gradually increased from room temperature (about 5 °C/min) to 700 °C. The oven was then held at that target temperature for 4 hours.

The clay from the loaded/pyrolyzed PILC or sepiolite was removed using HF, rinsed to neutral pH and refluxed with concentrated HCl for 2 hours. The sample was washed with distilled water until the pH was > 5 to ensure that there was no acid left. The resultant carbon was oven dried overnight at 120 °C.

X-ray powder diffraction (XRD) patterns of clay precursors and carbons were determined using a Rigaku Miniflex, with Cu K_α radiation and a beryllium solid-state detector at a scan rate of 0.5° 2Θ/min.

SANS experiments were conducted at the Intense Pulsed Neutron Source at Argonne National Laboratory. The powders were held in 1mm path quartz cells. The incident neutron spectrum is supplied by a cold moderator. The wavelength of the scattered neutrons range between 0.5 and 14 Å, binned into 67 wavelength channels with 5% wavelenght spread in each channel. This instrument uses a BF_3 detector, and the scattered neutrons are detected by a 20 x 20 cm^2 ^{3}He area detector with 64 x 64 spatial channels. The q range covered is 0.005-0.35 $Å^{-1}$. The measurements took about two hours per sample. SAXS data were obtained at the Center for Micro-Engineered Materials, University of New Mexico. Both a Bonse-Hart and pin-hole instrument were used, resulting in a q range of 0.0002-0.8 $Å^{-1}$.

RESULTS AND DISCUSSION

Figure 1 shows SANS data for PILC, PILC loaded with pyrene before pyrolysis and the carbon obtained after pyrolysis at 700 °C and removal of the clay matrix. Scattering curves are nearly identical for the PILC and the loaded clay, indicating no appreciable structural changes of the pillared clay upon organic incorporation. Both the pillared clay and the loaded pillared clay exhibit a hump in the middle-q region that suggests a high degree of aggregation. The scattering

in the middle-q region of the carbon sample did not show the aggregation feature observed in the PILC and PILC/pyrene.

Figure 2 shows SANS data for five carbons derived from PILC and different organic precursors. Note that for the carbons derived from trioxane/pyrene copolymer, ethylene and propylene, a certain degree of aggregation is observed at the middle-q region. The low and high q regions are very similar. These data were evaluated as described by Freltoft *et al.* (4) to fit the experimental data in terms of the adjustable parameters d_f (fractal dimension), r_0 (cluster size) and ξ (cutoff length). It is not possible to discriminate between voids and clusters, thus, r_0 represents an average of both voids and clusters. ξ is related to the macroscopic density of the material, and d_f represents the particle distribution; it is a description of the geometrical arrangement of the particles in a cluster. A perfectly layered material such as graphite under well dispersed, conditions would exhibit d_f=2.

Table I summarizes the above parameters calculated for carbons and their precursors. The fractal dimensions for the carbon are similar to those calculated for the PILC, indicating that there is some layering in these disordered systems. Furthermore, r_0 of the holes for the carbonaceous materials range from about 4 to 8 Å, the largest radius corresponding to the carbon derived from PILC/pyrene. SAXS data of a carbon sample prepared from PILC/pyrene is shown in Figure 3. In the middle-q range the scattering intensity is characterized by a fractal dimension of 2.56, whereas at low q the fractal dimension corresponds to 3.88, which suggest that they have a small amount of roughness.

Another clay template used in the preparation of holey carbons is called sepiolite. It has the general structure $Si_{12}Mg_9O_{30}(OH)_6(OH_2)_4\ 6H_2O$ (5). It is a clay that does not have to be pillared since it contains a channeled structure. Preliminary results using pyrene as the organic precursor demonstrated that some carbon is incorporated into the clay. However, smaller molecules such as propylene or ethylene may be incorporated at a faster rate. Figure 5 shows an X-ray powder diffraction (XRD) of the carbon synthesized by incorporating propylene within sepiolite in the gas phase. The broad peak corresponds to the 002 reflection and is indicative of a disordered system. Further characterization of this carbon by SANS, SAXS and electrochemical testing is in progress.

CONCLUSIONS

Analysis of SANS and SAXS data of carbons synthesized using clays as templates show that they contain holes with a radius range from 4 to 8 Å. These holes are accessible to lithium ions when the intercalation process takes places in a lithium secondary battery. The values of the fractal dimension for the carbons are similar to those found for the clays, suggesting that there is some layering in the disordered system.

ACKNOWLEDGMENTS

The help in acquiring SANS data from Mr. D. Wozniak and Dr. C. Y. Ku, from the Intense Pulsed Neutron Source at Argonne National Laboratory, is greatly appreciated. This work was performed under the auspices of the Office of Basic Energy Sciences, Division of Chemical Sciences, U.S. Department of Energy, under contract number W-31-109-ENG-38.

REFERENCES

1. G. Sandí, R. E. Winans, and K. A. Carrado, *J. Electrochem. Soc.*, **143**, L95 (1996).

2. G. Sandí, K. A. Carrado, R. E. Winans, J. R. Brenner and G. W. Zajac, Mater. Res. Soc. Symp. Proc., *Macroporous and Microporous Materials* **431**, 39 (1996).

3. J. R. D. Copley, J. Appl. Cryst., **21**, 639 (1988).

4. T. Freltoft, J. K. Kjems, and S. K. Sinha, *Physical Review B* **33**, 269 (1986).

5. J. M. Thomas, in *Intercalation Chemistry*, M. S. Whittingham, and A. J. Jacobson, Editors, p. 61, Academic Press, New York (1982).

Table I: Experimental parameters calculated from SANS data.

Sample	r_0/Å	ξ/Å	d_f
PILC	3.70	876	2.469
Carbon from PILC/pyrene	7.66	1080	2.660
Carbon from PILC/styrene	6.60	148	2.650
Carbon from PILC/ethylene	4.00	143	2.690
Carbon from PILC/propylene	4.30	534	2.880
Carbon from PILC/trioxane/pyrene	1.40	NA	2.930

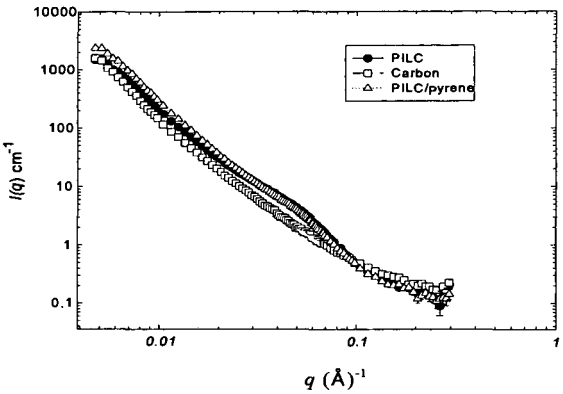

Figure 1: log I vs log q plot of the small-angle neutron scattering for (●) PILC, (△) PILC/pyrene and (□) carbon obtained after pyrolysis and clay removal.

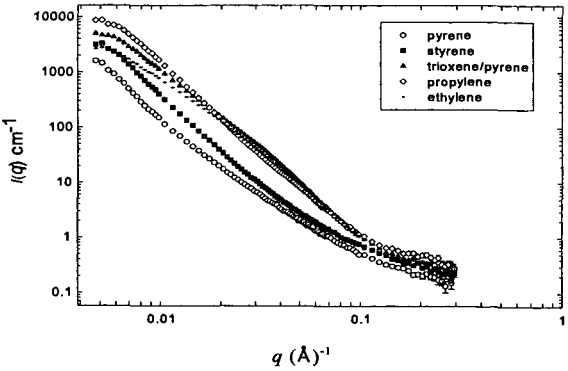

Figure 2: log I vs log q plot of the small-angle neutron scattering for carbon samples prepared using PILC and different organic precursors. (○) pyrene, (■) styrene, (▲) trioxane/pyrene, (◇) propylene and (·) ethylene.

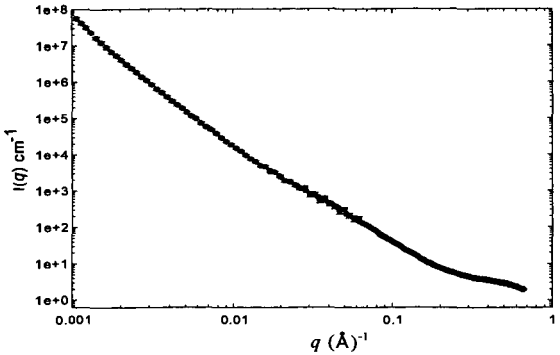

Figure 3: log I vs log q of the small angle X-ray scattering of a carbon sample derived from PILC/pyrene.

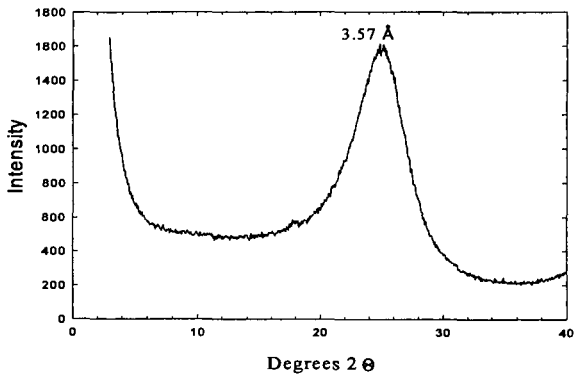

Figure 4: XRD of a carbon derived from sepiolite/propylene.

FRACTAL ANALYSIS OF GRANULAR ACTIVATED CARBONS USING ISOTHERM DATA

Nasrin R. Khalili, and Minzi Pan, Department of Chemical and Environmental Engineering, Illinois Institute of Technology, Chicago, IL 60616
Giselle Sandi, Chemistry Division, Argonne National Laboratory, Argonne, IL 60439

INTRODUCTION

Utilization of adsorption on solid surfaces was exercised for the first time in 1785. Practical application of unactivated carbon filters, and powdered carbon were first demonstrated in the American water treatment plant, and a municipal treatment plant in New Jersey, in 1883 and 1930, respectively. The use of activated carbon became widespread in the next few decades. At present, adsorption on carbons has a wide spread application in water treatment and removal of taste, odor, removal of synthetic organic chemicals, color-forming organics, and desinfection by-products and their naturally occurring precursors.

Along with the application of adsorption, the theoretical study has been more and more profound. The concept of adsorption isotherm introduced to specify the equilibrium surface concentration of adsorbate on adsorbent as a function of bulk concentration of adsorbate. The three famous mathematical models Langmuir, BET, and Freundlich were developed to describe the adsorption isotherm for single adsorbates. Langmuir adsorption isotherm describes equilibrium between surface and solution as a reversible chemical equilibrium between species. Adsorbent surface is considered to be made up of fixed individual sites where molecule of adsorbate, may be chemically bounded. Each site is assumed to be capable of binding at most one molecule of adsorbate. Langmuir model allows accumulation only up to a monolayer while the total amount of mass adsorbed is assumed to approach a saturating value when concentration becomes very large. Since both BET and Freundlich models were used in this study, settings of these models are presented.

The BET adsorption isotherm, extended the Langmuir model from a monolayer to several molecular layers. Model assumes that above the monolayer, each additional layer of adsorbate molecules is in equilibrium with the layer below it. Therefore layers of different thickness are allowed to co-exist. Under this circumstances, the process of sorbing a new layer of adsorbate onto old layers is assumed to be identical to the process of condensing adsorbate from solution to solid or liquid. The resulting isotherm is known to have the form of:

$$\frac{V}{V_m} = \frac{cX}{1-X}\sum_{n=1}^{\infty} B_n\left(\frac{1-(n+1)X^n + nX^{n+1}}{1+(c-1)X - cX^{n+1}}\right) \qquad (1)$$

In this model, V is the volume of adsorbate per mass of adsorbent at equilibrium, V_m is the volume of monolayer adsorbate per mass of adsorbent, c is a dimensionless constant that is related to the difference in free energy between adsorbate on the first and successive layers, n represents the number of layers adsorbed, B_n is the fraction of adsorbent surface that is covered by n layers of adsorbate, and X is the value of p/p_0 (p = equilibrium partial pressure of adsorbate, p_0= the saturated vapor pressure). The parameter B_n introduces the unsimilarity between the area at the nth layer and adsorbent surface, for adsorbents with uneven surfaces. Traditionally, since B_n is difficult to be determined, it is assumed that all layers have the same surface area as that of the adsorbent, and therefore an infinite number of layers of adsorbate would be expected. The summation in the above equation has a single term with B_n =1 for n = ∞. Recently using fractal theories parameter B_n has been estimated for fractal surfaces.

For low concentration systems (X<<1) the BET model can be simplified as:

$$\frac{X}{V(1-X)} = \frac{1}{V_m c} + \frac{c-1}{V_m c}X \qquad (2)$$

The BET adsorption isotherm suggests that surface concentration reaches a plateau as the monolayer is filled, then increases proportional to increase in p. Langmuir and BET models incorporate an assumption that the energy of adsorption is the same for all surface sites and not dependent on degree of coverage. In reality, the energy of adsorption may vary because real surfaces are heterogeneous.

Another isotherm model which has been used widely is the Freundlich adsorption isotherm. This model attempt to account for energy of adsorption, assuming that, the frequency of sites associated with a free energy of adsorption decreases exponentially with increasing free energy. The Freundlich isotherm has the form of $q = k\,C^{1/n}$, where k and n are constants. In this model the surface concentration of adsorbate does not approach a saturating value as C increases, since there are always surface sites with higher free energies of adsorption to fill. The Freundlich

isotherm is very widely used to fit observed data empirically even when there is no basis for its underlying assumptions.

Fractal Dimension

Fractal geometry is a mathematical tool for dealing with complex systems that have no characteristic length scale. The scale-invariant systems, are usually characterized by noninteger or "fractal" dimensions. The concept of fractal dimension, d, can be expressed as how the mass M(L) changes with the linear size L of the system with uniform density. In fractal systems, a smaller part of the system of linear size bL (b<1), the M(bL) is decreased by a factor of b^d, such as $M(bL)= b^d M(L)$. Simply we can assume that $M(L)=AL^d$, with A being constant.

The Koch Curve is one of the most common deterministic fractals. In Koch curve, by each iteration the length of the curve is increased by a factor of 4/3. The mathematical fractal then is defined in the limit of infinite iterations, $n\rightarrow\infty$, where the total length of the curve approaches infinity. If the linear size is decreased by a factor of b=1/3, the total length (mass) of the curve will be decreased by a factor of 1/4 (i.e., $M(\frac{1}{3}L)=\frac{1}{4}M(L)$). Therefore, it can be assumed that $1/4=(1/3)^d$, and d=log4/log3. Such non integer dimensions are called "fractal dimension" and those objects described by a fractal dimension are called fractals.

Applying fractal dimension theory, one can derive different methods to measure the dimension of a fractal surface. In the traditional adsorption theories, the adsorbent's surface is simplified to be a locally flat surface, giving d=2. But many adsorbents' surfaces are sufficiently porous and irregular. For example, the radius of micropores in activated carbon can be smaller than 1 nm, while that of the macropores can be bigger than 25 nm. For such surfaces, a minor changes in the size of adsorbate molecules can result in a great change for monolayer coverage.

The geometrical complexity of the surface of many irregular adsorbents, such as activated carbons and wood suggests that, surfaces structure of these adsorbents can be easily described according to the fractal theory. The fractal dimension "d" then would be a measure of adsorbent's surface irregularity. Recent studies showed that, values of "d" that expresses the degree of complexity of surface and/or porous structure, fall in the range of 2-3, representing extremely heterogeneous surfaces (Pfeifer etal., 1983, Jaroniec and Kruk, 1997). A specific value of "d" demonstrate self similarity, showing that any section of surface unfolds into m^d similar sections upon m-fold magnification. A dimension higher than 2 implies that any monolayer on a surface with d>2 correspond to a three dimensional bulk rather than a two dimensional film. Under this condition, the number of adsorption sites within distance L from any fixed site grows as L^d.

Many methods have been developed in order to obtain "d" on the basis of adsorption, mercury porosimetry, scanning electron microscopy, and small-angle X-ray and neutron scattering measurements (Jaroniec and Kruk, 1997). Among those, adsorption method play an important role. Some of the fractal oriented adsorption theories are simple and convenient since they require only one complete adsorption isotherm for a given solid to calculate the value of "d".

This paper presents the results of a study conducted to investigate the extent of association between surface fractal dimension and adsorption capacity of a group commercial and disorder carbons, using BET isotherm data and a model proposed by Segars etal., 1996.

STUDY APPROACH

The purpose of this study was to: a) use an appropriate model and gas phase isotherm adsorption data to estimate fractal dimensions of a range of carbons with different surface structure, and b) propose a model that can predict adsorption capacity of carbons in a single component liquid phase system, using estimated fractal dimensions.

Study was conducted in four steps: 1) using volumetric isotherm test (BET test), adsorption-desorption isotherms of nitrogen on selected carbons were determined, 2) using a model proposed by Segars et al., 1996, and gas phase isotherm data, fractal dimensions and other specific surface parameters were evaluated, 3) liquid phase isotherm data were determined using a single component liquid phase system containing phenanthrene-9-^{14}C, and 4) a modified adsorption model that relates liquid phase adsorption capacity to the surface dimension "d" was proposed. While liquid phase modeling is in progress, the obtained results of fractal analysis are presented.

RESULTS

Volumetric (gas phase) isotherm data were determined for two granular activated carbons (GAC 1240 and Sorbonorite 4), and four disorder carbons synthesized at the Argonne National Laboratory, using clay as templates (carbons # 1 to 4). An example of the adsorption-desorption isotherms for these carbons are presented in Figures 1. As it is shown adsorption type II and III were observed for these carbons. Using volumetric isotherm data and modified BET model proposed by Segars et al., 1996 (this model introduces the fractal dimension to the adsorption isotherms), important parameter B_n in BET model was estimated as follows:

$B_n = (\frac{r}{L})^{d-d_{n-1}} - (\frac{r}{L})^{d-d_n}$, where :

$$d_{n+1} = [1 - LN(\frac{r}{L})] - \sqrt{[1 - LN(\frac{r}{L})]^2 + 2[d_n * LN(\frac{r}{L}) + (d-2) * LN2 - LN(3-d_n)]}$$

The fitting parameters to the model were the gas phase isotherm adsorption data. The pressure p was ranging from 0 to to p_0 and parameter "r" was the size of adsorbed molecule. The computer simulation predicted parameters : d, r/L, V_m, c, and the maximum number of adsorbed layer, N. The results of modeling simulation are provided in Table 1. As it is indicated fractal dimension of commercial carbons were above 2.5, endorsing a non- flat surface structure for these adsorbents. However the modeled "d" for disorder carbons were about 2.1 representing relatively flat surfaces. For comparison, the V_m values estimated by the traditional BET model are also included in the Table 1. The estimated standard deviation for V_m indicated that model can accurately predict the volumetric isotherm data, using estimated parameters. Figures 2, shows examples of the modeled (line) and measured isotherm curves for these carbons. In general results of modeling showed that modified BET model can accurately estimate gas phase adsorption isotherms, and adsorption for these carbons matches type II adsorption isotherm better than type III.

The liquid phase adsorption isotherms were evaluated for carbons from measured concentration of Phenantherene-9-^{14}C at equilibrium, using Freundlich isotherm model ($q = kC^{1/n}$). Table 2 shows calculated adsorption capacity k, and degree of bonding , 1/n for all six carbons. The adsorption capacity of disorder carbons was much lower than commercial carbons. The liquid phase adsorption data were in a good agreement with the results of fractal modeling, suggesting that carbons with fractal surface have higher adsorption capacity in liquid phase systems.

CONCLUSION

Using a modified BET isotherm model and volumetric isotherm data, fractal dimensions of two commercial carbons, GAC 1240 and Sorbonorite 4, were estimated. The fractal dimension "d" for these carbons were about 2.7 and 2.6 respectively. The estimated monolayer volumes for these two carbons were 25-27 % larger than the volumes determined by BET. The disordered (synthesized) carbons showed a surface dimension of near 2, representing a flat surface. The monolayer volumes for these four disordered carbons were similar to the results of BET analyses. Liquid phase isotherm data showed a much higher adsorption capacity for commercial carbons with fractal dimension than disorder carbons. Development of a model that can predict liquid phase adsorption capacity of these adsorbers as a function of their surface dimensions is in progress.

ACKNOWLEDGMENT

Part of this work was performed under the auspices of the Office of Basic Energy Sciences, Division of Chemical Sciences, U.S. Department of Energy, under contract number W-31-109-ENG-38.

REFERENCES

Jaroniec, M., Kruk, M., Olivier J. 1995. Verification of selected relationships for Fractally Porous Solids by Using Adsorption Isotherms Calculated from Density Functional Theory. Surface Science 342, L1127-L1130

Jaroniec, M., Kruk, M. 1997. Fractal Analysis of Composit Adsorption Isotherms Obtained by Using Density Functional Theory Data for Argon in Slitlike Pores. Langmuir, 13, pp 1031-1035

Pfeifer, P., Anvir, D. 1983. Chemistry in Noninteger Dimensions Between Two and Three.I. Fractal Theory of Heterogeneous Surfaces. J.Chem.Phys. 79(7), pp 3558-3565

Segars R. and Piscitelle, L. 1996. Verification and Application of a New Adsorption Model for Fractal Surfaces. Mat. Res. Soc. Symp. Proc. Vol 407, pp 349-354

Table 1. Estimated Surface Parameters Using Modified BET Model

Adsorbent		d	r/L	C	N	Vm	S
Sorbonorite 4	fractal	2.7	0.1	100	11	405	4.24
	B.E.T.	--	--	99	--	293	
GAC 1240	fractal	2.6	0.1	250	45	282	2.03
	B.E.T.	--	--	67	--	210	
Carbon #1	fractal	2.1	1E-5	90	90	48	21.1
	B.E.T.	--	--	107	--	55.5	
Carbon #2	fractal	2.2	1E-5	31.2	45	1.39	0.25
	B.E.T.	--	--	23.8	--	1.36	
Carbon #3	fractal	2.45	0.01	400	95	115	10.6
		--	--	111	--	100	
Carbon #4	fractal	2.1	1E-6	90	90	6.57	3.08
	B.E.T.	--	--	406	--	6.68	

D=fractal dimension
C= constant
r/L= ratio of molecule radius to the linear size of fractal system
N= number of layers
Vm= volume of a monolayer

$s = \sqrt{\frac{\sum_{i=1}^{n}(y_i - \overline{y_i})}{n-2}}$ = standard deviation of the volume adsorbed. n is the number of data point, $\overline{y_i}$ is the modeled volume.

Table 2. Calculated Freundlich Adsorption Isotherm Parameters

	Sorbonorite 4	GAC 1240	Carbon #1	Carbon #3	Carbon #4
k	332	278	0.09	0.08	3.19
1/n	0.77	0.79	0.37	0.35	0.59
R^2	0.92	0.96	0.92	0.89	0.96

* Carbon #2 presented inconclusive results

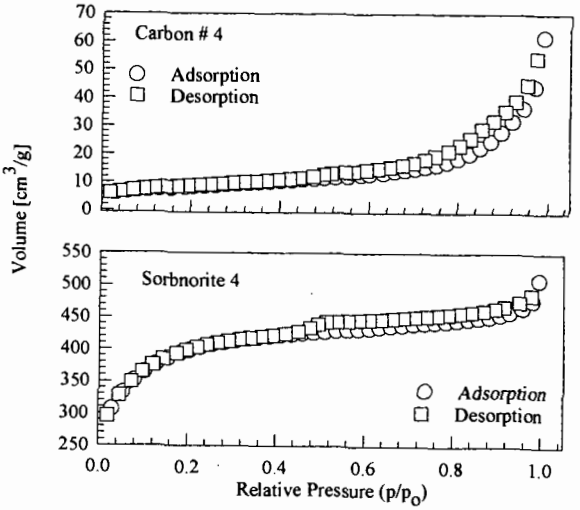

Figure 1. Adsorption and Desorption Isotherms Determined for Carbon #4 and Sorbonorite 4

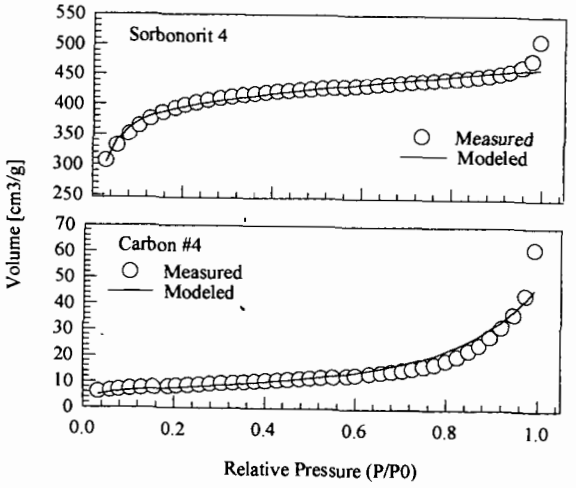

Figure 2. Modeled and Measured Adsorption Isotherms For Sorbonorit 4 and Carbon #4.

HIGH YIELD ACTIVATED CARBON FROM BIOMASS BY AIR ACTIVATION

Xiangfeng Dai and Michael J. Antal, Jr.
Hawaii Natural Energy Institute and the Department of Mechanical Engineering
University of Hawaii at Manoa
Honolulu, HI 96822

INTRODUCTION

With its large internal surface area, activated carbon has extraordinary adsorptive capabilities. It is employed in a wide range of applications, mostly as a purifying agent to remove trace quantities of undesirable species from gas or liquid phase as well as an economical medium to recover precious materials. The demand for activated carbon has been continuously increasing in the past decade. In 1988, the consumption of activated carbon in industrialized countries was 300,000 tons (Roskill, 1990). The United States accounts for 43% of this amount -- around 130,000 tons. Since then, the demand in the U.S. market is estimated to have increased at a rate of 5% per year to around 230,000 tons by the year 2000. Because of worldwide increasing environmental problems and stricter regulations set by governments in both industrialized and developing countries, the demand for activated carbon will continue to increase.

Commercial production of activated carbon employs high temperatures of above 800°C using steam or carbon dioxide as an activating agent from coal and limited amount of biomass by thermal activation process. On the other hand, yield of activated carbon from biomass is low, e.g., 5 - 8 % from coconut shell. Consequently, activated carbon produced by conventional method is expensive. The retail price of activated carbon ranges from $2 - $6 per kg depending on the type.

In this article, a novel thermal process of producing high-yield activated carbon from Macadamia shells by air or a mixture of air and inert gas at low temperature is discussed. Characteristics of the carbon are presented.

EXPERIMENTAL

Macadamia shells as agricultural by-products in Hawaii are employed as the original material in this work. Raw Macadamia shells are in hemispherical shape with about 25 mm diameter and 3 mm thickness. Macadamia shells undergo a series of pretreatments and post-treatments before forming the final products -- activated carbons. Pretreatments include pyrolysis in a pressurized lab reactor, in which high yield charcoal is obtained as described elsewhere [Dai, 1995; Antal, 1996], and then followed by high temperature carbonization process at atmospheric pressure without oxygen presence. Afterwards, carbonized charcoal is subjected to oxygenation process, in which various operating conditions are investigated to fine tune the final product. The major operating parameters include temperature, total pressure, oxygen partial pressure (P_{O2}), oxygenation time and carbon burn-off, etc. Finally, oxygenated charcoal receives post-treatment at high temperature, namely, the activation process as termed in this work, degassing or desorption process as termed commonly, thereby forming activated carbon. The raw charcoal retains the shape of its raw shell. The hemispherical charcoal is employed only in the lab reactor. Granulated charcoal particles with 6×14 mesh are employed in both the lab reactor and the ceramic reactor which will be discussed next.

The key step is the oxygenation process. Part of the oxygenation process has been conducted in the lab reactor, with which a detailed arrangement and operating procedure similar to the ceramic reactor is described elsewhere [Dai, 1995]. However, most significant progress was made in the ceramic reactor. The ceramic reactor system is schematically shown in Fig. 1. Pretreated granulated charcoal is loaded in the upper portion of the reactor. Due to strong exothermic reaction in the oxygenation process, nitrogen or helium is mixed with air to serve as a thermal ballast. Air passing a regulator from the air tank is controlled by a micrometering valve and measured using a mass flow controller (Aalorg model GFM-1700) before reaching an on/off valve. Similarly, nitrogen or helium is controlled by a micrometering valve and measured using a rotameter (Brook model 1110-01F1B1A) before passing an on/off valve. Then air and nitrogen/helium are mixed and fed into the 50 mm diameter ceramic reactor. The product gas leaves the reactor to a 3-way valve, one way going to the sampling bag while the other going to a rotary flow meter (GCA/Precision Scientific wet test meter) after a cooling section. The desired temperature is obtained by controlling an external heater with a variable voltage transformer and an internal heater with a temperature controller. A thick bed of glass beads is packed upstream of the charcoal sample layer to improve heat transfer and uniformity of flow. Two type K thermocouples contact the charcoal sample to record the charcoal temperature. Flow meters are calibrated at room temperature before onset of the experiment using a soap film flow meter. Gas samples are taken in the sampling bag as well as in an in-line port with a septum downstream of the 3-way valve. Then, the sample gas is analyzed by a Gas Chromatograph (Hewlett Packard

Model 6890) equipped with a thermal conductivity detector and a column made of two concentric columns capable of separating nitrogen and oxygen (Alltech CTR). The adsorptive properties are reported in terms of iodine number, BET (N_2) surface area, and pore size distribution. Iodine number test follows ASTM D4607-86. BET surface area and pore characteristics are analyzed by a gas sorption analyzer (Quantachrome Autosorb-1).

RESULTS AND DISCUSSION

A series of experiments have been conducted under a range of operating conditions in oxygenation process using nitrogen/air mixture in the lab reactor. A set of typical results is shown in Table 1. As seen in the table, both large and small sized oxygenated charcoal have low iodine number, i.e., 121 mg/g and 282 mg/g, respectively. When surface oxides are removed after post-treatment, iodine number of both activated carbons increases dramatically -- 366 mg/g and 506 mg/g for large and small size. Higher iodine number of small particles is partly due to higher burn-off and probably mostly due to its small size, in which case, the effect of mass transport within charcoal pores is much less important than in large particles. From this result and the fact that granulated or powdered activated carbon is predominantly used in applications, granulated charcoal has been used in this study since then.

Another series of experiments were conducted in the ceramic reactor to reveal conditions for producing high yield, good quality activated carbon. A typical experimental result is shown in Table 2, in which a thick bed of charcoal samples is employed and post-treatment is followed. As seen in the table, yield and iodine number of activated carbon is quite different, depending upon the location in the packed bed. Activated carbon at the bottom layer has a higher iodine number of 652 mg/g with an overall mass yield of 12%, while the top layer has a lower iodine number of 260 mg/g but with a higher mass yield of 29%. This suggest that the overall reaction rate highly depend upon oxygen partial pressure. Activated carbon at the layer next to the bottom seems the best compromise in terms of yield and quality (iodine number). This sample would have an overall yield of around 20% with an iodine number over 700 mg/g if the oxygenation time were longer.

The result of one experiment with a thin layer of carbonized charcoal treated with pure air in the oxygenation process shows that activated carbon with an iodine number of 700 mg/g is obtained, compared to iodine number of 181 mg/g for carbonized charcoal as listed in Table 2. A fraction of this sample burned during oxygenation process as ash was collected from the reactor. Thus, it is crucial to control temperature and oxygen partial pressure in this process. This is one of the reasons why activated carbon is difficult to produce by air/oxygen activation.

The pore size distribution of a typical activated carbon with an iodine number of 625 mg/g is shown in Fig. 2. A double-peaked distribution is observed, one at around 0.8 nm in micropore regime while the other at around 36 nm in mesopore regime. From engineering point of view, this activated carbon has potential to be oxygenated for longer time by creating more pores and/or enlarging micropores so that higher surface area would be obtained. From application point of view, this kind of structure favors fast mass transport of adsorbates with a micropore size into the deep part of the pores compared to uniform micropore dominated pore structure, hence increasing process efficiency.

A TGA analysis on post-treatment of oxygenated charcoal by a colleague (Dr. G. Varhegyi) in Hungarian Academy of Science shows that desorption of surface oxides as CO_2 reaches its peak rate at around 500°C and as CO at around 700°C. Further increase in temperature will shorten the pre- and post-treatment time but may take a risk of having carbon annealed at above 800°C. This confirms our earlier results that a temperature of 750°C is best for pre- and post- treatment of charcoal among temperatures examined at 600°, 750° and 950°C.

CONCLUSION

Activated carbon with a high yield of above 20% from Macadamia shells is realized in a novel process including a series of pre- and post-treatments. This is compared to the 5 - 8% realized by conventional thermal activation method. The key process -- oxygenation is carried out at low temperatures using air or a mixture of air and inert gas as an activating agent. The pore structure and iodine number of 600 - 700 mg/g suggest that this activated carbon have potential of further increasing its surface area by finer tuning of the operating parameters.

ACKNOWLEDGMENTS

This work is supported by the National Science Foundation (Grant # CTS95-21423) and the Coral Industries Endowment of the University of Hawaii. The authors would like to thank Dr. Maria Burka (NSF) for her continuing interest of this work, Dr. Gabor Varhegyi with Hungarian Academy of Science for TGA analysis, Guilherme Bezzon, Dr. Angela Garcia and Dr. Makoto Sakurai for their assistance.

REFERENCES

Antal, M. J., Croiset, E., Dai, X. et al. "High yield biomass charcoal". *Energy & Fuels*. Vol. 10, No. 3, 652-658, 1996.

Dai, X., Norburg, N., and Antal, M. J. "Production of charcoal and activated carbon at elevated pressure". *Symposium on Materials and Chemicals Synthesis from Fossil Fuels and Biomass*. ACS, 285-287, 04/95.

Roskill Information Service, Ltd. "The economics of activated carbon 1900". *PTS Research Studies*. 1-180, 08/90.

Table 1. Results of Macadamia shell activated carbon from the lab reactor

size	burn-off	I.N. (ox)[a]	I.N. (ac)[b]	yield
ϕ25x3 mm	0.194	121 mg/g	366 mg/g	24%
6x12 mesh	0.667	282 mg/g	506 mg/g	9.4%

[a] iodine number of oxygenated charcoal treated at 339°C, P_{O2}=4.2 kPa in N_2 for 90 min;
[b] iodine number of activated carbon.

Table 2. Results of Macadamia shell activated carbon from the ceramic reactor[a]

location	yield	iodine number
(carbonized charcoal)	0.30	181
#1 (bottom)	0.12	652
#2	0.25	552
#3	0.27	420
#4	0.28	---
#5 (top)	0.29	260

[a] oxygenated at 250°C, P_{O2}=12.7 kPa in N_2 for 62 min.

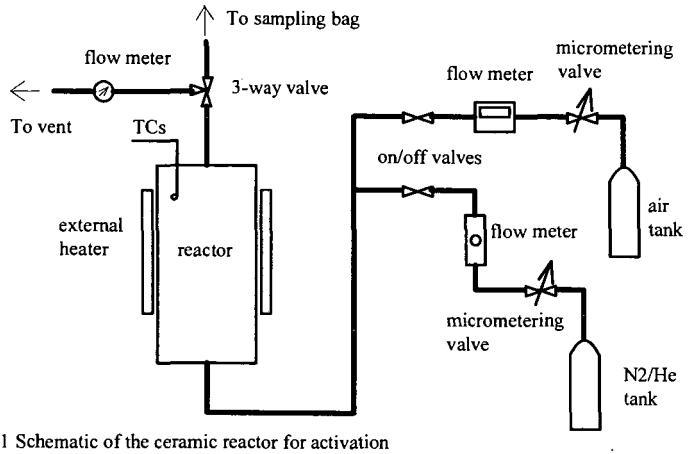

Fig. 1 Schematic of the ceramic reactor for activation

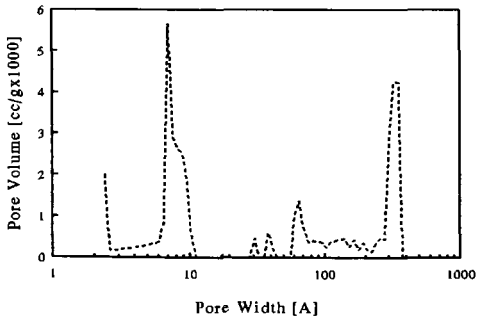

Fig. 2. Pore size distribution of Macadamia shell activated carbon

ACTIVATED CHAR FROM ILLINOIS COAL FOR COMBINED SO_2/NO_x REMOVAL

Anthony A. Lizzio[1], Alex M. Chang[2] and John L.Haslbeck[2]

[1]Illinois State Geological Survey, 615 East Peabody Drive, Champaign, IL 61820
[2]NOXSO Corporation, 2414 Lytle Road, Bethel Park, PA, 15102

Keywords: activated char, sulfur dioxide, nitrogen oxides.

INTRODUCTION

Carbon-based processes for flue gas cleanup operating in Europe [1] and Japan [2] today typically use two reactors, one to remove SO_2 and the other to remove NO_x with ammonia injection. One of the major impediments to the commercialization of this technology in the U.S. has been the cost of the activated carbon used and the fact that there is no commercial carbon on the market today that can simultaneously remove both SO_2 and NO_x from coal combustion flue gas. The NOXSO Corporation has developed a dry, post-combustion flue gas treatment system that uses a regenerable sorbent (alumina beads impregnated with 5% sodium) in a fluidized bed for combined SO_2/NO_x removal [3]. The ISGS and NOXSO are working together to develop a low cost sorbent from bituminous coal to use as an alternative sorbent in this process [4].

Numerous studies have examined NO_x removal by carbon at 300-600°C, although it is most convenient and economical to remove NO_x from flue gas at lower temperatures (100-150°C). Some studies have not used O_2 in the simulated flue gas when testing their carbons, and nearly all studies have neglected the effect of H_2O on NO_x removal. Whether activated carbon can remove significant amounts of NO_x in the presence of both H_2O and SO_2, i.e., without having to inject ammonia into the flue gas, remains to be determined. With such a carbon, only one reactor would be required to remove both SO_2 and NO_x from coal combustion flue . Today, two reactors are used because ammonia tends to react with sulfur dioxide and carbon to form ammonium sulfate, which is detrimental to activated carbon performance.

The overall objective of this study [4, 5] has been to develop a low cost activated char from bituminous coal for simultaneous removal of SO_2 and NO_x from coal combustion flue gas. Such a carbon could be used in the NOXSO process as well as in traditional fixed-bed and (less capital intensive) carbon injection processes. In this paper, we begin by examining the effect of H_2O and SO_2 on NO_x removal by activated chars shown previously in our laboratory to work well in removing SO_2 from simulated flue gas [6]. We also develop new carbons and explore the possibility of adding a catalyst to or ammonia treating activated char to enhance its combined SO_2/NO_x removal capabilities.

EXPERIMENTAL

Activated chars were prepared from an Illinois hvC bituminous coal (IBC-102) [7]. Figure 1 shows the various processing steps that were used. A 2 in. ID batch, fluidized-bed reactor (FBR) was used to pyrolyze 200 g of 48x100 mesh coal (N_2, 900°C, 0.5 h) and activate the resultant char (H_2O, 860°C, 30% conversion). The steam activated char was treated with nitric acid (10 M HNO_3, 80°C, 2 h) and thermally desorbed in N_2 or H_2 at 925°C for 1 h to desorb carbon-oxygen (C-O) complexes. A KOH activated char was prepared by mixing KOH with IBC-102 coal (2:1 KOH/coal) and pyrolyzing in the FBR (N_2, 800°C, 1 h). To prepare catalyzed chars, potassium (acetate) or sodium (carbonate) was added to IBC-102 coal by incipient wetness (IW) and pyrolyzed in N_2 (750°C, 0.5 h); the resultant char was activated in CO_2 (720°C, 2 h). In addition, K or Na was ion-exchanged (IE) onto HNO_3 treated char. Selected chars were also treated with anyhdrous NH_3 at 900°C for 2 h.

A fixed-bed adsorber (1 cm ID x 30 cm stainless steel tube) connected to a quadrupole mass spectrometer (VG Quadrupoles, Fisons Instruments) was used to obtain SO_2 and NO breakthrough curves. Typically, 6 g of char (8 cm bed height) was placed between two layers of quartz wool and heated to 120°C in flowing He (0.2 L/min). The He flow was switched to 2500 ppm SO_2, 500 ppm NO, 5% O_2 and 7% H_2O, balance He (space velocity = 2000 h^{-1}). The char sample was regenerated in situ by heating it in flowing N_2 to 525-925°C.

RESULTS AND DISCUSSION

Figure 2 presents NO breakthrough curves for several IBC-102 chars and a commercial activated carbon, Centaur carbon (Calgon Carbon). Centaur (B) removed little NO_x at 120°C, whereas the thermally desorbed IBC-102 chars (C-G) performed significantly better. The air oxidized/thermally desorbed IBC-102 char (D) was slightly better than the KOH activated char (A). Exposure of the char sample to ambient air for 48 h prior to a NO_x removal run had a detrimental effect on performance (compare C and E). Chemisorbed oxygen may poison active sites for NO adsorption/reduction. The absence of adsorbed oxygen enhances SO_2 removal by carbon [8, 9]. Carbon atoms not occupied by adsorbed oxygen atom have valence electrons more available and reactive towards SO_2. These unoccuppied or free sites control adsorption of SO_2 [9] and perhaps NO_x. Figure 2 also shows that Sample G (sample E heated to 925°C in H_2 instead of N_2) removed nearly twice as much NO_x as sample E. Treatment of char with H_2 at this temperature serves to gasify the most reactive carbons leaving behind a more stable surface, but one that still contains free sites. The more stable surface adsorbs less O_2 and H_2O at room temperature, which leads to more available sites for reaction with NO_x at 120°C.

Recent results in the literature seem to suggest that low temperature NO_x removal by activated carbon in the presence of SO_2 is not possible [10]. Figure 3 shows the effect of SO_2 and H_2O on NO_x removal by the IBC-102, HNO_3, 925°C char. The char removes 98% of the NO_x for about 1.5 h, then NO partially breaks through to about 200 ppm. For the next 15 h the [NO] increases from 200 to 300 ppm. Two NO_x removal mechanisms seem to be in effect. One where NO is simply adsorbed on the char surface and the other where the char converts NO to N_2. The catalytic mechanism

could account for incomplete breakthrough. When both SO_2 and H_2O are added at t = 17 h, large amounts of NO are desorbed. Figure 3 shows that SO_2 or H_2O (or both) displace adsorbed NO_x. This char also adsorbed the expected amount of SO_2 (111 mg SO_2/g char) even though the char was saturated with NO_x. Note that when SO_2 and H_2O were added, NO_2 was also desorbed from the char. The NO_2 desorption peak appears to coincide with the NO peak. Figure 4 shows the effect of adding H_2O and SO_2 at different times during NO_x removal. Note that the catalytic component of the breakthrough curve (200-500 ppm) no longer persists after H_2O is added. The SO_2 capacities of the IBC-102, HNO_3, 925°C chars in Figures 3 and 4 were quite similar, 111 and 99 mg SO_2/g char, respectively.

Effect of Potassium

Figure 5 shows NO breakthrough curves for char prepared from IBC-102 coal loaded with 6% K by IW. This char has a N_2 BET surface area of only 100 m^2/g compared to 500-600 m^2/g for the uncatalyzed chars shown in Figures 3 and 4. The NO breakthrough curve (no H_2O) fails to exhibit a initial period of 95-100% NO_x removal. Thermal desorption at 925°C, however, results in a 2 h period of > 98% NO removal. Thermal desorption creates free sites for NO adsorption. Figure 5 shows that this char also removes > 98% NO for about 1 h after 7% H_2O is added. A Na-loaded char prepared in a similar fashion also adsorbed NO_x with H_2O, but not to this extent.

The data shown in Figure 5 were promising. The surface area of this char could be increased through further activation, and the surface chemistry or in this case, catalyst dispersion, could be enhanced by using ion exchange instead of impregnation to load K onto the char. In an attempt to do this, steam activated IBC-102 char was treated with nitric acid, then placed in a solution of 1 M potassium acetate. The ion-exchanged char (IBC-102, HNO_3, K, IE) was then thermally desorbed at 925°C to remove chemisorbed oxygen and fix potassium atoms on the carbon surface. Figure 6 presents NO breakthrough curves with and without H_2O and SO_2 for an activated char prepared in this way (IBC-102, HNO_3, K, IE, thermally desorbed at 525°C and/or 725°C). Sample A (525°C) removed > 98% of the NO for more than 12 h without H_2O in the simulated flue gas. With H_2O and SO_2 added at t = 0 h, this char (B) performed very well in removing 98% of the NO_x for 2 h. Regeneration at 725°C (C) reduced its effectiveness, perhaps because K volatilizes at T > 700°C. When H_2O and SO_2 were again removed from the gas stream (D), NO_x removal performance improved, but not to previous levels (A).

Recent studies [11-13] have shown that K is a good catalyst for NO_x removal (without H_2O or SO_2) at relatively high temperatures (300-600°C). In TPR experiments (5°C/min), K-loaded char appeared to remove some NO_x beginning at 100°C, but it was not clear how much or whether it was even a significant amount [13]. To the best of our knowledge, the results obtained with IBC-102, HNO_3, K, IE char show for the first time that significant amounts of NO_x can be removed by activated char at 120°C in the presence of H_2O and SO_2.

Effect of Ammonia Treatment

Figure 7 shows NO breakthrough curves for steam activated IBC-102 char and the same char treated with ammonia at 900°C for 2 h. These runs, performed without H_2O in the flue gas, show that the NH_3 treatment increases the NO_x breakthrough time from 0 h to about 3 h. The ammonia treatment incorporates nitrogen into the char structure as NH_3 dissociates into N and H_2 at elevated temperaures. The H_2 can gasify the carbon if the temperature is high enough, and also deposit on the carbon surface to preserve the free sites for NO_x removal as shown in Figure 2. The surface area of the steam activated IBC-102 char increased from 465 to 580 m^2/g after the 2 h ammonia treatment. The incorporated nitrogen can have special catalytic properties. Stohr et al. [14] discussed how treatment of carbon with ammonia or hydrogen cyanide at elevated temperatures resulted in a dramatic increase in catalytic activity in oxidation reactions. The catalytic nitrogen was hypothesized to be surrounded by three carbon atoms and was situated near or at the edge of the basal plane. Most recently, Fei et al. [15] postulated that the relatively high nitrogen content of activated carbon fibers derived from shale oil was responsible for their enhanced SO_2 removal capabilities at room temperature compared to a commercial activated carbon fiber made from coal tar pitch. In our case, the NH_3 treatment has apparently increased the catalytic activity of steam activated IBC-102 char for reduction of NO to N_2 and O_2. Without the NH_3 treatment, the steam activated IBC-102 char has no activity for NO_x reduction (Figure 7).

Figure 8 show the effect of H_2O on NO_x removal by the NH_3 treated, H_2O activated IBC-102 char. Water in the flue gas inhibits NO_x removal by IBC-102 char, but it is important to note that even in the presence of H_2O, the NH_3 treated char removes 90% of the NO_x for about 1 h, which means that the catalytic properties of incorporated nitrogen are retained even in the presence of H_2O. Figure 9 shows the effect of thermal desorbing the NH_3 treated, H_2O activated IBC-102 char at 925°C for 1 h prior to a NO_x removal experiment (with no H_2O in the flue gas). There is no appreciable difference in these two NO breakthrough curves indicating that the NH_3 treatment at 900°C for 2 h essentially acts as a thermal desorption treatment in N_2 at 925°C for 1h with respect to its effect on free site concentration.

Figure 10 shows NO breakthrough curves for the NH_3 treated, H_2O activated char and the NH_3 treated, HNO_3 treated, H_2O activated char. HNO_3 treatment of the char following H_2O activation, but prior to NH_3 treatment, increases the breakthrough time from about 4 h to 10 h (without H_2O in the flue gas), a significant improvement in NO_x removal performance. Ammonia will tend to react more vigorously with the free sites generated by the nitric acid treatment than with those of the steam activated char. Nitric acid treatment of steam activated char and subsequent desorption of carbon-oxygen complexes has been shown to increase the number of carbon free sites for SO_2 adsorption [6, 9]. The generation of free sites also seems to enhance NO_x removal by activated char. Figures 3 and 4 show that SO_2 and NO_x compete for similar adsorption sites since NO_x is desorbed from the char when SO_2 is first introduced into the flue gas. Figure 10 also shows the effect of H_2O in the flue gas on NO_x removal by the NH_3 treated, HNO_3 treated, H_2O activated IBC-102 char. The NO breakthrough time is reduced by about one half, but this char still shows considerable catalytic activity. The combination of free sites and incorporated nitrogen atoms generated from the HNO_3 and NH_3 ammonia treatments, respectively, has resulted in the best performing char to date, i.e., greater than 90% NO_x removal for 4 h in

the presence of H_2O. This performance is twice as good as our previous best char (see sample B, the ion exchanged K loaded IBC-102 char, in Figure 5). A way to lower the cost of making this char would be to air oxidize (instead of HNO_3) the H_2O activated char and then react it with ammonia. The goal would be to achieve comparable SO_2/NO_x removal performance with air oxidation as was achieved with the HNO_3 treatment. The ion exchange of potassium onto this char under pH controlled conditions (pH = 9-11) could further enhance its combined SO_2/NO_x removal capabilities.

Figure 11 presents SO_2 adsorption profiles for the Centaur carbon; H_2O activated IBC-102 char; HNO_3 treated, H_2O activated char; and KOH activated char, and for these same chars treated with NH_3 at 900°C for 2 h. Three of the six IBC-102 chars outperform the commercial carbon. Ammonia treatment increases by up to 50% the SO_2 capacity (at 6 h) of these chars, which is quite remarkable. We postulate that the incorporation of nitrogen into the char and possibly the deposition of hydrogen on the char surface contributes to this dramatic increase in SO_2 adsorption capacity. The N_2 BET surface areas of the H_2O activated char and HNO_3 treated, H_2O activated char increased from 465 and 827 m^2/g to 580 and 860 m^2/g, respectively. The surface area of the NH_3 treated, KOH activated char remained unchanged at 1100 m^2/g. The NH_3 treated, HNO_3 treated, H_2O activated char had the highest SO_2 capacity (520 mg SO_2/g at 6 h) of any Illinois coal char or commercial activated carbon tested to date. This char performed well in removing NO_x in the presence of H_2O and shows tremendous potential in removing SO_2 from simulated flue gas. It is the leading candidate for use in the NOXSO process.

Integration of Activated Char into NOXSO Process

Several options are being considered for integrating ISGS activated char into the NOXSO process. One process configuration involves using activated char in a two stage system, each stage being a fluidized- or fixed-bed adsorber. The first bed could contain activated char (e.g., H_2O activated IBC-102 char) that removes greater than 98% of the SO_2 from the flue gas, but little NO_x. The second bed could contain activated char (e.g., H_2O activated, HNO_3 or air oxidized, K-catalyzed IBC-102 char) that removes greater than 90% of the NO_x from essentially SO_2-free flue gas that contains 5-12% H_2O. This char could achieve relatively high NO_x removal rates without the use of additional reagents such as ammonia. Another and probably the best scenario is to use one char and one reactor to remove both SO_2 and NO_x from the flue gas. This char could be the NH_3 treated, oxidized (either by air or nitric acid) IBC-102 char shown to remove large amounts of NO, and SO_2 from simulated flue gas (Figures 10 and 11). Another place to use activated char in the NOXSO process would be in the reheater recycle stream. If NO_x could be removed at this point in the process it would increase the overall operating efficiency of the power plant that uses the NOXSO process to clean flue gas. Instead of sending NO_x laden flue gas back to the boiler where excess NO_x is converted to N_2, a bed of activated char could be used to remove NO_x from this waste stream. The power plant could then operate independently of the NOXSO process, which is more favorable. Based on the results obtained in this study, addition of activated char to these locations in the NOXSO process (in or downstream of the fluidized-bed adsorber and/or in the reheater recycle stream) could improve the overall efficiency and lower operating costs of the NOXSO process.

CONCLUSIONS

Activated chars were prepared from Illinois coal and combined SO_2/NO_x removal experiments performed to examine the competitive effects of H_2O and SO_2 on low temperature NO_x removal. The SO_2 capacity of the char was not affected to any appreciable extent by NO in the flue gas. Both H_2O and SO_2 appeared to inhibit NO adsorption by activated char. One ion exchanged K-catalyzed char showed exceptional promise since it adsorbed significant amounts of NO even with H_2O in the gas stream. Nitric acid and/or ammonia treatment of steam activated IBC-102 char also enhanced its NO_x removal capabilities. The combination of free sites and incorporated nitrogen atoms generated from the HNO_3 and NH_3 ammonia treatments, respectively, resulted in a char that removed greater than 90% NO_x removal for 4 h in the presence of H_2O. Moreover, the NH_3 treatment of IBC-102 char increased its SO_2 adsorption capacity by up to 50%. The NOXSO process could incorporate activated char in one or more locations in their process or it may be that an entirely new process is designed based on the unique SO_2/NO_x removal capabilities of activated char.

ACKNOWLEDGEMENTS

This work was supported by the Illinois Clean Coal Institute through the Illinois Coal Development Board and the United States Department of Energy. The authors gratefully acknowledge the technical assistance of Gwen Murphy, Gwen Donnals and Sheila Desai.

REFERENCES

1. Hartenstein, H.-U., *ACS Preprints, Div. Fuel Chem.* 41 (1), 409 (1996).
2. Tsuji, K. and Shiraishi, *ACS Preprints, Div. Fuel Chem.* 41 (1), 404 (1996).
3. Ma, W.T. and Haslbeck, J.L., *Environmental Progress* 12, 163 (1993).
4. Lizzio, A.A., Cal, M.P., DeBarr, J.A., Donnals, G.L., Haslbeck, J.L., Chang, A.M. and Banerjee, D.D., "Development of Activated Char for Combined SO_2/NO_x Removal," Final Technical Report to Illinois Clean Coal Institute, 1996.
5. Lizzio, A.A., DeBarr, J.A. and Kruse, C.A., *Energy and Fuels* 11, 250 (1997).
6. Lizzio, A.A. and DeBarr, J.A., *Fuel* 75, 1515 (1996).
7. Demir, I., Lizzio, A.A., Fuller, E.L. and Harvey, R.D., *J. Coal Quality* 13, 93 (1994).
8. Mochida, I., *Energy and Fuels* 11, 272 (1997).
9. Lizzio, A.A. and DeBarr, J.A., *Energy and Fuels* 11, 284 (1997).
10. Jang, B.W.-L., Spivey, J.J., Kung, M.C. and Kung, H.H., *Energy and Fuels* 11, 299 (1997).
11. Illan-Gomez, M.J.; Linares-Solano, A.; Salinas-Martinez de Lecea, C. and Calo, J.M., *Energy and Fuels* 9, 97 (1993).
12. Illan-Gomez, M.J.; Linares-Solano, A., Radovic, L.R., Salinas-Martinez de Lecea, C. *Energy and Fuels* 9, 104 (1995).
13. Garcia-Garcia, A., Linares-Solano, A., Salinas-Martinez de Lecea, C., Energy and Fuels 11, 292 (1997).
14. Stohr, B., Boehm, H.P. and Schlogl, R., *Carbon* 29, 707 (1991).
15. Fei, Y., Sun, Y., Givens, E. and Derbyshire, F., *ACS Preprints, Div. Fuel Chem.* 40 (4), 1051 (1995).

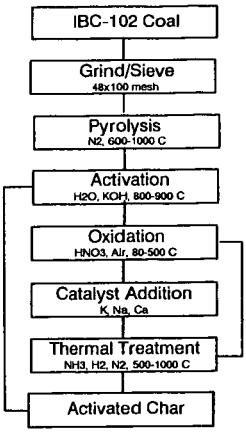

Figure 1. Production of activated char from Illinois coal.

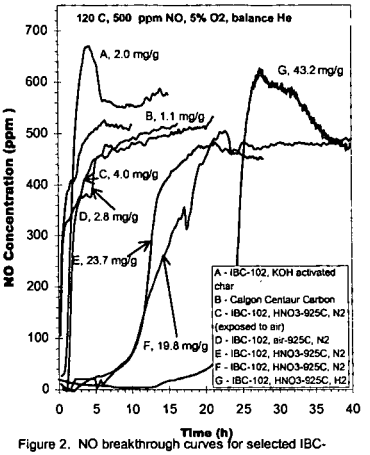

Figure 2. NO breakthrough curves for selected IBC-102 chars and a commercial activated carbon.

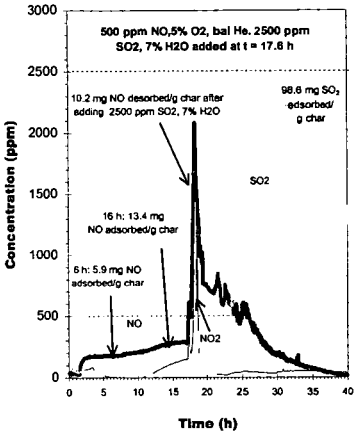

Figure 3. Effect of adding SO2 and H2O at the same time on NOX removal by IBC-102, HNO3, 925 C char.

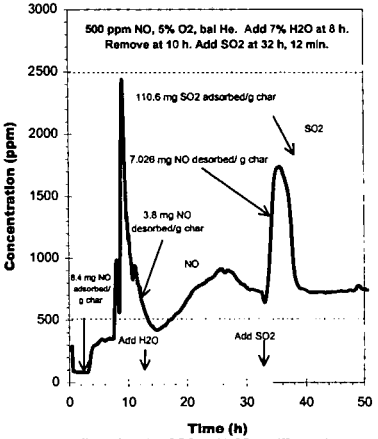

Figure 4. Effect of adding SO2 and H2O at different times in NOX removal by IBC-102, HNO3, 925 C char.

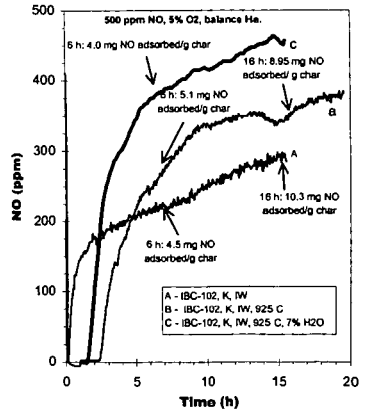

Figure 5. Effect of thermal desorption treatment (925 C) and H2O on NOx removal by IBC-102, K, IW char.

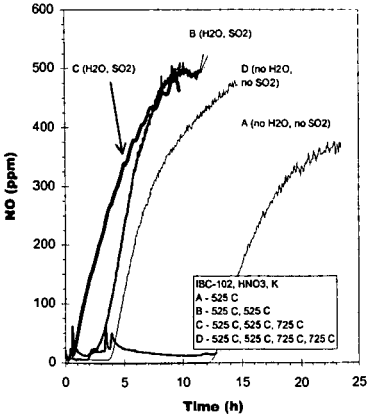

Figure 6. Effect of thermal desorption temperature and H2O/SO2 on NOX removal by IBC-102, HNO3, K, IE char.

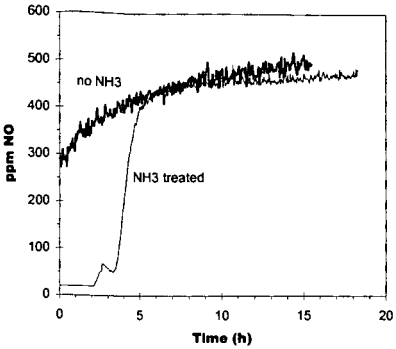

Figure 7. Effect of NH3 treatment on NOX removal by steam activated IBC-102 char.

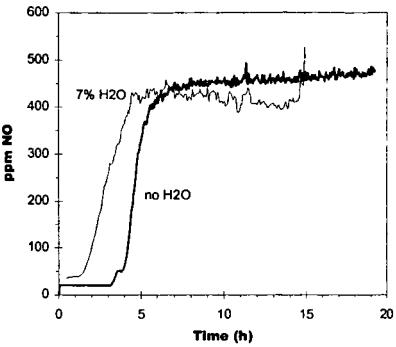

Figure 8. Effect of H2O on NOX removal by NH3 treated, steam activated IBC-102 char.

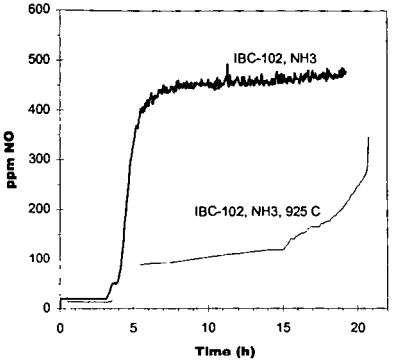

Figure 9. Effect of thermal desorption treatment at 925 C on NOX removal by NH3 treated, steam activated IBC-102 char.

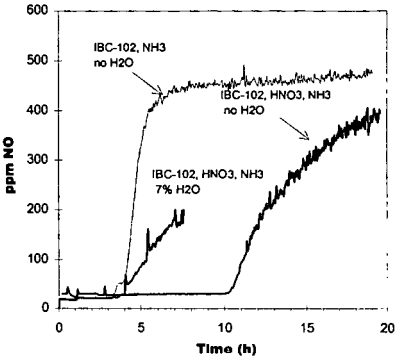

Figure 10. Effect of HNO3 treatment on NOX removal by NH3 treated, steam activated IBC-102 char.

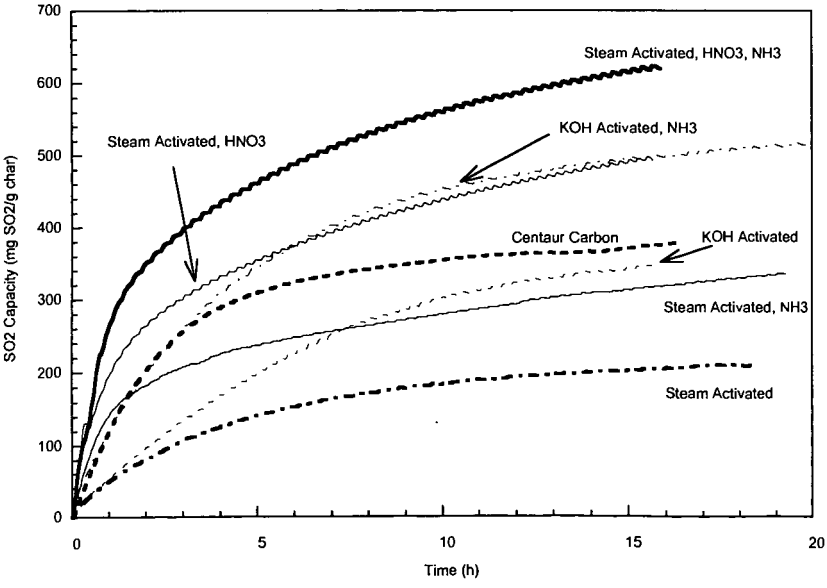

Figure 11. Effect of NH3 treatment on SO2 adsorption capacity of selected IBC-102 chars.

CLEANUP OF HOT COAL GAS WITH CARBON-BASED SORBENTS

Mark P. Cal[1,2], Brooks W. Strickler[1,2], Anthony A. Lizzio[1], Mark J. Rood[2]
[1]Illinois State Geological Survey, 615 E. Peabody Dr./MC-650, Champaign, IL 61820
[2]University of Illinois, Department of Civil and Environmental Engineering/MC-250, Urbana, IL

Keywords: gasification, adsorption, hydrogen sulfide.

INTRODUCTION

Integrated Gasification Combined Cycle (IGCC) power systems are emerging as the most promising technology to convert high sulfur coal into electricity. Illinois Basin coal is a proven feedstock for IGCC, e.g., the Destec process in Terre Haute, IN. Hot gas cleanup for desulfurization is needed to accelerate the successful demonstration and commercialization of advanced coal gasification systems worldwide. In IGCC processes, hydrogen sulfide is removed from the coal gas before it enters the turbine. To achieve maximum efficiency in IGCC systems, H_2S should be removed from the fuel gas while hot. Although H_2S can be removed quite effectively by cooling the hot gases to temperatures less than 100°C, removal of H_2S at 300-800°C can lead to significant increases (up to 3%) in overall thermal efficiency. More efficient IGCC processes expand for markets hot gas cleanup sorbents and for high sulfur Illinois coal.

Numerous metals and mixed metal compounds have been studied as possible desulfurization sorbents. Current leading sorbents include zinc titanate and Z-Sorb (a proprietary zinc-oxide-based sorbent). However, not only are these sorbents expensive (up to $7-15/lb), they are also prone to chemical and/or physical degradation during cycling. Zinc titanate suffers from spalling due to formation of sulfide and sulfate which have 2 to 3 times higher molar volume than the oxide. Z-Sorb degrades in the presence of steam present in coal gas. Both sorbents sinter during regeneration and typically their reactivity drops by around 50 percent in just 50 cycles.

One may conclude by reviewing the literature on hot gas cleanup sorbents that while research on sorbent materials has been extensive, continuing efforts are important because these sorbents are not yet used commercially in coal gasification processes, and there is still time for the development of improved sorbents. Another reason to encourage research in this area is that not all gasification systems are alike, and because of these differences in operating conditions and requirements, it is likely that more than one type of sorbent will be needed to satisfy the market. Every sorbent examined to date has had at least one major deficiency that prevents its widespread use. The fact that there is still ample opportunity to develop new types of sorbents for hot gas cleanup provides incentive for research on new types of materials.

One material that should be examined in more detail as a potential hot gas cleanup sorbent is carbon. Although, the use of carbon for hot gas cleanup has significant potential, the possibility of using carbon-based materials to remove sulfur containing gases from the products of coal gasification has been overlooked as other sorbents such as zinc ferrite, zinc titanate, and copper oxides have been extensively studied. Carbon has several advantages compared to metal-based hot gas cleanup sorbents: 1) the harsh coal gas environment should not affect the properties of the carbon during operation (carbon will not gasify in a reducing atmosphere at temperatures less than 700°C), 2) carbon, itself, adsorbs large quantities of H_2S, meaning that it could be used as an active support for metals such as copper and zinc which also adsorb H_2S; most metal-based sorbents have an inert support matrix, sometimes constituting up to 60% of the mass of the sorbent, 3) carbon will not chemically spall unlike metal based sorbents and it is more physically stable, since there is little or no volumetric change in a carbon-based sorbent due to sulfur loading, and 4) coal, which is used to make the carbon-based sorbents, is a very inexpensive starting material.

EXPERIMENTAL PROCEDURES

Sorbent Preparation

Activated chars were produced from size-graded Illinois coal in a fluidized-bed reactor (2 in. ID) under controlled preoxidation, pyrolysis, and activation conditions. Preoxidation of the chars was typically performed for 2 hr at 225°C, pyrolysis for 1 hr at 425°C and activation in steam for 2-6 hr at 825°C. Coal samples were activated until a specified carbon conversion was achieved (10-50%). Chars were oxidized using nitric acid (45 wt. % HNO_3) to achieve oxygen concentrations on the chars of up to 15 wt. %. An thermal desorption treatment (200-1000°C) was used to prepare chars with varying amounts of oxygen, which served as a starting material for the metal impregnation step. Various metals (Zn, Cu, etc.) known to chemically react with H_2S were added to the activated char using either incipient wetness or ion exchange methods.

Fixed-Bed Breakthrough Experiments

H_2S removal tests were performed on the various carbon-based sorbents produced in this study. A simulated coal gas stream was used containing 0-50% CO_2, 49-99.5% N_2, and 0.5-1% H_2S at 1 atm and 400-550°C. Initial H_2S adsorption experiments were performed using a 1 cm I.D. 316L stainless steel reactor, but since H_2S reacts with stainless steel at the temperatures examined, only total sulfur measurements are reported for those experiments and not breakthrough times. The measurement technique used to determine the total sulfur added to the carbon is discussed below.

A quartz reactor with a 1.5 cm O.D. and a fritted quartz plate was used for the sulfidation breakthrough tests. The fittings and tubing entering and exiting the reactor are made of teflon in order to minimize the adsorption of H_2S onto anything other than the sorbent being tested. Breakthrough curves were developed at space velocities of about 2000 hr^{-1} (200 cm^3/min) for packed-beds containing the carbon-based sorbents. H_2S influent and effluent concentrations were measured with a mass spectrometer (MS). For most experiments, breakthrough curves were run until the effluent concentration reached 200-300 ppmv. At which time, the experiment was terminated and the breakthrough curve was integrated to yield the total H_2S capacity and the time to breakthrough. Total sulfur analysis was performed on valid samples as a quality assurance/ quality control (QA/QC) procedure.

Total Sulfur Measurements

After adsorption and regeneration experiments, total adsorbed sulfur was determined by elemental analysis of the char using a solid state infrared detector (LECO SC-32). Samples were combusted in an oxygen atmosphere where the sulfur oxidizes to SO_2 and were then measured by a solid state infrared detector. The measured SO_2 was then converted to total percentage of sulfur. The sulfur content of samples before and after H_2S adsorption experiments was measured in order to calculated the total sulfur adsorbed.

RESULTS AND DISCUSSION

The best carbon-based sorbents developed for H_2S removal to date had a breakthrough time to 200 ppmv outlet H_2S concentration of over six hours and sulfidation capacities of up to 13 wt. % were observed. Numerous adsorption experiments were performed to evaluate the adsorption capacities and breakthrough times of various carbon-based sorbents. Activated, nitric acid oxidized, desorbed (with more active carbon sites), and metal impregnated chars were used for adsorption experiments. Experimental conditions were altered for a few adsorption experiments to determine their effect on H_2S adsorption. The inlet gas stream was modified to include only H_2S and N_2 in two experiments (Char F & G) and the reactor temperature was lowered from 550 to 400°C for one experiment (Char I). The characteristics and total added sulfur (initial sulfur in the sorbents was about 1 wt. %) for adsorption experiments run with the stainless steel reactor are shown in Table 1. The sulfur content of the chars before and after H_2S adsorption was measured.

A comparison of the sulfur contents of different chars produced several interesting results. As displayed in Table 1, char E had the highest sulfur content after adsorption experiments. Char E was oxidized with nitric acid and impregnated by ion exchange with zinc. The nitric acid oxidized chars (A and B) adsorbed 10.2 to 11.3 wt. % sulfur. A char desorbed of oxygen (char C) adsorbed a significant amount of sulfur (6.5 wt. %), but did not perform as well as the oxidized or metal impregnated chars. This suggests that while carbon sites will adsorb H_2S, oxygen and metal content are also important to achieve optimal adsorption. Char B and C differ in oxygen content only. The oxidized char (B) adsorbed about 50% more sulfur than the desorbed char (C) for comparable adsorption times. It may be concluded from Table 1 that the presence of chemisorbed oxygen enhances H_2S adsorption on activated char. Based upon our measurements to date, we propose three possible routes for H_2S adsorption on carbon:

$$C\text{-}O + H_2S \dashrightarrow C\text{-}S + H_2O$$
$$C + H_2S \dashrightarrow C\text{-}S + H_2$$
$$C\text{-}X + H_2S \dashrightarrow C\text{-}X\text{-}S + H_2$$

where X is an active metal

The total sulfur results in Table 1 suggest the importance of the inlet gas stream. The inlet gas was modified to include only H_2S and N_2 for adsorption experiments with chars F and G. Without CO_2 present in the influent gas stream, the measured adsorption capacities were significantly lower with CO_2. This occurrence can be seen when chars F and G are compared to A and J, respectively. Char A adsorbed about 50% more sulfur than char F for comparable adsorption times and char J adsorbed about 50% more sulfur than char G for a shorter adsorption time. The only difference between these experiments was the presence of CO_2. This occurrence suggests

some interaction between the carbon surface and CO_2, but it is known that carbon should not gasify in a reducing environment below 700°C. The importance of CO_2 in H_2S adsorption continues to be studied and more research is necessary before any type of conclusion can be suggested.

The total sulfur results in Table 1 indicate the importance of char surface area and reactor temperature. By comparing the surface areas of metal impregnated chars (E, H, N, and O), it can be seen that incipient wetness (IW) reduces surface area to a greater extent than ion exchange (IE). The reduced surface area appears to slightly lower adsorption capacity for similar chars (H and O). The influence of reactor temperature can be seen by comparing chars I and J in Table 1. Char J (550°C) adsorbed significantly more sulfur than char I (400°C) during a shorter run time.

Table 1 also displays total sulfur content of chars after adsorption experiments with the quartz reactor. Chars impregnated with metals (N and O) adsorbed about 10.5 wt. % sulfur before the effluent H_2S concentration reached 500 ppmv (350-390 min). An oxidized char (K) that was run for a longer time (610 min) attained a added sulfur content of 12.7 wt. %. A steam activated char (M), with no nitric acid oxidation, achieved a added sulfur content of 6.1 wt. %. The results show that significant amounts of sulfur (6.1-10.6 wt. %) can be added to carbon in fairly short adsorption times (<400 min). The sulfur contents for chars K-O (quartz reactor) are comparable and slightly better than those of chars A-J (stainless steel reactor). The improvements in adsorption capacities and breakthrough times are most likely due to improved char preparation methods.

Figure 1 displays breakthrough curves for four adsorption experiments with the quartz reactor. Breakthrough times to 200 ppmv outlet H_2S concentration for chars K, M, N, and O ranged from 4-6.5 hours. These breakthrough times were performed at 550°C, a space velocity (SV) of 1700-2000 hr^{-1} (200 cm^3/min), and an influent concentration of 5000 ppmv H_2S. The oxidized char impregnated with zinc by ion exchange performed the best, followed by the copper impregnated char. The oxidized char (K) displayed a leveling off of outlet concentration at 1300-1500 ppmv H_2S which is similar to previous adsorption experiments. This may indicate that a catalytic reaction might be occurring which converts H_2S to another compound or it may mean that H_2S adsorption on carbon exhibits a two-stage breakthrough curve. An interesting discovery of the adsorption experiments was that the steam activated char (M) had a breakthrough time (200 ppmv) that was very similar to that of the oxidized char (K).

SUMMARY AND CONCLUSIONS

Results of this project to date have shown that carbon-based sorbents are still adsorbing H_2S at sulfur loadings of 6 to 13 wt. % sulfur from a gas stream containing 0.5% hydrogen sulfide (H_2S) in CO_2 and N_2 at 550°C. Fixed-bed breakthrough curves have been obtained for several chars using a simulated coal gas stream containing 0.5% H_2S at a space velocity of 2000 hr^{-1} (200 cm^3/min). Breakthrough times to 200 ppmv effluent H_2S concentration ranged from 2 to 6.5 hours, depending on the char used. These breakthrough times are comparable to some metal-based sorbents. Results of adsorption properties are encouraging and show that carbon may be a viable hot gas cleanup sorbent. With further research, we believe that we can increase both the sulfidation capacity and breakthrough time of carbon-based sorbents. It remains to be determined how the pore structure and surface chemistry of the char can be modified to maximize H_2S adsorption capacity. The mechanism of H_2S removal by carbon is also not well understood, and any research to optimize the H_2S removal capabilities of carbon will inevitably lead to new insights into H_2S adsorption and conversion to elemental sulfur on the carbon surface. One distinct advantage carbon has over metal-based is that carbon, itself, adsorbs large quantities of H_2S, meaning that it could be used as an active support for metals such as copper and zinc which also adsorb H_2S. Most metal-based sorbents have an inert support matrix, sometimes constituting up to 60% of the mass of the sorbent. Metal-based sorbents, such as zinc titanate and Phillips Z-Sorb have an inert support matrix that does not participate in the H_2S adsorption reaction.

ACKNOWLEDGEMENTS

This work was supported by the Illinois Department of Energy and Natural Resources through the Illinois Coal Development Board and the Illinois Clean Coal Institute. Discussions with John Lytle and Deepak Tandon of the Illinois State Geological Survey and Santosh Gangwal of the Research Triangle Institute are also appreciated.

Table 1: Carbon-Based Sorbents Anaylzed for H_2S Adsorption.

Sorbent ID	Inlet Gas Composition	Oxygen on Sorbent [wt %]	BET Surface Area [m^2/g]	Char Description	Sulfur Added [wt %]	Adsorption Time [min]
Stainless Steel Reactor						
A	0.5% H_2S, 49.5% N_2, 50% CO_2	12-15	567	HNO_3 oxidized	10.2	750
B	0.5% H_2S, 49.5% N_2, 50% CO_2	12-15	567	HNO_3 oxidized	11.3	1200
C	0.5% H_2S, 49.5% N_2, 50% CO_2	~0	-	desorbed of oxygen	7.55	1350
D	0.5% H_2S, 49.5% N_2, 50% CO_2	12-15	465	HNO_3 oxidized	11.6	1100
E	0.5% H_2S, 49.5% N_2, 50% CO_2	12-15	509	HNO_3 oxidized + Zn by IE	13.2	1100
F	0.5% H_2S, 99.5% N_2	12-15	465	HNO_3 oxidized	6.54	830
G	0.5% H_2S, 99.5% N_2	~0	-	desorbed of oxygen	3.12	460
H	0.5% H_2S, 49.5% N_2, 50% CO_2	12-15	130	HNO_3 oxidized + Cu by IW	10.0	1060
I	0.5% H_2S, 49.5% N_2, 50% CO_2	12-15	465	HNO_3 oxidized, 400°C	2.41	410
J	0.5% H_2S, 49.5% N_2, 50% CO_2	12-15	465	HNO_3 oxidized	4.78	180
Quartz Reactor						
K	0.5% H_2S, 49.5% N_2, 50% CO_2	10-15	567	HNO_3 oxidized	12.7	610
L	0.5% H_2S, 49.5% N_2, 50% CO_2	10-15	-	HNO_3 oxidized + Ca by IW	10.7	640
M	0.5% H_2S, 49.5% N_2, 50% CO_2	-	520	steam activated	6.1	300
N	0.5% H_2S, 49.5% N_2, 50% CO_2	10-15	509	HNO_3 oxidized + Zn by IE	10.4	390
O	0.5% H_2S, 49.5% N_2, 50% CO_2	10-15	250	HNO_3 oxidized + Cu by IE	10.6	350

Table 1 Notes:

- All chars were preoxidized, pyrolized and steam activated.
- Reactor temperture = 550°C, inlet gas flow rate = 200 cm^3/min, and space velocity = 1700 to 2000 hr^{-1}.
- IE = ion exchange method, and IW = *incipient wetness method.*

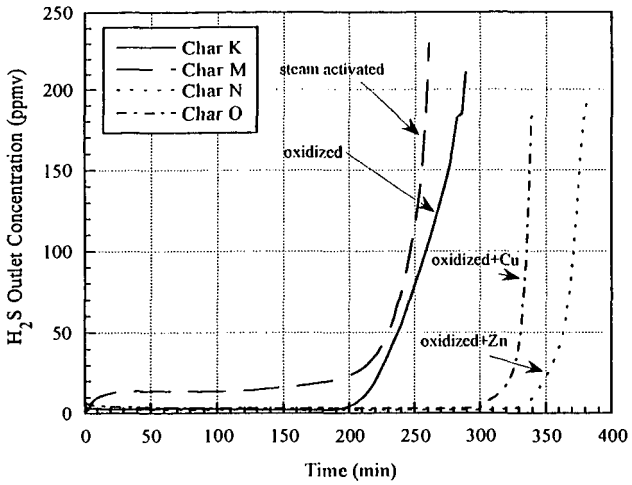

Figure 1. H_2S Breakthrough Curves for Carbon-Based Sorbents using Quartz Reactor

Conditions: SV = 1700-2000 hr^{-1}, 0.5% H_2S, 49.5% N_2, 50% CO_2, 550°C, 1 atm.

METAL IONS REMOVAL FROM WASTEWATER BY ADSORPTION

S. B. LALVANI, T. WILTOWSKI AND A. WESTON*

Department of Mechanical Engineering and Energy Processes
*Department of Engineering Technology
Southern Illinois University
Carbondale IL 62901

ABSTRACT

Three different carbonaceous adsorbents consisting of (i) commercially available lignin (L); (ii) carbon soot produced by arc evaporation of graphite rods (AC); and (iii) commercially available carbon (RC) were employed for the removal of hexavalent and trivalent chromium, and the cations of lead and zinc. AC carbon was found to selectively adsorb only the hexavalent form of chromium which exists as a number of anionic species in the water. Insignificant metal cation adsorption was observed with AC. However, lignin is found to adsorb all the metal ions employed in the study. RC used in this investigation adsorbs only the metal cations and does not remove the hexavalent form of chromium used. Equilibrium as well as kinetic data obtained are analyzed in light of a mathematical model developed which assumes that the overall metal removal rate is controlled by the rate of mass transport of solute from bulk to the surface of the adsorbent.

INTRODUCTION

The presence of heavy metals in the environment is a major concern due to their toxicity to many life forms. Unlike organic pollutants, the majority of which are susceptible to biological degradation, heavy metals will not degrade into harmless end products. Thus, treatment of aqueous wastes containing soluble heavy metals requires concentrations of the metals into smaller volume followed by recovery or secure disposal. Heavy metals can be found in a variety of industries, in particular mining, metal processing, finishing and plating. Effluents from these industries contain heavy metals, the concentrations of which are regulated by governmental agencies. Thus, it is often required to remove heavy metals before discharge of various effluents. The major techniques employed for heavy metal removal from industrial wastewaters include precipitation, reduction, ion-exchange, and adsorption. Attempts have been made by several researchers to develop alternate inexpensive methods for heavy metal removal using industrial waste materials (discarded tires, fly ash, sludge), agricultural products, and byproducts (starch, tree barks, onion skin, coconut shell, palm pressed fibers, lignin), and naturally occurring minerals (coal, peat moss, pyrite).

The choice of adsorbents used in this study was motivated by the following rationale. Lignin, an inexpensive naturally occurring material is a component of woody biomass. It is available in large quantities as a byproduct from the paper and pulp industry. Lignin contains many oxygen functionalities such as phenols and ketones which can serve as adsorption sites for binding heavy metals. Carbon produced from graphite rods by electrical arcing method under inert atmosphere is expected to have unusual properties. The carbon soot produced under these conditions also leads to fullerene formation. A commercially available activated carbon (RC) was used as a control to compare the metal removal properties of lignin (L) and the carbon produced by arc evaporation of graphite rods (AC).

EXPERIMENTAL METHODS

Lignin was obtained from Westvaco Corporation. It is characterized as Indulin AT, a purified powder form of kraft lignin, which is completely free of all hemicellulosic materials. The arc-assisted synthesis of carbons (AC) is reported in a previous paper(1). The method involves arcing of graphite electrodes under flowing helium atmosphere. The alternating current applied to the electrodes ranged from 100-160 amperes. The application of this high current resulted in vaporization of the graphite. The condensed soot was collected and used as an adsorbent. In addition, a commercially available activated carbon (RC), Darco TRS obtained from American Norit Company was also used as an adsorbent for the metal ion removal from aqueous solutions.

Batch sorption experiments were conducted at a constant room temperature of 25 °C using a 500 ml Erlenmeyer flask. The stirred reaction mixture consisted of a total volume of 250 ml. When necessary, the initial pH of the solution was adjusted. The metal concentration was determined by inductively-coupled plasma spectroscopy (ICP).

RESULTS AND DISCUSSION

The effect of initial chromium concentration on the removal of hexavalent chromium at solution pH (initial) of 4.5 using the arc assisted produced carbon (AC) is shown in Figure 1. The adsorbent loading used was 5 g/l and the experiments were conducted for a period of 24 h. The chromium removal (%) is found to increase with the initial metal concentration reaching a maximum value of approximately 94%, however, with a further increase in metal concentration, the removal is found to decrease. Similar albeit lower hexavalent chromium removal vs. concentration trends are observed when lignin is used as an adsorbent in the metal ion containing solution prepared at an initial pH value of 2.5 (Figure 1). Up to 53% metal removal was observed in the case of lignin. It must be noted that when the commercially available activated carbon (RC) was used very small amount of hexavalent chromium removal was obtained. For example, the use of initial metal concentration of 20 ppm in experiments conducted at three different initial pH values of 2.5, 3.0 and 4.5 resulted in 24.6, 14.0, and 9.1% chromium removal, respectively. The data reported in Figure 1 were used to prepare adsorption isotherms. AC adsorbent does not seem to follow either Langmuir or Freundlich isotherm models. The maximum adsorption capacity for the Cr^{6+}/AC system was found to be 8.9 mg/g of sorbent. On the contrary, data for the Cr^{6+}/lignin system represents a relatively good fit to the Langmuir equation and can be expressed by the following equation:

$A^{-1} = 2.9*C_e^{-1} + 0.18$, where A is the adsorption capacity and C_e is the equilibrium concentration in mg/l. The maximum adsorption capacity is estimated to be 5.64 mg/g of sorbent.

The data on removal of trivalent chromium at an initial pH value of 3.0 as function of the metal concentration for the three adsorbents are shown in Figure 2. Experiments were conducted for 24 h using 5 g/l of adsorbent loading. RC adsorbent is found to remove practically all the metal present in the solution. In the case of lignin, about 90% metal removal is observed at low metal ion concentrations. However, an increase in metal concentration results in corresponding lower removal (%). On the other hand, essentially no trivalent chromium removal is noted when the arc-assisted produced carbon (AC) was used in these experiments.

In the experiments involving metal cations of lead and zinc, practically no metal removal was observed when the arc-assisted produced carbon (AC) was used especially at low pH values. For example, in the case of experiments involving lead (Pb^{2+}), 0, 2 and 25% metal removal was noted at pH values of 3.0, 4.5 and 9.0 respectively. RC carbon was observed to remove 100% lead at pH values ranging from 2 to 9.5. Lignin also showed a great affinity for lead. The metal removal (%) increases with pH. For example, the removal of lead by lignin is 47, 74 and 98% at pH values of 2.0, 2.5 and 3.0 respectively. Both, RC and lignin showed 100% zinc removal while no metal removal was observed for AC up to a pH value of 6.0. AC showed about 30% zinc removal at a pH value of 9.0.

The data obtained above can be explained as below. Hexavalent chromium is present in aqueous solutions mainly as anionic chromate species. Therefore, AC carbon is capable of removing this form of chromium as it is hypothesized to contain positive charge on the surface. It must be noted that this carbon is produced by arc evaporation of graphite rods in the absence of air or oxygen. This hypothesis also explains the inability of this form of carbon to remove cations of chromium, lead and zinc at relatively low pH values. At high pH values the surface charges of AC are neutralized, therefore it is able to adsorb limited amount of metal cations. Lignin contains mainly oxygen functionalities, therefore it is able to remove metal cations in addition to the anionic chromate species. On the other hand, RC is activated using steam or air, therefore its surface has mainly oxygen functionalities which serve as negatively charged sites for binding only the metal cations.

REFERENCES

1. Weston, A. and Murthy, M., "Synthesis of Fullerenes: An Effort to Optimize Process Parameters," Carbon, 34, 10, 1267-1274, 1996.

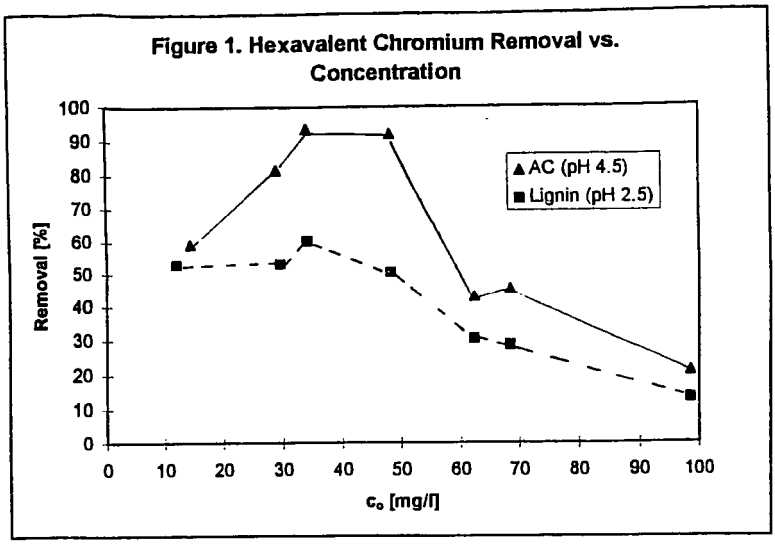
Figure 1. Hexavalent Chromium Removal vs. Concentration
Removal [%]
100
90
80
70
60
50
40
30
20
10
0
0
10
20
30
40
50
60
70
80
90
100
c_o [mg/l]
AC (pH 4.5)
Lignin (pH 2.5)

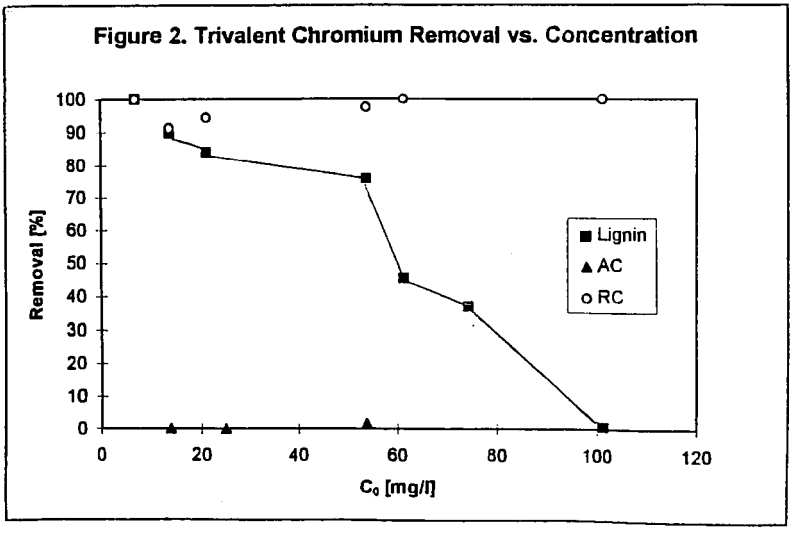
Figure 2. Trivalent Chromium Removal vs. Concentration
Removal [%]
100
90
80
70
60
50
40
30
20
10
0
0
20
40
60
80
100
120
C_0 [mg/l]
Lignin
AC
RC

HAZARDOUS AIR POLLUTANT EMISSIONS FROM THE EXTERNAL COMBUSTION OF HYDROCARBON GASEOUS FUELS CAN BE PREDICTED!

James G. Seebold
Chevron Research and Technology Company
Richmond, California 94804-0054

INTRODUCTION

Passage of the 1990 Amendments to the Clean Air Act made it clear that maximum available control technology ("MACT") regulations on the emission of hazardous air pollutants ("HAPs") from process heaters and industrial boilers, used extensively in the petroleum and petrochemical industries, would be promulgated under congressional mandate by the U. S. Environmental Protection Agency in the year 2000. Unfortunately, it had also become clear that *understanding*, the "good science" upon which we aspire to base sensible regulations, was simply non-existent and, further, that the little field data then extant was severely flawed. To amend those deficiencies, a 4-year $7-million fundamental attack on the origin and fate of trace toxic emissions in the external combustion of gaseous hydrocarbon fuels has been conducted by a government-university-industry collaboration[1] that has been, by all accounts, one of the most successful ever.

A number of challenges were encountered during the course of the project. Perhaps foremost among them and exemplary of the remarkable strength of this collaboration, was the need not only to expand the capabilities of the Sandia National Laboratories, Livermore, Combustion Research Facility Burner Engineering Research Laboratory (BERL) by the addition of 4-component fuel mixing capability (formerly natural gas only); and bunkering and delivery capability for the various gases to be employed in the full-scale burner trials (hydrogen, propane, propylene, ethylene); but also, at the cost of over a quarter of a million dollars that was quickly raised by the CRADA-signatories, to convert the former BERL flame laboratory into a process heater laboratory by the addition of a convection section simulator.

This allowed the project successfully to reproduce at full-scale the generally very low normal-operation gaseous-combustion emissions that are observed in the field, as well as higher hypothetical extreme failure-mode emission levels of aldehydes, volatile organic compounds, polycyclic aromatic hydrocarbons and total organics fully comparable to the highest levels reported in field tests, however sparse and unreliable they might be, observed under extreme combustion conditions that would neither be tolerated nor observed in actual field operations but that, nevertheless, proved to be required to generate toxic emissions of any significance.

Through the rigorous and highly reliable measurements of regulatory development quality, as guaranteed by the project's exemplary Quality Assurance Project Plan that was produced in cooperation with U. S. Environmental Protection Agency experts, carried out during the full-scale burner trials conducted at the Sandia National Laboratories, Livermore, Combustion Research Facility Burner Engineering Research Laboratory, a great deal has been learned, in far more detail and under many more conditions, about the normal and hypothetical extreme limiting emissions from full-scale burners than was heretofore known. However, this paper discusses only the findings that most pertinently address the question, "Can we predict HAP emissions based on fuel composition?"

HAP EMISSIONS UNIFORMLY LOW

In this program we saw over and over again that the nature of the gaseous hydrocarbon fuel mixture doesn't make much difference, neither in the total toxic emissions nor in the individual species levels. This observation includes natural gas which is itself, after all, merely just another hydrocarbon mixture; *i.e.*, there is no reason to distinguish "refinery fuel gas" from "natural gas." Figures 1 and 2 illustrate this equivalency on a speciated basis, there being only small and statistically insignificant differences in the individual species emissions.

Almost stochastic in nature, the individual species levels are uniformly exceedingly low, seemingly less dependent upon physics and chemistry and more dependent upon the vagaries of the sophisticated sampling methods and precise analytical techniques that are required to detect them at all in the minute concentrations in which they appear in the combustion products. In Figures 3-6, these facts are illustrated by the mass emission of total hydrocarbons. Except for an operationally unrealistic super-aerated (450% stoichiometric air) case, we see that there is no significant effect of heating value, combustion zone stoichiometry, propylene or ethylene spikes, nor hydrogen content in the gaseous hydrocarbon fuel mixtures.

The heating value variation was achieved at the constant base case 16% hydrogen content simply by increasing the proportion of propane in the hydrogen, natural gas, propane mixture. The field-operational typical ±15% theoretical air variation around the base case 125% was extended substoichiometrically in the combustion zone to 50% or one-half of the air theoretically required for complete combustion with overfire air added to simulate a leaky furnace while still maintaining the base case 125% theoretical air in the stack. The theoretical air variation was extended super-stoichiometrically in the combustion zone to 450% or four-and-one-half times the air theoretically required for complete combustion simply by increasing the air delivery to the

[1] Petroleum Environmental Research Forum Project Number 92-19 sanctioned under a Stevenson-Wydler (15 USC 3710) Cooperative Research and Development Agreement

burner. The effect of spikes of ethylene and propylene on the emissions of the base case 16% hydrogen, 1050 Btu/scf fuel mixture was tested by utilizing the four component mixing capability that was added by this program to the Sandia National Laboratories, Livermore, California, Combustion Research Facility's Burner Engineering Research Laboratory, while the effect of hydrogen variation on emissions from the 1050 Btu/scf base case was tested simply by compensating adjustments to the natural gas and propane fractions in the fuel mixture.

The absence of systematic variability in the trace emission of toxic byproducts in gaseous external combustion is strikingly illustrated in Figures 7 and 8. We see that the reproducibility of the reference regulatory base cases ("A1" was a 1050 Btu/scf mixture of 16% hydrogen, natural gas, and propane while "A4" was 1050 Btu/scf natural gas) remained good throughout all of the conventional diffusion flame burner ("CDFB") trials in test sequences A, B and C. While test sequence A spanned a broad range of fuel compositions and operating conditions around the normal-operation base cases A1 and A4, we saw no systematic variation in emissions; all emissions remained exceedingly low and the small differences were well within the typical bounds of experimental variability.

Worried that, even in the sequence B "failure mode" tests, we were not able to reproduce polycyclic organic hydrocarbon ("PAH") emissions as high as those reported in some field tests, however unreliable those field tests may have been, we redoubled our efforts to fail combustion and, in the sequence C "super-failure mode" trials, we were rewarded with stack emissions up to 5E-6 lb-PAH/mmBtu (*e.g.*, B13' in Figures 7 and 8), fully as high as any in the "real world" field data base. These high emissions are often attributed, but without much definition and no detailed understanding, to "gross mixing failures." We saw in this program, as illustrated in Figures 7 and 8, that to generate high stack emissions from gaseous hydrocarbon mixtures in external combustion, fuel-air mixing failures of the grossest kind are indeed required, egregious hypothetical extreme combustion conditions that would hardly be tolerated nor permitted to persist in any well-run plant.

HIGH VELOCITY JET MIXING ACCOUNTS FOR LOW TOXICS

The strong mixing potential of sonic jets is well known. In the case of the multiple, small reacting jets of the conventional diffusion flame burner, surrounded as they are under normal conditions with an excess supply of air, why would we not expect very low toxic emissions?

Early in the program, we hypothesized that the hot, rich combustion regions that are necessarily present in a diffusion flame ought to be prolific generators of toxics. The early stirred-reactor, plug-flow computations carried out by Lawrence Livermore National Laboratory supported the hypothesis, while later the laboratory flame measurements carried out at the UCLA Chemical Engineering Laboratory, as well as the research furnace experiments carried out at the Sandia National Laboratories, Livermore, Combustion Research Facility, confirmed it. The Lawrence Livermore calculations also suggested that, in the presence of excess air, the toxics that are necessarily profusely-generated in the rich zone would subsequently quickly be consumed to near-extinction, a prediction that we have now seen borne out time and time again in the full-scale burner trials carried out at the Sandia Combustion Research Facility's Burner Engineering Research Laboratory.

Most significant are the results of Sandia's application of a two-stage Lagrangian jet model to a typical conventional diffusion flame burner jet. Based upon the observed flame structure of the conventional burner, the jet model was applied twice: first to the individual jet flames that emerge from the burner tips inside the quarl and again for the merged jet exiting the quarl; thereafter, when mixing is completed, a plug-flow reactor model is utilized to represent the remaining flow to the furnace exit. To give confidence in the results, it may be observed that the model predicted a final CO level of 2 ppm, consistent with the actually measured level below the detection limit of 5 ppm, and a final NOx concentration of 106 ppm, compared with the measured value of 118 ppm. The jet model predicts that the air toxic species should be produced to significant levels within the in-quarl flames but should be consumed well within the substoichiometric regime, both just as we have seen in the full-scale trials.

The Lagrangian jet model confirms and illustrates the expected behavior. Initially, where the reactions are just beginning, there is nothing but the original fuel reactants and oxidant in abundance. As the reactants and oxidant begin to mix, the reacting part of the "reacting jet" begins, too, and the reaction products begin to appear. Then as more and more air is mixed into the jet, with theoretical air % increasing but still well within the substoichiometric regime, the reaction products peak but then are rapidly consumed even before the mixture reaches stoichiometric.

The prediction confirmed that toxic species, manufactured in abundance in the hot, rich diffusive regime, are subsequently consumed in the high-mixing-potential jet well before it reaches even stoichiometric conditions, is, of course, extremely significant, not only with regard to its implication upon the robustness of practical combustion systems in the field but also with respect to the predictability of HAP emissions based on fuel composition.

Moreover, it is perhaps remarkable to note that, in the super-failure mode full-scale trials carried out at the Sandia National Laboratories, Livermore, Combustion Research Facility's Burner Engineering Research Laboratory, it was not until severely substoichiometric conditions (stoichiometric ratio below 0.80) were achieved in the combustion zone and maintained right

through and out the stack to the atmosphere, and just as predicted by the Lagrangian jet model, that high levels of toxics emerged.

This goes a long way toward explaining why the conventional diffusion flame burner, composed as it is of burner tips out of which emerge high-mixing-potential jets surrounded by an abundant supply of oxidant, simply has to be a low toxics burner.

CONCLUSION

Jet-mixed gaseous hydrocarbon diffusion flames, such as those produced by the burners that are typically used in petroleum industry process heaters and industrial boilers, result in a combustion process that is extremely robust, producing predictable, exceedingly low emissions of hazardous air pollutants even when subjected to extreme mixing failures. Readers who are interested in learning more about this interesting subject are referred to the papers published in learned journals that emerged from this program, many of which are listed in the references.

REFERENCES

Pitz, W.J., C.K. Westbrook, A.E. Lutz, R.J. Kee, S.M. Senkan and J.G. Seebold (1994). Numerical Modeling Capabilities for the Simulation of Toxic By-Products Formation in Combustion Processes, *Combust. Sci. and Tech.*, **101**, pp. 383-396.

Castaldi, M.J., A. Vincitore and S.M. Senkan (1995). Micro-Structures of Hydrocarbon Flames, *Combust. Sci. and Tech.*, **107**, pp. 1-19.

Edwards, C.F. and P.J. Goix, Effect of Fuel Gas Composition and Excess Air on VOC Emissions from a Small-Scale, Industrial-Style Burner (1996). *Combust. Sci. and Tech.*, **116**, pp. 1-6.

Senkan, S.M. and M.J. Castaldi, Formation of Polycyclic Aromatic Hydrocarbons (PAH) in Hydrocarbon Combustion: Comparative New Results from Premixed Flames (1996). *Combust. and Flame*, **107**, pp. 141-150.

Castaldi, M.J. and S.M. Senkan, Micro-Structures of Hydrocarbon Flames: Ethane (1996). *Combust. Sci. and Tech.*, **116**, p. 167.

Marinov, N., W.J. Pitz, C.K. Westbrook, M.J. Castaldi and S.M. Senkan, Modeling of Aromatic and Polycyclic Aromatic Hydrocarbon Formation in Premixed Methane and Ethane Flames (1996). *Combust. Sci. and Tech.*, in press.

Castaldi, M.J., N. Marinov, W.J. Pitz, C.K. Westbrook, C.F. Melius and S.M. Senkan - "Experimental and Modeling Investigation on Aromatic and Polycyclic Aromatic Hydrocarbon Formation in a Premixed Ethylene Flame." *26th Symposium (Intl) on Combustion*, 1996.

Gittins, M.J., M.J. Castaldi, S.M. Senkan and E.A. Rohlfing, Real-Time Quantitative Analysis of Combustion Generated Polycyclic Aromatic Hydrocarbons by Resonance Enhanced Multiphoton Ionization Time-of-Flight Mass Spectrometry (1996). *Analytical Chemistry*, submitted.

Vincitore, A., N. Marinov, W.J. Pitz, C.K. Westbrook, C.F. Melius and S.M. Senkan, Micro-Structures of Opposed Flow Diffusion Flames: Methane (1996). *Combust. Sci. and Tech.*, submitted.

Castaldi, M.J., J.W. Huang and S.M. Senkan, Micro-Structures of Hydrocarbon Flames: Ethylene (1996). *Combust. Sci and Tech.*, submitted.

Senkan, S.M., and M.J. Castaldi, Real Time Ultrasensitive Monitoring of Ar Toxics by Laser Photoionization Time of Flight Mass Spectrometry (1996). *J. Air and Waste Mgmt. Assoc.*, submitted.

Castaldi, M.J., and S.M. Senkan, Laser Photoionization Time of Flight Mass Spectrometry of Polycyclic Aromatic Hydrocarbons (1996). *Rev. Sci. Instrum.*, in preparation.

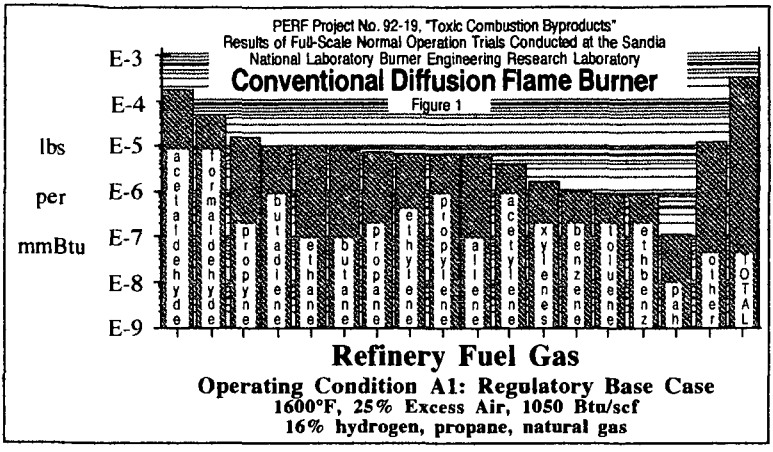
PERF Project No. 92-19, "Toxic Combustion Byproducts"
Results of Full-Scale Normal Operation Trials Conducted at the Sandia
National Laboratory Burner Engineering Research Laboratory
Conventional Diffusion Flame Burner
Figure 1
lbs per mmBtu
E-3
E-4
E-5
E-6
E-7
E-8
E-9
acetaldehyde
formaldehyde
propyne
butadiene
ethane
butane
propane
ethylene
propylene
allene
acetylene
xylenes
benzene
toluene
ethbenz
pah
other
TOTAL
Refinery Fuel Gas
Operating Condition A1: Regulatory Base Case
1600°F, 25% Excess Air, 1050 Btu/scf
16% hydrogen, propane, natural gas

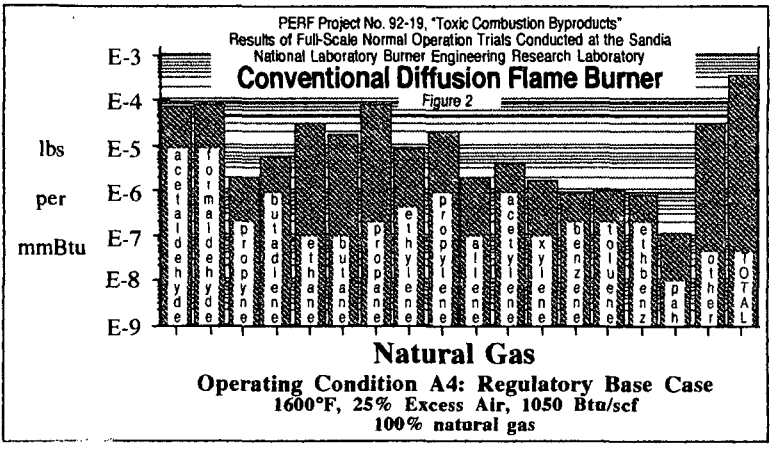
PERF Project No. 92-19, "Toxic Combustion Byproducts"
Results of Full-Scale Normal Operation Trials Conducted at the Sandia
National Laboratory Burner Engineering Research Laboratory
Conventional Diffusion Flame Burner
Figure 2
lbs per mmBtu
E-3
E-4
E-5
E-6
E-7
E-8
E-9
acetaldehyde
formaldehyde
propyne
butadiene
ethane
butane
propane
ethylene
propylene
allene
acetylene
xylene
benzene
toluene
ethbenz
pah
other
TOTAL
Natural Gas
Operating Condition A4: Regulatory Base Case
1600°F, 25% Excess Air, 1050 Btu/scf
100% natural gas

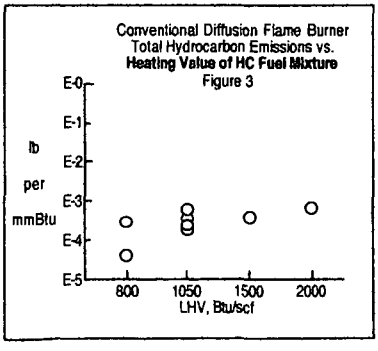
Conventional Diffusion Flame Burner
Total Hydrocarbon Emissions vs.
Heating Value of HC Fuel Mixture
Figure 3
lb per mmBtu
E-0
E-1
E-2
E-3
E-4
E-5
800
1050
1500
2000
LHV, Btu/scf

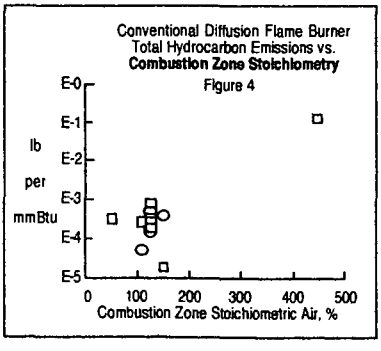
Conventional Diffusion Flame Burner
Total Hydrocarbon Emissions vs.
Combustion Zone Stoichiometry
Figure 4
lb per mmBtu
E-0
E-1
E-2
E-3
E-4
E-5
0
100
200
300
400
500
Combustion Zone Stoichiometric Air, %

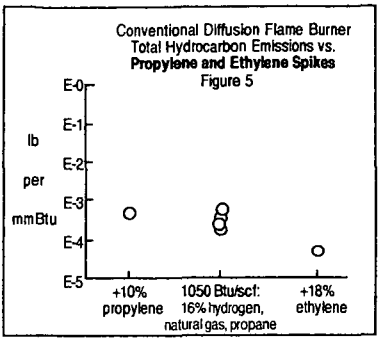

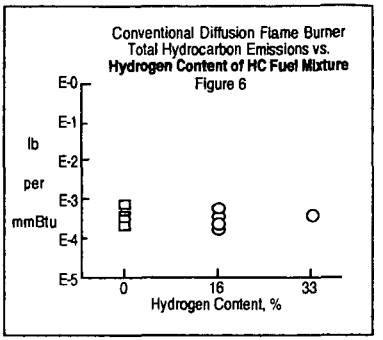

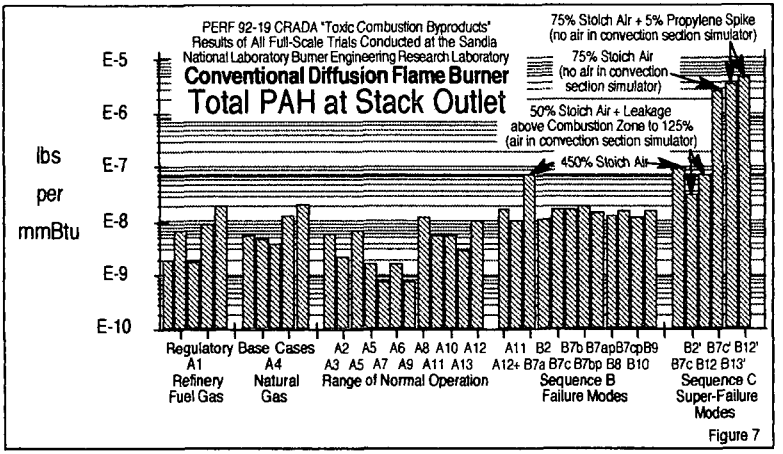

Figure 7

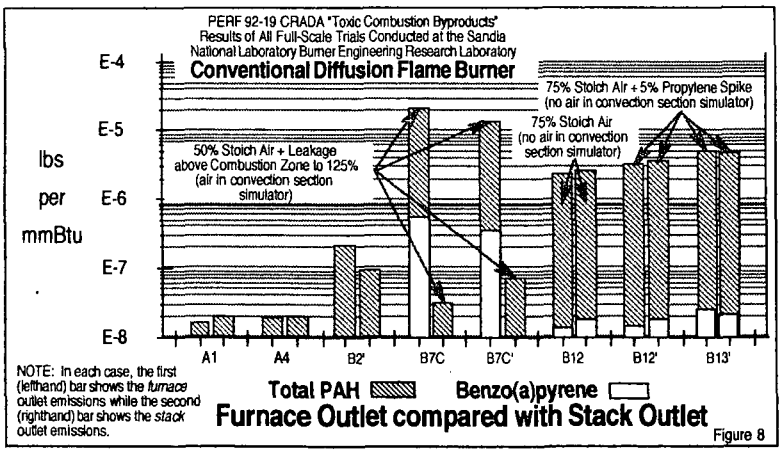

Figure 8

IMPACT OF OPERATING CONDITIONS AND FUEL COMPOSITION ON VEHICLE EMISSIONS

E. W. Kaiser
Ford Motor Company, Mail Drop 3083/SRL
Dearborn, MI 48121-2053

INTRODUCTION

Control of exhaust hydrocarbon (HC) emissions is an important feature in the design of motor vehicles. Both the Federal Government (1990 Clean Air Act Amendments[1]) and the State of California[1] instituted 25% decreases in the permitted HC emission levels in the early 1990's. The California regulations required an additional reduction in fleet-averaged, new automobile HC emissions from 0.25 gm/mile NMHC in 1993 to 0.062 gm/mile NMOG in 2003.

The Federal Clean Air Act defines specific toxic exhaust species, which may be subject to future control (e.g. benzene, butadiene, formaldehyde, acetaldehyde). California will require that the reactivity of the emissions for smog formation (the Ozone Forming Potential), rather than total HC mass, form the basis of the regulations. To meet these species-specific requirements, concentrations of individual HC species in the exhaust must be measured, and the chemistry of the emissions process must be understood better.

The bulk of the FTP (Federal Test Procedure) emissions from current vehicles occur early in either a cold start or a warm restart before the catalytic converter reaches its minimum operating temperature.[2] Therefore, these start-up emissions are engine-out emissions, unaffected by the catalyst. The effects of fuel composition and engine operating conditions on engine-out HC emissions (both total and individual species) are the subjects of this presentation. Initially, sources of unburned hydrocarbon emissions will be presented. The effects of fuel composition, engine operating conditions, and air/fuel mixing on these emissions will then be discussed in the context of the ability to accurately predict HC emissions from vehicles.

SOURCES OF EXHAUST HCS

Oxidation in the combustion chamber is generally an efficient process with little HC escaping combustion during fuel-lean operation. Nonetheless, unburned fuel and fuel-derived combustion products are exhausted from engines, and this section examines major sources of these emissions.[3,4]

CREVICE VOLUMES - For all operating conditions, a principal source of HC emissions is storage of unburned fuel in crevice volumes around the piston rings (~5-7% of the intake charge). Because the entrances are narrow, the flame cannot enter these crevices, leaving the fuel in them unburned. This fuel leaves the crevices during the expansion stroke, and a large fraction of the stored HC (~50-90% depending upon operating conditions and fuel composition) is converted to CO or CO_2 in the hot burned gases within the cylinder or in the exhaust system. Thus, late cycle burn up of stored HCs affects both the total HC emissions and the concentrations of important partial combustion products such as olefins, butadiene, and benzene.

BULK GAS QUENCHING - When an engine runs fuel rich, the contributions of methane and acetylene in the exhaust rise rapidly.[5,6] These species are present in the core gas within the cylinder after flame propagation is complete. This occurs because the low level of oxygen in the post-flame gas slows the conversion of these intermediate combustion products to CO and CO_2. Incomplete combustion during marginal operation (i.e. very fuel lean or high exhaust gas recirculation) can also increase emissions of all HC species because the flame speed is too slow to complete fuel consumption within the cylinder during the power stroke. These sources are unrelated to crevice storage but are affected by late-cycle burn-up.

WALL WETTING BY FUEL - Another important exhaust HC source arises when liquid gasoline enters the combustion chamber and strikes its walls during cold start of a port-fuel-injected (PFI) engine, producing a fuel film which does not evaporate and burn completely during flame passage.[7] This can increase the total HC emissions early in a cold start relative to the emissions observed with prevaporized gasoline fuel, which minimizes wall wetting (see Figure 1). As the engine warms, the HC emissions from the two fueling techniques approach one another. Wall wetting increases the contribution of lower volatility species such as aromatics to the exhaust emissions. The HC emissions from this source are influenced by the design of the port, combustion chamber, and

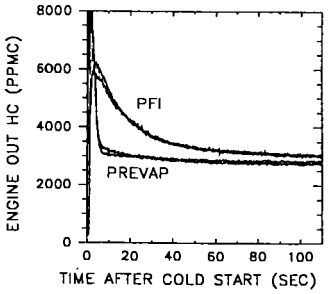

Figure 1. Total HC emissions vs time after cold start for PFI and prevaporized starts in a V8 engine.

injection system. Wall wetting does not contribute appreciably to HC emissions during warmed-up operation because fuel evaporation occurs more rapidly.

EXPERIMENT

To assess the effect of fuel composition on emissions of individual HC species, we have carried out a series of experiments in which the same single-cylinder engine was run at four operating conditions using single-component hydrocarbon fuels. The fuels tested span most classifications found in gasoline and several alternative hydrocarbon fuels: alkanes;[8] naphthenes;[9] olefins;[10] and aromatics.[8, 9, 10] Emissions from one gasoline and selected synthetic fuel mixtures were also measured[9, 10] providing information about interactions between fuel components.

A 475 cm^3, port-fuel-injected, single-cylinder engine with 9:1 compression ratio was used in these experiments. The head and piston have geometries typical of modern multi-cylinder engines. The engine was run at four steady-state conditions. The baseline condition was 10% fuel-lean, 1500 rpm, mid-load, optimum spark timing, and 90°C coolant temperature. Fuel injection took place onto a closed intake valve. Additional conditions studied were: 2500 rpm; retarded spark; or 15% fuel-rich with the other parameters as defined for baseline.

Total emissions were measured by a heated, flame ionization detector (HFID) connected to the exhaust pipe by a heated sample line. Samples were also taken for gas chromatographic (GC) analysis of HCs.[9] With the exception of benzaldehyde, MTBE, and methacrolein, oxygenated organics were not quantified. However, the measured hydrocarbon species account for approximately 90% of the organic emissions and atmospheric reactivity.

FUEL STRUCTURE EFFECTS ON TOTAL HC EMISSIONS

The total HC emissions vary with fuel structure as illustrated in Figure 2 for nine fuels even though nearly the same amount of fuel mass is stored within crevices for all fuels. The total exhaust HC emissions increase from 320 $ppmC_1$ [$ppmC_1 = \Sigma_i(ppm_i x \#carbons_i)$ for all exhaust species i] for ethylene fuel to ~2200 $ppmC_1$ for an aromatic blend (80% xylenes/ 20% ethylbenzene). Only a small portion of this increase arises because the carbon content of the inlet charge is 20% larger for the blend than for ethylene fuel as a result of the different H/C ratio. Similar trends in total HC emissions with fuel structure are observed for the other engine operating conditions.[8, 9, 10] Total HC emissions from olefinic fuels are lower than those from their paraffinic analogs in all cases.[10] The results in Figure 2 demonstrate that, during the exhaust stroke, burn up of fuel stored in crevices is affected by fuel structure and exerts a large influence on HC emissions.

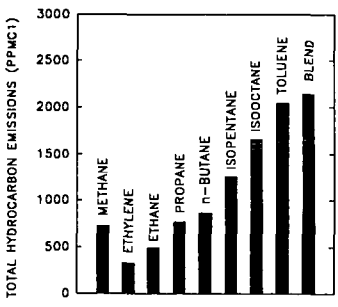

Figure 2. Effect of fuel structure on total HC emissions for nine fuels at baseline condition.

Table I. Exhaust composition as a percentage of total HC emissions for isooctane and toluene fuels.

	ISOOCTANE		TOLUENE	
exhaust species	base (%)	2500 (%)	base (%)	2500 (%)
methane	1.7	4.8	0.8	1.3
ethylene	3.5	9.3	0.8	3.0
propylene	8.9	13.7		
butadiene	0.5	0.9	0.3	n.a.
isobutene	22.9	25.3		
isooctane	46.5	21.7		
benzene	0.3	0.6	5.9	11.0
benz-aldehyde			5.0	7.3
toluene			80.0	63.9
total HC ($ppmC_1$)	2006	1207	2040	1320

Recent experiments[11] in which HC oxidation in the exhaust system was stopped by introducing a cold quench gas near the exhaust valve show that the fuel structure effect on total emissions occurs within the engine cylinder. Continuing oxidation in the exhaust system influences the individual HC species concentrations significantly and reduces the total emissions by ~40% for all fuels at baseline condition. These results illustrate the importance of burn up late in the engine cycle and in the exhaust system on HC emissions.

EXHAUST HC SPECIES

PARAFFINIC FUELS - Table I presents distributions of selected HC species (as a percentage of the total HC emissions) and the total HC emissions measured by the HFID for isooctane (2,2,4 - trimethylpentane) fuel operated at two steady-state conditions (base and 2500 rpm).[9] Although the concentrations of specific species depend on the fuel structure,

the trends shown by isooctane fuel are typical of other straight chain and branched chain alkanes.[8, 9, 10]

Increasing the engine speed results in a decrease in the percentage of unburned isooctane fuel (47% to 22%) in the exhaust, while the sum of the olefinic combustion products increases (43% to 56%). The total exhaust HC concentration decreases indicating an increase in burn-up of stored HCs, primarily because of higher exhaust temperatures. Similar trends with speed have been observed using a multi-cylinder engine[12] and on-road vehicles.[13]

The single cylinder engine results in Table I are similar to the species distributions obtained from two multi-cylinder engine experiments using pure isooctane fuel. In a 2.3 L 4-cylinder engine at baseline condition, [6] the contributions of the major HC species were: methane (1.5%); ethylene (6.3%); propylene (13.5%); isobutene (28%); isooctane (48%). Shore et al[12] determined distributions from a Fiat 4-cylinder engine at 2400 rpm: methane (7%); ethylene (11.1%); propylene (12.7%); isobutene (20.5%); isooctane (23.6%). The agreement of the data in refs. 6 and 12 with the base and 2500 rpm results in Table I, respectively, is reasonably good. This indicates that HC species distributions from very different engines operated under similar conditions can resemble one another, although they are not identical

Alkene emissions from alkane combustion can be explained qualitatively by known high temperature reactions of alkyl radicals (see ref. [10]), formed by H atom abstraction from fuel species. The primary reactions of these radicals are to break a C-C bond one removed from the free radical site (β C-C bond scission[14]) or a C-H bond, both forming alkenes.

AROMATIC FUELS - Table I also presents data for toluene fuel.[8, 10] For toluene as well as for the aromatic blend,[9] unburned fuel constitutes a much larger portion of the exhaust HC than for isooctane fuel and is the predominant species under all operating conditions. In addition, these experiments show that benzene, a toxic species, constitutes an appreciable fraction of the total emissions (6-11%) in contrast to isooctane fuel. This confirms that dealkylation of substituted benzenes is a significant source of benzene emission.

Table II. Exhaust composition as a percentage of the total HC emissions for cyclohexane and 1-hexene fuels.

	c-HEXANE		1-HEXENE	
exhaust species	base (%)	2500 (%)	base (%)	2500 (%)
methane	1.3	4.8	1.6	3.1
ethylene	23.3	31.7	24.1	37.5
propylene	5.2	6.0	11.0	12.4
butadiene	12.1	11.7	9.5	10.8
benzene	4.8	6.5	0.6	1.3
c-hexane	30.0	11.7		
c-hexene	6.2	4.0	0.5	0.5
1-hexene			36.9	12.5
total HC ($ppmC_1$)	1190	575	1110	400

OLEFINIC AND CYCLIC ALKANE FUELS - Table II presents selected species measured at base condition and at 2500 RPM for 1-hexene[10] and for cyclohexane[9] fuels. These types of fuels, which have no branching groups, produce large quantities of ethylene, (which is very reactive in the atmosphere), again by β C-C bond scission reactions.[9,10] In addition, they emit more 1,3-butadiene than any of the other fuels tested. It is interesting to note that cyclohexane fuel produces appreciable quantities of benzene in the exhaust. The concentration of benzene is approximately one half of that emitted by toluene fuel and 10x more than is present in the exhaust from isooctane.

ATMOSPHERIC REACTIVITY - The reactivity of individual exhaust HC species for forming photochemical smog varies widely. Olefins and highly alkylated aromatics can have reactivities 5-10 times larger than paraffinic fuels.[15] As discussed above, the distribution of HC species in the exhaust changes as the fuel type and engine operating conditions change. Thus, the atmospheric reactivity of the exhaust gas, which is an important factor in the California regulations, can change significantly, and engine operating strategies different from those used in meeting total HC standards may be required. Fuel structure and operating parameter effects on reactivity are complicated as has been discussed elsewhere.[16]

TOXIC EMISSIONS - The brief descriptions of the species emissions for selected examples of fuel components encountered in gasoline have demonstrated that each class of fuel produces a very characteristic distribution of species in the exhaust gas. Thus, control of the emission of specific species such as the toxic compounds defined in the Clean Air Act Amendments (e. g. benzene and 1,3-butadiene) can be achieved only after identifying the likely precursors of these emissions in gasoline. Benzene is formed in substantial quantity by toluene (5% of the total emissions at baseline condition). The xylene-ethylbenzene blend produces benzene emissions at a lower level (2.5% at baseline), and also generates appreciable toluene (3.7% at baseline).[9] Thus, these results show that reduction of benzene emissions can be achieved by reduction of aromatics in the fuel but that all alkyl-substituted benzene fuels do not produce the same amount of benzene in the exhaust.

1,3-Butadiene is a very characteristic emission from both cyclic alkane and terminal straight chain olefin fuels as shown in Table II and expanded upon in reference[10] (e.g. butadiene from

1-hexene fuel is 10% of the total emissions at baseline). Little butadiene (0.7% at baseline) is formed from a branched olefin such as diisobutylene or the paraffins n-butane (0.8%) or isooctane (0.5%). Thus, these experiments have clearly identified potential sources of butadiene emission from gasoline fuel.

Table III. Exhaust mole fraction ($ppmC_1$) of toluene for three engine operating conditions using pure toluene and a 53%/47% toluene-hexane mixture.

operating condition	toluene fuel	hexane/ toluene	predicted for mix[a]
base	1763	669	936
retarded spark	1215	408	645
fuel rich	2807	1292	1491

[a] Predicted toluene mole fraction using the measured exhaust toluene for toluene fuel scaled by the known (53.1%) amount of toluene in the mix.

ADDITIVITY OF FUEL COMPONENTS IN A MIXTURE - To predict HC emissions of fuel mixtures based on measured emissions from pure fuels, additivity of fuel components must be established. Ideally, if an engine is run on a 50/50 mixture of fuel components, the exhaust HC species emissions from each component would be one half of those from the pure fuel. In some cases, this is observed. As an example, when 20% diisobutylene (DIB) was added to gasoline, the emissions arising from DIB could be predicted well from the measured emissions from pure DIB and the known amount of DIB in the fuel mixture.[10] However, additivity is not always observed. Table III presents the mole fraction of toluene in the exhaust for two fuels: pure toluene; and a blend of toluene with n-hexane. Based on the measured mole fraction of toluene from the pure fuel at three engine operating conditions and the known amount of toluene in the mixture, predictions of the expected exhaust toluene emission can be made. It is evident that in this case, the prediction is not as accurate. In all cases, the exhaust toluene is predicted to be substantially larger than is observed. Therefore, addition of a more volatile fuel to toluene actually reduces the emissions from the toluene in the mixture. In another experiment, a very low volatility component (1,2,4-trimethyl benzene) was added to gasoline. In this case, the emissions of all components in the gasoline, including high volatility ones (e.g. isopentane), increased relative to expectation,[17] opposite to the result in Table III. Thus, it appears that if the vaporization characteristics of a fuel are changed by addition of another fuel component, the emissions may not follow a simple additivity relationship. Increasing the volatility decreases the emissions even of low volatility components. Decreasing the volatility increases the emissions even of high volatility components. In the DIB example, DIB has a volatility approximately equal to the mid-point of gasoline. Thus, the volatility of the mixture was not changed significantly from that of the base gasoline, and this may explain why additivity was observed. Similar conclusions were drawn during the AUTO/OIL Air Quality Improvement Research Program[18] in which it was observed that "the presence of heavy hydrocarbons in the fuel seems to increase the mass emissions of all unreacted fuel species of a given hydrocarbon class equally, regardless of boiling point." These Auto/Oil tests were performed on a wide variety of engine designs.

SUMMARY

In this presentation, the sources of hydrocarbon emissions have been discussed, showing the importance of crevice storage, in-cylinder wall wetting by fuel, and burn-up of stored fuel late in the engine cycle in determining both total emissions and the distribution of individual species. Engine operating conditions influence exhaust HC emissions. Conditions that result in higher in-cylinder or exhaust temperatures (e.g. higher speed or retarded spark timing) result in reduced total HC emissions accompanied by an increase in the importance of partial oxidation products such as olefins. The volatility of the fuel can affect emissions of all components in a gasoline. These observations indicate that the emissions process is a complicated one that will be difficult to model with accuracy for any given vehicle. However, the experiments summarized above show that the sources of particular exhaust gas species can be evaluated effectively by pure fuel experiments. Thus, benzene is formed from substituted aromatic fuel components and from cyclic alkanes. Terminal, straight-chain olefins and cyclic alkanes form substantial amounts of butadiene. While cyclic alkanes are not normally present in large quantity in gasoline and the concentrations of olefins are being reduced, particularly in California, it is important to understand the emissions properties of all types of gasoline fuel components to avoid changing gasoline formulation in ways that will be detrimental to the environment. It is also critical to understand the effect of engine calibration (speed, spark timing, fuel/air ratio, etc) on the hydrocarbon emissions process in order to most efficiently meet government regulations, whether they are based on total HC mass or on atmospheric reactivity.

REFERENCES

1. Chang, T. Y., Chock, D. P., Hammerle, R. H., Japar, S. M., and Salmeen, I. T., Critical Reviews in Environmental Control 22, 27 (1992).
2. Kelly, N. A., and Groblicki, P. J., J. Air Waste Manage. Assoc. 43, 1351 (1993).
3. Kaiser, E. W., Siegl, W. O., and Anderson, R. W. Soc. Auto. Eng. Tech. Pap. No. 941960 (1994).
4. Cheng, W. K., Hamrin, D., Heywood, J. B., Hochgreb, S., Min, K., and Norris, M., Soc. Auto. Eng. Tech. Pap. 932708 (1993).
5. Dempster, N. M., and Shore, P. R., Soc. Auto. Eng. Tech. Pap. 900354 (1990).
6. Kaiser, E. W., Rothschild, W. G., and Lavoie, G. A., Comb. Sci. Technol. 32, 245 (1983).
7. Kaiser, E. W., Siegl, W. O., Lawson, G. P., Connolly, F. T., Cramer, C. F., Dobbins, K. L. Roth, P. W., and Smokovitz, M., Soc. Auto. Eng. Tech. Pap. 961957 (1996).
8. Kaiser, E. W., Siegl, W. O., Henig, Y. I., Anderson, R. W., and Trinker, F. H., Environmental Science and Technology 25, 2005 (1991); corr. ibid. 26, 2618 (1992).
9. Kaiser, E. W., Siegl, W. O., Cotton, D. F., and Anderson, R. W., Environmental Science and Technology 26, 1581 (1992).
10. Kaiser, E. W., Siegl, W. O., Cotton, D. F., and Anderson, R. W., Environmental Science and Technology 27, 1440 (1993).
11. Drobot, K., Cheng, W. K., Trinker, F. H., Kaiser, E. W., Siegl, W. O., Cotton, D. F., and Underwood, J., Combustion and Flame 99, 422 (1994).
12. Shore, P. H., Humphries, D. T., and Haddad, O. Soc. Auto. Eng. Tech. Pap. 930373 (1993).
13. Bailey, J. C., Schmidl, B., and Williams, M. L., Atmospheric Environment 24A, 43 (1990).
14. Dryer, F. L., and Glassman, I. Progress Astronaut. Aeronaut. 62, 255 (1979).
15. Carter, W. P. L., J. Air and Waste Manage. Assoc 44, 881 (1994).
16. Kaiser, E. W., and Siegl, W. O., J. High Resolution Chromatography 17, 264 (1994).
17. Kaiser, E. W., Siegl, W. O., and Russ, S. G. Soc. Auto. Eng. Tech. Pap. 952542 (1995).
18. Leppard, W. , Benson, J., Gorse, R., Knepper, J., Rapp, L., Burns, V., Hochhauser, A., Koehl, W., and Reuter, R., Soc. Auto. Eng. Pap. 932725 (1993).

TOXICITY EVALUATION OF GASOLINE EXHAUST EMISSIONS.

Robert. A. Barter
Health and Environmental Sciences Department
American Petroleum Institute
Washington, D.C. 20005.

INTRODUCTION

The health effects of gasoline exhaust was examined previously in two animal toxicology studies (Brightwell et al., 1986a, 1986b, 1989; Heinrich et al., 1986). These studies were part of larger efforts examining the health effect of gasoline or diesel exhausts. The Brightwell study examined the systemic and pulmonary toxicity and carcinogenicity in rats and hamsters of engine-out (uncatalyzed) and tailpipe (catalyzed) exhaust emissions from engines burning unleaded gasoline. Two studies by Heinrich examined the subchronic and chronic toxicity and carcinogenicity in rats and hamsters of engine-out exhaust emission using leaded gasoline.

The results of Brightwell and Heinrich studies provide no evidence that gasoline engine exhaust is an animal carcinogen. The strongest dose-response and time-response relationships observed in these studies were linked to carbon monoxide (CO) exposure. The authors of these reports speculated that the respiratory and histopathological changes of the lung were associated with nitrogen oxides (NOx), CO or lead particulate. Although some uncertainty exists in this analysis, the lesions that were observed are typical of these toxicants. It is well known that CO has marked effects on hematological and cardiac indices (USEPA, 1991). Nitrogen oxides are known to adversely affect the respiratory tract (USEPA, 1993). Thus, although Brightwell and Heinrich speculated on these findings, this hypothesis appears reasonable based on the known toxicity of CO and NOx.

Automotive gasoline composition has changed since the time these studies were conducted. Oxygenated winter fuel (oxyfuel) and reformulated gasolines (RFG) were introduced in areas of CO or CO and ozone nonattainment, respectively, in the 1990s. These fuels differ from regular gasoline by the addition of an oxygenate to promote a more efficient combustion of fuel. Oxygen content of RFG and oxyfuels are be 2.0 and 2.7 wt. percent, respectively resulting in 8 to 17 volume percent of gasoline depending on the oxygenate. With the introduction of these fuels into the marketplace, there has been concern regarding the toxicity of the combustion emissions of these fuels.

Components of automotive engine exhaust have been characterized. The Auto/Oil Air Quality Improvement Research Program (AQIRP) developed an extensive database on the level and composition of exhaust and evaporative emissions from up to 20 well-maintained model year 1989 cars and light trucks operated on industry average gasoline (RFA), and gasoline blended with the oxygenates methyl-tertiary-butyl ether (MTBE), ethanol (EtOH) and ethyl-tertiary butyl ether (ETBE). From the AQIRP speciation data, extrapolations can be made to determine if the toxicity of gasoline exhaust emissions has changed, and if further animal toxicology testing will to characterize gasoline exhaust toxicology will provide additional information from that which can be inferred from the above studies.

METHODS

Two sets of data from AQIRP were used for this paper. AQIRP Pilot Study includes both engine-out and tail-pipe exhaust measurements of 156 hydrocarbon and oxygenated species sampled and composited over three phases of the FTP driving cycle. The Phase I Working Data Set includes exhaust tailpipe measurements of 156 hydrocarbon and oxygenated species, sampled and composited over three phases of the FTP driving cycle. Detailed descriptions of the data in these two data sets are presented in technical papers contained in SAE Publication SP-920, *Auto/Oil Air Quality Improvement Research Program,* February 1992.

AQIRP data (g/mile) can be used to estimate concentrations in an inhalation toxicology study (ppm) by developing a molar ratio between a particular hydrocarbon species and CO. As CO will be the limiting exhaust component, hydrocarbon/CO molar ratio can be

multiplied by the fixed concentration of CO to produce the estimated exposure concentration of hydrocarbon. The conversion is illustrated in the equation below.

$$\left(\frac{\left([HC_{exh}] \div HC\,mol.wt.\right)}{\left([CO_{exh}] \div CO\,mol.wt.\right)}\right) \times \left[CO_{exp\,chamb}\right] = \left[HC_{exp\,chamb}\right]$$

Where $[HC_{exh}]$ is the measured concentration in mg/mile of a hydrocarbon species from Auto/Oil; HC mol. wt. is the molecular weight for a given hydrocarbon species; $[CO_{exh}]$ is the measured concentration in mg/mile of carbon monoxide from Auto/Oil; CO mol. wt. is the molecular weight of carbon monoxide; $[CO_{exp\ chamb}]$ is the expected chamber concentration of carbon monoxide set at 200 ppm; and $[HC_{exp\ chamb}]$ is the expected animal exposure chamber concentration of a particular hydrocarbon species in ppm.

The entire speciated exhaust component data sets were converted. As noted above the expected chamber concentration of CO was set at 200 ppm based on a large number of toxicity endpoints (developmental and systemic) following review of the health effects of CO. The expected exposure concentrations from the converted AQIRP data were compared to exposure concentrations from previous studies.

Toxicology databases were searched to determine No Observable Effect Levels (NOELs) for exhaust components derived from animal toxicity studies. NOELs represent exposure concentrations at which no effects were observed in an animal toxicity study. NOELs were compared to expected exposure concentrations from the converted AQIRP data. Only a few representative exhaust components are presented due to space limitations.

RESULTS

Based on a dose limiting concentration of 200 ppm for CO, the expected chamber concentrations of CO, CO_2, NOx and total hydrocarbon can be extrapolated from AQIRP data using the equation listed above (Table 1). These data demonstrate that for a CO concentration of 200 ppm, total hydrocarbon concentrations will be approximately 70 ppm for RFA gasoline. These data are similar to data obtained in the Brightwell and Heinrich studies, which also are listed in this table.

Hydrocarbon speciation data from the Brightwell study can be directly compared to extrapolated data from AQIRP (Table 2). The extrapolated AQIRP data have been converted from ppm to mg/m^3 to make a direct comparison to Brightwell data easier. The extrapolated data is not directly comparable as the Brightwell data is the average and range of ten measurements on one vehicle over the course of two years, and AQIRP data is the average and range of two FTP tests for three vehicles. However, it is apparent that the expected concentrations for individual hydrocarbons is similar to what was actually measured in the Brightwell study.

Comparison of extrapolated animal exposure concentrations of hydrocarbon species for RFA and oxygenated fuel mixtures MTBE, EtOH or ETBE gasoline (Table 3) indicates that the addition of oxygenate to gasoline produces minor alterations in the composition of gasoline exhaust. As seen with the engine-out data, parent oxygenate was observed in the exhaust stream, at concentrations of approximately 1 ppm. Additionally, the concentration of aldehydes was increased with the addition of oxygenate, most notably formaldehyde and acetaldehyde. The remaining hydrocarbon species are not affected greatly by addition of oxygenate.

Extrapolated animal exposure concentrations of speciated exhaust components are compared to these components NOELs in Table 4. The comparison indicates that the exposure concentrations will be well below the observable effects level for all components.

DISCUSSION

Extrapolation of the AQIRP data indicate that total hydrocarbon concentrations will be low in animal exposures using RFA gasoline. These data also indicate the hydrocarbon exposure levels will be similar to the levels observed in the previous gasoline engine exhaust toxicology studies, where only CO and/or NOx effects were observed.

Small analytical differences in speciated exhaust components do exist between the extrapolated AQIRP data for gasoline and gasoline with MTBE and the speciated data measured in the Brightwell study. However, the composition of the exhaust atmosphere between the two data sets are fairly similar. This is not entirely surprising since the specifications for the fuel used in the Brightwell study are similar to the specifications for RFA used in AQIRP. Thus, results observed in the Brightwell study appear to be applicable to exhaust emissions generated from RFA and gasoline with MTBE. Further, although there are slight analytical differences the anticipated animal exposure atmospheres for the different reformulated fuels, exposures to exhaust components in toxicology studies on reformulated or oxygenated fuels will be fairly similar to the exposures in the Brightwell study. Thus, it can be concluded that addition of oxygenate does not dramatically alter the subsequent composition of an animal exposure to gasoline engine exhaust. Therefore, the Brightwell study results can be used to evaluate the health effects of engine exhaust from oxygenated gasolines.

Comparison of anticipated animal exposure levels and NOELs for exhaust components indicates no adverse effects are likely to be observed. Dilution of engine exhaust to reduce CO toxicity provides an inherent safety facto for the hydrocarbon component of exhaust. At 200 ppm CO it is unlikely that hydrocarbon effects will be observed as the anticipated exposure levels are well below the NOELs for these compounds. Doubling the CO concentration to 400 ppm will not sufficiently increase the hydrocarbon concentration above the NOEL fot the individual hydrocarbons.

CONCLUSION

Although slight analytical differences exist in exhaust HC compositions for different oxygenated fuel blends, the likelihood of discerning differences in the toxicity of HC exhaust emissions from different gasoline blends is small.

REFERENCES

Brightwell, J. Fouillet, X., Bernstein, D., Crawley, F. Duchosal, F., Gatz, R., Perczel, S., and Pfeifer, H. (1986a). Investigation into the possible toxicological and carcinogenic effects of diesel and gasoline engine exhaust emissions (Long term tests). Final Report. Battelle, Geneva, Switzerland.

Brightwell, J. Fouillet, X., Cassano-Zoppi, A.L., Gatz, R., and Duchosal, F. (1986b). Neoplastic and functional changes in rodents after chronic inhalation of engine exhaust emissions. In *Carcinogenic and Mutagenic Effects of Diesel Engine Exhaust*, (N. Ishinishi, A. Koisumi, R.O. McClellan and W. Stober, Eds.), pp 471-485. Elsevier Science Publishers B.V. New York, NY.

Brightwell, J. Fouillet, X., Cassano-Zoppi, A.L., Bernstein, D., Crawley, F. Duchosal, F., Gatz, R., Perczel, S., and Pfeifer, H. (1989). Tumors of the respiratory tract in rats and hamsters following chronic inhalation of engine exhaust emissions. *J. Appl. Toxicol.* **9**, 23-31.

Burns, V.R., Ingham, M.C., and Doherty, H.M. (Eds.). (1992). *Auto/Oil Air Quality Improvement Research Program (SP-920).* Society of Automotive Engineers, Inc., Warrendale, PA.

US Environmental Protection Agency. (1991). Air Quality Criteria for Carbon Monoxide. Research Triangle Park, NC: Office of Health and Environmental Assessment, Environmental Criteria and Assessment Office; EPA report no. EPA-600/8-90-045F.

US Environmental Protection Agency. (1993). Air Quality Criteria for Oxides of Nitrogen. Research Triangle Park, NC: Office of Health and Environmental Assessment, Environmental Criteria and Assessment Office; EPA report no. EPA-600/8-91-049aF.

Heinrich, U., Peters, L., Mohr, U., Bellman, B., Fuhst, R., Ketkar, M.B., Konig, J. Konig, H., and Pott, F. (1985). Studies of the subacute and long-term effects of gasoline engine exhaust gases. 107 06 015/106 06 04. Franhofer Institute for Toxicology and Aerosol Research. Hannover, Germany.

Table 1
Extrapolated and Measured Combustion Gas Concentrations (ppm)

Compound	AQIRP	Brightwell	Heinrich
CO	200	224	305
Total Hydrocarbon	68	61	36.5[1]
NO_x	32	49	23[2]
CO_2	4200	6000	4000

[1] Non-methane hydrocarbon
[2] Measured as NO

Table 2
Concentration of Selected Hydrocarbons From Measured and Extrapolated Data

	Brightwell	AQIRP Pilot Study	
Fuel Type	California	Baseline Gasoline	Gasoline with MTBE
Units	mg/m^3	mg/m^3	mg/m^3
Compound	Range (Average)	Range (Average)	Range (Average)
Methane	1.90 - 4.94 (2.96)	1.00 - 1.08 (1.03)	1.02 - 1.14 (1.09)
Benzene	0.45 - 2.26 (1.39)	1.27 - 1.53 (1.39)	1.13 - 1.26 (1.20)
Toluene	2.59 - 6.86 (4.1)	2.00 - 2.10 (0.82)	1.36 - 1.51 (1.45)
Formaldehyde	0.104 - 0.590 (0.308)	0.48 - 1.15 (0.82)	0.71 - 1.03 (0.91)
Acetaldehyde	0.073 - 0.297 (0.148)	0.20 - 0.35 (0.26)	0.20 - 0.29 (0.24)
MTBE			1.65 - 2.16 (1.95)

Table 3
Expected Hydrocarbon Chamber Concentration (ppm) for Baseline Gasoline, Gasoline/MTBE, Gasoline/EtOH, Gasoline/ETBE at 200 ppm CO

Hydrocarbon	Gasoline	Gasoline/MTBE	Gasoline/EtOH	Gasoline/ETBE
Methane	1.57	1.72	1.71	1.71
Toluene	0.71	0.75	0.68	0.72
Formaldehyde	0.55	0.49	0.41	1.35
Benzene	0.33	0.34	0.32	0.44
13-Butadiene	0.17	0.20	0.18	0.20
Acetaldehyde	0.14	0.15	0.29	0.43
E-Benzene	0.13	0.13	0.12	0.15
o-Xylene	0.09	0.09	0.08	0.10
ETBE	0.02	0.02	0.02	1.22
MTBE	0.00	1.24	0.00	0.00
EtOH	0.00	0.00	1.35	0.00

Table 4
Comparison of NOELs and Expected Chamber Concentration for Selected Hydrocarbons

Compound	Chamber Conc. (ppm)	NOEL[1] (ppm)	Endpoint	Species	NOEL to Exposure Ratio
Formaldehyde	0.580	15 mg/kg[2] 74 mg/kg[2]	Systemic Developmental	rat rat	
Acetaldehyde	0.145	150	Systemic	rat	1000
1,3-Butadiene	0.351	6.25[3]	Reproductive	mouse	18
Benzene	0.436	10 300 30 300	Developmental Reproductive Reproductive Neurological	rat rat mouse mouse	23 700 70 700
Toluene	0.545	56 500 750	Neurological Reproductive Developmental	rat rat rat	100 1000 1400
m- and *p*-Xylene	0.407	99 250 1000	Neurological Developmental Reproductive	rat rat rat	240 600 2500
Ethylbenzene	0.188	100 100	Developmental Systemic	rat rat	500 500
MTBE	0.542	1000 1000 400	Reproductive Developmental Neurological	rat mouse rat	1900 1900 200
Ethanol	1.35	20,000	Developmental	rat	15,000
ETBE	1.22	500	Neurological	rat	400

[1] No Observable Effect Level
[2] Oral Exposure
[3] Low Observable Effect Level

PREDICTING THE TOXICITY OF GASOLINE VAPORS BASED ON KNOWLEDGE OF FUEL COMPONENTS

M. A. Medinsky
Chemical Industry Institute of Toxicology,
Research Triangle Park, North Carolina 27709

ABSTRACT

The toxicity of chemicals in mixtures such as gasoline may differ greatly from that observed when the chemicals are tested as pure compounds. For example, metabolic activation is the critical first step in the development of toxicity after exposure to benzene. Gasoline components inhibit benzene metabolism and thus reduce benzene's toxicity. The extent to which inhibition occurs depends on the gasoline vapor composition and inhaled concentration. Gasoline vapors vary in inhibitory effects based on the aromatic content of the mixture. Additionally, metabolic inhibition is dependent on concentration, with inhibition increasing with increasing concentration. The challenge in estimating the effect of gasoline components on the inhibition of benzene metabolism is to determine the shape of the concentration-inhibition function.

INTRODUCTION

Benzene is a ubiquitous industrial and environmental pollutant (Runion and Scott, 1985). It is present in automobile emissions, both evaporative and combustive, and has been detected in cigarette smoke (Wallace, 1990; Wallace and Pellizzari, 1986). Exposure to benzene is most likely associated with coexposure to other volatile organic chemicals normally present in the environment.

Benzene is myelotoxic and carcinogenic at high concentrations. Epidemiology studies have shown that people develop blood dyscrasias, such as pancytopenia, aplastic anemia, and acute myelogenous leukemia following repeated exposure to high concentrations of benzene (Goldstein, 1977; Rinsky et al., 1987). Cytogenetic damage has been observed in humans who have developed benzene-associated hemopathies, especially leukemia (Huff et al., 1989). This correlation between cytogenetic damage in leukemia suggests that cytogenetic alterations in bone marrow cells may be a good marker for genetic alterations in bone marrow stem cells that precede the development of leukemia.

Benzene is not thought to be a direct-acting agent in the bone marrow, but rather is converted to bioactive metabolites (in the liver) which cause myelotoxicity (Irons, 1985; Eastman et al., 1987; Barale et al., 1990). The metabolism of benzene involves a series of oxidations of the benzene ring by cytochrome P450 monooxygenases (Figure 1). After absorption into the blood and translocation to the liver, benzene is metabolized by cytochrome P450 2E1 to its major metabolite, phenol (Figure 1; Smith et al., 1989). Phenol is be further oxidized by the same cytochrome P450 to the polyhydroxylated metabolite, hydroquinone (Koop et al., 1989; Schlosser et al., 1993). Both phenol and hydroquinone can translocate in the blood to the bone marrow where they interact with critical blood cell components. Alternatively phenol and hydroquinone are detoxified by Phase II conjugating enzymes such as sulfotransferases and glucuronyl transferases. Muconaldehyde, a reactive metabolite of benzene, is also thought to be formed by a two step oxidation of benzene although the mechanism and isozyme involved are unknown.

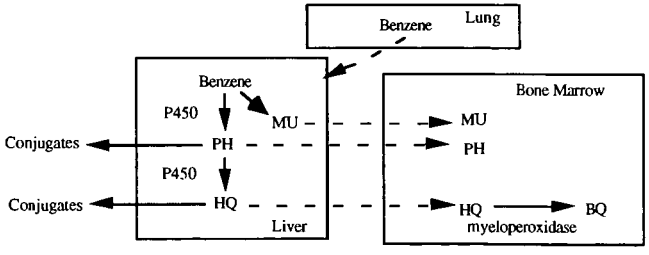

Figure 1. Metabolic scheme for benzene and its major metabolites. BQ = Benzoquinone, HQ = Hydroquinone, PH = Phenol, MU = Muconaldehyde

INTERACTIONS WITH OTHER VOLATILE ORGANICS

The multiplicity of benzene's metabolic pathways provides opportunities for modulation of benzene metabolism, either by competition with other organic chemicals for available

enzyme sites, by induction or inhibition of the oxidation or conjugation enzymes, or by direct competition among benzene and its metabolites for enzyme sites. Other volatile organics can modulate the toxicity and metabolism of benzene. Gad-El-Karim et al. (1984) investigated the genotoxicity of benzene in mice treated orally with benzene or combinations of benzene and toluene. Benzene alone was clastogenic to bone marrow cells and elevated numbers of micronucleated polychromatic erythrocytes (micronuclei, MN) were detected in mice receiving benzene compared with controls. When both benzene and the aromatic hydrocarbon, toluene, were coadministered, the clastogenic effect of benzene was reduced considerably. Similar results were noted when chromosomal aberrations were analyzed. These investigators hypothesized that toluene inhibited the metabolism of benzene and that one or more metabolites of benzene were responsible for the myeloclastogenic effects.

Andrews et al. (1977) used incorporation of ^{59}Fe into maturing red blood cells to evaluate the effects of benzene on erythropoiesis. Mice were given injections of benzene alone or combinations of benzene plus toluene. In parallel studies, the effect of toluene on the pharmacokinetics of benzene and its metabolites was also investigated. Coadministration of toluene and benzene resulted in reduction in the quantity of benzene metabolites measured in urine compared with the benzene-only exposed group. Unmetabolized benzene was exhaled. Coexposure to toluene also counteracted the benzene-induced reduction in ^{59}Fe uptake. Thus, toluene both reduced benzene metabolism and protected against benzene-induced suppression of iron utilization by red cells. The concentration of benzene in bone marrow was similar in mice given only benzene compared with mice given benzene and toluene. In contrast, concentrations of benzene metabolites in bone marrow of mice given benzene alone were much higher than those found when benzene was coadministered with toluene. In summary, the observation that toluene reduced both the level of benzene metabolites and the inhibition of iron uptake suggests that metabolism of benzene is closely related to its hematotoxicity. Toluene protects against benzene-induced hematotoxicity by reducing the level of benzene metabolites in bone marrow through suppression of benzene metabolism.

Mutual metabolic suppression between benzene and toluene also occurs in people. For example, Inoue et al. (1988) examined both the exposure concentration during a workshift and the benzene metabolite concentrations in urine of male Chinese workers exposed to either benzene, toluene, or a mixture of both chemicals. Urinary levels of the benzene metabolites phenol and hydroquinone were lower in the workers exposed to both toluene and benzene compared with those exposed to benzene alone. The investigators hypothesized that biotransformation of benzene to its hydroxylated metabolites in people is suppressed by coexposure to toluene.

Gasoline, one important source of environmental exposure to benzene, also contains toluene and other aromatic and aliphatic hydrocarbons such as xylene and hexane. These hydrocarbons could inhibit benzene metabolism. Travis et al. (1992) examined the effect of coexposure to gasoline vapor on the metabolism of benzene. Coexposure to gasoline vapors increased the maximum rate for benzene metabolism and decreased the apparent affinity of the enzyme for benzene. Generally, enzymatic inhibition is associated with a decrease in the maximum rate and an increase in the apparent affinity. Thus, the results of this study are in contrast with the demonstration of the inhibition of benzene metabolism by toluene previously reported by these investigators using a similar experimental system (Purcell et al., 1990). Clearly more research on the interaction of benzene with gasoline components is necessary to adequately assess the potential human health risks for this environmentally important mixture.

MODEL SIMULATIONS OF BENZENE-GASOLINE INTERACTIONS

Figures 2 and 3 show the results of physiologically-based pharmacokinetic model simulations of four different benzene-gasoline exposure scenarios. Figure 2 assumes that the major gasoline components are aromatic chemicals. Figure 3 assumes that the major gasoline components are aliphatic chemicals. Simulations in the A panels are for an exposure to gasoline at the threshold limit value (300 ppm) and simulations in the B panels are for an exposure at 2000 ppm, the concentration used in the chronic toxicity studies with unleaded gasoline. Comparison of simulations for the aromatic and aliphatic volatiles at the high doses (Panel B) compared with the lower dose (Panel A) demonstrates the dose dependence of inhibition by gasoline components on benzene metabolism. Less benzene is metabolized (more inhibition) at the higher (B) compared with the lower (A) dose. This can be determined by comparing the differences for the simulations for benzene alone to benzene plus other volatiles for each figure. At the low dose, the difference is small; at the high dose, the difference is large.

A comparison of the relative effect of gasoline vapor composed primarily of aromatics to that composed primarily of aliphatics can be seen by comparing results of model simulations at the low dose (Figures 2A and 3A). The aromatic chemicals appear to be better inhibitors of benzene at this lower concentration than do aliphatics. Again, this can be seen by the difference in the predicted benzene metabolized when benzene is given alone compared with the predictions when benzene plus other volatiles are given. The results of these simulations suggest that the scientific answer to the question, "Does gasoline inhibit benzene metabolism?", is that inhibition depends both on dose and on chemical composition.

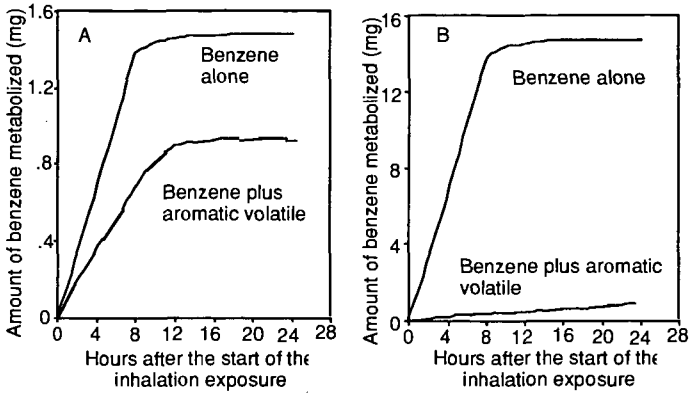

Figure 2. Model simulations for the effect of aromatic volatiles on the metabolism of benzene by one mouse after an 8-hr exposure to (A) 300 ppm of aromatics together with 5 ppm benzene or to a 5 ppm benzene exposure only or to (B) 2000 ppm of aromatics together with 40 ppm benzene or to a 40 ppm benzene exposure only.

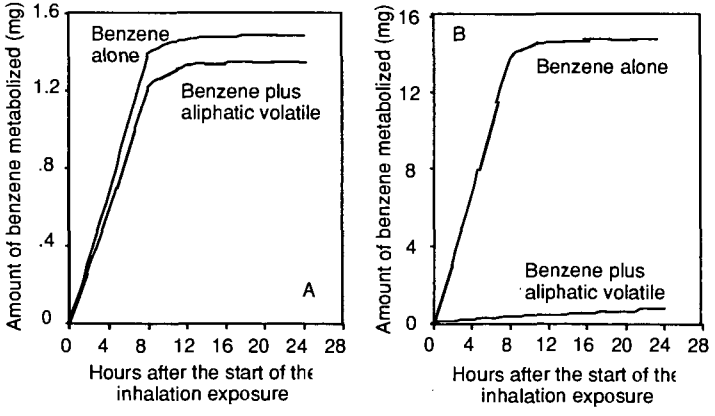

Figure 3. Model simulations for the effect of aliphatic volatiles on the metabolism of benzene by one mouse after an 8-hr exposure to (A) 300 ppm of aliphatics together with 5 ppm benzene or to a 5 ppm benzene exposure only.or to (B) 2000 ppm of aliphatics together with 40 ppm benzene or to a 40 ppm benzene exposure only.

CONCLUSIONS

There are two major factors that influence the potential interaction of benzene and gasoline components. These issues relate to the composition of the gasoline vapor and the inhaled concentration (or dose) of the vapor. Some components of gasoline may be better inhibitors of benzene metabolism than are others. The aromatic components, such as xylene and toluene, may be more effective competitors against benzene for active enzyme sites by nature of their greater solubility in tissues compared with benzene. Concentrations of these chemicals might be higher in the metabolizing organs such as liver and therefore these aromatics might be better able to compete with the benzene for active metabolic sites.

The fractional composition of volatile gasoline components changes with increasing vaporization temperature. Of most importance is the composition of the vaporized fuel relative to the whole gasoline. With increasing temperature, the aliphatic volatile organics make up an increasing percentage of the total percent of the gasoline organics and the aromatics become a decreasing percent. The scientific question relevant for risk assessment relates to the range of composition of vapors that people are likely to be exposed to when using gasoline.

Inhibition of one chemical on the metabolism of another is typically a dose-dependent phenomenon. At very high doses, inhibition can approach 100%. At very low doses, inhibition may be insignificant. The challenge in estimating the effect of gasoline components on the inhibition of benzene metabolism is to determine the shape of the concentration-inhibition function. The added complexity is that the shape of the benzene concentration-target tissue dosimetry function is also highly nonlinear. In actuality, it is not just the effect of gasoline components on the total benzene metabolized that must be addressed, but also the effect of possible inhibition of the formation of oxidized metabolic products such as hydroquinone.

ACKNOWLEDGMENTS

Research supported in part by the American Petroleum Institute.

REFERENCES

Andrews, L.S., Lee, E.W., Witmer, C.M., and Kocsis, J.J., and Snyder, R. (1977) Effects of toluene on the metabolism, disposition and hemopoietic toxicity of [^{3}H]benzene. Biochem Pharmacol, 26: 239-300.

Barale, R., Marrazzini, A., Betti, C., Vangelisti, V., Loprieno, N. and Barrai, I. (1990) Genotoxicity of two metabolites of benzene: phenol and hydroquinone show strong synergistic effects *in vivo*. Mutat Res, 244: 15-20.

Eastmond, D.A., Smith, M.T., and Irons, R.D. (1987) An interaction of benzene metabolites reproduces the myelotoxicity observed with benzene. Toxicol Appl Pharmacol, 91: 85-95.

Gad-El Karim, M.M., Harper, B.L., and Legator, M.S. (1984) Modifications in the myeloclastogenic effect of benzene in mice with toluene, phenobarbital, 3-methylchloranthrene, Aroclor 1254 and SKF-525A. Mutat Res, 135: 225-243.

Goldstein, B.D. (1977) Hematotoxicity in humans. J Toxicol Environ Health, Suppl 2: 69-105.

Huff, J.E., Haseman, J.K., DeMarini, D.M., Eustis, S., Maronpot, R.R., Peters, A.C., Persing, R.L., Chrisp, C.E., and Jacobs, A.C. (1989) Multiple-site carcinogenicity of benzene in Fischer 344 rats and B6C3F1 mice. Environ Health Perspect, 82: 125-163.

Inoue, O., Seiji, K., Watanabe, T., Kasahara, M., Nakatsuka, H., Yin, S., Li, G., Cai, S., Jin, C., and Ikeda, M. (1988) Mutual metabolic suppression between benzene and toluene in man. Int Arch Occup Environ Health, 60: 15-20.

Irons, R.D. (1985) Quinones as toxic metabolites of benzene. J Toxicol Environ Health, 16: 673-678.

Koop, D.R., Laethem, C.L., and Schnier, G.G. (1989) Identification of ethanol-inducible P450 isoenzyme 3a (P4502E1) as a benzene and phenol hydroxylase. Toxicol Appl Pharmacol, 98: 278-278.

Purcell, K.J., Cason, G.H., and Gargas, M.L. (1990) *In vivo* metabolic interaction of benzene and toluene. Toxicol Lett, 52: 141-152.

Rinsky, R.A., Smith, A.B., Hornung, R., Filloon, T.G., Young, R.J., Okun, A.H., and Landrigan, P.J. (1987) Benzene and leukemia, and epidemiological risk assessment. N Engl J Med, 316: 1044-1050.

Runion, H.E., and Scott, L.M. (1985) Benzene exposure in the United States 1978-1983: An overview . Am. J. Ind. Med., 7, 385-393.

Schlosser, P.M., Bond, J.A., and Medinsky, M.A. (1993) Benzene and phenol metabolism by mouse and rat liver microsomes. Carcinogenesis, 14: 2477-2486.

Smith, M.T., Yager, J.W., Steinmetz, K.L., and Eastmond, D.A. (1989) Peroxidase-dependent metabolism of benzene's phenolic metabolites and its potential role in benzene toxicity and carcinogenicity. Environ Health Perspect, 82: 23-29.

Travis, C.C., Fox, M.T., Simmons, W.M., and Lyon, B.F. (1992) Co-exposure to gasoline vapor decreases benzene metabolism in Fischer-344 rats. Toxicol Lett, 62: 231-240.

Wallace L. (1990) Major sources of exposure to benzene and other volatile organic chemicals. Risk Anal., 10 59-64.

Wallace, L.A., and Pellizzari, E.D. (1986) Personal air exposures and breath concentrations of benzene and other volatile hydrocarbons for smokers and non-smokers. Toxicol Lett, 35: 113-116.

HEALTH RESEARCH DIRECTIONS FOR NEW FUELS.

J. Michael Davis
National Center for Environmental Assessment-RTP (MD-52)
U.S. Environmental Protection Agency
Research Triangle Park, NC 27711

INTRODUCTION

Throughout much of the twentieth century, the general population has been routinely exposed to conventional gasoline and its evaporative and combustion emissions. However, with the introduction of new fuel additives and formulations, attention has become focused in recent years on the potential for public health impacts from widespread exposure to motor vehicle fuels. The Clean Air Act required the Administrator of the U.S. Environmental Protection Agency (EPA) to promulgate requirements for testing the health effects of evaporative and combustion emissions of fuels and fuel additives (F/FAs). The Fuels and Fuel Additives Rule, promulgated on May 27, 1994, established new health testing requirements for the registration of designated F/FAs, organized within a three-tier structure. Tier 1 requires F/FA manufacturers to perform a literature search on the health and welfare effects of F/FA emissions and to characterize F/FA emissions. Tier 2 requires toxicological testing by subchronic inhalation exposure and designated assays for specific health endpoints if adequate information is not already available. When necessary, Tier 3, which may include follow-up or additional studies, can be required.

Additionally, the rule includes a provision known as Alternative Tier 2, which gives EPA the flexibility to prescribe additional tests to be performed along with the standard Tier 2 program, to substitute different tests, and/or to modify the underlying vehicle/engine specifications for Tier 2. EPA may also use the Alternative Tier 2 authority to waive certain Tier 2 endpoint evaluations (generally on occasions when additional and/or more rigorous tests are being required for other Tier 2 endpoints). However, testing for Tier 2 endpoints may not be waived in the absence of adequate information or requirements for more rigorous testing.

At the time of this writing, EPA is about to issue proposed Alternative Tier 2 testing requirements for baseline (conventional) gasoline and various oxygenate-gasoline blends (collectively referred to here as "oxyfuels"), including methyl tertiary butyl ether (MTBE), ethyl tertiary butyl ether (ETBE), ethyl alcohol (EtOH), tertiary amyl methyl ether (TAME), diisopropyl ether (DIPE), and tertiary butyl alcohol (TBA). The primary objective of this testing program is to develop an information base that will support quantitative, comparative risk assessments of baseline and oxygenated gasolines. The risks, and benefits, of a given fuel are relative to its alternatives. Therefore, to determine whether a particular oxyfuel is better or worse than conventional gasoline or some other oxyfuel, comparable data must be available by which to evaluate the comparative risks. More extensive discussions of needed information and research relative to oxyfuels may be found in EPA's "Oxyfuels Information Needs" (U.S. Environmental Protection Agency, 1996) and other recent reports (e.g., Health Effects Institute, 1996; Interagency Oxygenated Fuels Assessment Steering Committee, 1996, 1997; National Research Council, 1996). This paper will explain the rationale underlying the proposed Alternative Tier 2 testing program and summarize key features of the program as an illustration of a scientifically sound and efficient approach for obtaining data needed for comparative risk assessment purposes.

RATIONALE FOR ALTERNATIVE TIER 2 TESTING REQUIREMENTS

To understand the rationale behind the Alternative Tier 2 testing program, one must first understand the purpose of standard Tier 2 requirements in the F/FA rule. Standard Tier 2 assessments include a basic subchronic inhalation toxicology study as well as tests to determine potential reproductive, developmental, neurotoxic, mutagenic, and carcinogenic effects (summarized in Table I). These assays, while sufficient for screening level evaluations of the toxicological effects of inhalation exposure to the emissions of designated F/FAs in test animals, were not intended necessarily to provide an adequate base for quantitative risk assessments. Rather, the intent was to provide for the collection of basic toxicological data that, along with information on exposure potential and other considerations, could guide decisions on whether or not more extensive toxicological evaluation would be required. If the results from standard Tier 2 assays indicated low toxicity for a particular F/FA and little potential for human exposure existed, then further testing would probably not be warranted. However, in the case of oxyfuels, a testing regimen that exceeds the standard screening requirements of Tier 2 is considered necessary and appropriate because of continuing uncertainties regarding the public health effects of gasoline and oxyfuels, and the widespread public exposure to these fuels and related emissions. This approach is clearly more cost-effective and time-efficient than simply requiring standard Tier 2 testing, waiting for the completion of such testing, and then

Table I. Fuel/Fuel Additive (F/FA) Rule Standard Tier 2 Tests

90-Day Subchronic Inhalation General Toxicity: Screening information on target organ toxicities and on concentrations useful for running chronic studies.

30 rodents per concentration per group (add specified numbers for different assessments combined with general toxicity); recovery group (N = 20) observed for reversible, persistent, or delayed effects

Observation (including body weight)
Clinical exams: hematology (e.g. Hct, Hb, RBC, DLC); clinical biochemistry (e.g., electrolyte balance, liver and kidney function, Ca-P-Cl-Na-K, glucose, BUN)
Ophthalmological exam
Urinalysis
Gross pathology
Histopathology (especially respiratory tract)

Fertility/Teratology: Information on potential health hazards to fetus and on gonadal function, conception, and fertility.

25 males, 40 females per group; mating after 9 weeks of exposure, then exposure of females continues through GD 15
Limit test (if no effects at highest concentration, then omit lower concentrations)

Observation for ≤13 weeks
Vaginal cytology
Mating and fertility
Gross necropsy (especially including reproductive organs)
Fetal anomalies, resorptions
Histopathology of reproductive organs

In Vivo Micronucleus: Detect damage to chromosomes or mitotic apparatus of cells (based on increase in frequency of micronucleated RBCs); provides information on potential carcinogenic and/or mutagenic effects.

5 females and 5 males per group
Positive control

In Vivo Sister Chromatid Exchange: Detect enhancement of exchange of DNA between two sister chromatids of a duplicating chromosome (using peripheral blood lymphocytes grown to confluence in cell culture); provides information on potential mutagenic and/or carcinogenic effects.

5 females and 5 males per group
Positive control

Neuropathology: Provides data on morphologic changes in central and peripheral nervous system.

N = 10 per group; N = 20 for reversible, persistent, or delayed effects
Positive control
Limit test (if no effects at highest concentration, then omit lower concentrations)

Observation (including body weight, movement disorders, etc.)
Brain size and weight; light (and possible electron) microscopy of sections
Peripheral nerve teasing

Glial Fibrillary Acidic Protein: An indicator of neurotoxicity associated with astrocytic hypertrophy at site of damage.

10 animals per group
Change in amount of GFAP for specific brain region as a function of treatment and dose

***Salmonella Typhimurium* Reverse Mutation:** Microbial assay that measures histidine (*his*) reversions (*his*$^-$ to *his*$^+$), which cause base changes or frame-shift mutations in the genome; provides data on mutagenicity.

Positive controls
Data presented as number of revertant colonies per plate, per kilogram (or liter) of fuel, and per kilometer (or mile) for each replicate and dose.

Source: U.S. Environmental Protection Agency (1996)

developing follow-up test requirements at the Tier 3 level that would be necessary to support quantitative, comparative risk assessments.

Although both evaporative and combustion emissions are encompassed by the F/FA rule, the proposed test program focuses on evaporative emissions of the fuels. A full discussion of the reasons for deferring combustion emissions testing is outside the scope of this paper, but the evaporative emissions amply serve to illustrate a testing strategy for new F/FAs. The proposed Alternative Tier 2 test program has been structured so as to obtain rather extensive data on baseline gasoline. Several considerations have led EPA to propose more extensive test requirements for baseline gasoline and MTBE-gasoline than for the other oxygenates. First, and most important, conventional gasoline and MTBE-gasoline predominate within the U.S. fuel marketplace, and thus present the highest potential for human and environmental exposures. A thorough understanding of the individual and comparative public health risks of these fuels thus constitutes a critical need. Second, the fact that nearly all fuels have some degree of toxicity means that the relative risk of different fuels is particularly important. Accordingly, a comprehensive database on baseline gasoline toxicity is vitally needed to provide a level basis for comparison with other F/FAs in the gasoline family. Similarly, since MTBE is the most frequently used oxyfuel, comprehensive data on MTBE-gasoline is needed not only in comparison with baseline gasoline but also to provide an additional reference point for evaluating the relative toxicity of other oxyfuels.

Third, previous scientific work on conventional gasoline and on MTBE has identified specific information gaps which cannot be satisfactorily addressed by the short-term screening tests required under Standard Tier 2. For example, the comparative carcinogenic potential of baseline gasoline emissions relative to those of MTBE-gasoline emissions is an outstanding fundamental issue which must be evaluated in the context of long-term emission exposures. In addition, dose-response relationships for developmental, reproductive, and neurotoxic effects have not been adequately characterized. Fourth, even though each oxygenate has its own chemical characteristics and, perhaps, toxicological potencies, the test results obtained on one such fuel can still help to inform the Agency's decision-making about potential testing needed on other oxyfuels. For example, if certain test results for baseline gasoline and MTBE-gasoline are negative, this may support the validity of negative results for analogous screening tests on other oxyfuels. On the other hand, a positive result obtained on MTBE-oxyfuel under relatively rigorous study conditions may indicate that comparative results are needed for the other oxyfuels. These illustrations help explain why the more extensive set of requirements are initially to be applied on a selective basis to baseline gasoline and MTBE-gasoline, rather than applying the same, relatively stringent set of Alternative Tier 2 requirements across the board to all registered oxyfuels.

SUMMARY OF ALTERNATIVE TIER 2 TESTING REQUIREMENTS

For baseline gasoline and MTBE-gasoline, the standard Tier 2 testing regimen is to be supplemented by (1) two additional neurotoxicity assessments, the functional observational battery and motor activity assessment; (2) a two-generation reproductive study; (3) a two-species developmental study; (4) a two-year carcinogenicity study; and (5) a screening panel for immunological effects. (The two-generation reproductive study and two-species developmental study replace the Standard Tier 2 fertility/teratology combined screening assessment.) The testing requirements for the other oxyfuels are much less extensive, consisting of the Standard Tier 2 requirements modestly expanded to include a screening panel for immunological effects and certain histopathological requirements. Because there is a paucity of inhalation toxicity data on these other oxyfuels, the screening level studies required in Standard Tier 2 are appropriate for determining whether additional studies are necessary. The results of these studies will determine whether additional studies are required at the Tier 3 level.

The Alternative Tier 2 program also incorporates provisions for pharmacokinetic studies on "neat" oxygenates. An understanding of the pharmacokinetic characteristics of the oxygenates as pure compounds is important to our understanding of their relative toxicities when mixed in gasoline. Basic pharmacokinetic characterization (i.e., absorption, distribution, metabolism, and elimination of the pure inhaled oxygenates) can provide mechanistic information on disposition that will be useful to determining whether the toxicological testing results for one oxyfuel (e.g., MTBE-gasoline) can be compared with another. Such studies can also shed light on the relevance of animal-based study results to humans and help determine the extent to which effects by one route of exposure may be relevant to another route.

Comprehensive inhalation pharmacokinetic studies have already been conducted for MTBE; therefore, additional such testing is not required. But, the availability of inhalation pharmacokinetic data for the other oxygenates varies considerably. For example, pharmacokinetic studies are already underway for TAME. In addition, EPA has been informed that such testing on pure ETBE is being conducted by industry on a voluntary basis. To our knowledge, however, there are currently no

similar test plans for pure EtOH, DIPE, TBA, or other oxygenates. Consequently, the proposed Alternative Tier 2 test regimen for the oxygenates other than MTBE includes pure compound inhalation pharmacokinetic test requirements.

CONTINGENT STUDIES

As discussed above, the proposed Alternative Tier 2 testing program has been designed to fill critical data gaps and act as a screen to determine the need for additional studies. Thus, the results of the Alternative Tier 2 tests may indicate that additional studies are required at the Tier 3 level. In the case of baseline gasoline and MTBE-gasoline, follow-up tests may be required to further characterize significant unexpected positive findings. For example, mechanistic studies may be required to determine if positive results of concern in the Alternative Tier 2 animal studies were applicable to humans.

In the case of the other oxyfuels, additional testing may be required for a particular gasoline-oxygenate mixture, not only to explicate Alternative Tier 2 positive results on the mixture in question, but also to resolve uncertainties created by positive results that might be obtained on MTBE-gasoline, another oxygenate mixture, and/or baseline gasoline. Similarly, a two-year inhalation bioassay may be required if either positive results are obtained in the Alternative Tier 2 mutagenicity studies for a given oxyfuel or if significant unexpected results are obtained in the cancer bioassay conducted for baseline gasoline and/or MTBE-gasoline. Additional contingent tests for the oxyfuels may be required to further characterize other significant unexpected positive findings in the Alternative Tier 2 test battery. Other tests may also be required at the Tier 3 level, based on data from ongoing studies not related to the Alternative Tier 2 testing regimen, or to fill other existing data gaps of concern. Such additional tests could include evaluation of acute health symptoms in humans.

ACKNOWLEDGMENTS

I thank John Brophy, Judith Graham, Lester Grant, Judith Gray, David Kortum and others for their contributions to this paper. The views expressed in this paper are those of the author and do not necessarily reflect the views of policies of the U.S. Environmental Protection Agency. The U.S. Government has the right to retain a nonexclusive royalty-free license in and to any copyright covering this article.

REFERENCES

Health Effects Institute (1996) The potential health effects of oxygenates added to gasoline: a review of the current literature, a special report of the Institute's Oxygenates Evaluation Committee. Cambridge, MA: Health Effects Institute, Oxygenates Evaluation Committee.

Interagency Oxygenated Fuels Assessment Steering Committee (1996) Interagency assessment of potential health risks associated with oxygenated gasoline. Washington, DC: National Science and Technology Council; Office of Science and Technology Policy.

Interagency Oxygenated Fuels Assessment Steering Committee (1997) Interagency assessment of oxygenated fuels. Washington, DC: National Science and Technology Council, Office of Science and Technology Policy.

National Research Council; Committee on Toxicological and Performance Aspects of Oxygenated and Reformulated Motor Vehicle Fuels (1996) Toxicological and performance aspects of oxygenated motor vehicle fuels. Washington, DC: National Academy Press.

U.S. Environmental Protection Agency (1996) Oxyfuels information needs. Research Triangle Park, NC: National Center for Environmental Assessment; report no. EPA/600/R-96/069. Available from: NTIS, Springfield, VA; PB96-190665REB.

DIFFERENTIAL GENE EXPRESSION OF ANTIOXIDANT ENZYMES IN MACROPHAGES EXPOSED TO CARBON PARTICLES ADSORBED WITH BENZO-[a]-PYRENE.

Beek Yoke Chin*, Terence Risby# and Augustine MK Choi*, The Johns Hopkins Schools of Medicine* and Public Health#. Baltimore, Maryland.

Introduction

Airborne particulate matter can carry pollutants to the deep distal lung bypassing the respiratory defenses. In urban environments, up to 50% of the respirable particulate matter is carbonaceous. The major source of carbonaceous particles are cigarette smoke, diesel exhaust and incomplete combustion of fossil fuels (1-2). After deposition on bronchial and alveolar epithelium, the load of carbonaceous particles, if not exceeding the normal clearance capacity, are removed by the resident macrophages. Macrophages containing carbonaceous particles have been found in sputum of smokers (1). It has been hypothesized that the impairment of macrophage clearance of carbonaceous particles and the pollutants that they carry, mainly the polyaromatic hydrocarbons, may contribute to the lung-associated injury, presumably initiated by the inflammatory responses that may result in the release of cytokines inducing inflammatory cell recruitment, epithelial cell hypertrophy and hyperplasia (3). If the exposure is chronic, the persistence of these cellular functions can eventually lead to tumorigenesis. Unlike the other environmental pollutants such as ozone, sulfur dioxide and nitrogen dioxide, little is known about the mechanism of particle-induced lung injury. Since most pollutants produce injury that is oxidant-mediated and that cells respond to oxidant-stress by increasing the expression of antioxidant enzymes and stress response genes (4), we investigated whether exposure to carbonaceous particles induce expression of antioxidant enzymes and stress-response genes in macrophages and if so, how are they regulated. We have focused our studies on the stress-response gene product called heme oxygenase 1 (HO-1).

HO-1 is a microsomal membrane enzyme that catalyzes the first and rate-limiting reaction in heme catabolism, to yield equimolar quantities of biliverdin, iron and carbon monoxide. Biliverdin is subsequently converted to bilirubin by biliverdin reductase. There are two isoforms of heme oxygenase, HO-1, the inducible form and HO-2, the constitutive form. Exposure of mammalian cells to cellular stresses such as heme, hypoxia, hyperoxia, lipopolysaccharide, cytokines, heavy metals, ultraviolet irradiation, gluthathione depletors, and hyperthermia have been shown to induce HO-1 gene expression (5-8). A common feature among the various inducers of HO-1 is that these agents, including heme, generate production of reactive oxygen species and/or modify gluthathione levels. This correlation and the observation that bilirubin, one of the end products of heme catabolism, functions as an antioxidant, has led to the hypothesis that HO-1 induction is part of a general response to oxidant stress and that this enzyme plays a protective role during such conditions (9).

In this study we hypothesized that carbon particles carrying the pollutant, Benzo-[a]-pyrene induce HO-1 gene expression in macrophages.We further examined the molecular regulation of HO-1 induction by carbon particles in macrophages.

Materials and Methods

Cell culture - A rat peritoneal macrophage cell line RAW 264.7 were obtained from American Tissue Cell Culture and were maintained in Dulbecco's Modified Eagles Medium supplemented with 10 % fetal bovine serum and gentamicin (50 µg/ml). Cultures were maintained at 37°C in a humidified atmosphere of 5% CO_2/95% air. All experiments were performed with confluent cultures.

Model Carbon Particles -Two model carbon particles N339 and N339ox had preadsorbed on their surfaces a 0.75 monolayer of Benzo-[a]-Pyrene. To prevent agglomeration, the model particles were homogenized in DMEM media at 3000 *rpm* for 1 hour. Cells were exposed to N339+BAP and N339ox+BAP at [2 µg/ml] for up to 24 hours. Controls used for this study were model particles alone (N339 and N339ox) and also BAP alone. When stated, cells were pretreated with Actinomycin D (0.5 µg/ml), Cyclohexamide (1 µg/ml), Cytochalasin B (10 µg/ml) and N-Acetyl-cysteine (20 mM) for 1 h prior to carbon exposure.

RNA Extraction and Northern Blot Analysis - Total RNA was isolated by the STAT-60 RNAzol method with direct lysis of cells in RNAzol lysis buffer followed by chloroform extraction (10). Northern Blot analysis were performed as described

previously (11). Briefly, 10 µg aliquots of total RNA were fractionated on a 1% denaturing agarose gel, transferred to a nylon membrane by capillary action and cross-linked to the membrane by UV irradiation. The nylon membranes were incubated in hybridization buffer (1% bovine serum albumin, 7% SDS, 0.5M phosphate buffer, pH 7.0, 1.0 mM EDTA) containing ^{32}P labelled rat HO-1 cDNA (12) at 65°C for 24 hours. Nylon membranes were then washed twice in buffer A (0.5% bovine serum albumin, 5% SDS, 40 mM Phosphate buffer, pH 7.0, 1.0 mM EDTA) for 30 min. at 55°C followed by 4 washes in buffer B (1%SDS, 40mM Phosphate buffer pH 7.0, 1.0 mM EDTA) for 15 minutes at 55°C and exposed to X-OMAT film. To normalize for the amount of RNA in different samples or loading errors, blots were stripped and hybridized with radiolabelled oligonucleotide probe (5'-ACGGTATCTGATCGATCGTCTTCGAACC-3') complimentary to 18S rRNA. The values for the HO-1 mRNA transcript (1.8kb) were normalized to values for 18s rRNA obtained on the same blot. The HO-1 mRNA levels in the RAW exposed to model particles were expressed in densitometric absorbance units, normalized to control untreated samples, and expressed as fold induction relative to controls.

Western Blot Analyses - Cells were homogenized in lysis buffer (1% Nonidet P-40, 20 mM Tris, pH 8.0, 137.5 mM NaCl, 1 mM Na_2VO_4, 1 mM phenylmethylsulfonylfluoride, 10 µg aprotinin). Protein concentration of the lysates were determined by coomasie blue dye-binding assay (BioRad, NJ). An equal volume of 2X sample buffer (0.125M Tris-Hcl, pH 7.4, 4% SDS and 20% glycerol) was added to the sample and boiled for 5 minutes. Samples (100 µg) were electrophoresed in a 12% SDS-PAGE and transferred onto a polyvinylidene fluoride membrane. The membranes were incubated with a rabbit polyclonal antibody against HO-1 (1:1000 dilution) for 1.5 hours following incubation with goat anti-rabbit IgG antibody for 1.5 hours. Signal development was carried out using an ECL detection kit (Amersham Corp, England).

DNA fragmentation assay - Genomic DNA were extracted as directed by the manufacturer for the Puregene™ DNA isolation kit (Gentra, NC). Twenty µg of DNA was load onto a 1.5% agarose gel in 1X Tris-Acetate buffer and subjected to electrophoresis.

RESULTS

Exposure to model particles adsorbed with Benzo-[a]-Pyrene (N339+BAP and N339ox+BAP) induces HO-1 gene expression in RAW cells -Cells were exposed to 2 µg/ml of both model particles, N339+BAP and N339ox+BAP for 1 h, 2 h, 4 h, 8 h and 24 h and HO-1 gene expression was examined by Northern blot analyses. There was a marked increase in the steady-state levels of HO-1 mRNA was observed at 4 h with the highest level of induction obtained after 8h of continuous exposure to N339+BAP and N339ox+BAP (Figure 1a). The accumulation of HO-1 mRNA levels correlated with increased HO-1 protein levels (Figure 1b).

Induction of HO-1 expression in RAW cells is dependent on phagocytosis of the model particles.
Cells exposed to N339+BAP for 8h demonstrated a 22 fold increase in HO-1 mRNA (Figure 2).To demonstrate that internalization of N339+BAP is required for HO-1 induction, we pretreated the RAW cells with 10 µg/ml of cytochalasin B, a potent inhibitor of phagocytosis for 1 h prior to exposure. Cytochalasin B pretreatment inhibited the N339+BAP induced HO-1 mRNA accumulation. Cytochalasin B treatment alone did not affect HO-1 mRNA levels.

HO-1 mRNA is dependent on gene transcription and de novo protein synthesis.
To further delineate the molecular basis for increased expression of HO-1 in response to N339+BAP, we examined whether HO-1 mRNA induction was dependent on gene transcription. Cells were pretreatment for 1 h with Actinomycin D, a potent inhibitor of RNA synthesis, prior to an 8 h exposure to N339+BAP. As shown in Figure 3, actinomycin D completely prevented N339+BAP induced HO-1 mRNA accumulation. We then determined whether HO-1 mRNA induction is dependent on *de novo* protein synthesis. Cells were pretreated with cycloheximide, a potent inhibitor of protein synthesis, for 1 h prior to an 8 h exposure to N339+BAP. Cyclohexamide also completely inhibited N339+BAP induced HO-1 mRNA expression.

Do reactive oxygen species (ROS) mediate N339+BAP induced HO-1 expression? We determined whether phagocytosis of the model particle N339+BAP liberate ROS that may be responsible for inducing HO-1 expression. Pretreatment of cells with an antioxidant N-acetyl-cysteine (20 mM) 1 h prior to exposure to N339+BAP did not prevent the increase of HO-1 mRNA (Figure 4).

Phagocytosis of the model particle +BAP induces apoptosis in macrophages Cells exposed to both model particles, N339+BAP and N339ox+BAP, for 24 h underwent apoptosis. Characteristic endonuclease generated DNA fragments of 160-180 bp are evident in RAW cells after 24h of continuous model particle exposure (Fig. 5)

Discussion

There has been much interest generated recently by reports demonstrating the induction of HO-1 gene expression by a variety of pro-oxidants (ultraviolet irradiation, hyperoxia and lipopolysaccharide) (13-16). This study demonstrates that exposure to model particles preadsorbed with Benzo-[a]-pyrene (N339+BAP and N339ox+BAP) also induces HO-1 gene expression in macrophages. The model particles selected for this study are well-defined carbon particles which are carbon blacks manufactured under conditions determined by the American Society for Testing Material (17). Since the surfaces of the environmental carbonaceous particles are heterogeneous, containing both oxidized and non-oxidized active sites, we decided to separate them and study their potential adverse effects. As controls for this study, the model particles alone (N339 and N339ox) as well as BAP separately did not induce HO-1 gene expression significantly (data not shown). The criteria for HO-1 induction requires both types of model particles to be a) adsorbed with BAP and b) internalized. The observation that we do not have a significant attenuation of HO-1 gene expression after pretreatment of the cells with NAC may suggest that HO-1 induction may not be modulated by reactive oxygen species. We have also examined other "prototypical" antioxidant enzymes that were exposed to these model particles. There were no significant changes in the mRNA levels of both CuZnSOD and MnSOD (data not shown).

Programmed cell death or apoptosis is a gene regulated process in which coordinated series of morphological changes such as nucleus and chromatin condensation, cell membrane blebing and fragmentation of cell into membrane-bound apoptotic bodies occur resulting in cell death. Removal of apoptotic bodies by phagocytosis by neighboring cells, in particular macrophages, occurs without initiating inflammation. Apoptosis is often a physiologic process, especially important during embryogenesis, organ atrophy and normal adult tissue turnover. However, accumulating evidence suggest that genotoxic and oxidant stress can induce cell death via apoptosis. Preliminary studies show that carbon particles can induce apoptosis in macrophages, and further studies are necessary to understand the regulation and function of carbon-induced apoptosis.

Future work will focus on delineating the transcriptional regulation and signal transduction pathways involved in the activation of the HO-1 gene by carbon particles. Furthermore, we will investigate whether carbon-induced HO-1 expression can serve to protect the macrophages from further cellular oxidant stress.

References

1. Hutzinger, O., ed. (1986). In:*The Handbook of Environmental Chemistry.* No.37/Part D. Springer -Verlag Berlin, Heidelberg.
2. Tokiwa, H., Sera. N., Horikawa, K., Nakamishi. Y., and Shigematu, N. (1993). *Carcinogenesis.* **14**(9):1933-1938.
3. Hetz, PM., (1994) *Hum. Exp. Toxicol.* **13**(10):700-715.
4. Camhi, SL., Lee, PJ., and Choi, AMK., (1995). The Oxidative Stress Response in *New Horizons.* **3(2):**170-182.
5. Lee, PJ., Jiang, BH., Chin, BY., Iyer, NV., Alam, J., Semenza, GL., and Choi, AMK. (1997) *J. of Biol. Chem.* **272:**9,5375-5381.
6. Lee, PJ., Alam, J., Slyvester, SL., Inamder, N., Otterbein, L., and Choi, AMK (1996) *Am. J. Resp. Cell Mol. Biol.* **14:**556-568.
7. Camhi, SL., Alam, J., Otterbein, L., Sylvester, SL., and Choi, AMK. (1995) *Am J. Resp. Cell. Mol. Biol.* **13**:387-398.
8. Maines, MD., (1992). Heme Oxygenase:Clinical Application and Function, pp 145-201. CRC Press, Boca Raton, FL.
9. Stocker, R., Glazer, AN., and Ames, BN. (1987) *Proc. Natl. Acad. Sci.* U.S.A.**84**:5918-5922.
10. Chomczyski., P., and Sacchi, N. (1987) *Anal. Biochem.* **162**:156-159.
11. Camhi, SL., Alam, J., Otterbein, L., Sylvester, SL., and Choi, AMK. (1995(*Am. J. Resp. Cell Mol. Biol.* **13**:387-398.

12. Shibahara, S., Muller, R., Taguchi, H., and Yoshida, T. (1995) *Proc. Natt Acad. Sci.* **92**:5510-5514.
13. Otterbein, L., Sylvester, SL., and Choi AMK. (1995). *Am J of Resp.Cell Mol. Biol.* **13**:595-601.
14. Nath. DA., Balla, G., Vercelloti, GM., Balla, J., Jacob, HS., Levett, MD., and Rosenberg, ME.(1992) *J. Clin. Inves.* **90**:267-270.
15. Vile, GF., Basu-Modak, S., Waltner, C., and Tyrrel, RM. (1994) *Proc. Natl. Acad. Sci.* **91**:2607-2610.
16. Abraham, NG., Lavrosky, Y., Schwartzmer, MC., Stoltz, RA., Levere, R., Gerritsen, ME., Shibahara, S., and Kappas, A. (1995) *Proc. Nat. Acad. Sci.* **92**:6798-6802
17. Jakab, GJ., Risby, TH., Sehnert., SS., Hmieleski, R., and Gilmour, MI. (1990) *Environ. Health Perspective* **89**:169-174.

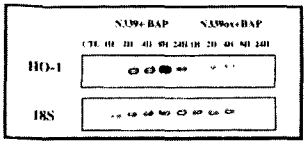

Fig. 1a. Northern blot analyses of HO-1 in RAW cells. Total RNA was extracted at the indicated times following continuous exposure to the model particles and analyzed for HO-1 mRNA expression. The ribosomal RNA 18s is shown as a normalization control.

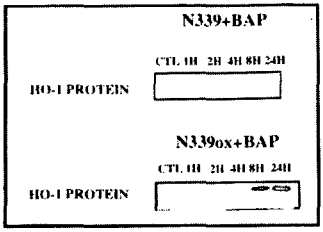

Fig. 1b. Western blot analyses of HO-1 protein in RAW cells. Total protein was extracted at the times indicated following continuous exposure to model particles and probed for HO-1 protein.

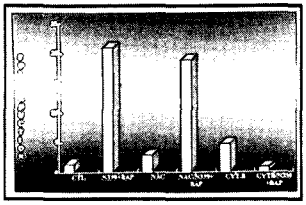

Fig. 2. Effects of NAC (20mM) and cytochalasin B (4ug/ml) on RAW cells exposed continuously to 8h N339+BAP. NAC pretreatment prior to N339+BAP exposure had no effect on HO-1 mRNA expression in RAW cells exposed to N339+BAP. Cytochalasin B pretreatment prior to exposure inhibited HO-1 mRNA expression. The results represent mean fold inducton by Northern blot analyses. 18s rRNA hybridization was used as a normalization control.

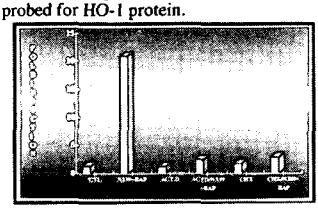

Fig. 3. Effects of Act. D (0.5ug/ml) and cyclohexamide (1ug/ml) on RAW cells exposed continuously to 8h N339+BAP. Act. D pretreatment prior to N339+BAP exposure prevented HO-1 mRNA expression in RAW cells exposed to N339+BAP. Cyclohexamide pretreatment prior to exposure also inhibited HO-1 mRNAexpression. The results represent mean fold induction by Northern blot analyses. 18s rRNA hybridization was used as a normalization control.

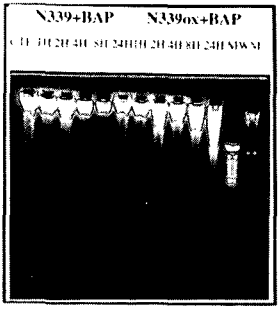

Fig. 4. Genomic DNA fragmentation gel assay of RAW cells. DNA (20 ug) was extracted at the times indicated following continuous exposure to model particles. Characteristic DNA fragments of 160-300 base pairs are evident at 24h of model particle exposure.

LASER DESORPTION MASS SPECTROMETRY AND SMALL ANGLE NEUTRON SCATTERING OF HEAVY FOSSIL MATERIALS

Jerry E. Hunt[1], Randall E. Winans[1], and P. Thiyagarajan[2]
[1]Chemistry Division
[2]Intense Pulsed Neutron Division
Argonne National Laboratory
9700 South Cass Ave.
Argonne, IL 60439

INTRODUCTION

The determination of the structural building blocks and the molecular weight range of heavy hydrocarbon materials is of crucial importance in research on their reactivity and for their processing. The chemically and physically heterogenous nature of heavy hydrocarbon materials, such as coals, heavy petroleum fractions, and residues, dictates that their structure and reactivity patterns be complicated. The problem is further complicated by the fact that the molecular structure and molecular weight distribution of these materials is not dependent on a single molecule, but on a complex mixture of molecules which vary among coals and heavy petroleum samples. Laser Desorption mass spectrometry (LDMS) is emerging as a technique for molecular weight determination having found widespread use in biological polymer research, but is still a relatively new technique in the fossil fuel area. Small angle neutron scattering (SANS) provides information on the size and shape of heavy fossil materials. SANS offers the advantages of high penetration power even in thick cells at high temperatures and high contrast for hydrocarbon systems dispersed in deuterated solvents. LDMS coupled with time of flight has the advantages of high sensitivity and transmission and high mass range. We have used LDMS to examine various heavy fossil-derived materials including: long chain hydrocarbons, asphaltenes from petroleum vacuum resids, and coals. This paper describes the application of laser desorption and small angle neutron scattering techniques to the analysis of components in coals, petroleum resids and unsaturated polymers.

EXPERIMENTAL

The coals used in this study are the Argonne Premium Coal Samples. The procedures for the pyridine extract of the Argonne Premium Coals have been reported previously. The laser desorption mass spectra were recorded on a linear time-of-flight mass spectrometer constructed at Argonne and a Kratos Kompact MALDI III linear/reflectron time-of-flight mass spectrometer. The spectra were produced by exposing the samples distributed as thin layer on a stainless steel sample holder to laser pulses a nitrogen laser. The laser is operated close to the ionization threshold to minimize possible fragmentation of the desorbing material and to optimize resolution. The polyethylene sample were purchased from Petrolite.

Pentane soluble, heptane precipitated asphaltenes and the deasphalted oil (DAO) from vacuum resids of Maya crude oil were obtained from Amoco. The d10-1-methylnaphthalene (d_{10}-1MN) was obtained from Aldrich. Five wt.% dry asphaltene was dissolved in d_{10}-1MN and the solution was stirred overnight. Small angle neutron scattering was performed by placing the sample cell in a boron nitride furnace tube in the small angle diffractometer (SAD) at the Intense Pulsed Neutron Source (IPNS) at Argonne National Laboratory. The temperature of the furnace was measured using a type K thermocouple and maintained within 0.5°C using a Micricon controller. The SAD instrument uses neutrons produced in pulses by spallation due to the deposition of 450 MeV protons on a depleted uranium target, followed by a solid methane moderator (22 K) yielding a wavelength range of 1 to 14Å. Detection of scattered neutrons was accomplished with a 128 x 128 array, 40X40 cm^2 area sensitive, gas-filled proportional counter, and the wavelength of the scattered neutrons was determined by their times-of-flight. Data were corrected for unit transmission of the sample, the scattering from the stainless steel cell, and incoherent scattering. The accessible q range ($q= 4\pi\sin(q)/l$ where l is the wavelength of the probing neutrons and q is half the scattering angle) using SAD is from 0.008 to 0.2 $Å^{-1}$.

RESULTS AND DISCUSSION

The mechanisms at work in laser desorption of ions from surfaces is a subject of much speculation and conjecture. Despite the complexity of the ionization mechanism, the facts remain that mass spectra of a large number of volatile organic compounds can be generated by laser desorption at threshold powers and that fragmentation of the parent molecule is minimal at best. Higher laser fluences may alter the ionization process to result in destructive fragmentation, in structurally significant fragmentation, or even ion-molecule reactions. In addition, the desorption event may cause 'clustering' of molecules leading to mis-interpretations of the data, i.e., incorrectly assuming that larger molecules are present.

Figure 1 presents the laser desorption mass spectrum of a polyethylene sample of 1000 molecular weight. A silver nitrate matrix is used to produce LD mass spectra of polyethylene by cationization. Each ion is an adduct of silver.

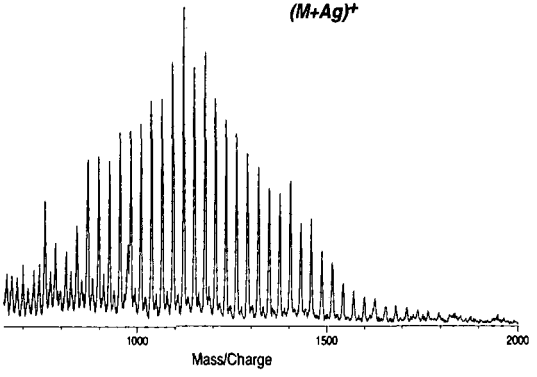

Figure 1. The LDMS spectrum of polyethylene 1000. The ions are produced by cationization with Ag.

Polymer statistics can be calculated from the data. The repeat unit of the polymer can be directly calculated from the mass difference of the oligomer units, and the end groups can also be ascertained. The integrated peak areas (N_i) are used with oligomer molecular weights (M_i) to calculate the number average (M_n) and weight average (M_w) as follows:

$$M_n = N_iM_i / N_i$$
$$M_w = N_iMi^{2}/N_i$$
$$\text{polydispersity} = M_w/M_n$$

For the polyethylene polymer the number average is 1006 and the weight average is 1045 with a polydispersity of 1.04. To be sure there are some difficulties in these analyses. The lack of polar sites on this compound makes ionization difficult, as ionization in LD generally depends on either low ionization potential with adsorption of the compound (an example is aromatic compounds) or availability of a polar group to which either proton attachment or cationization can occur. One of the practical difficulties of integrating spectra of polymer distribution is knowing where to draw a representative baseline. Very polydisperse systems tend to be problematic.

Coal extracts are readily amenable to LD. Figure 2 shows the LDMS spectra of a homologous ion series found in the pyridine extract of Wyodak coal (APCS 2). One of the strengths of direct LD is that aromatic components are easily ionized and detected.

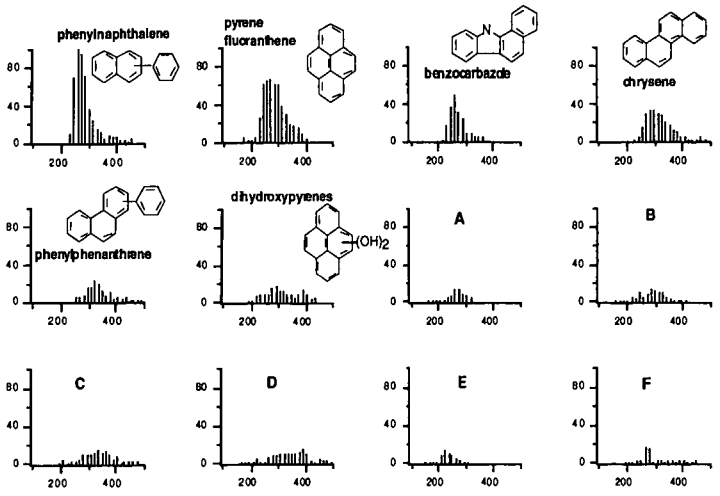

Figure 2. LDMS spectra of the homologous ion series in the pyridine extract of Wyodak-Anderson subbituminous coal (APCS 2)

An interesting result is the four ring systems found in the subbituminous coal. Other ion series, at lower intensities, that have yet to be completely identified (labeled as A, B, C, etc.) show strong evidence for five and six ring systems.

As LDMS is known to chiefly access the aromatic content of a sample, the LDMS of Maya petroleum resid asphaltenes show intense mass spectra like the coal extracts because of their strong aromatic content. The asphaltenes, however, show a higher average molecular weight and a broader molecular weight distribution. The asphaltene has ion intensity extending form a m/z range of ca. 200 to ca. 750. The mass distribution tails to 1000 with exponentially decreasing intensity. Very large molecular species (>1500) are not observed in the asphaltene. The number average molecular weight is quite low, on the order of 500, while the weight average molecular weight, which is more sensitive to the extent of the mass distribution, is on the order of 750. The sample can be considered as a very polydisperse system, at least to first order. Thus, drawing a base line for the high mass region is difficult at best so an upper bound on mass is not possible. However, the bulk of sample has a fairly low molecular weight (about 500 amu).

Gel permeation chromatography and vapor phase osmometry experiments on the asphaltenes indicate that they are rather large structures. GPC shows two size distributions for asphaltenes at approximately 225 and 80 Å. Such structures should have molecular weight very much higher than those found by mass spectrometry. We have, thus, turned to small angle neutron scattering (SANS) to determined the size and shapes of the asphaltenes in solution. SANS was used to investigate the structural changes of a 5 wt.% asphaltene solution in perdeuterated 1-methylnaphthalene (d-1MN) as a function of temperature. A special stainless steel cell was constructed and used for the measurements. The SANS data measured at various temperatures from 20°C to 400°C show that the scattering intensity continuously decreases with increasing temperature. A nonlinear curve in the Guinier plot for asphaltene solutions at 20°C suggested polydispersity in the sizes. Maximum entropy analysis using the form factor for a cylinder allowed extraction of particle size distributions in the radius and length space.

At 20°C the asphaltenes self-associate in d-1MN forming long rod-shaped particles whose radius was around 18Å, but vary in length over 500Å. At 50°C these aggregates break down, as evidenced by the decrease in signal intensity.

In the temperature range of 100 - 320°C the maximum length of the particles decreases and the polydispersity varies in both radius and length dimensions. Between 340 and 400°C, the particles become smaller having a spherical shape with a radius around 12Å.

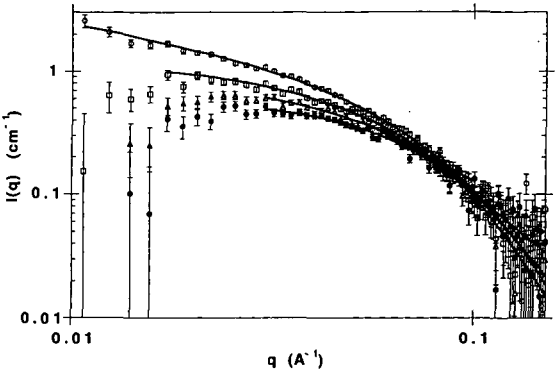

Figure 3: Maximum entropy fits of the SANS data for 5 wt.% asphaltenes in d-1MN at 20°C (o), 50°C (square), 150°C (triangle) and 400°C (filled o).

Upon returning the sample to 20°C, the SANS signal was too weak to derive any structural information, implying irreversible thermochemistry. Interestingly, the structural properties of asphaltenes in d-1MN at temperatures below irreversibility are remarkably reproducible, irrespective of the temperature sequence steps.

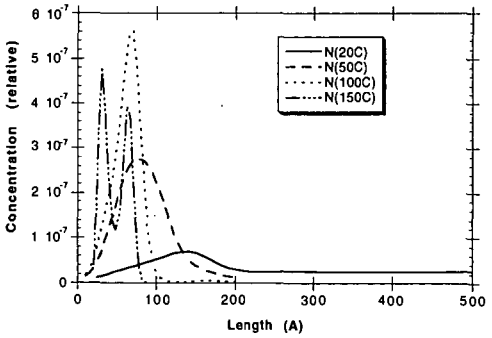

Figure 4: The length distributions for the asphaltene solutions in d-1MN: 20°C (solid line), 50°C(dashed line), 100°C (dotted line), 150°C (dashed-dotted line). The radius is approximately 20 Å for all samples.

Figure 3 shows that maximum entropy analysis is very effective in obtaining the morphology and polydispersity information of the asphaltenes. Figure 4 shows the length distribution for particles of a given radius at 4 different temperatures. The mass spectrometric data and SANS data show that asphaltenes are indeed composed of chiefly low molecular weight molecules (perhaps as low as 500 amu) and that at ambient temperatures aggregate strongly.

Acknowledgment. This work was supported by the Division of Chemical Sciences, Office of Basic Energy Sciences, U. S. Department of Energy, under contract W-31-109-ENG-38.

ANOMALOUS SMALL ANGLE X-RAY SCATTERING STUDIES OF HEAVY METAL ION SOLVATION BEHAVIOR IN CLAY MINERALS

Kathleen A. Carrado*, Kang Song, Randall E. Winans, and P. Thiyagarajan†
Chemistry Division and †Intense Pulsed Neutron Source Division
Argonne National Laboratory, 9700 S. Cass Ave., Argonne, IL 60439

ABSTRACT

We have exploited anomalous small angle x-ray scattering (ASAXS) to monitor the solvation behavior of Cu(II), Er(III) and Yb(III) ions within the interlayers of the natural aluminosilicate clay mineral montmorillonite. The ASAXS technique can reveal the distribution of specific metallic species within a heterogeneous and disordered matrix. The variations of signal intensity as a function of absorption energy were monitored for all of the metal-clays as a function of hydration. Two different hydration levels were probed: as prepared at ambient conditions, or so-called "dry" powders, and "wet" pastes. ASAXS intensities should increase as the energy of the probing x-rays approaches the absorption energy of a given metal ion if it is associated with the interlayer solvent (water in this case), and decrease if the metal ion is associated with the solid matrix. The results show that: (1) Cu(II) is solvated within the interlayers of the wet sample, as expected, and (2) Er(III) and Yb(III) decrease in ASAXS intensity with increased hydration. This latter result was not expected and there is speculation that these ions have associated as hydrolyzed products with the clay surface. The basic principles underlying SAXS and ASAXS will also be presented in this paper.

INTRODUCTION

Clay Minerals

Our interest in clays in terms of fuels science applications has two origins: (1) they are an inherent constituent in the mineral matter of coal and (2) their use as catalysts or catalyst supports in such processes as heavy petroleum upgrading. Small amounts of metal loadings on clays has relevance to both of these facets. Smectite clay minerals are layered metal silicates whose sheets can swell to incorporate up to several layers of water molecules. Each sheet is made up of one octahedral metal oxide layer, usually aluminum or magnesium, that is sandwiched by two tetrahedral silicate layers. Isomorphous substitutions within this framework give rise to a net negative charge on the lattice that is compensated for by the presence of exchangeable ions within the hydrated interlayer. Clays have a long history of applications as catalysts, catalyst supports, adsorbents, and ion-exchangers[1]. They are also prevalent in the mineral matter of coal, effecting it's combustion, processing, and conversion properties[2].

Clay minerals can incorporate heavy metal ions both within the lattice framework and between the interlayer regions. Our ASAXS investigation into the former situation has been published elsewhere[3]. For the latter case, clays ion-exchanged with various transition metal and lanthanide ions (Fig. 1), have been examined in hydrated and non-hydrated forms. The exchangeable interlayer metal ions impart a surface acidity on the clay that is variable depending upon the type of metal cation and the amount of water present within the interlayer[1]. This surface acidity is vital to many hydro-processing reactions of importance to petroleum refining, for example. In addition to catalytic applications, these experiments are also pertinent to the structure, diffusion, and reactivity of species involved in, for example, environmental remediation issues. A preliminary report of Er(III)-clay ASAXS[3] has now been expanded to include several different metal ions.

SAXS And ASAXS Methodology

A description of both local and long-range atomic order associated with molecular assemblies in disordered media is essential for understanding the molecular basis for such issues as catalysis. Examples of such order include the structure and dynamics of molecular catalysts in solution, and the distribution of solvent, solute, and counterions around catalytic surface sites. X-ray scattering provides a powerful tool for the measurement of long-range atomic order in globally disordered media. Disordered systems far more frequently describe materials used in the "real" world, yet they do not lend themselves to characterization by many of the standard techniques appropriate

only for well-defined, ordered materials. In addition to this, the use of ASAXS to probe atomic order in condensed media is in its infancy because it has been limited by the inherent weakness of the signals. Our initial studies[3] represent the first preliminary steps into this arena.

Small angle X-ray scattering (SAXS) has numerous applications in chemistry, metallurgy, biology, polymer science, and colloidal systems. It examines correlations at distances from 10 Å to 1000 Å and provides information about the size, morphology, and interactions of a system of particles or pores in solution or the solid state. SAXS can also be used to follow the phase transitions, crystallization, and aggregation within a system. The SAXS intensity as a function of the momentum transfer is due to the distance correlations of all the atoms in the particles of interest. Anomalous small angle X-ray scattering (ASAXS) refers to extensions of standard SAXS experiments in which the energy of the probing X-rays are tuned near the absorption edge of an element in the sample. By performing SAXS experiments near the characteristic absorption edge of any given atom, it is possible to vary the contrast for scattering of that particular element. This systematic variation in contrast yields the partial scattering functions of the specific atomic species. In general, the atomic scattering can be expressed as:

$$f(q,E) = f_o(q) + f'(q,E) + if''(q,E) \qquad (1)$$

where E is the energy of the probing X-rays and q is the momentum transfer ($q=4\pi\sin\theta/\lambda$, where 2θ is the scattering angle and λ is the wavelength of X-rays). The parameters f' and f'' are the real and imaginary parts of anomalous dispersion. They each vary sharply at energies within 10 eV of the absorption edge. The imaginary scattering factor, f'', represents the absorption of X-rays which results in photoemission of a core electron. Variation in f' is responsible for the change in contrast seen in ASAXS signals. These two quantities are related by the Kramers-Kronig relation. Typically f' is determined by measuring the energy-dependent absorption spectrum, f'', and applying the Kramers-Kronig transformation. Near the absorption edge of a given atom the scattering intensity, I, varies as a function of energy or wavelength (equation 2).

$$I(q,\lambda) = I_o(q) + f'(\lambda)I_C(q,\lambda) + [f'^2(\lambda) + f''^2(\lambda)]\, I_R(q) \qquad (2)$$

Here I_o represents the nonresonant, energy-independent scattering. The cross term, I_C, reflects scattering between the specific element of interest and the remainder of the material, while I_R corresponds to the distance correlations of just the resonant scatterers.

Since f' and f'' are sharply varying functions near the edge, these experiments require the highest possible energy resolution (of the order of $\Delta\lambda/\lambda=10^{-4}$) for the probing monochromatic X-rays. In these experiments we determine the small angle scattering using incoming X-rays with 4 to 5 different energies. All but one of these energies are near the absorption edge of the atom of interest. The last measurement, using X-rays whose energy is 150 eV below the edge, gives a direct measurement of the nonresonant scattering, I_o, since at this energy f' and f'' are effectively zero. From these sets of data, in principle one can obtain a set of 3 to 4 differential scattering data after the subtraction of I_o. If the SAXS data as a function of energy are placed on an absolute scale, one can then use f' and f'' values to obtain the partial structure factors, I_C and I_R, by least square analysis. The maximum variation in the SAXS signals near the edge depends on the maximum value of the variation of f' for a given atom. In general, the variation of f' is larger near the L_{III} edges than for the K edges. Therefore, if a transition metal ion is of interest, generally a larger weight % is necessary. This is true until higher power sources such as the Advanced Photon Source come on line in the very near future.

ASAXS is a very new technique, first reported in 1985 for the analysis of metal alloys[4a] (and somewhat earlier for biochemical systems[4b,c]). Some review articles are available with general background information for the interested reader[5,6]. Only a few references exist where ASAXS has been exploited to characterize heterogeneous catalysts or supports[3,7].

EXPERIMENTAL

Bentolite L, a natural Ca^{2+}-bentonite that has been purified to remove all but 0.2 wt% Fe impurities, was obtained from Southern Clay Products. This was ion-exchanged with Cu(II), Er(III), and Yb(III) ions by stirring 1 gm clay in 100 ml of 0.1M solutions of the hydrated chloride salts overnight, followed by centrifugation, washing, and drying at room temperature. X-ray powder diffraction patterns were obtained on a Scintag PAD V instrument with Cu K_α radiation.

The powder and thick slurry samples were contained in a cell with kapton windows for SAXS measurements. The samples were measured at SAXS beamline BL 4-2 at the Stanford Synchrotron Radiation Laboratory in Stanford, CA. This beamline has a platinum coated mirror which focuses the X-rays in the horizontal direction. A 62 μRad slit upstream from this mirror defines the energy resolution of the probing X-rays at <2 eV. The reflected beam from the mirror is monochromated by a double-crystal Si(111) monochromator. The cross-sectional area of the X-ray beam, 3 mm x 1 mm, is defined by two slits. The beam was focused at a 20 cm long 1-dimensional position sensitive gas detector. The sample was located approximately 2.2 m upstream to the detector. Two ionization chambers, one before and one after the sample, monitored the intensity of the incident and absorbed X-rays. These monitors were also used to determine the absorption edge for the metal of interest in each of the samples. The entire beam path was under vacuum except at the sample. In this configuration the SAXS instrument can measure data in the q region from 0.008 to 0.25 $Å^{-1}$.

The acquisition time for each scattering profile was 5 minutes. During the acquisition of the scattering data, the energy of the incoming X-rays was cycled through each of the energies for 5 to 10 cycles, depending on the desired statistical precision. This procedure aided in the assessment of the stability of the sample, as well as the position of the X-ray beam. For Er-clays, an absorption edge at 8372.6 eV corresponding to the L_{III} edge of Er(III) was found. The ASAXS for the powder samples were then measured at 8100, 8355, 8368, 8370 and 8372 eV. Similar procedures were used for the remaining metal ions using their respective absorption energy edges.

RESULTS AND DISCUSSION

The dry and wet samples were analyzed by ASAXS and x-ray powder diffraction (XRD). XRD revealed that the interlayer spacings for all metal-clays increased by 4-5 Å upon hydration (formation of a wet paste) to 19.5 - 20 Å. This indicates that the interlayer has accommodated more water layers. Typically, they expand from one or two layers of water to three layers[3]. Modified Guinier analysis of the ASAXS data was used to extract the correlations for these sheet-like particles. This approach is based on the fact that the intensity of scattering for infinitely large sheets varies as q^{-2}.[8] When a Guinier analysis is performed in the low-q region by plotting $\ln[q^2 \cdot I(q)]$ as a function of q^2, a linear region indicates the presence of sheet-like particles. Figures 1 and 2 display the modified Guinier sheet analyses for the Cu(II)-clay and Yb(III)-clay systems, respectively. Results for Er(III)-clay were similar to Yb(III)-clay.

ASAXS intensities should increase with absorption energy if the metal ion is associated with the interlayer solvent (water, in this case), and decrease if the metal ion is associated with the solid matrix[3]. The following discussion is provided to explain these various intensity changes. The scattering cross section of a given system is determined by the atomic scattering factor f' of the constituent atoms. The f' factor includes two terms: Z, which is the number of electrons in a given atom, and a dispersion term which strongly varies only near the edge. Near the characteristic absorption edge f' has a minimum.

Let us consider the system of dispersed clay particles in water. The scattering from this system is determined by the number density of the particles, square of the volume of the particles, and the square of the difference in the electron densities of the particles and water. Note that the electron density of clays will always be higher than that of water. In this scenario, if the labels of interest are located within the clay lattice itself (e.g. Ni-SMM clay[3]), the difference in the electron density between the clay and the water will decrease as one approaches the absorption edge of a given metal atom. This is because the net f' value will decrease while that of the H_2O remains the same. That means that the electron density difference decreases as the energy of the probing x-rays approaches the edge and thus the scattering intensity should monotonically decrease with increasing energy[6].

On the other hand, if the metal atoms are associated with the solvent but not with the clays, then f' of the clay remains the same, but that of the solvent decreases. This means that the net electron density difference increases as one approaches the absorption edge. This will result in a monotonic increase in the scattering intensity with increasing energy as the energy of the probing x-rays approaches the absorption edge of a given atom[6].

For the same concentration of the metal atoms, the above effect will be much larger for the former case (ion-clay interaction) than that for the latter (ion-solvent interaction). This is because the signal intensity that is due to constructive interference from the scattering waves from the labels in clays is completely lost from similar atoms in solution.

Although there is a very slight ASAXS effect observed in the "dry" samples (Figs. 1a and 2a), the margin of error precludes us from deducing where the ions might reside. Much more of an effect is observed for the wet samples. Based on the XRD results of increased basal spacings with addition of water, we were expecting in all cases to see that the ions would be associated with the solvent (water) in the slurries. This did occur for the Cu-clay, corroborating our results from a local-environment, short-range order study by x-ray absorption spectroscopy9. However, neither of the Ln-clays showed an ion-solvent interaction upon increased hydration. The layer-layer correlations of the ln q^2 vs. q^2 plots clearly indicate that the Ln ions remain associated with the clay, but the decrease in scattering intensity with absorption energy indicates that these ions apparently are not fully solvated within the interlayer. This latter result was not expected and there is speculation that these ions are instead associated as hydrolyzed species with the clay surface.

The pH of each metal ion-clay slurry during ion-exchange was monitored, and were well below the hydrolysis constants of the respective ion in every case (see Table I). It has been shown that at pH's above the pK_h values, Pb(II) and Cr(III) will form oxide-hydroxide precipitates on clay surfaces[10]. Below this critical pH, these ions simply exist as exchangeable cations within the interlayer. Cu(II) behaves in this manner.

Table I. Hydrolysis Study

ion-clay	pH during ion-exchange	pK_h[a]
Cu(II)	4.5	7.6
Er(III)	5.5	8.7
Yb(III)	5.5	8.0

[a]negative log of the hydrolysis constant[11].

Lanthanide ions appear to behave somewhat differently, however. Several years ago, a suite of articles reported how lanthanide sorption by montmorillonite was effected by pH, concentration, temperature, and pressure[12]. One finding reported that lanthanide hydrolysis occurs at lower pH values than are observed for aqueous solutions in the absence of clay[12c]. The presence of montmorillonite modifies the pH value at which the hydrolysis occurs, and "precipitation" commences at a lower value. This value was determined to be >5, which is in fact the case for our materials (pH 5.5). Hydrolysis is halted when the pH of the medium is acidified to <5. Er(III) and Yb(III) have similar ionic radii at 1.14 nm and 1.12 nm, respectively (coordination number 8)[11b]. Therefore, they likely have similar hydration energies and are expected to behave the same within the clay interlayer environment. It has been proposed that the specialized, localized electrostatic environment within a clay interlayer is strong enough to dissociate water ligands about a lanthanide ion, releasing OH- ions which then react to form hydroxides[12c].

The clay surface may have an even more active role, however. With large basal spacings (ca. 20 Å), hydrated ions experience an equipotential clay surface and can interact with the clay either through hydrogen bonding (complete hydration sphere) or direct residence on the interlayer surface (partial hydration sphere)[12b]. This latter state has been the one proposed for clay suspensions and pastes. In this case, hydrolysis involves dissociation of a coordinated water molecule followed by fixation of the metal ion to the clay. Sites available for this complexation are (1) the hexagonal holes created by the basal silicate surface and (2) other surface oxygen atoms. Both of these sites have been proposed to account for an adsorption of lanthanide ions in excess of that predicted by the cation exchange capacity[12b]. Our ASAXS results appear to support the view that the ions have indeed bonded to the silicate itself, rather than simply precipitate out separately as oxide-hydroxide phases on the surface.

CONCLUSIONS

We have demonstrated that the ASAXS effect can be observed in aluminosilicate clays containing 2-3 wt% transition metal and lanthanide ions. Further, that effect can be used to elucidate how the ions solvate when the clay is hydrated to form suspensions or pastes. For instance, Cu(II) solvates within the interlayer and therefore behaves as a mobile species capable of facile ion-exchange. Under similar conditions, ASAXS has also shown that some lanthanides (at least the smaller Er(III) and Yb(III) ions) will behave in an opposite manner and instead bind to the clay lattice. A thorough understanding of the kinetics and mechanisms of heavy metal ion sorption on clay mineral surfaces is a critical issue, and the subject of recent intensive study[13]. Our results will certainly add to the view of metal ion interactions at the clay-water interface.

ACKNOWLEDGEMENTS

This work was performed under the auspices of the U.S. Dept. of Energy, Office of Basic Energy Sciences, Divisions of Chemical Sciences and Materials Sciences, under contract no. W-31-109-ENG-38. Research at SSRL is supported by the Department of Energy, Office of Basic Energy Sciences. We thank H. Tsuruta for assistance with BL-4-2 at SSRL, and L. Xu (ANL) for assistance with XRD measurements.

REFERENCES

1. Grim, R. E. *Clay Mineralogy*; McGraw-Hill: NY, 2nd ed., 1953.
2. (a) Schobert, H. H. Coal: *The Energy Source of the Past and Future*, ACS: Washington, DC, 1987, p. 76 (b) Mraw, S. C.; De Neufville, J. P.; Freund H.; Baset Z.; Gorbaty, M. L.; Wright, F. J. in *Coal Science*, volume 2, Academic Press: NY, (Gorbaty, M. L.; Larsen, J. W.; Wender, I., Eds.), 1983, chap. 1.
3. Thiyagarajan, P.; Carrado, K.A.; Wasserman, S.R.; Song, K.; Winans, R.E. *Rev. Sci. Instrum.* **1996**, *67*(9), 1.
4. (a) Lyon, O. *J. Appl. Crystallogr.* **1985**, *18*, 480 (b) Miake-Lye, R. C.; Doniach, S.; Hodgson, K. O. *Biophys. J.* **1983**, *41*, 287 (c) Stuhrmann, H. B. and Notbohm, H. *Proc. Natl. Acad. Sci. USA* **1981**, *78*, 6216.
5. (a) Naudon, A. *NATO ASI Ser., Ser. C.* **1995**, *451*, 203 (b) Simon, J. P. and Lyon, O. in *Resonance Anomalous X-Ray Scattering*, North-Holland: Amsterdam, (Materlik, G.; Sparks, C.J.; Fischer, K., Eds.), 1994, 305-322.
6. Epperson, J. E. and Thiyagarajan, P. *J. App. Cryst.* **1988**, *21*, 652-662 and references therein.
7. (a) Haubold, H.-G.; Wang, X. H.; Jungbluth, H.; Goerigk, G.; Schilling, W. *J. Mol. Struct.* **1996**, *383*, 283 (b) Gerber, T. *J. Phys. IV* **1993**, *3*(C8, IX Int'l Conf. on Small Angle Scattering, 1993), 385.
8. Glatter, O. and Kratky, O. in *Small Angle X-ray Scattering*, Academic Press: NY, 1982.
9. Carrado, K. A. and Wasserman, S. R. *J. Am. Chem. Soc.* **1993**, *115*, 3394.
10. Gan, H.; Bailey, G. W.; Yu, Y. S. *Clays Clay Miner.* **1996**, *44*, 734.
11. (a) Baes, C. F. and Mesmer, R. E. *The Hydrolysis of Cations*, Wiley & Sons: NY, 1976 (b) Huheey, J. E. *Inorganic Chemistry*, Harper & Row: NY, 1978, p. 266.
12. (a) Miller, S. E.; Heath, G. H.; Gonzalez, R. D. *Clays Clay Miner.* **1983**, *31*, 17 (b) *ibid.* **1982**, *30*, 111 (c) Bruque, S.; Mozas, T.; Rodriguez, A. *Clay Minerals* **1980**, *15*, 413 (d) *ibid.* **1980**, *15*, 421.
13. (a) Stumm, W. *Chemistry of the Solid-Water Interface*, Wiley-Interscience: NY, 1992 (b) Scheidegger, A. M.; Lamble, G. M.; Sparks, D. L. *J. Coll. Interf. Sci.* **1997**, *186*, 118.

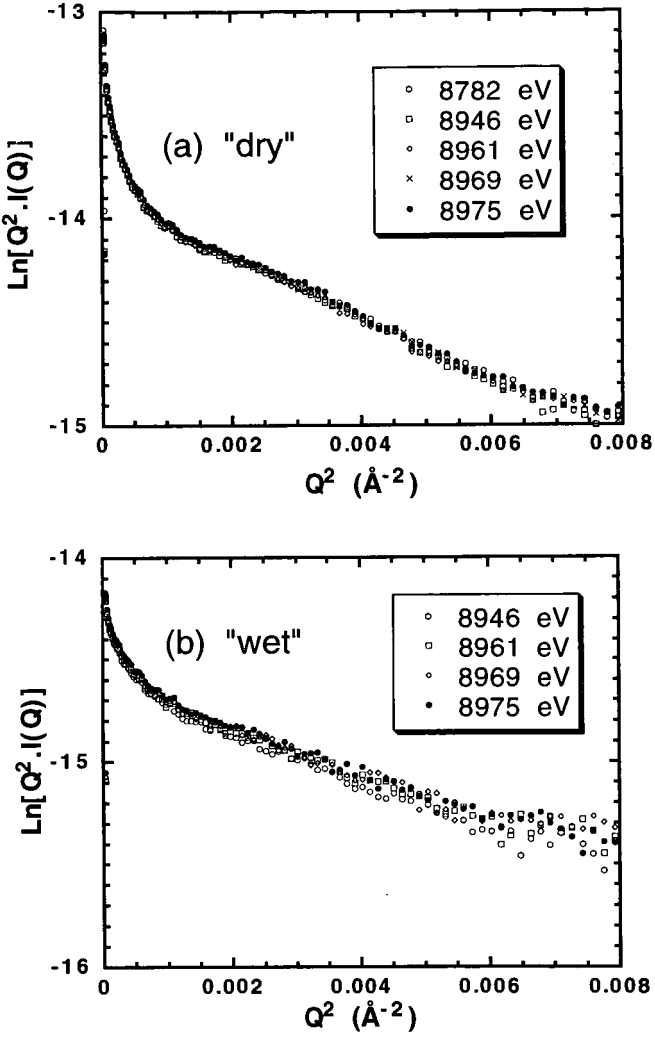

Figure 1. Modified Guinier sheet analysis of the ASAXS data for Cu(II)-clay as (a) the "dry" powder and (b) the "wet" paste.

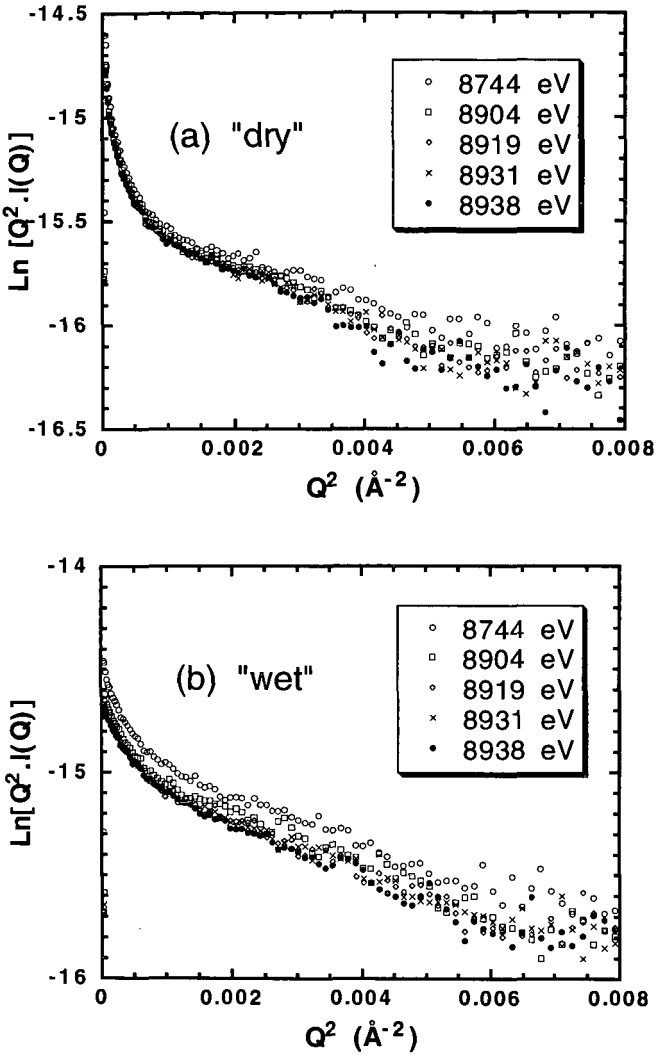

Figure 2. Modified Guinier sheet analysis of the ASAXS data for Yb(III)-clay as (a) the "dry" powder and (b) the "wet" paste.

SOLID STATE CARBON-13 NUCLEAR MAGNETIC RESONANCE STUDY OF AMORPHOUS AND CRYSTALLIZABLE PARAFFIN WAX FRACTIONS IN ASPHALT.

Laurent C. Michon, Daniel A. Netzel, and Thomas F. Turner
Western Research Institute, 365 North 9th Street, Laramie, Wyoming 82070, USA

Didier Martin and Jean-Pascal Planche
Centre de Recherche d'Elf Solaize, 6 Chemin du Canal, 69360 Solaize, France.

KEY WORDS

Solid State NMR, Wax, DSC

ABSTRACT

An asphalt cement is a viscoelastic material and as such its rheological properties are dependent on temperature. The temperature dependency of the rheological properties in turn can be attributed to the motion of the numerous chemical structures present in asphalt. With time, the molecular associations and the formation of crystalline structures tend to restrict molecular motion. Nuclear magnetic resonance is a powerful technique to record data on molecular motion. Solid state carbon-13 nuclear magnetic resonance measurements have been made at room temperature to characterize crystalline and amorphous methylene carbon atoms in asphalts. Cross-polarization with magic angle spinning experiments were performed on five asphalt samples with varying wax content. The amounts of amorphous and crystallizable methylene carbon atoms were determined using spectral deconvolution methodology and correlated with the wax content determined from differential scanning calorimeter measurements.

INTRODUCTION

Properties of asphalt cements are dependent on temperature and in a recent study, Lessueur *et al.* [1] have demonstrated that asphalt behaves like a Newtonian liquid between 60 to 180 °C, a viscolelastic material between the glass-transition temperature to 60 °C, and a rigid material below the glass-transition temperature. The temperature dependency of the asphalt properties can be attributed to the motion of its numerous chemical structures. At any given temperature, the extent of molecular motion depends on the intramolecular configuration of the various asphalt components and the manner in which they interact by intermolecular association. Among these components, the wax content in asphalt strongly influences asphalt properties.[2,3] In addition these wax components can produce crystalline material with time. The type and extent of molecular motion can be obtained from Solid-State carbon-13 Nuclear Magnetic Resonance (SS-NMR).[4,5] In these experiments variable contact time and dipolar dephasing sequences were conducted to obtain information on the crystalline and the amorphous aliphatic components in asphalt. Using the same type of methodology, it was interesting to see if SS-NMR measurements of the crystalline and amorphous components in asphalt are correlated to wax content determined using the Differential Scanning Calorimeter (DSC) measurements.

EXPERIMENTAL

Cross-Polarization with Magic Angle Spinning (CP/MAS) measurements were made using a Chemagnetics 100 solid-state nuclear magnetic resonance spectrometer operating at a carbon-13 frequency of 25 MHz. Experiments were conducted using a 7.5 mm rotor spinning at a rate of 4.5 kHz. Parameters included a pulse width of 5 μs, a pulse delay of 1 s, a contact time of 1 ms, a sweep width of 16 kHz, a free induction decay size of 1024 points, and 3600 acquisitions.

Conventional DSC measurements were performed on a TA instrument model 2920 Modulated DSC. After annealing, the sample was cooled at 10 °C/min to below 60 °C, held isothermally for 15 min, and then heated at 10 °C/min to the annealing temperature. The

different regions in thermogram were integrated with baseline correction. The energy associated with the melting endotherm was used to calculate the percentage of wax given in Table 1.

RESULTS AND DISCUSSION

Cross-polarization experiments were performed on five asphalts: A (Venezuelan crude), B (Middle East crude), C (Italian crude), D (African crude), and E (Middle East crude). These asphalts were provided by Elf-Antar France and were selected to have a large range in wax percentage (see Table 1). The NMR measurements were made at room temperature for the initial asphalt and after two months of phase evolution in the rotor. The aliphatic part of the spectrum was deconvoluted into fourteen different carbon types in accordance with the work of Netzel *et al.*[5] Figure 1 shows an example for asphalt D. The two peaks at 32 and 30 ppm correspond respectively to the crystalline methylene and to the amorphous methylene carbon atoms present in the paraffinic component of asphalt. The relative fraction for the two peaks (f CH_2-crys and f CH_2-amor) are given in Table 2. These values permit a calculation of the percentage of rigid (% C-rigid) and flexible (% C-flexible) carbon atoms (see Table 3) using the following expressions:

(% C-rigid) = (% C)(f C-aliph)(f CH_2-crys) and (% C-flexible) = (% C)(f C-aliph)(f CH_2-amor)

In these calculations, the % C is the percentage of total carbon atoms determined by elemental analysis and f C-aliph is the fraction of aliphatic carbon in the aromatic part of the ^{13}C SS-NMR spectrum.

After two months, an increase in the rigid carbon atoms content and, at the same time, a decrease in the flexible carbon atoms content were observed. This result suggest that, with time, crystalline materials are formed in a asphalt.

Most investigators report that the crystalline part of the asphalt corresponds to the wax fraction. Figure 2 shows the plot of the percentage of wax versus the percentage of rigid and flexible carbon atoms initially and after two months of phase evolution. The correlations obtained are relatively good (R^2 in the range 0.80 to 0.99). The high correlation suggests that the wax content of an asphalt is very well characterized by the two methylene carbon atom peaks at 32 and 30 ppm. The correlation is better with the amorphous part of the methylene carbon atoms because this part represents around 85 % of the total methylene carbon initially and 82 % after the two months of transformation.

CONCLUSIONS

Solid-state nuclear magnetic resonance spectroscopy appears to be a powerfull tool to study the crystalline and amorphous content of an asphalt. In this work, it has been demonstrated that the crystalline and the amorphous methylene carbon atoms present in an asphalt are correlated with the wax content.

REFERENCES

[1] Lessueur, D.; Gerard, J.-F.; Claudy, P.; Letoffe, J.-M.; Planche, J.P. and Martin, D., Journal of Rheology, *40*, 813, (1996).
[2] Claudy, P.; Letoffe, J.M.; Rondelez, F.; Germanaud, L.; King, G. and Planche, J.-P., Preprint Div. Fuel Chem. A.C.S., *37*, 1408, (1992).
[3] McKay, J.F.; Branthaver, J.F. and Robertson, R.E., Preprint Div. Fuel Chem. A.C.S., *40*, 794, (1995).
[4] Netzel, D.A.; Turner, T.F.; Miknis, F.P.; Soule, J. and Taylor, A.E., Preprint Div. Fuel Chem. A.C.S., *41*, 1260, (1996).
[5] Netzel, D.A.; Turner, T.F.; Forney, G.E. and Serres, M., Preprint Div. Polymer A.C.S., *38*, 829, (1997).

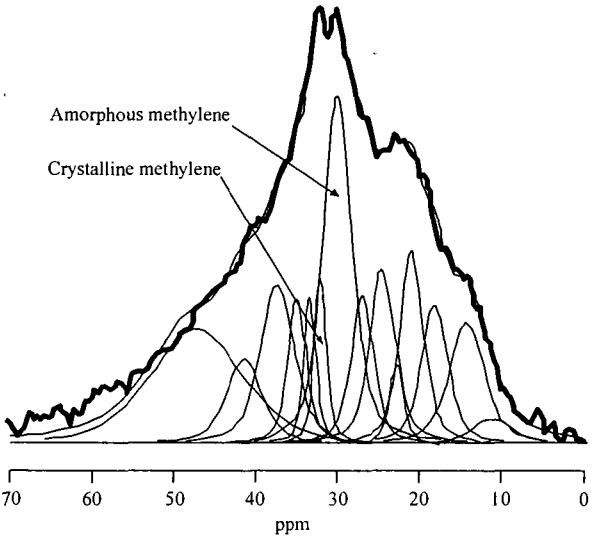

Figure 1: Deconvoluted ^{13}C NMR cross-polarization spectrum for asphalt D.

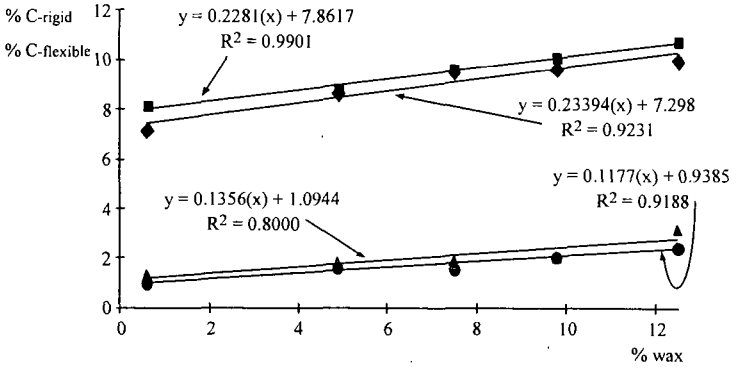

Figure 2: Correlation for the five asphalts between the percentage of wax and the percentage of rigid and flexible carbon atoms. The squares and the diamonds correspond to the flexible carbon atoms respectively initially and after two months of phase evolution. The circles and the triangles correspond to the rigid carbon atoms respectively initially and after two months of phase transformation.

Table 1: Percentage of wax determined by DSC measurements.

Asphalt	A	B	C	D	E
% of wax	0.60	4.90	7.50	9.80	12.50

on copper surfaces with relatively small amount of deposits produced on nickel and stainless steel surfaces. Large lumps of deposits seen as black spots in the micrograph for the copper deposits in Figure 1, did not give any C-H stretching bands, indicating that the deposit in these regions consisted mainly of solid carbon. An SEM examination of these lumps showed that they consisted of short fibers which were fused together[10]. The relatively thin layers of the deposits around the spotty deposits gave, however, distinctly different FTIR spectra with a strong aromatic C-H stretching band at 3050 cm^{-1}, as shown in Figure 1. The spectra obtained from these regions also showed aliphatic C-H stretching bands at 2955, 2925, and 2865 cm^{-1} attributed to CH_3 and CH_2 groups. These observations confirm the activity of the copper surface in catalyzing the formation of fibrous deposits from aromatic PAH produced during the pyrolysis of JP-8 jet fuel as proposed and discussed in more detail elsewhere[10].

The FTIR spectrum of the deposit found on the nickel coupon showed much less intense aromatic C-H band and more broad aliphatic C-H bands, as shown in Figure 1, compared to those obtained from the deposit on copper. A SEM examination of the nickel deposit did not show any filamentous carbon[10]. As different from copper and stainless steel coupons, the two sides of the nickel coupons appeared different under the microscope. The micrograph of the nickel surface in Figure 1 shows the more smooth side of the nickel foil with visible streaks; the other side appears to be more rough and grainy. No apparent difference was observed between the different sides of the coupons after stressing with the jet fuel, however, different deposition pattems were observed on the different sides of the nickel coupons during the pyrolysis of Norpar-13, as discussed later.

The deposits on the 304 stainless steel coupon gave a featureless spectrum, as shown in Figure 1, and no filamentous carbon was observed by SEM examination. The layers of deposits shown in the micrograph in Figure consist most likely of pyrolytic carbon.

The differences observed in the FTIR spectra of deposits on the three metal substrates indicate that the nature of the metal surface strongly affects the solid deposition from thermally stressed jet fuel. Both precursors to solids and the deposition mechanisms can be different on different metal surfaces.

Figure 2 shows the FTIR spectra and the micrographs of the deposits obtained on different sides of the nickel coupon from pyrolysis of Norpar-13 at 575°C and 500 psig in the flow reactor. Side A is the relatively smooth, and side B is the rough and grainy side of the coupons. Much heavier deposition was observed on the rough side of the coupon, as shown in the micrographs. The deposits on the rough side consisted mostly of filamentous carbon which gives the featureless spectrum in Figure 2. In contrast, the smooth side did not contain much filamentous carbon, seen as black spots on the micrograph, and the spectra obtained from regions other than the black spots gave relatively strong aliphatic C-H bands, as shown in Figure 2. The high activity of the rough surface for filamentous carbon formation can be explained with the relative ease of lifting metal particles from the surface in accordance with the mechanism proposed for filamentous carbon formation[11].

Figure 3 compares the FTIR spectra obtained from the deposits on the three metal coupons from pyrolysis of n-dodecane in a batch reactor at 450°C and 1500 psig for 3 and 5 hours. After 3 hours of reaction, the deposits on copper and nickel coupons gave stronger aromatic C-H bands than that seen from the 304 stainless steel deposits. There is not much difference in the spectra of the deposits on the different metal coupons after 5 hours of reaction. In all the cases, the aromatic C-H bands became more intense with time, indicating that the formation of aromatic compounds dominate the deposition process, as proposed earlier [5]. Under these conditions, incipient fibrous deposits were observed on the copper coupons, indicating, again, the catalytic activity of copper in producing fibrous carbon from aromatic compounds. Filamentous carbon was observed on the nickel coupon after 5 hours, suggesting that the precursors to filamentous carbon on the nickel surface are different from those leading to fibrous deposits on the copper surface. No filamentous carbon was observed on the 304 stainless steel coupon under the reaction conditions used for n-dodecane pyrolysis in the batch reactor.

ACKNOWLEDGMENTS

This work was supported by the US DOE Federal Energy Technology Center and the US Air Force Wright Laboratory/Aero Propulsion and Power Directorate, Wright-Patterson AFB. Funding was provided under contract DE-FG22-92PC92104. We thank Mr. W. E. Harrison III and Dr. T. Edwards of WL and Dr. S. Rogers of FETC for helpful discussions.

REFERENCES

1. Edwards, T. and Zabarnick, S. *Ind. Eng. Chem. Res.* **1993**, 32, 3117.
2. Edwards, T. and Atria, J. V., *ACS Preprints, Div. of Petrol. Chem.* ,**1995**, 40, 649.
3. Hazlett, R. N.; Hall, J. M.; and Matson, M. *Ind. Eng. Chem. Prod. Res. Dev.* **1977**, 16,171.
4. Eser, S. *Carbon* **1996**, 34, 539.
5. Song, C.; Eser, S.; Schobert, H. H.; and Hatcher, P. G. *Energy Fuels* **1993**, 7, 234.
6. Yu, J. and Eser, S. *Ind. Eng. Chem. Res.* **1996**, 36, 574.
7. Li, J. and Eser, S., *Extended Abstracts 22nd Biennial Conference on Carbon*, San Diego, CA (1995), p.314.
8. Edwards, T. *ACS Preprints, Div. of Petrol. Chem.*. **1996**, 41, 481.
9. Li, J. and Eser, S. *ACS Preprints, Div. of Petrol. Chem.* **1996**, 41, 508.

10. Li, J. and Eser, S., *Extended Abstracts 23rd Biennial Conference on Carbon*, University Park, PA (1997), in press.
11. Baker, R. T. K. and Harris, P. S., in *Chemistry and Physics of Carbon*, Edited by P. L. Walker, Jr. and P. A. Thrower, Vol. 14, Marcel and Dekker, New York, 1978, p. 83.

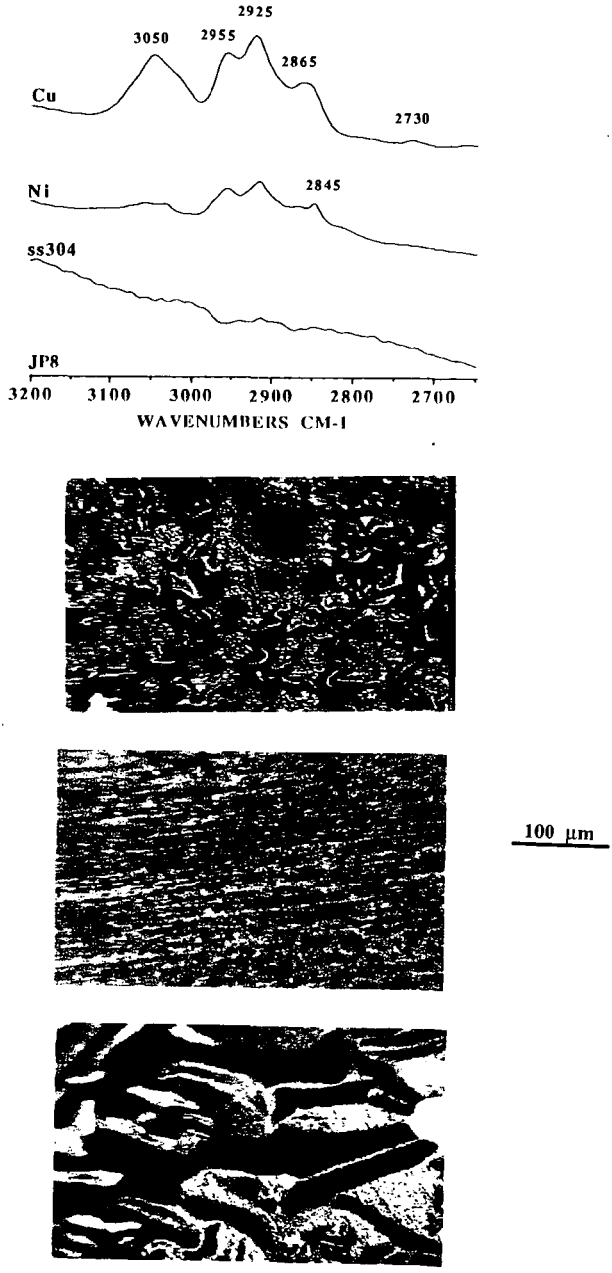

Figure 1. Micro FT-IR spectra and micrographs of solid deposits from JP-8 jet fuel on different metal substrates.

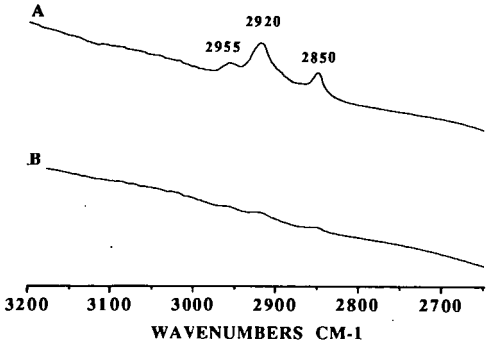

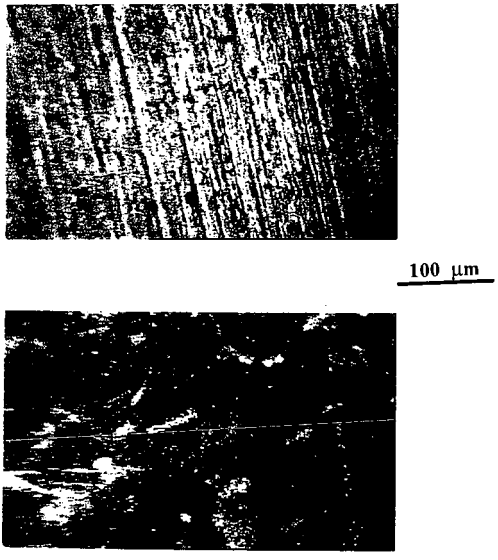

Figure 2. Micro FT-IR spectra and micrographs of solid deposits from Norpar-13 on different sides of a nickel foil: A: smooth side, B: rough side.

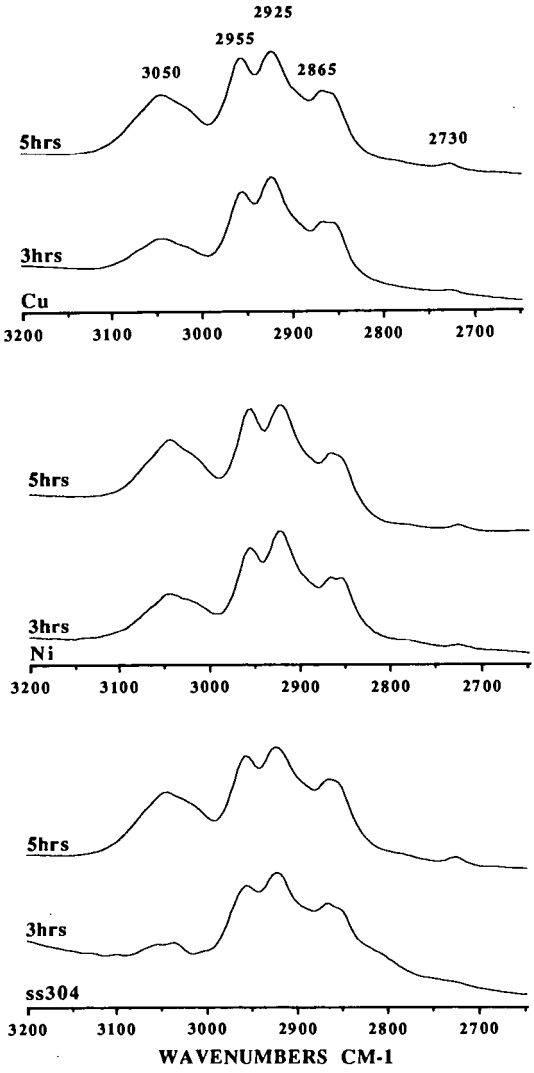

Figure 3. Micro FT-IR spectra of solid deposits from n-dodecane on different metal substrates as a function of time at 450°C.

SOME APPLICATIONS OF NUCLEAR MAGNETIC RESONANCE IMAGING TO RUBBER MODIFIED ASPHALTS

Francis P. Miknis and Laurent C. Michon
Western Research Institute
365 N. 9th Street
Laramie, WY 82070

Key Words: NMR imaging, asphalt, rubber

INTRODUCTION

In 1991, the United States Congress passed the Intermodal Surface Transportation Efficiency Act (ISTEA), which mandated the use of rubber from scrap tires in Federally funded roadway construction projects. The rationale for the mandate is easily understood when considering that the United States discards more than 300 million tires each year and that a large portion of these end up in stockpiles, which may create environmental problems and health hazards. Initially, the mandate called for 5% of scrap tire rubber to be used in 1992, increasing to 20 % by 1997. However, when the mandate was imposed systematic studies concerned with the effects of such variables as asphalt type, rubber type, particle size, mixing time and temperature on the asphalt-rubber rheological properties, as well as handling, safety and health effects of scrap tires had not been carried out. In 1995, the Federal mandate was lifted and States are no longer required by law to utilize scrap tires in paving projects. Nevertheless, between 1991 and 1995 systematic studies of various aspects of crumb rubber modified asphalts were made [1-5], and use of crumb rubber modified asphalts for paving has continued in California, Arizona and Florida.

Crumb rubber generally refers to scrap tires that are ground to a particle size of less than 4 mesh, although in the so-called "dry process" particle sizes of up to 12.5 mm might be used. Regardless of particle size, rubber tires are complex mixtures of elastomers (natural and synthetic rubber), curatives (sulfur, peroxides, etc.), cure-system activators (e.g., stearic acid), fillers and reinforcing agents (carbon black, fibers, etc.), process oils, plasticizer(s), and additives (antioxidants, antiozonents, etc.). Likewise, asphalts are complex mixtures of chemical compounds, consisting functionally of such compound classes as strong and weak acids, strong and weak bases, neutral (aromatic and aliphatic) compounds, and amphoterics. Therefore, questions about what happens when these complex materials are blended at mix temperatures (~170 °C) have not been satisfactorily answered. The influence of crumb rubber on rheology is somewhat understood [2], but the mechanisms of interaction of rubber and asphalt have been difficult to elucidate. For example, does the rubber dissolve in the asphalt, does it swell in the asphalt, do volatile components(extender oils, plasticizers) in the rubber migrate into the asphalt, and how might these reactions influence the rheological properties of the mixture? This work was undertaken to address some of these questions.

Although the crumb rubber mandate of ISTEA has been removed, there are enough successful applications of crumb rubber in asphalt to maintain an interest to more fully understand the compatibility and physicochemical interactions of these materials. This has been a difficult task because of the lack of suitable instrumental techniques to study these interactions. In this paper some preliminary results on the use of NMR imaging to study asphalt- rubber mixtures are presented. The results suggest that NMR imaging may provide a method to obtain information about asphalt-scrap tire rubber interactions. However, applications of NMR imaging to study asphalt behavior are still in their infancy [6,7].

EXPERIMENTAL

Sample Preparation. Natural tire rubber and styrene butadiene tire rubber samples were obtained from Rouse Rubber Industries, Inc. The natural rubber samples were roughly conical in shape (~8 mm dia x ~10 mm height) and sat on a circular base (16 mm dia x 2 mm height). The styrene-butadiene samples had the shape of a triangular prism (~16 mm base x ~8 mm height x ~1 0 mm length).

The natural rubber and styrene-butadiene samples were attached to the bottom of 23 mm (OD) glass vials with epoxy glue. This was to prevent their floating and moving during heating in the asphalt and to ensure that images taken after the heating experiments were made of the same sample orientation. The vials were then

placed in 25 mm(OD) flat-bottom glass tubes. The tubes were inserted into the MRI probe and were positioned in the probe using O rings such that the cross sections to be imaged were contained in the experimental field of view (FOV).

Two sets of samples were made for each rubber. One set was used for heating experiments in the absence of asphalt; the other set was used for heating experiments in the presence of asphalt. The asphalt chosen for study was derived from a crude oil from the San Joacquin valley, California and had a high carboxylic acid content (0.025 mol/l). Carboxylic acids have been shown to dissolve different rubber materials when heated to 200 °C for extended periods of time [2]. The asphalt was heated and then poured into the glass vials such that the rubber samples were several mm below the level of the asphalt.

Each sample was heated in an oven which was set at 170° C for periods of 1, 2, 4, 8, 12, 24 and 48 hours. Between the different heating periods, images were recorded while the sample cooled and after the sample was at room temperature. A temperature of 170 °C corresponds closely to the temperature at which the paving industry produces asphalt-rubber binders [3]. The temperature at which the images were acquired during the cooling phase was not known because the NMRI probe was not capable of variable temperature measurements. By convention, the samples were allowed to set for 3 minutes after they were removed from the oven. Images were then acquired using the same conditions described below, except only 2 acquisitions were obtained.

NMR Imaging Experiments. NMR imaging experiments were carried out at a nominal proton resonance frequency of 200 MHz using a Chemagnetics/Otsuka Electronics microimaging probe. For elastomeric and viscous materials, the relaxation times of the protons are generally too short for spin echo imaging. Consequently, a 3D imaging technique was used.

Images using the 3D method were acquired using an echo time of 2 ms, a pulse delay of 0.5 s, a free induction decay size of 256 data points, 64 phase encodes, 20 acquisitions and a gradient strength of 70 G/cm. Eight 3 mm thick slices were obtained in a FOV of 22 mm. The measuring time was ~1.4 hrs for these experiments. Images taken during cooling were acquired under the same conditions, except that 2 acquisitions were made. These images were acquired in ~8.5 minutes. All images were recorded in the XZ plane, where the z axis is the direction of the magnetic field and also corresponds to the cylindrical axis of the glass vial.

RESULTS AND DISCUSSION

Images of natural tire rubber (Figure 1) and styrene butadiene tire rubber (Figure 2) in the absence and presence of asphalt were acquired before and after heating, and during cooling using the 3D technique. NMR images of the protons in asphalt are not obtained at room temperature because the lack of molecular mobility (high viscosity) shortens the NMR relaxation times such that the NMR signal decays away before any spin echoes can be formed. Only the protons in the rubber are imaged at room temperature. However, at higher temperature the NMR relaxation times are lengthened so that asphalt protons that do not image at room temperature might be imaged at the higher temperature. In the lower sets of images in Figures 1 and 2, signals from the heated asphalt can be seen as the light contrast surrounding the rubber samples. In the bottom set of images in Figure 2 b- d, the signal (light area) below the triangularly shaped styrene-butadiene is an artefact. In reality, this signal is the top of the asphalt covering the rubber, but has been folded into the image because the positioning of the sample in the image probe was such that the field of view (FOV) was not large enough to encompass the sample. In all cases, the 5th slice of an image set of 8 slices is shown. This slice is a 3 mm thick slice through the approximate center of the sample in the XZ plane.

In Figure 1, the set of 4 images at the top are for the natural tire rubber heated at 170 °C for 0 (unheated), 2, 8, and 24 hrs in the absence of asphalt. The middle set of 4 images are for another natural tire rubber sample heated for the same time periods, but in the presence of asphalt. These images were recorded when the sample returned to room temperature after having been heated at 170 °C for the different periods of time. The bottom set of 4 images was acquired while the sample was cooling to room temperature. Analogous sets of images were acquired for styrene-butadiene crumb rubber heated in the same manner and are shown in Figure 2.

The intensity of the NMR images decreases with increased time of heating. This is true for both the natural tire rubber and styrene-butadiene tire rubber, heated in the presence and absence of asphalt (Figures 1 and 2, top and middle). The loss of signal

is more evident for the rubber pieces that were heated in asphalt, and more so for styrene-butadiene compared to natural rubber.

From an NMR perspective, the loss of signal intensity could have different origins: The rubber could have become more rigid in the asphalt and as a result, the relaxation times would have become shorter. This could happen, for example, if oils and plasticizers were driven from the rubber and/or cross linking reactions occurred as a result of heating.

Another reason for the loss of signal intensity could be that the rubber had dissolved in the asphalt, and the only signal remaining was due to the undissolved material. Others [2,3] have shown that, depending on asphalt crude oil source, crumb rubber particles dissolve in asphalt when heated at elevated temperatures (170 - 200 °C) for extended periods of time.

Natural rubber and styrene-butadiene rubber samples that were heated in the absence of asphalt had undergone changes in structure and became more rigid. This was apparent both from the hardness of the rubber samples after heating, and the fact that the rubber samples were impervious to solvents, such as chloroform, after heating (i.e., did not swell). The apparent change in the physical state of the rubber could be due to oxidation at the rubber surface and/or devolatilization and cross linking reactions in the rubber. Loss of the extender oils could also account for some of the rigidity and brittleness exhibited by the rubber samples after heating in the absence of asphalt. Thermal gravimmetric analysis data show that loss of volatile matter in elastomers begins at temperatures around 100 °C [8]. Thus, heating the samples at 170 °C for extended periods of time, as was done in this study, could lead to loss of volatile matter.

The real effect on the tire rubber samples when heated in the presence of asphalt is betrayed by the lower sets of 4 images in Figures 1 and 2. These images were acquired during cooling and clearly show that the rubber had swelled substantially with no evidence of dissolution. However, because the experiments were conducted using large pieces of rubber to enhance the NMR image signal intensity, observation of the swelling behavior would be enhanced over any dissolution that may have taken place. In fact, the cross-section of the natural tire rubber had swelled to about 1.6 times its normal size and the edges did not show any discernible deterioration as would be expected if dissolution had occurred. The images of the swollen rubber could be reproduced by simply reheating the sample for 10 minutes after it had been at room temperature and re-imaging the sample. These images indicate that the loss of signal in the middle sets of images is not due to dissolution of the rubber. However, these images were acquired on rubber pieces that are large compared to crumb rubber particles used in paving, which are typically 4 mesh or less. Therefore, whether dissolution would occur for finer rubber particles mixed in asphalt cannot be ruled out based on these results. Others [2,3] have observed dissolution of fine particles of rubber when heated in asphalt. The images of the swollen rubber also negate the notion that the rubber had crosslinked and became more rigid when heated in the asphalt.

There was little or no swelling of the rubber samples when heated in the absence of asphalt. This is seen by the top set of images in Figures 1 and 2. The lack of swelling was also verified visually immediately after the samples were removed from the oven. Thus, the swelling of the rubber in asphalt appears to have been caused by solvent penetration of components in the asphalt, possibly maltenes. Valkering et al.[9] have shown that maltenes from asphalt cause considerable swelling in styrene-butadiene- styrene block copolymer/asphalt blends. In addition, oils used in tire manufacture are similar to compounds found in neat asphalts. During heating, interaction and/or exchange of these oils with oils in the asphalt could account for the swelling of the rubber. This exchange might also account for the loss of signal at room temperature if the relaxation times of the rubbers took on those of the asphalt components.

SUMMARY

Applications of NMR imaging to study polymer modified asphalts are in their infancy. In this study, exploratory NMR images were acquired on large pieces of natural and styrene-butadiene tire rubbers soaked in asphalt. These measurements demonstrated the feasibility of using NMR imaging to study different interactions between tire rubbers and asphalt, such as swelling by asphalt molecules, possible dissolution of rubber components in asphalt, and devolatilization and cross-linking in rubber when heated at mix temperatures of 170 °C.

Observation of swelling of crumb rubber in asphalt has been extremely difficult, but these results clearly show that swelling of tire rubber in asphalt is a significant mechanism in crumb rubber modification of asphalt, at least for larger pieces of rubber.

DISCLAIMER

ACKNOWLEDGMENTS

The authors gratefully acknowledge support of this work by the Federal Highway Administration under Contract No. DTFH61-92-C-00170. One of the authors, L.C.M., gratefully acknowledges Elf-Antar, France, for financial support.

REFERENCES

1. Labib, M. E., Memon, G. M. and Chollar, B. H., *Prepr..Pap.-Amer. Chem. Soc. Div. Fuel Chem.*, 1996, **41(4)**, 1209.

2. Tauer, J. E. and Robertson, R. E., *Prepr. Pap.-Am. Chem. Soc. Div. Fuel Chem.*, 1996, **41(4)**, 1214.

3. Billiter, T. C., Chun, J. S., Davison, R. R., Glover, C. J. and Bullin, J., *Prepr. Pap.-Am. Chem. Soc. Div. Fuel Chem*, 1996, **41(4)**, 1221.

4. Shih, C.-T., Tia, M. and Ruth, B. E., *Prepr. Pap.-Am. Chem. Soc. Div. Fuel Chem.*, 1996, **41(4)**, 1227.

5. Coomarasamy, A., Manolis, S. and Hesp, S., *Prepr. Pap.-Am. Chem. Soc. Div. Fuel Chem.*, 1996, **41(4)**, 1322.

6. Miknis, F. P. and Netzel, D. A., *Prepr. Pap.-Am. Chem. Soc., Div. Fuel Chem.*, 1996, **41(4)**, 1327.

7. Miknis, F. P. and Pauli, A. T., *Prepr. Pap.-Am. Chem. Soc., Div. Fuel Chem*, 1997, **42(2)**, 374.

8. Sircar, A. K., *Thermal Characterization of Polymeric Materials.*, Academic Press In, New York, 1997, 888.

9. Valkering, C. P., Wonk, W. C. and Whiteoak, C. D., *Shell Bitumen Review*, 66, May 1992, 9-11.

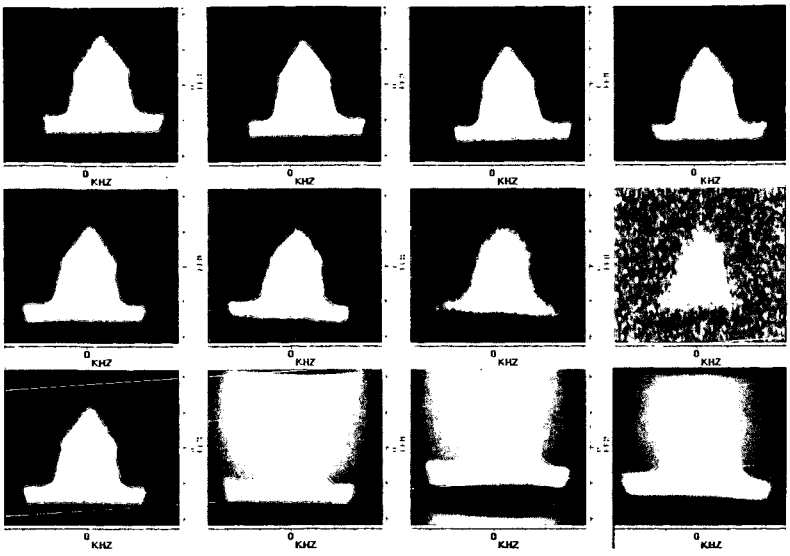

Figure 1. NMR images showing the cross section of a conical piece of natural tire rubber taken after heating at 170 °C for (a): 0, (b) 2, (c) 8, and (d) 24 hrs. (top) natural tire rubber heated in the absence of asphalt; (middle) natural tire rubber heated in the presence of asphalt. Both sets of 4 images were acquired when the sample was at room temperature. (bottom) natural tire rubber heated in the presence of asphalt and imaged while the sample cooled to room temperature.

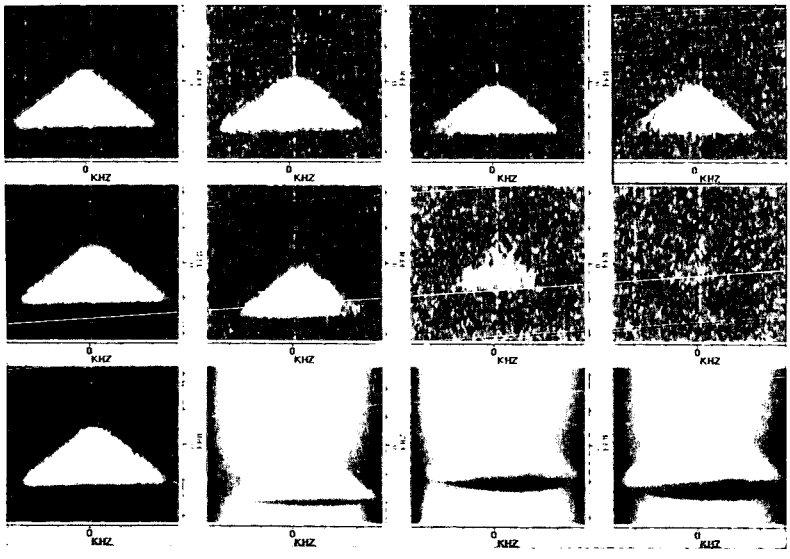

Figure 2. NMR images showing the cross section of a triangular prism-shaped piece of styrene-butadiene tire rubber taken after heating at 170 °C for (a): 0, (b) 2, (c) 8, and (d) 24 hrs. (top) styrene-butadiene tire rubber heated in the absence of asphalt; (middle) styrene-butadiene tire rubber heated in the presence of asphalt. Both sets of 4 images were acquired when the sample was at room temperature. (bottom) styrene-butadiene tire rubber heated in the presence of asphalt and imaged while the sample cooled to room temperature.

DIGITAL IMAGE ANALYSIS OF OPTICAL TEXTURE AND POROSITY OF PETROLEUM COKES

Gao Lin Qiao and Semih Eser
Fuel Science Program
Department of Materials Science & Engineering
209 Academic Projects Building
The Pennsylvania State University, University Park, PA 16802, USA

INTRODUCTION

The microstructure of coke particles can be considered to consist of their optical texture and porosity[1]. Optical texture refers to the appearance of the surface under a polarized-light microscope. The size and shape of isochromatic areas observed on polished surfaces can be used to identify different types of texture[2]. Characterization of the optical texture is very difficult, since the optical domains in petroleum cokes are often connected and tortuous. Several image analysis techniques have been used to determine the size, shape, and orientation of the optical domains in calcined petroleum cokes[3-6]. For texture analysis of calcined cokes, the pores are either ignored[4], or masked out by image processing[3]. In the present study, we propose a digital analysis method to simultaneously characterize the texture and porosity of the calcined cokes. An image analysis method was developed to extract the boundaries of optical domains and pores in petroleum cokes. For semi-cokes, only the boundaries of optical domains were extracted to characterize the optical texture. For calcined cokes, the boundaries of the optical domains and the pores were used to characterize the microstructure of the samples. Feature indices were defined and calculated based on the shape and orientation of the extracted boundaries for the optical domains and pores. Before image analysis, thermal expansion measurements were carried out on the same calcined coke particles to see if there is any relationship between the feature indices and the thermal expansion coefficients (CTE) of calcined coke samples. The CTE is one of the critically important properties of the calcined needle cokes used for manufacturing graphite electrodes for electric-arc furnaces[7].

IMAGE PROCESSING TECHNIQUES

It is well known that there are no distinct gray levels which separate two different isochromatic regions in a polarized-light image of an anisotropic carbon[3]. Therefore, one cannot readily identify the boundaries of these isochromatic regions. It is, however, possible to use a local derivative operator to extract the boundaries of different objects in a given image. For example, the Robert's cross operator[8] acts on a 3x3 pixel region of an image (the z's are gray levels), using the two arrays shown below to obtain a new gray level at point z_5 as $|(z_1+z_3)-(z_7+z_9)|+|(z_3+z_9)-(z_1+z_7)|$.

z_1	z_2	z_3
z_4	z_5	z_6
z_7	z_8	z_9

1	0	1
0	0	0
-1	0	-1

-1	0	1
0	0	0
-1	0	1

These operators are adopted to detect the edges and to draw the boundaries of the objects. using horizontal and vertical gradients. Figure 1 shows different images of a domain structure in a semi-coke sample, including a gray level image (a), boundary image (b), and a binary boundary image (c), created by image processing techniques. As seen Figure 1(a), interpreting optical domains as objects would give complex object shapes. In many cases, an optical domain is not an enclosed object. Therefore, instead of analyzing the complex shapes of optical domains directly, one can analyze the boundaries of these optical domains. The boundary image shown in Figure 1(b) was created by the Robert's cross operator. Although the boundary image does not exactly reflect the shape and size of the optical domains it preserve many features of the optical domains from which it was derived.

After a boundary image is created, it is necessary to expand the gray levels of boundary image to the whole gray scale (0=black, 245=white) by using the stretching technique[8], since the gray levels of the boundary image occur only at the dark end of the gray scale. The stretching technique is used to increase the contrast of the image. Figure 2 shows the linear operation of contrast transformations. After stretching the gray levels of the boundary image shown in Figure 1(b), a threshold of gray level 67 was chosen to obtain the binary image shown in Figure 1(c). Only binary images can be used for feature analysis.

EXPERIMENTAL

Both commercial calcined needle coke samples and semi-coke samples produced in the laboratory were used for image analysis. Thirteen semi-coke samples were prepared by carbonizing commercial coker feedstocks in closed tubing reactors at 500°C for 3h. Before carbonization, 4 g of each sample was weighed in an aluminum foil tube and then placed in the stainless steel reactor. After carbonization, the resultant lump coke was mounted in an epoxy resin

pellet longitudinally. Polished pellets of semi-coke samples were placed on the microscope stage such that the long axis of the coke samples was parallel to the x-axis of the stage.

Before the calcined coke particles were examined under the microscope, thermal expansion measurements were performed in an ORTON 1600D dilatometer. Nine particles were picked from four calcined coke samples and cut into cylinders of approximately 2.50 cm in length and 0.75 - 1.00 cm in diameter. The particles were cut such that their apparent long dimension was parallel to the long axis of the cylinders. For CTE measurements, samples were heated at a rate of 3°C/min in an argon atmosphere and linear changes of samples were recorded from room temperature to 800°C. For comparison with the published literature[3,5], the CTE values were calculated for the same temperature range (300-700°C) for all the particles. When three replicate measurements were performed on each sample, the results showed a standard deviation of 1-2%. After CTE measurement, the samples were placed longitudinally in epoxy resin blocks to prepare polished pellets for microscopic examination.

Image acquisition from a polarized-light microscope (Nikon, Microphot-FXA) was carried out via a high resolution video camera and an image analysis system (PGT, IMAGIST)[9]. After the binary image was created from the boundary image as described in the previous section, it was used for feature analysis[10]. Usually, thirty images were analyzed for each pellet. Only the features in the size range of 50 μm^2 and 1500 μm^2 were analyzed to exclude large cracks and polishing artifacts from the measurements.

A manual point counting technique was also used to characterize the semi-coke samples to compare the results with those obtained by digital image analysis. An automated microscope stage was used to scan the sample by moving a mask of 1mmx1mm on each pellet[8].

RESULTS AND DISCUSSION

For feature analysis of the binary boundary image, we used three parameters, longest dimension (LD), breadth(B), and horizontal chord (HC). Using these three parameters, a feature Index, called FRI, was defined to reflect the shape and orientation of the boundaries of optical domains. The following equation was used to calculate the feature indices for each pellet:

$$FRI = (1/n)\sum^{n}((\sum_{j=1}^{m}\frac{LD_j}{B_j}\times HC_j)/m) \qquad (1)$$

where: m is the number of features in an image; n is the number of images (normally, n=30). Cokes with more anisotropic and well oriented structures should have higher values of feature index. Using a semi-automated point counting data and the assigned factors for four texture classifications, another optical texture index (OTI) was calculated as described before[8].

Figure 3 shows a plot of feature index (FRI) against optical texture index (OTI) for semi-coke samples. It appears that the boundary analysis of optical domains can represent the characteristics of the optical texture of semi-cokes. Unlike point counting, the boundary analysis method does not require texture identification for each image. Instead of analyzing the complex shape of the optical domains, the method relies on the boundary properties of the texture domains.

Figure 4 shows a gray level image (left) and a binary boundary image (right) of a calcined coke sample with a highly anisotropic needle coke texture. The comparison of the two images shows that the extracted boundaries represent both the texture domains and the pores seen in the gray level image. It can also be seen that there is a close correspondence between the boundaries of the texture domains and the pores. For feature analysis of the boundary image, an area exclusion formula was used to remove the large cracks (>1500 μm^2) and small pores (< 50 μm^2). From the feature analysis, a feature index (FRI) of 106 was calculated by Equation 1, which reflects the highly anisotropic microstructure of the needle coke image.

In comparison, Figure 5 shows images of a less anisotropic calcined coke sample, with much smaller sizes of optical texture elements and more isometric boundaries of the pores. The feature analysis of the binary boundary image gave a much smaller FRI (25) compared to that obtained for the highly anisotropic needle coke structure shown in Figure 4 (106). These examples show that FRI calculated from the boundary images of the texture domains and pores in the calcined cokes provides a measure of the degree of miscrostructural anisotropy.

Figure 6 shows a plot of the coefficient of thermal expansion (CTE) against the calculated feature index of the nine calcined coke particles. The plot shows that there is a good correlation between the CTE and FRI within a narrow range of low CTE values desired for the needle cokes used for manufacturing graphite electrodes. This sensitive relationship between the CTE and FRI suggests that the characteristics of both the optical texture and the pores which have the similar size range of optical texture can affect the CTE of calcined cokes [11]. The apparent close correspondence between the optical texture and the pore structure can be explained by considering that the pores analyzed in this study were produced most likely by shrinkage during calcination[7].

CONCLUSIONS

Boundary imaging and analysis can be used to characterize the microstructure of semi-cokes and calcined cokes in terms of a feature index, A feature index was defined to represent the size, shape, and orientation of the optical domains obtained by polarized-light microscopy and digital image processing. The principal advantage of this technique is that there is no need to identify the individual texture elements in a given image. A good correlation was observed between the thermal expansion coefficients of the calcined cokes and feature indices derived by digital image

analysis of the optical texture and pore structure. For feature analysis, there is no need to exclude the pores which have a comparable size range to that of the texture elements.

ACKNOWLEDGMENTS

This study was supported by the Carbon Research Center at the Pennsylvania State University, and Conoco, Inc. We thank Dr. Robert E. Miller of UNOCAL Corporation and Dr. Bruce E. Newman and Dr. Walter A. Kalback of Conoco, Inc. for helpful discussions and thank Ronald M. Copenhaver for polishing the optical pellets and assembling the tubing reactors.

REFERENCES

1. Eser, S. and Hou, L., *Carbon* **1996**, 34, 805.
2. Edwards, I. A. S., in *Introduction to Carbon Science*, Edited by H. Marsh, Butterworths, London, 1989, p.20.
3. Eilersten, J. L., Rrvik, S., Foosns, T., and Øye, H.A., *Carbon* **1996**, 34, 375.
4. Mochida, I., Korai, Y., and Oyama, T., *Carbon* **1987**, 25, 273.
5. Eilersten, J. L., Hole, M., Foosns, T., and Øye, H.A., *Extended Abstracts, 21st Biennial Conf. on Carbon*, Buffalo, New York (1993), p. 675.
6. Lewis, R. T., Lewis, I. C., Greinke, R.A. and Stong, S.L., *Carbon* **1987**, 25, 289.
7. Mochida, I. Fujimoto, K. and Oyama, T. In *Chemistry and Physics of Carbon* (Edited by P.A. Thrower), Vol. 24, pp. 111-212, Marcel Dekker, New York, 1994.
8. Gonzalez, R. C. and Words, R. E., in *Digital Image Processing*, Addison-Wesley, Reading, Mass., 1992.
9. Qiao, G. L., Wang, Y., Zeng, S. M. and Eser, S., *Proceedings of the European Carbon Conference Carbon'96* , Newcastle, UK (1996), p.176.
10. Qiao, G. L. and Eser, S., *Extended Abstracts, 23rd Biennial Conf. on Carbon*, University Park, Pennsylvania, (1997).
11. Kakuta, M., Tanaka, H., Sato, J., and Noguchi, K., *Carbon* **1981**, 19, 347.

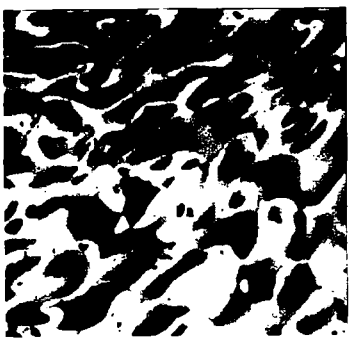

100 μm

(a)

(b)

(c)

Figure 1. Typical images of domain structure in semi-cokes: (a) gray level image; (b) boundary image; (c) binary boundary image.

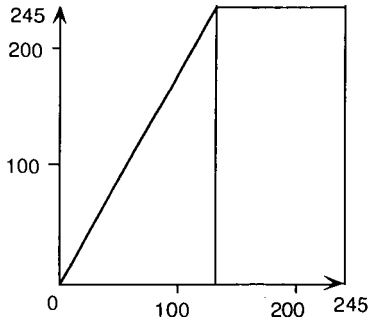

Figure 2. The linear form of transformation function used in contrast stretching.

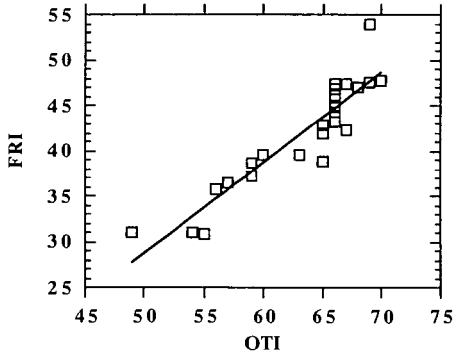

Figure 3. Comparison of feature index (FRI) with optical texture index (OTI).

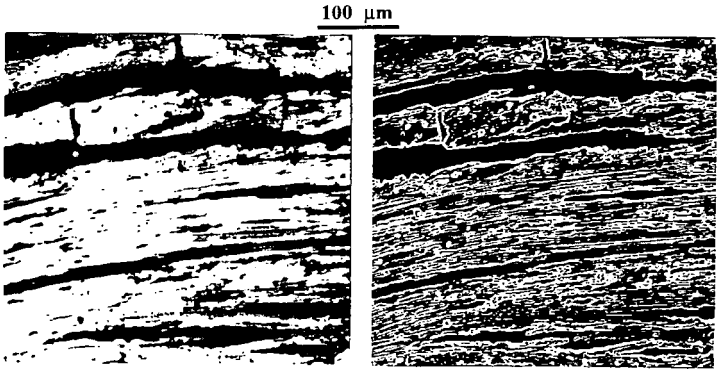

Figure 4. The images of calcined cokes with needle structure; gray level image (left), binary image (right), FRI = 106.

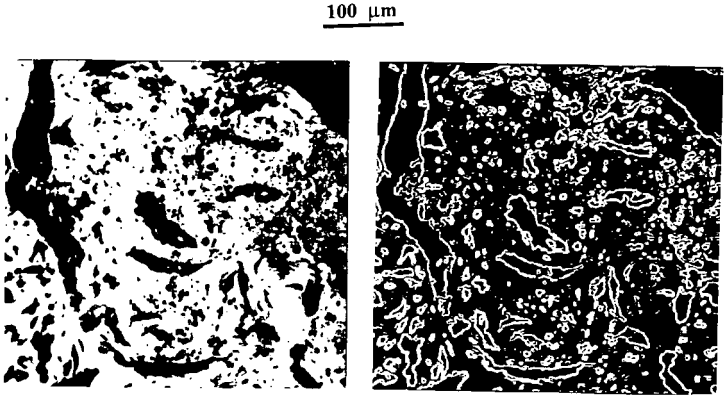

Figure 5. The images of calcined cokes with small domain structure; gray level image (left), binary image (right), FRI = 25.

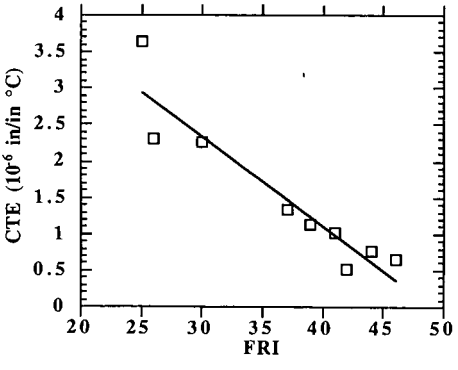

Figure 6. The relationship between coefficient of thermal expansion (CTE) and feature index (FRI) of calcined cokes.

APPLICATION OF ISOTOPE-RATIO-MONITORING GAS CHROMATOGRAPHY/MASS SPECTROMETRY TO STUDY CARBONIZATION REACTIONS OF FCCU SLURRY OILS

T. R. Filley, R. M. Filley*, S. Eser*, and K. H. Freeman, Department of Geosciences
*Department of Materials Science and Engineering, The Pennsylvania State University
University Park, PA 16802

ABSTRACT

Delayed coking of Fluid Catalytic Cracking Unit (FCCU) slurry oils produces needle cokes which are used in the manufacture of graphite electrodes for electric-arc furnaces. The structure and properties of needle cokes depend on the formation of a liquid crystalline phase (carbonaceous mesophase) during delayed coking. Thermal reactivity of individual compounds in slurry oils effectively controls the initial carbonization reactions, and, thus, the degree of mesophase development. In this study, isotope-ratio-monitoring gas chromatography mass-spectrometry was used *in conjunction with* a ^{13}C-labeled dopant (4-methyldibenzothiophene) to determine the distribution of the labeled methyl group on the GC-amenable products from carbonization of three different FCCU slurry oils. Selective removal of the unreacted dopant and its methylated analogs from the reaction products by ligand exchange chromatography allowed the isotope analyses of selected aromatic compounds. The ^{13}C enrichment of selected aromatic compounds, including some isomers, was determined to compare the relative thermal reactivities of different compounds as well as the reactivities of different sites on a given aromatic compound.

INTRODUCTION

The complex chemical constitution of fossil fuels and many associated refinery products precludes the use of simple chromatographic or bulk spectroscopic analytical techniques to accurately evaluate reaction mechanisms and rates of thermal and catalytic conversion of individual compounds. A relatively recent approach to studying the reactivity of individual compounds within complex organic mixtures combines the addition of organic compounds or gaseous media enriched in stable isotopes that participate in alkylation/dealkylation and/or hydrogen abstraction/addition reactions. The rationale for this approach is that the labeled compound or atom can be accurately tracked though a reaction sequence by the use of instrumentation such as, NMR, high resolution mass spectrometry, and isotope-ratio-monitoring gas chromatography mass-spectrometry (irmGCMS). Valuable insights into complex reactions in resid/coal coprocessing[1], crude oil maturation[2], jet fuel thermal stability[3] and the carbonization of FCCU slurry oils[4,5] have been obtained by this application.

In a previous publication, (Filley et al.[4]), we reported the results from irmGCMS of the reaction products from the carbonization of an FCCU slurry oil (referred to in this paper as Oil A) and 4-methyldibenzothiophene, ^{13}C-labeled at the methyl carbon (4-^{13}MDBT). We observed the progressive ^{13}C-enrichment of methylated PAH within the reaction products during the course of the reaction indicating that ^{13}C-enriched methyl radicals were formed by thermolysis of the labeled methyl group and dibenzothiophene. The reactivity of specific methyl substituted and unsubstituted PAH toward reaction with the ^{13}C-enriched methyl carbon were documented. Filley et al.[4] observed that the relative enrichment in ^{13}C between structural isomers of specific methyl PAH could be explained based upon calculated reactivities from free valence indices. In this report we present the irmGCMS analysis of the carbonization products of two additional FCCU slurry oils (Oil B and Oil C) with 4-^{13}MDBT to compare the relative reactivities of specific PAH toward reaction with the ^{13}C-enriched methyl radicals.

EXPERIMENTAL

The FCCU slurry oils were carbonized (500 °C) in closed tubing bomb reactors with 2 wt% 4-methyldibenzothiophene, ^{13}C-labeled at the methyl substituent. Reaction conditions, product extraction and molecular quantification were described in Filley and Eser[5]. The carbon isotopic compositions of individual compounds were determined by isotope-ratio-monitoring gas chromatography-mass spectrometry.[6-8] The irmGCMS system used in this study consists of a Varian model 3400 GC coupled to a Finnigan MAT 252 isotope-ratio-monitoring mass spectrometer by a micro-volume combustion furnace. A fused silica capillary chromatographic column (25 m x 0.32 mm i.d. DB-5MS with 0.5 μm film thickness) was used with helium as a carrier gas. As the compounds elute from the gas chromatograph they are quantitatively combusted to CO_2 and H_2O within the combustion furnace (Cu:Pt, 2:1 maintained at 850°C). Masses 44 ($^{12}C^{16}O_2$), 45 ($^{13}C^{16}O_2$, $^{12}C^{17}O^{16}O$) and 46 ($^{12}C^{18}O^{16}O$) are simultaneously monitored. The isotopic compositions of individual compounds were determined by comparison to reference CO_2 gas calibrated relative to NBS-19 standard. Isotopic compositions are reported relative to the international standard, Pee Dee Belemnite (PDB) in delta ($\delta^{13}C$) notation as described in the following equations.

$$\delta^{13}C(‰) = [(R_{sa} - R_{st}) / R_{st}] \times 1000$$

where:

R_{st} = the isotopic ratio $^{13}C/^{12}C$ of PDB standard (0.011237)
R_{sa} = the isotopic ratio $^{13}C/^{12}C$ of the sample compound

The values measured by irmGCMS represent the average isotopic composition of all carbon atoms in the molecule. The ^{13}C-enriched carbon is associated only with the methyl groups on the substituted PAH[4]. Therefore, the isotopic enrichment of the methyl carbons associated with monomethyl substituted PAH was calculated with a mass balance expression. The isotopic enrichment of the methyl group, expressed as $\Delta\delta^{13}C_m$, is determined by difference between the $\delta^{13}C$ of the methyl substituent on the methyl PAH produced in the labeled ($\delta^{13}C_{mL}$) and unlabeled ($\delta^{13}C_{mU}$) experiments. The $\delta^{13}C_{mL}$ and $\delta^{13}C_{mU}$ cannot be, however, uniquely measured by the technique used in this study, therefore; the $\Delta\delta^{13}C_m$ is calculated by difference between the measured isotopic composition of a methyl PAH produced during an unlabeled carbonization and the structurally identical methyl PAH produced at 30, 45, and 60 minutes in the ^{13}C labeled carbonization experiments. All enrichments in ^{13}C of alkylated PAH are then reported as the change in isotopic composition of methylated PAH from the unlabeled carbonization experiment. Table 1 gives $\delta^{13}C$ values of individual compounds in Oil C and the following equations were used to calculate the ^{13}C enrichment of the methyl carbons of a given compound:

$$\Delta\delta^{13}C_m\ (‰) = N_m(\delta^{13}C_{mL} - \delta^{13}C_{mU}) = N_{mP}(\delta^{13}C_{mPL} - \delta^{13}C_{mPU})$$

where:

$\Delta\delta^{13}C_m$ = Calculated ^{13}C enrichment due to the labeled methyl carbons.

$\delta^{13}C_{mL}$ = Isotopic composition of the labeled methyl carbons.

$\delta^{13}C_{mU}$ = Isotopic composition of the unlabeled methyl carbons.

$\delta^{13}C_{mPL}$ = Measured isotopic composition of the methyl substituted PAH molecule in the labeled experiment

$\delta^{13}C_{mPU}$ = Measured isotopic composition of the methyl substituted PAH molecule in the unlabeled experiment.

N_{mP} = Number of carbon atoms in the methyl substituted PAH.

N_m = Number of methyl substituents on the PAH.

For example, consider 1-methylnaphthalene at 45 minutes reaction of Oil C,

$N_{mP} = 11$
$N_m = 1$
$\delta^{13}C_{mPL} = 12.7\ ‰$
$\delta^{13}C_{mPU} = -27.4\ ‰$
$\Delta\delta^{13}C_m = 441\ ‰$

The high level of ^{13}C enrichment at the methyl carbon becomes evident with this calculation, as illustrated in Table 1 for $\Delta\delta^{13}C_m$ values for Oil C.

RESULTS AND DISCUSSION

Figure 1 plots the ^{13}C enrichment of specific isomers of monomethyl PAH and pyrene during the course of the reaction for Oil C. All methyl PAH show an increase in isotopic composition with time indicating continual uptake of the ^{13}C-enriched methyl radical. Pyrene, however, does not exhibit any measurable increase in the ^{13}C content. The difference in isotopic composition between methyl substituted and unsubstituted PAH indicates that the ^{13}C-enriched methyl groups do not participate in PAH formation. This behavior was also observed in Filley et al.[4] for Oil A.

A substantial difference in reactivity is evident between methylpyrenes and methyl-substituted naphthalenes and phenanthrenes where the substituted pyrene compounds consistently demonstrate greater uptake of the labeled methyl group. The greater enrichment of methyl- pyrene is a direct indication of higher reactivity of pyrene in alkylation/dealkylation reactions compared to phenanthrene and naphthalene. The methylphenanthrene and methylnaphthalene isomers overlap in Fig. 1.

There are large differences in reactivity between isomers of methylnapthalene, methylphenanthrene and methylpyrene. For example, the α positions of 9- and 1-methylphenanthrene are observed to have greater reactivity with respect to the β substituted 3- and 2-methylphenanthrene. Similarly, the α position of 1-methylnaphthalene is more reactive than the β substituted 2-methylnaphthalene. These results are consistent with calculated free valence indices (FVI) of the positions on the unsubstituted PAH which predict greater reactivity at the α positions toward radical attack[9]. Table 2 shows the FVI for each position on the three PAH. Identical relative reactivities were observed for methylPAH in Oil A (Filley et al.[4]) and Oil B. Figure 2 shows the ^{13}C enrichment of 1-methylnaphthalene and 1-methylpyrene for the three oils,

indicating a higher intrinsic reactivity of pyrene compared to that of naphthalene. High reactivity of pyrenes in methylation/demethylation reactions suggests that pyrenes would also be reactive in radical hydrogenation/dehydrogenation reactions. Eser and Jenkins[10] have discussed the significance of hydrogen transfer reactions in controlling the rate of carbonization and fluidity of the carbonizing medium which are critically important for mesophase development. Liu and Eser[11] reported that high concentrations of pyrenes in coker feedstocks lead to a high degree of mesophase development, which results in the production of needle cokes with high graphitizability.

The consistent reactivity data obtained from three different feedstocks indicates that the reactivity of individual compounds in FCCU slurry oils can control the initial carbonization chemistry. In other words, the molecular composition of a feedstock can dictate the initial reaction pathways during carbonization, and, thus, control the mesophase development[5, 11].

REFERENCES

1. Ettinger, M.; Stock, L.; Gatsis, J. *Energy Fuels* **1994**, 8, 960-971.
2. Voigtment M. F.; Yang K.; Batts, B. D. and Smith, J. W. Fuel **1994**, 12, 1899-1903.
3. Mckinney, D.; Bortiatynski, J.; Hatcher, P. *Energy Fuels* **1993**, 7, 578-581.
4. Filley, T. R.; Filley, R. M.; Eser, S.; Freeman, K.H. *Energy Fuels* **1997**, In Press.
5. Filley, R. M. and Eser, S. *Energy Fuels* **1997**, In Press
6. Ricci, M. P.; Merritt, D. A.; Freeman, K. H.; Hayes, J. M.; *Org. Geochem.* **1994**, 21, 561-571.
7. Merritt, D. A.; Freeman, K. H.; Ricci, M. P.;.Studely, S.; Hayes, J. M.; *Anal. Chem.* **1995**, 67, 2461.
8. Hayes, J. M.; Freeman, K. H.; Popp, B. N.; Hoham, C. H.*Adv. Org. Geochem.* **1990**, 16, 115-1128.
9. Coulson, C. A. and Streitwiesser, A. *Dictionary of π-Electron Calculations*. W.H.Freeman and CO. San Francisco, CA, 1965.
10. Eser, S. and Jenkins, R. G. *Carbon* **1989**, 27, 889-897.
11. Eser, S. and Liu, Y. *ACS Preprints*, Div. Fuel Chem. **38**, 452-459, 1993.

Table 1. Measured $\delta^{13}C$ values and calculated ^{13}C enrichment for the methyl group on selected methyl-substituted PAH formed during the carbonization of FCCU slurry oil C with ^{13}C-labeled4-methyldibenzothiophene.

Compound	30 min		45 min		60 min	
	$\delta^{13}C$ (‰)	Δ	$\delta^{13}C$ (‰)	Δ	$\delta^{13}C$ (‰)	Δ
2-methylnaphthalene (MN)	-22.0	65	-18.5	103	-13.3	161
1-methylnaphthalene (MN)	-3.7	261	12.7	441	27.6	605
3- and 2-methylphenanthrene (MPh)	-20.0	87	-15.0	162	-5.0	312
9- and 1-methylphenanthrene (MPh)	-7.5	260	6.3	467	14.7	593
Pyrene	-25.1	4.8	-24.7	11	-24.4	16
4-methylpyrene (MPy)	16.4	706	39.5	1098	63.1	1499
1-methylpyrene (MPy)	25.1	869	44.8	1204	74.8	1714

Table 2. Calculated Free Valence Indices of different positions on naphthalene, phenanthrene and pyrene (Coulson, et al.)[9]

	FVI
Naphthalene (position 1)	0.452
Naphthalene (position 2)	0.404
Phenanthrene (position 1)	0. 451
Phenanthrene (position 2)	0.402
Phenanthrene (position 3)	0.408
Phenanthrene (position 9)	0.451
Pyrene (position 1)	0.393
Pyrene (position 2)	0.468
Pyrene (position 4)	0.452

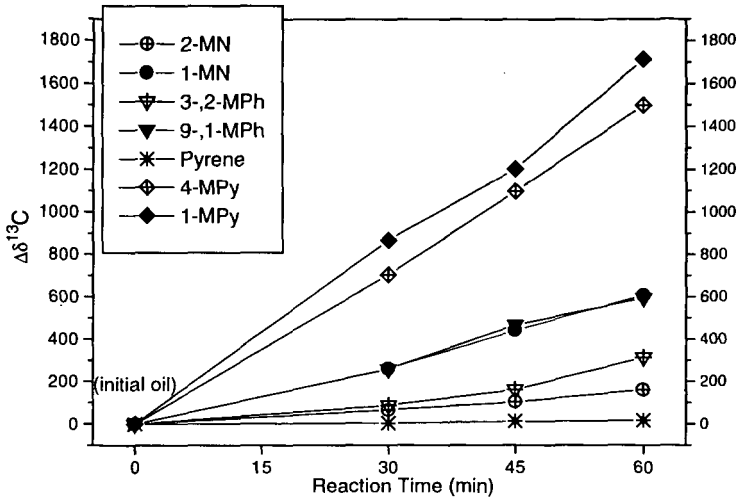

Figure 1. ^{13}C enrichment of the methylsubstituent on selected methylPAH formed during the carbonization of FCCU slurry oil C with ^{13}C-labeled4-methyldibenzothiophene.

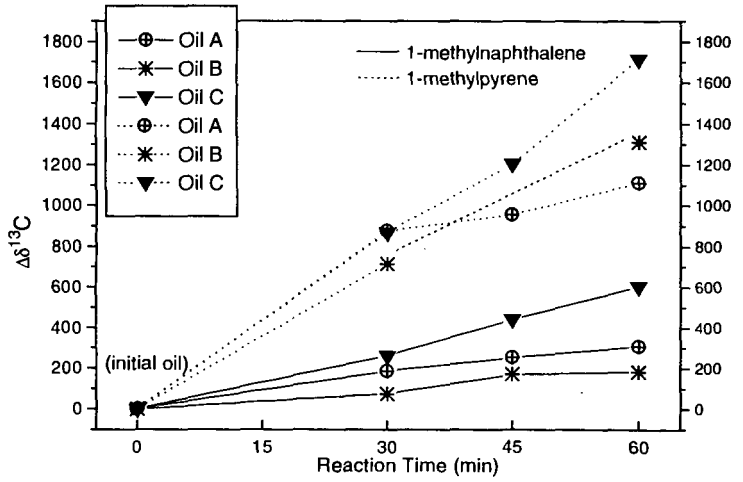

Figure 2. ^{13}C enrichment of the methyl substituent on 1-methylnaphthalene and 1-methylpyrene formed during the carbonization of FCCU slurry Oils A, B, and C with 13C-labeled 4-methyldibenzothiophene.

METALS DETERMINATION BY MICROWAVES DIGESTION AND ICP-AES TECHNIQUE OF UPGRADED LIQUIDS FROM HEAVY PETROLEUM RESIDS

Loredana Caldiero, Monica A. Anelli, Riccardo Nodari, Paolo Pollesel
Eniricerche SpA, Via Maritano 26, 20097 S. Donato Mil. (Milan), Italy

INTRODUCTION

The utilization of heavy petroleum resids and heavy crudes inside the refinery has become one of the most important issues considered and studied by major oil companies. A simple way to utilize heavy fractions with high sulphur and metals' content is blending them with gasoil to produce a fuel to be burned in boilers or furnaces. This route however is becoming more and more difficult, because of increasing stringent environmental regulations. The present work is part of a research project concerning the utilization and the upgrading of heavy oils and of their residues. One of the objectives of the study is to define a process allowing the recovery from heavy resids of lighter and more valuable products which could be reutilized in the standard refinery cycle.
For the upgrading of the residues a continuous pyrolysis process has been considered. Pyrolysis tests, carried out in a rotary kiln system, were aimed to individuate best experimental conditions to maximize the production of liquid products and to increase their quality. The characteristics of the fraction derived from the pyrolysis oils, in fact, must approach the specifications of conventional refinery unit operations, in order to lessen further upgrading treatments. Most of the refinery conversion and upgrading units presents severe limitation on the feedstock heavy metals' content. Therefore the presence of Ni and V in the liquids coming from the pyrolysis process results one of the most important parameters to be investigated to obtain a picture of products' quality.
Laboratory scale runs often produce small quantity of sample to be analyzed and quick responses are requested to direct experimental program. Alternative analytical procedures to traditional ASTM methods are to be defined in order to meet such requirements. Microwaves' digestion to dissolve liquid sample is an advantageous way to perform elemental analysis. The opportunity to work in closed vessels, under elevate pressures and controlled temperatures, avoids time consuming steps, such as incineration and sulphation, and experimental errors due to leaks of volatile compounds or sample contamination. This technique, coupled with an ICP-AES detection, has been emploied to determine Ni and V content in pyrolysis oils as described in this paper.

EXPERIMENTAL

Two different feedstocks were tested: an Italian heavy crude, named "Gela", and the atmospheric residue deriving from the same crude (A.R. ex-Gela). Feedstocks characterization is reported in Table 1. A rotary kiln reactor was chosen to accomplish the pyrolysis step. This system allows to carry on continuous operations and to treat very high viscosity feedstocks. Agglomeration phenomena can be controlled and avoided by a proper optimization of plant operative conditions and by feeding a solid (e.g. sand, coke, dolomite) together with the liquid feed. Liquids feedrate is about 1 kg/h. Temperature, solid residence time and vapor residence time can be set for every run. The coke is dicharged at the reactor exit and collected in a proper vessel. The vapor stream passes through two condensers, where the liquid products are separated, while the gas is filtered, metered ant burned in a flare. Gas samples can be collected after metering and off-line analyzed.
As said above, pyrolysis oil is the most important product. The oil is fractionated according to ASTM D-1160. The oil and the fraction are normally characterized to determine: elemental composition, bromine number (an index of the amount of olefins) for lighter fractions, density for lighter fractions, Conradson Carbon Residue for heavier fractions.
For the most significant runs, i.e. those yielding the largest amount of liquid products, the presence of Ni and V has been investigated. Liquid organic samples (up to 500 mg) have been directly mineralized using a microwaves' digestion system (CEM MDS 2000) which is able to simultaneously process up to twelve PFA closed vessels, under controlled pressure and temperature conditions. The dissolution goes through three subsequent steps involving oxidizing agents as H_2SO_4, HNO_3 and $HClO_4$.
The obtained clear solutions were analyzed by a sequential ICP-AE spectrometer (Perkin-Elmer Plasma 1000) equipped, when necessary, with an ultrasonic nebulizer (Cetac) to reach lower sensitivity, each element at its optimized condition of emission.
All the samples have been added of a proper amount of Sc solution as internal standard. A sample of a NIST standard fuel oil (1634c) was submitted to the same analytical procedure to verify the accuracy of the adopted method.
All the used reagents were of analytical grade of purity.

RESULTS AND DISCUSSION

Pyrolysis tests

Pyrolysis results showed that maximum liquids yield is obtained at a temperature of 500°C. Vapor residence time (τ_{gas}) did not show pronounced effects on products distribution. However runs with higher residence time produced lighter, and therefore more valuable liquids. Table 2 shows products yield and fractions' distribution for two runs with A.R. ex-Gela and for the best run with Gela crude.
Pyrolysis oil is the main product in every run, yielding more than 50 wt. %. Gela test gives a higher liquid yield, being a less heavy feedstock compared to the atmospheric residue. 170-350°C fraction is the most important in all the pyrolysis oils obtained. Even if only a few runs are reported here, some results can be pointed out. The positive effect of an increased τ_{gas} is highlighted by the comparison between fraction distributions for run RATM10 and run RATM18. The latest (τ_{gas}= 53 s) shows a distribution clearly shifted towards lighter fractions, concerning the run with shorter τ_{gas} (21 s). Fractions' characterization for the three runs are listed in Table 3. More details about overall mass balances and products analyses are reported elsewhere /1/.

Analytical results

Ni and V were determined on unfractionated pyrolysis oils and on the related distillation fractions. The adopted procedure utilizes the idea of subsequential oxidations performed by stronger and stronger agents. The optimization proceeded by varying microwaves' power, expressed as percentage of full scale, run time, reaction pressure and temperature.
All the samples were pretreated at the same way:
Up to 500 mg of sample was put in a PFA vessel and added with 2-3 ml of H_2SO_4. The vessel, opened, was then subjected to the following microwaves' steps:

STEP	1	2
Power (%)	20	0
Run Time(min)	20	20
P (psi)	-	-
T (°C)	-	room

Vessels: up to twelve

The H_2SO_4 (boiling point 330°C) is a strong oxidizing agent when hot. In this mild step it is preferred working with open vessel to reach higher temperature regarding those achievable under control by the optical fiber. After the treatment the sample looks like a "char".
The sample is then added of up to 10 ml HNO_3 and the closed vessel is put in the microwaves' system to undergo the following steps:

STEP	1	2	3	4	5
Power (%)	40	60	70	90	0
Run Time (min)	15	15	15	20	0
P (psi)	80	120	160	200	20
T (°C)	80	120	160	185	room

Vessel: up to twelve

To the cool solutions 1-2 ml $HClO_4$ are added. The final digestion steps are following described:

STEP	1	2	3	4	5
Power (%)	50	60	75	90	0
Run Time (min)	10	15	15	30	0
P (psi)	50	100	120	200	20
T (°C)	120	140	160	185	room

Vessel: up to twelve

The clear yellow solutions containing all metal perchlorates, very soluble in water, were then prepared to be analyzed by ICP-AES.
The described procedure, what's more it is based on simple analytical concepts of gradual oxidation, allows in a very short time (less than three hours) to process up to twelve samples having organic matrix, employing quite small amounts of reagents, and assuring prevention of leaks or external pollution.
The solutions were transferred into calibrated flasks, in which an aqueous solution of Sc was added. The Sc as internal standard is suggested by the instrument supplier to use the Myer-Tracy system /2/ which allows a more correct analyte determination as it reduces the short term noise and signal fluctuation due to the sample nebulization process. Ni and V were detected at λ=

231.604 nm and λ=309.311 nm respectively. The instrument calibration was performed utilizing three standard solutions and a blank containing all the same reagents present into the unknown solutions.
Results obtained on unfractionated oils and on respective distillation cuts are summarized in Table 4, together with mass balance to check the method's precision.
As expected metals concentrate in the heaviest cut. The small amount of Ni and V detected in the 170-350°C fractions seems quite unusual, with respect to conventional petroleum products, where metals are normally absent in lighter cuts. Moreover in 350-500°C fractions, metals are in fact almost absent. However repeated tests have confirmed present results. This particular aspect will be further investigated more thoroughly.
Mass balance data confirm the initial results and suggest the reliability of this method. The good comparison between the experimental data obtained applying the described procedure on a standard fuel oil and the certified values (Table 5) also guarantees the accuracy of the technique.

CONCLUSIONS

Upgradated liquid products have been obtained from heavy petroleum resids through a pyrolysis process. The presence of Ni and V in these products has been investigated using a particular technique of sample preparation and treatment. The method allows to treat small quantity of sample, prevents the occurrence of leaks oor external contamination and can process up to twelve samples in less than three hours. Results have been compared and validated by process mass balance and by the succesful application of the technique to a standard fuel oil.

REFERENCES

/1/ A. Carugati, L. De Vita, G. Pederzani, P. Pollesel, Proc. of "Gasification Technology in Practice", February 26-27, 1997, Milan (Italy).
/2/ Tiggelman, J.J., Oukes F.J. et al., Spectrochim. Acta, Part B, 1990, 45B(8), 927-32

Table 1. Feedstocks characterization.

	Gela crude	A.R. ex-Gela
Elemental analysis (wt. %)		
Carbon	81.11	81.49
Hydrogen	10.7	9.91
Nitrogen	0.41	0.56
Sulphur	7.42	7.97
Metals (ppmw)		
Nickel	90	127
Vanadium	125	186
Conradson Carbon R. (wt. %)	12.86	18.13
Density at 15°C (g/ml)	0.9977	1.0892
Viscosity at 100°C (c.St)	115	2,177

Table 2. Pyrolysis products distribution.

Run	T	τ_{gas}	τ_{solids}	Products (wt. %)			Liquid fractions (wt. %, oil basis)			
	°C	s	min	gas	oil	coke	ibp-170	170-350	350-500	500°C+
RATM10	500	21	30	39.3	51.2	9.5	6.67	45.40	31.50	16.33
RATM18	500	53	30	37.5	50.7	11.8	16.91	60.98	16.08	6.02
GELA3	500	50	30	30.5	58.4	11.1	16.53	49.93	23.89	9.65

Table 3. Characterization of the fractionated pyrolysis oils.

	C	H	S	N*	n.Br**	CCR**	ρ**
	(wt. %)					(wt.%)	(g/ml)
RATM10 ibp-170	82.51	13.37	2.51	43	93.4		0.7683
RATM10 170-350	83.24	12.56	3.82	555	43.7		0.8497
RATM10 350-500	79.80	9.94	6.83	0.19		0.75	
RATM10 500°C+	81.46	8.51	8.46	0.39		23.19	
RATM18 ibp-170	83.25	13.32	1.55	56	85.7		0.7566
RATM18 170-350	83.22	12.34	4.04	912	48.3		0.8410
RATM18 350-500	82.43	9.92	7.29	0.23		1.11	
RATM18 500°C+	81.45	7.98	8.92	0.50		29.12	
GELA3 ibp-170	83.64	13.19	2.23	48	98.4		0.7758
GELA3 170-350	83.34	11.91	4.24	452	43.1		0.8799
GELA3 350-500	80.63	9.83	6.45	0.21		0.83	
GELA3 500°C+	80.67	7.72	8.99	0.42		31.58	

* = Nitrogen amount is expressed in ppmw for ibp-170 and 170-350 cuts; while it is wt. % for 350-500 and 500°C+ cuts.

** = Bromine number and density have been determined only for the lighter fractions. CCR has been determined only for the heavier fractions.

Table 4. Ni and V samples' content (ppmw) and mass balance.

Run	Unfractionated oil		Distillation cuts						Sum of fractions	
			170-350		350-500		500°C+			
	Ni	V	*Ni*	V	*Ni*	V	*Ni*	V	*Ni*	V
RATM10	8.4	9.0	1.6	1.3	0.9	<0.5	46.1	52.6	8.5	9.2
RATM18	3.2	2.9	1.7	2.0	<0.5	<0.5	42.3	46.4	3.6	4.0
GELA3	4.9	3.9	2.3	0.6	2.2	<0.5	24.9	28.8	4.1	3.1

Table 5. Ni and V results (ppmw) on NIST standard: comparison between experimental and certified values (the expanded uncertainties are level of confidence of 95%).

	NIST 1634C Standard Fuel Oil
Ni certified	7.5 ± 0.2
Ni experimental	7.2 ± 0.4
V certified	28.2 ± 0.4
V experimental	28.3 ± 0.3

RADIOISOTOPE STUDY INTO Co AND Ni CONTAINING CATALYSTS FOR PETROLEUM RESIDUA HYDROTREATING

Victor M. Kogan[a], Natalia M. Parfenova[b]

[a]*N.D.Zelinsky Institute of Organic Chemistry, Russian Academy of Sciences, 47 Leninsky prospect, Moscow 117913, Russian Federation;*

[b]*Institute of Chemistry, Turkmenian Academy of Sciences, 92 Pogranichnicov st, Ashgabat 744012, Turkmenistan.*

A comparative radioisotope study into alumina- and silica supported Co, Ni and Co+Ni catalysts has been carried out. Catalysts were characterized by physical and chemical methods and tested during hydrotreating (HTR) of oil residua of West-Sibirian petroleum. Some dependencies among catalyst composition, carrier support, the number, type and productivity of active sites, and catalyst functioning under oil residua HTR have been found. The study has permitted us to put forward some criteria to evaluate the results of radioisotope testing with the aim of designing a catalyst composition optimum for a definite refining process. Some cheap catalysts-adsorbents for preliminary treating of heavy crudes, before they are applied to the main oil refining processes have been designed.

1. INTRODUCTION

Involving heavy residual oils into refining processing makes it of major importance to have effective catalysts for oil HTR. Some major concepts of HTR reactions and architecture of the supported catalysts have been already formulated [1 - 22]. Nevertheless, studies into supported catalyst composition and principles of their functioning are still very urgent to which fact testifies a great number of articles and reviews [10, 11, 23 - 29] which are mainly focused on the issue of catalyst composition and not so often on reaction mechanisms. Radioisotope technique offers us extra opportunities to obtain unique information on active sites number and their functioning and heterocompound transformation mechanisms. [30 - 36].

In this paper the comparison of the results of catalyst radioisotope testing during model reaction of thiophene HDS with the data of residual oil HTR on the same catalysts is being undertaken. It aims at adequate evaluating of both methods potentials to design the best catalyst composition for an actual HTR process.

2. EXPERIMENTAL

2.1. Catalyst preparation, characterization and pretreatment

More than 70 Ni- and Co-containing catalysts were synthesized and studied. Catalyst samples were prepared by wet impregnation of γ-Al_2O_3 (specific surface - 212 m^2/g, pore volume - 0.8 cm^3/g, pore average D - 124 Å) and of SiO_2 (specific surface - 363 m^2/g, pore volume - 0.96 cm^3/g, pore average D - 98 Å). Impregnation procedure was carried out (i) using water solutions of Ni or Co nitrates for preparing Ni or Co catalysts, or (ii) using join solution of Co and Ni nitrates - for Ni+Co catalyst samples preparing. After impregnation the catalysts were air dried for 24 h at room temperature and 2 h at 110°C. Metal surface amount in the samples varied in the range of 1 - 25 %.

All the carriers and catalysts were studied by physico-chemical methods. Pore structure was determined by Hg porometry technique using *Cultronix* automatic porometer. Metal reduction degree was determined by volumetric technique. Metal concentration in the catalysts was measured by atomic absorption technique.

Two forms of the catalysts were used - reduced and sulfidized. Sample reduction was carried out in the flow of purified H_2 for 10 h at 400°C. Sulfidation of preliminary reduced catalysts was made by elemental sulfur in hydrogen atmosphere (3 MPa, 380°C, 1 h).

2.2. Residual oil hydrotreating technique and product characterization

Residual oils of West-Sibirian petroleum contained: asphaltenes - 4.3 % wt, sulfur - 2.3 % wt, V - 40 g/t, Ni - 60 g/t. Residual oil HTR was carried out in a 250 cm^3 stainless steel autoclave (5 MPa H_2 pressure, 380°C, 5 h). Sulfur amount in crudes was determined analytically. Derivatographic measurements of coke deposits on the catalyst were made.

2.3. The technique of HDS experiments with radiochromatographic analysis of the products.

2.3.1. *Catalyst sulfidation* was carried out in a pulse microcatalytic installation. The microreactor in the form of U-tube made of pyrex was loaded with 100 mg of the catalyst and linked with the gas-liquid (GL) chromatograph. The rest of the reactor volume was filled with quartz. All catalysts were preliminary subjected to He flow at 200°C for 2 h, then by H_2 flow, 400°C, 4 h. After that they were sulfidized. As sulfidizing agent either 5 % H_2S/H_2, in which H_2S was labeled by ^{35}S isotope,

or thiophene-^{35}S was used. H_2S/H_2 sulfidation lasted for 1 h at 450°C. Further on the catalyst was again treated by He at the same temperature for 30 min. to get rid of adsorbed H_2S.

Sulfidation by thiophene-^{35}S was made by 3 μl thiophene pulsing into the reactor at 360°C with further chromatographic analysis of the products. After H_2S curve became constant thiophene-^{35}S pulsing was stopped. After sample sulfidation was over, reactor temperature stabilized at 360°C. Then the catalyst either was taken out of the reactor for sulfide sulfur amount measurement or was tested in the reaction of thiophene HDS.

2.3.2. *The technique of HDS experiments with radiochromatographic analysis of the products and mathematical treatment of experiment results.* After sulfidation procedure catalyst samples labeled by ^{35}S were tested in the thiophene HDS reaction. Unlabeled thiophene was injected into the reactor by pulses, 1 μl each. To measure reaction product radioactivity a flow proportional counter installed in the outlet of the chromatograph was used. Based on the results obtained some curves of H_2S molar radioactivity (MR) dependencies on H_2S amount (cm^3) are built equivalent to the dependencies on reacted thiophene amounts. Mathematical treatment of the experimental curves allows us to approximate the dependencies we obtained by exponential equations and to calculate the amount of mobile sulfur on each type of active site and productivities of these sites [35].

3. RESULTS AND DISCUSSION

3.1. Radioisotope testing

Preliminary experiments with various amounts of active metal on the catalyst have shown that catalytic activity curves of the samples under study pass through a maximum, depending on an active component amount. The maximum area for all the contacts under study is in the range of 7.0 - 7.6 %. So, those catalyst samples that contain the given amount of active metal have been studied in detail. The results are shown in Tables 1 and 2.

Measurements of radioactivity of thiophene hydrogenolysis products on all the catalysts containing sulfide sulfur labeled by ^{35}S show that radioactivity is present only in H_2S formed. Thiophene that leaves the reactor does not contain radioactivity, which points to the absence of isotope exchange between thiophene sulfur and catalyst sulfide sulfur. In the intervals of thiophene pulses into the reactor or under special experiments any noticeable amount of H_2S formed is not found, *i.e.* any marked sulfidized catalyst reduction does not occur. H_2S is formed only as a product of thiophene hydrogenolysis.

Table 2 gives equations for the curves of dependencies of H_2S molar radioactivity (MR) on the amount of H_2S formed under thiophene HDS on the catalysts sulfidized by radioactive sulfur. One can see that these equations are monoexponential, *i.e.* Co or Ni catalysts or Co+Ni catalysts have one type of H_2S formation site while Co(Ni) promoted Mo catalysts have two types of sites differing on the mobility of sulfur, *i.e.* productivity [35].

Figure 1 shows that treating the reduced catalyst by H_2S/H_2 always results in much deeper sulfidation as compared to thiophene. Share of mobile sulfur in samples sulfidized by H_2S/H_2 ranges within 11 - 50 % and in Ni or Co+Ni catalysts it is higher than in Co ones. It is true both for alumina- and silica supported catalysts and may be due either to high dispersion of Ni-sulfide particles as compared to Co-sulfide ones or to probable CoS_2 phase formation. It is also essential that on alumina supported catalysts, sulfidized by H_2S/H_2, mobile sulfur share is larger than on analogous catalysts supported on silica. It might also be accounted for by higher dispersion of sulfide particles supported on alumina as compared to that of particles supported on silica.

Unlike in catalysts sulfidized by H_2S/H_2, in catalysts sulfidized by thiophene sulfidation does not reach maximum possible values and all sulfide sulfur formed under sulfidation by thiophene is mobile. Major portion of mobile sulfur is on Co/SiO_2 sulfidized by thiophene (sample 2a in Table 1) - 2.42 % and the least (0.63 %) - on the same catalyst sulfidized by H_2S/H_2 (2b). In the first case mobile sulfur equals 100 % of all catalyst sulfide sulfur and in the second - only 11 %. Productivity of Co/SiO_2 catalyst active sites is also much dependent on a sulfidation procedure - under H_2S/H_2 sulfidation it is twice as high as under thiophene. It can be also noted here that this difference is common to other catalysts. In some cases it is noticeably large while in others not (for instance, for Ni/SiO_2 it is not higher than 10 %). We may suppose that under full sulfidation the formation of a substantial amount of immobile sulfur encourages active site formation that have more mobile SH groups as compared to a phase where all sulfur is mobile.If compare Co/SiO_2 and Co/Al_2O_3 catalysts, sulfidized in the same way, one can see that productivities (P) of active sites of these are close. It can be caused by an insignificant effect of carrier nature on reactivity of active sites and by an essential effect of a carrier on the number of the sites.

An effect of active phase metal nature on catalyst active site productivity is clearly seen in the sequence Co - (Co+Ni) - Ni. In all the catalysts supported by one and the same carrier and sulfidized in the same way the productivity grows in the sequence Co ≤ (Co+Ni) ≤ Ni. Thus, SH groups of Ni-sulfide particles demonstrate higher reactivity in H_2S formation under thiophene HDS conditions than analogous SH groups connected with Co. A possible explanation of these dependencies might be searched within Bond Energy Model, recently developed by Topsøe *et al* [37].

The results of radioisotope testing permit us to single out three catalysts with the best characteristics - Co/SiO_2 (sample 2a), $(Co+Ni)/Al_2O_3$ (5b) and Ni/Al_2O_3 (3b). Sample 2a is characterized by the highest amount of mobile sulfur, though its active site productivity is the lowest and it demonstrates no high activity in thiophene HDS. Sample 5b demonstrates the highest thiophene conversion, its mobile sulfur amount is actually the same as in sample 2a, and *P* is considerably higher than in most of catalysts under study. Finally, sample 3b has the highest *P*, highest thiophene conversion and relatively small amount of mobile sulfur. To evaluate the effect of the given parameters on the catalyst functioning under real conditions we have compared them with the data obtained in the course of hydroconversion of residual oil.

3.2. Hydrotreating of residual oil

In the course of the experiments it has been found that, the same as in the above described experiments, most effective have proved catalysts containing 7.5 % metal. Catalysts with 3.4 % metal loading were ineffective. Catalytic activity of samples with metal loading 10 % and higher did not exceed that of the catalysts with 7.5 % metal content.

The data about hydrotreating of residual oil is given in Table 3. First it should be stressed that all the catalysts show a rather high degree of selectivity towards residual oil containing metals (Ni, V) that are poisons for cracking catalysts. The catalysts demonstrate different degree of activity towards the desulfurization reaction, depending on the nature of an active metal and support (Fig. 2). The most active is Co/SiO_2 in reduced form (sample 2a, Table 3) - residua desulfurization degree is 55.7 %. Somewhat less active are reduced catalysts Co/Al_2O_3 (1a) and $(Co+Ni)/SiO_2$ (6a) - 26 % and 27 % correspondingly. Ni reduced catalysts on alumina (3a) and silica (4a) show much less desulfurization activity - 18.0 % and 16.5 % correspondingly. Reduced Co/SiO_2 shows the highest activity in relation to deasphaltization and the lowest towards coke formation. In this catalyst on the silica surface metallic Co of fine dispersion with crystallite size 25 Å has been found. No formation of surface compounds with support is observed. The catalyst has a high specific surface 307 m^2/g pore volume 0.78 cm^3/g, pore average D 46 Å. Co reduction degree is 97 %. If compare pore structure of the support and catalyst one can see that Co loading does not much change the value of specific surface and pore size. It is possible that in the course of the reaction with sulfur containing crudes Co-sulfide particles formation takes place and they are active in hydrogenation (HYD) reactions. Catalyzing residua asphaltenes HYD they practically completely adsorb metals (Ni and V), which leads to a high degree of residua demetallization. Co sulfides as well as pure Co on silica do not catalyze HYD process of hydrocarbons, which is proved by a low coke deposition on these catalysts.

Co/Al_2O_3 in its reduced form (1a) has a sharp difference from Co/SiO_2: desulfurization degree is twice as low and asphaltene disintegration degree is about 50 %. Demetallization degree is lower too. In all probability, incorporation of some part of Co particles in the Al_2O_3 carrier material decreases the ability of Co/Al_2O_3 to interact with the sulfur of residua heterocompounds.

Ni/SiO_2 reduced catalyst (4a) differs with Co one on its catalytic action. Its desulfurization degree is more than three times lower but it is active in asphaltene HYD, demetallization and coke formation. These data testifies to the fact that metallic Ni on silica weakly interacts with the sulfur of sulfurorganic compounds from residual oil and more actively in HYD and deHYD reactions. Reduced Ni/Al_2O_3 (3a) is more active than Ni/SiO_2 in reactions of C-C bond break and coke formation and less active in asphaltene HYD.

Sulfidized forms of Co and Ni catalysts are essentially different from reduced forms of this catalysts on their catalytic activity, which supposes other nature of their interaction with oil residua components. All the sulfide catalysts have proved to be less active in deasphaltization but more active in coke formation (Tab. 3, Fig. 3). Sulfidized Co/SiO_2 (2b) shows the least degree of desulfurization - 13.6 % and highest degree of demetallization among the sulfide catalysts. Obviously, Co sulfide particles in 2a are not so active in desulfurization than reduced Co particles of sample 2b. Sulfidized Ni/Al_2O_3 catalyst (3b) shows rather low activity in oil residua desulfurization, the same as in demetallization and tends to coke formation. A high activity in oil residua desulfurization has been shown by sulfidized $(Co+Ni)/Al_2O_3$ catalyst (5b) - 46 % and at the same time its degree of demetallization is the lowest - 61 %. Its coke deposition is 4.6 %.

3.3. Comparative study of radioisotope testing and residual oil hydrotreating data

While comparing the data of radioisotope testing with the results of residual oil HTR one can see a correlation between residual oil desulfurization degree and the amount of mobile sulfur on the catalyst (Fig. 4). Previously we observed a linear dependency between thiophene conversion and the amount of mobile sulfur in CoMo catalysts [33, 34]. However, as it was found later [35], this dependency was true not in all cases but only for the catalysts active sites of which are characterized by close values of productivity. In Table 1 one can see no correlation between thiophene conversion and the amount of mobile sulfur due to the fact that active site *Ps* of these catalysts differ from each other as much as two - threefold. In case of residual oil, however, such correlation is seen. One can suppose that a large number of contained in crudes and subjected to desulfurization sulfurorganic compounds which possess different degrees of stability in destruction processes as if levels the

values of P of different catalysts.

Hence, it seems we could conclude that such value as productivity is not essential when we deal with processes based on real crudes. But actually it not so at all. It was rather surprising to establish another linear dependency - between productivity of H_2S formation active sites and coke formation on the catalyst - a secondary process in relation to HDS and H_2S formation (Fig. 5). To some extent this dependency can be explained by carrier acidity on coke formation and hydrodesulfurization. The interdependency between carrier acidity and coke formation is commonly known and the dependency between catalytic activity and carrier acidity is marked by Welters *et al.* [38, 39]. Tables 1 and 3 show that the samples of analogous composition and sulfidized in the same way but supported on different carriers differ on the amount of coke deposition and site productivity - for Al_2O_3-supported catalysts these values are higher than for their SiO_2-supported analogs. But this fact can only partially serve as an explanation to the marked dependency. For instance, by acidity one cannot explain higher tendency of Ni-containing catalysts towards coke formation. It seems probable that the higher site productivity the more hydrocarbon fragments are formed in the course of destruction of sulfurorganic molecules and the higher coke formation is.

This supposition is confirmed when we compare the results of residual oil HTR on the above described catalysts non-containing Mo with the results of the same procedure on the commercial Ni-Mo/Al_2O_3 sulfidized catalyst (see Table 3, sample 7). This catalyst has a high desulfurization ability, being inferior only to catalysts 2a and 5b, but it displays rather low demetallization activity and the strongest tendency towards coke formation. The results of radioisotope testing of Ni-Mo/Al_2O_3 were submitted and discussed in [35]. In this paper we present radioisotope testing data only for one, mentioned above, commercial catalyst (the last lines of Tables 1 and 2, sample 7) for comparison with data obtained for non-containing Mo catalysts. Sample 7 is characterized by the presence of two types of active sites, "rapid" and "slow", Ps of which are 20.1×10^{-2} and 5×10^{-2} correspondingly and the number of the 'rapid" sites is 25 % of the total number of the both types of the sites. The amount of mobile sulfur is 41 % of the total sulfide sulfur in catalyst 7. On this catalyst under the same experimental conditions as for the other catalysts thiophene HDS conversion is 59 % *i.e.* much higher than on the catalysts without Mo.

We believe that on the Mo catalyst promoted by Ni or Co the "rapid" sites are related to Mo and the "slow" ones - to Ni or Co. It was shown [33 - 35] that the unpromoted Mo/Al_2O_3 catalyst has one type of the sites of low P ($\approx 5\times10^{-2}$), low catalytic activity in the thiophene HDS (conversion $\approx$ 12 %) and the share of mobile sulfur is about 20 % of the total sulfur amount on the catalyst. Introducing promoter (Ni or Co) increases P of active sites related to Mo, though some part of these are blocked by Ni(Co)-sulfide particles. The total of the active sites on the promoted catalyst grows as compared to the unpromoted one because of an increase in "slow" sites. Evidently, the role of the "rapid" sites in catalyst functioning is dual: on the one hand, the sites increase catalytic activity, on the other - they encourage coke deposition of the catalyst. It is particularly important when processing heavy crudes. It is this dual role of "rapid" sites that we observe during residual hydrotreating on sample 7: the total mobile sulfur is high (actually is the same as in sample 5b), which leads to a high desulfurization activity, and a high P of some part of active sites results in strong coke formation. Thus, there seems to be some ground to state that when selecting most efficient catalysts for residual oil preliminary hydrotreating one should consider as preferable the systems with great amount of mobile sulfur. *i.e.* relatively high number of active sites and low productivity of these.

The study discussed in this paper has permitted us to put forward two catalysts - 7.4 % Co/SiO_2 in its reduced form (sample 2a) and (3.4 % Co + 4.1 % Ni)/Al_2O_3 in its sulfide form (sample 5b) as catalysts-adsorbents for the first stage of hydrotreating of heavy crudes. An important advantage of these catalysts is their relative cheapness due to the absence of expensive Mo in them.

CONCLUSIONS

i. The present investigation gives us ground to state that when selecting most efficient catalysts for residual oil preliminary hydrotreating one should consider as preferable the systems with great amount of mobile sulfur. i.e. relatively high number of active sites and low productivity of these.

ii. The study has permitted us to put forward two catalysts - (7.4 % Co)/SiO_2 in its reduced form and (3.4 % Co + 4.1 % Ni)/Al_2O_3 in its sulfide form as catalysts-adsorbents for the first stage of hydrotreating of heavy crudes. An important advantage of these catalysts is their relative cheapness due to the absence of expensive Mo in them.

REFERENCES

1. J.M.J.G. Lipsh and G.C.A. Schuit, J. Catal., 15 (1969) 163, 174, 179.
2. S.C. Schuman and H. Shalit, Catal. Rev., 4 (1970) 245.
3. R.J.H. Voorhoeve and J.C.M. Stuiver, J.Catal., 23 (1971) 243.
4. G. Hagenbach, Ph. Courty and B. Delmon, J.Catal., 23 (1971) 295.
5. G. Hagenbach, Ph. Courty and B. Delmon, J.Catal., 31 (1973) 264.
6. G. Hagenbach, P. Menguy and B. Delmon, Bull. Soc. Chim. Belg., 83 (1974) 1.
7. C.H. Amberg, Less-Common Met., 36 (1974) 339.
8. P. Grange and B. Delmon, Less-Common Met. 36 (1974) 353.
9. T. Ohtsuka, Catal. Rev., 16 (1977) 291.
10. F.E. Massoth, Adv. Catal., 27 (1978) 265.
11. P. Ratnasamy and S. Sivasanker, Catal. Rev. - Sci. Eng., 22 (1980) 401.
12. H. Topsøe, B.S. Clausen, R. Candia, C. Wivel and S. Morup, Bull. Soc. Chim. Belg., 90 (1981) 1189.
13. H. Topsøe, B.S. Clausen, R. Candia, C. Wivel and S. Morup, J. Catal, 68 (1981) 433, 453.
14. N.-Y. Topsøe and H. Topsøe, Bull. Soc. Chim. Belg., 90 (1981) 1311.
15. H. Topsøe, R. Candia, N.-Y. Topsøe and B.S. Clausen, Bull. Soc. Chim. Belg., 93 (1984) 783.
16. S. Kasztelan, H. Toulhoat, J. Grimblot and J.P. Bonnelle, Appl. Catal., 13 (1984) 127.
17. B. Delmon, Surface and Interface Anal., 9 (1986) 195.
18. S. Kasztelan, L. Jalowiecki, A. Wambeke, J. Grimblot and J.P. Bonnelle, Bull. Soc. Chim. Belg., 96 (1987) 1003.
19. N.-Y. Topsøe, H. Topsøe and F.E. Massoth, J.Catal., 119 (1989)119, 252.
20. L. Viver, P. D'Araujo, S. Kasztelan and G. Perot, J. Mol. Catal., 67 (1991) 267.
21. L. Viver, P. D'Araujo, S. Kasztelan and G. Perot, Bull. Soc. Chim. Belg., 100 (1991) 807.
22. U.S. Oskan, L Zhang, S. Ni and E. Moctezuma, J.Catal., 148 (1994) 181.
23. M. Zdrazil, Appl. Catal., 4 (1982) 107.
24. M.L. Vrinat, Appl. Catal., 6 (1983) 137.
25. R. Prins, V.H.J. de Beer and G.A. Somorjai, Catal. Rev. - Sci. Eng., 31 (1989) 1.
26. B. Delmon, Catal. Lett., 22 (1993) 1.
27. B. Delmon, Bull. Soc. Chim. Belg., 104 (1995) 173
28. A.N. Startsev, Catal. Rev. - Sci. Eng., 37 (1995) 353.
29. H. Topsøe, B.S. Clausen and F.E. Massoth, Hydrotreating Catalysis - Science and Technology, Edited by J.R. Anderson and M. Boudart, Vol. 11, ISBN 3-540-60380-8 Springer-Verlag Berlin Heidelberg, 1996.
30. G.V. Isagulyants, A.A. Greish and V.M. Kogan, Kinetics and Catalysis, Engl. tr., 28 (1987) 220.
31. G.V. Isagulyants, A.A. Greish, V.M. Kogan, G.M.V'unova. G.V.Antoshin, Kinetics and Catalysis, Engl. tr., 28 (1987) 550.
32. G.V. Isagulyants, A.A. Greish and V.M. Kogan, Kinetics and Catalysis, Engl. tr., 28 (1987) 555..
33. G.V. Isagulyants, A.A. Greish and V.M. Kogan, in: "Proc. 9-th Int.Congress on Catalysis", (Calgary, 1988), eds. M.J. Philips and M. Ternan, 1988, Vol. 1, P. 35.
34. V.M. Kogan , A.A. Greish and G.V. Isagulyants, Catal. Letters, 6 (1990) 157.
35. V.M. Kogan, Nguen Thi Dung and V.I. Yakerson, Bull. Soc. Chim. Belg. 104 (1995) 303.
36. V.M. Kogan , A.A. Greish and G.V. Isagulyants, in "Proc. 2-th European Congress on Catalysis", Maastricht, 3-8 September 1995, P.23.
37. H. Topsøe, B.S. Clausen, N.-Y. Topsøe, J.K. Nørskov, C.V. Ovesen and C.J.H. Jacobsen, Bull. Soc. Chim. Belg., 104 (1995) 283.
38. W.J.J. Welters, G. Vorbeck, H.W. Zandbergen, J.W. de Haan, V.H.J. de Beer and R.A. van Santen, J.Catal., 150 (1994) 155.
39. W.J.J. Welters, V.H.J. de Beer and R.A. van Santen, Appl. Catal., 119 (1994) 253.

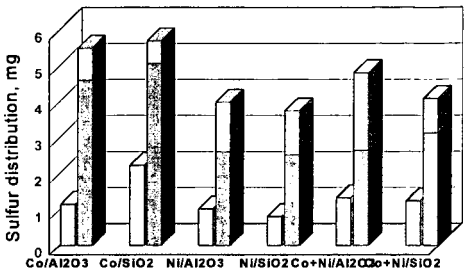

Figure 1. Sulfur distribution *vs.* catalyst composition and pretreatment procedure. Left bars - samples sulfidized by thiophene; right bars - by H_2S/H_2. Light parts of bars - mobile sulfur; dark ones - immobile sulfur (see experimental conditions in Tables 1 or 2).

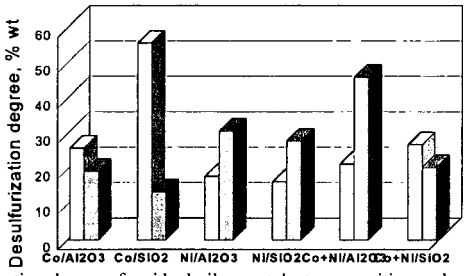

Figure 2. Desulfurization degree of residual oil *vs.* catalyst composition and pretreatment procedure. Left bars - reduced catalysts; right ones - sulfidized catalysts.

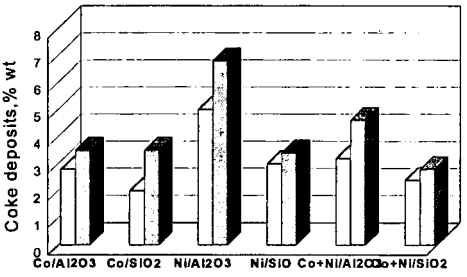

Figure 3. Coke deposition on the catalyst *vs.* composition and pretreatment procedure. Left bars - reduced catalysts; right ones - sulfidized catalysts.

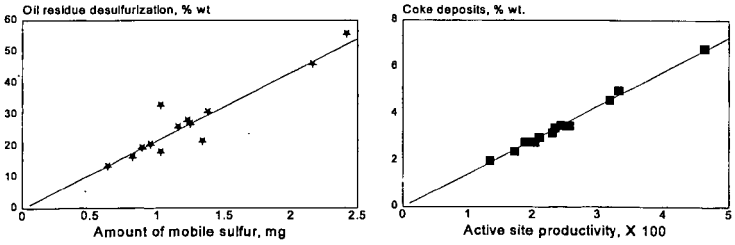

Figure 4. Oil residua desulfurization degree *vs.* amount of mobile sulfur on the catalysts under study.

Figure 5. Coke deposition on the catalyst samples *vs.* active site productivity.

Table 1: Results of radioisotope testing of catalysts in the reaction of thiophene HDS (100 mg sample loading, 360°C, H_2 flow, pulses of thiophene-1-l)

No. smp	Catalyst composition	Pretreatment agent	S_{total} % wt	S_{mob} % wt	S_m/S_t %	*, % mol	P** TM 10^2
1a	(7.0%Co)/Al_2O_3	thiophene	1.16	1.16	100	5.40	1.89
1b	(7.0%Co)/Al_2O_3	H_2S/H_2	5.50	0.89	16.2	5.34	2.43
2a	(7.4%Co)/SiO_2	thiophene	2.42	2.42	100	8.00	1.34
2b	(7.4%Co)/SiO_2	H_2S/H_2	5.70	0.63	11.1	4.00	2.56
3a	(7.6%Ni)/Al_2O_3	thiophene	1.03	1.03	100	8.43	3.33
3b	(7.6%Ni)/Al_2O_3	H_2S/H_2	4.00	1.38	34.5	15.70	4.63
4a	(7.3%Ni)/SiO_2	thiophene	0.82	0.82	100	4.25	2.10
4b	(7.3%Ni)/SiO_2	H_2S/H_2	3.76	1.23	32.7	7.25	2.34
5a	(3.4%Co+4.1%Ni)/Al_2O_3	thiophene	1.34	1.34	100	7.62	2.30
5b	(3.4%Co+4.1%Ni)/Al_2O_3	H_2S/H_2	4.82	2.16	45.0	17.00	3.19
6a	(3.5%Co+3.5%Ni)/SiO_2	thiophene	1.25	1.25	100	5.35	1.73
6b	(3.5%Co+3.5%Ni)/SiO_2	H_2S/H_2	4.10	0.95	23.2	4.15	2.03
7***	Ni-Mo/Al_2O_3	H_2S/H_2	6.08	2.49	41.0	59.00	20.1 5.4

*) γ - thiophene conversion; **) P - active site productivity; ***) commercial catalyst

Table 2: Change of H_2S molar radioactivity (α) in the course of thiophene HDS on sulfide-^{35}S catalysts (100 mg sample loading, 360°C, H_2 flow, pulses of thiophene-l-1)

No smp	Catalyst	H_2S MR	No smp	Catalyst	H_2S MR
1a	Co/Al_2O_3	= 100 exp(-1.23x)	4a	Ni/SiO_2	= 100 exp(-1.74x)
1b	Co/Al_2O_3	= 100 exp(-1.60x)	4b	Ni/SiO_2	= 100 exp(-1.16x)
2a	Co/SiO_2	= 100 exp(-0.59x)	5a	(Co+Ni)/Al_2O_3	= 100 exp(-1.07x)
2b	Co/SiO_2	= 100 exp(-2.26x)	5b	(Co+Ni)/Al_2O_3	= 100 exp(-0.66x)
3a	Ni/Al_2O_3	= 100 exp(-1.39x)	6a	(Co+Ni)/SiO_2	= 100 exp(-1.14x)
3b	Ni/Al_2O_3	= 100 exp(-1.04x)	6b	(Co+Ni)/SiO_2	= 100 exp(-1.50x)
7	NiMo/Al_2O_3	= 52.08 exp(-1.20x) + 47.92 exp(-0.32x)			

Table 3: Results of hydrotreating residual oil of West-Sibirian petroleum (initial residual oil contained: asphaltenes - 4.3 %, S - 2.3 %, V - 40g/ton, Ni - 20 g/ton).

No smp	Catalyst composition	Pre-treatment*	Desulfur. degree, % wt.	Demetall degree, % wt.	Residual asphaltenes % wt.	Coke deposits % wt.
1a	(7.0%Co)/Al_2O_3	R	26.0	80.0	2.1	2.8
1b	(7.0%Co)/Al_2O_3	S	19.4	80.0	2.0	3.5
2a	(7.4%Co)/SiO_2	R	55.7	95.6	0.5	2.0
2b	(7.4%Co)/SiO_2	S	13.6	89.0	1.3	3.5
3a	(7.6%Ni)/Al_2O_3	R	18.0	82.0	1.2	5.0
3b	(7.6%Ni)/Al_2O_3	S	30.8	80.0	2.0	6.8
4a	(7.3%Ni)/SiO_2	R	16.5	90.5	1.0	3.0
4b	(7.3%Ni)/SiO_2	S	28.0	78.0	1.8	3.4
5a	(3.4%Co+4.1%Ni)/Al_2O_3	R	21.5	76.0	2.7	3.2
5b	(3.4%Co+4.1%Ni)/Al_2O_3	S	46.0	61.0	3.8	4.6
6a	(3.5%Co+3.5%Ni)/SiO_2	R	27.0	79.0	2.4	2.4
6b	(3.5%Co+3.5%Ni)/SiO_2	S	20.5	76.0	2.6	2.8
7	(Ni+Mo)/Al_2O_3**	S	32.9	75.5	2.8	10.5

*) R - reduction; S - sulfidation after reduction; **) commercial catalyst

A NEW LASER DIAGNOSTIC TECHNIQUE TO EVALUATE CHEMICAL TIME DELAY IN HYPERGOLIC SYSTEMS

Lynette O. Mays, Mark J. Farmer, James E. Smith, Jr.
Department of Chemical and Materials Engineering
Material Science Building, Room 307
University of Alabama in Huntsville
Huntsville, Alabama 35899

INTRODUCTION

Diagnostic techniques that measure ignition delay times (IDT) of hypergolic reactants are normally classified into a few distinct types. Drop tests are techniques that drop one reactant from a set height into a stationary quantity of the second reactant. Mixing tests are techniques that use a method to enhance mixing of the reactant combinations. Impinging jet techniques are tests that use separate fuel and oxidizer injectors to enhance the mixing rate and simulate engine conditions. Also, a few small scale rocket engines have been equipped to measure ignition delay times.

A typical example of a drop test technique was performed by Broatch[4]. A light beam was focused on a photocell a set distance above the organic fuel, which was located in a crucible. The oxidizer, in a stream of droplets of varying size, broke the light beam as it fell into the fuel. A photocell ended the measurement when it sensed the appearance of a flame. The time between these two events defined the ignition delay for the hypergolic reactant combination. A technique used by Gunn[6] was defined as a mixing test by Paushkin[3] in his review of jet fuels. The only significant difference from Broatch's technique described above was that the quantity of fuel and oxidizer used by Gunn was several times as large. Several milliliters of one reactant was decanted into a similar quantity of the other reactant. The photocell used by Gunn to detect the flame, and the one used in Broatch's technique above, did not indicate the strength of the reaction.

In an effort to reduce the mixing time, a device constructed by Pino[7] caused the pressurized injection of oxidizer through 4 ports directed into a stationary quantity of fuel. The combined quantity of fuel and oxidizer used was approximately 4 milliliters for one test. The results of Pino's testing show no indication of the oxidizer to fuel ratio. Without this variable accounted for, the minimum ignition delay for a reactant combination will not likely be found. Ladanyi and Miller[1] placed a small glass ampoule containing approximately one milliliter of organic under the surface of several milliliters of acid. The glass ampoule was crushed by a steel rod to enhance mixing. The initial measurement was the moment of ampoule crushing. The final measurement was made by a photocell sensing the appearance of a flame. Kilpatrick and Baker[5] used a device that forced both fuel and oxidizer together using high pressure gas hydraulics. The reactants were initially located in separate chambers below pistons which forced the propellants together immediately prior to injection into the combustion chamber. The initiation of the timing measurement was through monitoring of piston movement above the fuel and oxidizer. The end of an ignition delay measurement corresponded to an increase of pressure in the test chamber.

Saad and Goldwasser[8] used impinging fuel and oxidizer jets in their technique. They initiated the ignition delay measurement at the moment the valves for fuel and oxidizer were released. Photocell detection of the flame was again used to end the measurement. The resolution of their oscilloscope was 100 milliseconds/division. As ignition delay values are generally less than 100 milliseconds, the resolution of their technique does not provide the accuracy needed for reactions of this speed. In addition to the drop test technique reported earlier, Broatch[4] also used the technique of impinging jets. He used high speed photography to capture pictures of the combined jets and flame. The ignition delay was calculated from the length of the combined jets to the fully developed flame front. The benefits of the photography technique were to capture the strength of the flame as Broatch varied oxidizer to fuel ratio and temperature, and the ability to photograph phenomena such as pre-ignition boiling of the liquid phase. Spengler and Bauer[9] used impinging jets to test the influence of pressure and varying chemical composition on ignition delay measurements. This technique consisted of starting the timing by contacting the fuel and oxidizer, which completed an electrical circuit. The timing measurement was ended by sensing the flame with a photocell located between the two injectors. This technique for impinging jets seemed to be the only true measure of ignition delay among the three discussed.

If the intent of the ignition delay technique is to screen reactant combinations, then the above testers should provide reliable information on relative performance between these combinations. The new laser diagnostic method developed in our laboratories was designed as a research tool to measure relative performance of hypergolic reactant combinations. The technique developed, more than met this expectation. The technique is the first to provide a measure of the chemical

performance of the reactant combinations. This chemical delay time is independent of the mixing technique used.

EXPERIMENTAL

The entire combustion system is designed to study the reaction rates and mechanisms of hypergolic reactants for the ability to propose alternate, enhanced chemistry. The equipment uses a variety of techniques, including visible and near infrared Raman spectroscopic measurements, to meet these objectives. The system, its component make-up, and procedural steps are detailed in recent publications by M. Farmer, L., Mays and J.E. Smith, Jr.[10,12,13].

RESULTS AND DISCUSSION

Figure 2 shows the digital storage oscilloscope traces resulting from a typical drop test for unsymmetrical dimethylhydrazine (UDMH) contacted with red fuming nitric acid (RFNA). The reactants for the test were obtained from Aldrich Company. The UDMH had a purity of 98%. The RFNA had a nitric acid concentration of 90-95%, with the balance being nitrogen tetroxide. The results in this figure are for an oxidizer to fuel ratio of 2. In Figure 2, the upper trace (channel 1) shows the output from photodiode #1, which monitors the surface of the oxidizer droplet. The lower trace (channel 2) shows the output from photodiode #2, which monitors flame emission.

Various reference points have been added to this figure to identify key features resulting from this technique. Point A on channel 1 represents the moment of contact between the fuel and oxidizer. A pinhole/diode geometry restricts he view of the photodiode to a region from the oxidizer surface to approximately 200 μm above the surface. Once the lower surface of the fuel droplet contacts the oxidizer, a region of rapid linear decrease follows. To consistently reference the ignition time delay to a definable point, we extrapolate this linear region to the initial reference level. An identical approach is used at point B to neglect the shape of the trailing edge of the droplet and any wake that it creates on entry. Thus, the region from point A to point B represents the droplet of fuel from initial contact to final entry into the oxidizer. When the fuel droplet completely enters the oxidizer, the laser light can again fully reach photodiode #1 as illustrated by the return of the signal to its initial reference level.

The response of photodiode #1 in the region from point B to C is representative of a still liquid to air interface. This is the region in which droplet mixing is taking place between fuel and oxidizer by a combination of convection and diffusion between the two reactants. In Figure 2 region B-C represents the time period when mass transfer limited kinetics are occurring. In other words, the rate of reaction is limited by mass transfer and mixing limitations. All methods reviewed above suffer from mixing limitations at some point in the process. Kilpatrick and Baker[5], in their study of mixing rates, stated, "If the complete intermixing could be effected in a time very short compared to the (total) ignition delay time, then the measured delay would be the true chemical delay...." Pino made the same observation during attempts to improve mixing with his technique. Following their logic, if the droplet entry and mixing stages, points A-C, could be minimized or eliminated, then region C-D in Figure 2 would represent the true chemical delay.

At point C, the chemical reaction rate increases rapidly, with the reaction producing a gas phase that decreases the signal from photodiode #1. This decrease in signal is due to the density of the vapor phase forming above the liquid surface. This vapor phase was noticed in the work of Ladanyi and Miller[1] using an injector technique with high speed photography. Upon mixing, they noted a thick vapor cloud released by the liquid phase that filled their combustion chamber. Close examination of the photographs was required to locate the appearance of flame within this dense cloud. This vapor phase results from reactive intermediates being released from the liquid phase.

The combination of heat release from the chemical reaction in the liquid phase and the reactivity of the gaseous intermediates causes ignition in the vapor phase, as defined by point D. This analysis is supported in the literature by the work of Saad and Goldwasser[8], Spengler and Bauer[9], Twardy[2], and Habiballah[15]. For example, Saad and Goldwasser[8] found in their work that the liquid phase generated heat 200 times more rapidly than the gas phase at atmospheric pressure. Twardy[2] found that a minimum droplet diameter was required to generate the heat necessary to cause ignition in the reactive vapor phase.

Durgapal and Venugopal[14] performed an ampoule crushing test similar to Ladanyi and Miller[1] to enhance mixing in the RFNA/UDMH combination. For RFNA that had 92% HNO_3 and 8% N_2O_4, they obtained an ignition delay value of 4.7 milliseconds. This value is much smaller than the IDT value, region A-D in Figure 4, of 16.5 milliseconds. If the time for droplet entry is ignored, then the measure would be of mixing time to ignition, i.e., region B-D in Figure 2, or 9.5 milliseconds. This is not surprising though, as no attempt was made to enhance mixing for

the technique presented in this paper. Therefore, Durgapal and Venugopal[14] should have recorded numbers smaller than those of region B-D. However, it one examines region C-D, then a delay of 1.8 milliseconds is measured. This time is a measure from the moment vaporization begins to increase exponentially to ignition. As all hypergolic systems, upon completion of mixing, produce a vapor phase reaction, this period represents a true measure of chemical performance or the chemical delay time.

The importance of the chemical delay time is seen when one compares hydrazine reacted with RFNA (Figure 3) to UDMH reacted with RFNA (Figure 2). Comparing these figures, we see that the ITD for UDMH/RFNA is only 25% faster than hydrazine/RFNA. When one compares the chemical delay time a 75% increase in the reaction rate is measured. This explains why UDMH/RFNA is preferred over hydrazine/RFNA for propulsion systems.

CONCLUSIONS

A new laser diagnostic technique has been developed to quantitatively measure the chemical performance of hypergolic systems. Past techniques and results show that enhanced mixing can reduce ignition delays in an attempt to approximate the chemical delay time. Regardless of technique, the mixing time associated with hypergolic systems can not be eliminated. This drop test technique shows a region after mixing that characterizes the speed of the reaction alone. The beginning of this region, point C, indicates when free radical generation should be observed to obtain information on the chemical mechanisms involved. This new technique requires smaller quantities of reactants than previous methods making it safer and more cost effective.

ACKNOWLEDGEMENTS

This research is funded by the Army Missile Command, grant #DAA H01-91-D R002/D053, and the Army Research Office, grant #DAA 1104-94-G-0265.

REFERENCES

1. D.J. Ladanyi and R.O. Miller, "Two Methods for Measuring Ignition Delay of Self-Igniting Rocket Propellant Combinations," *Jet Propulsion*, Vol. 26, No. 3, pp. 157-63.
2. H. Twardy, "Studies on the Effect of Fuel Injection on the Ignition Process of the Hydrazine-Nitric Acid System," Jet Propulsion Laboratory, DLR FB 68-85.
3. Y.M. Pauskin, The Chemical Composition and Properties for Fuels for Jet Propulsion, Pergamon Press, New York, 1962.
4. J.D. Broatch, "An Apparatus for the Measurement of Ignition Delays of Self-Igniting Fuels," *Fuels*, Vol. 29, 1950, pp. 106-109.
5. M. Kilpatrick and L. Baker, Jr., *Fifth Symposium on Combustion*, pp. 170-196, New York-London 1955.
6. S.V. Gunn, "The Effects of Several Variables Upon the Ignition Lag of Hypergolic Fuels Oxidized by Nitric Acid," *ARS Journal*, Vol. 22, No. 1, pp. 33-38.
7. M.A. Pino, "A Versatile Ignition Delay Tester for Self-Igniting Rocket Propellants," *Jet Propulsion*, Vol. 25, No. 9, pp. 463-466.
8. M.A. Saad and S.R. Goldwasser, "Role of Pressure in Spontaneous Ignition," AIAA Journal, Vol. 7, No. 8, pp. 1574-1581.
9. G. Spengler and J. Bauer, "Ignition Delay of Hypergolic Rocket Propellants," *Technical Translation 16-U.S. Army*, June 1966.
10. M. Farmer, L. Mays, and J.E. Smith Jr., "A Laser Diagnostic Method to Measure Ignition Time Delays of Hypergolic Reactions," AIAA, January 6-9, 1997.
11. Wade, L.G., Organic Chemistry, 2nd edition, Prentice-Hall, Englewood Cliffs, N.J., 1991, pp. 823-886.
12. Farmer, M., Mays, L., and J.E. Smith, Jr., "A Laser Diagnostic Technique to Measure Rapid Acid-Organic Reaction Phenomena," 1997 AIChE Spring Meeting, paper 140e, Houston, TX, February 1997.
13. Farmer, M., Mays, L., and J.E. Smith, Jr., "The Reaction Rates for Hypergolic Propellants Using Chemical Delay Times," submitted to AIAA, Journal of Propulsion and Power, May 1997.
14. Durgapal, U. C., and Venugopal, V. K., "Hypergolic Ignition of Rocket Propellants with Nitric Acid Containing Dissolved Nitrogen Tetroxide," *AIAA Journal*, Vol 12, No. 11, pp. 1611-1612.
15. Habiballah, M., et al., "Experimental Study of Combustion Processes Involved in Hypergolic Propellant Coaxial Injector Operation," *AIAA/SAE/ASME/ASEE 28th Joint Propulsion Conference and Exhibit*, AIAA-92-3388, July 6-8, 1992.

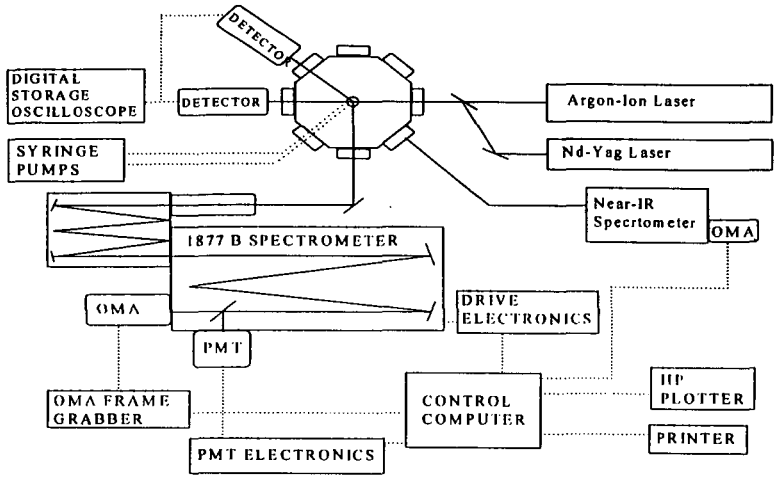

Figure 1. Schematic of the Entire System for Ignition Time Delay and Spectroscopic Analysis

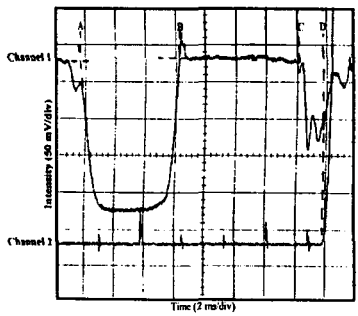

Figure 2. Test Results for UDMH/RFNA

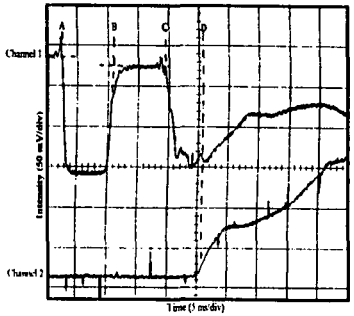

Figure 3. Test Results for Hydrazine/RFNA

USING STRUCTURAL MODELS TO SIMULATE THE POLY-CYCLICS IN COALS.

David L.Wertz
Department of Chemistry and Biochemistry
University of Southern Mississippi
Hattiesburg, MS 39406 USA

Keywords: Poly-cyclic aromatic compounds, molecular modeling, x-ray scattering

INTRODUCTION.

Both NMR[1-4] and other types of analysis[5-10] have recently made significant contributions to understanding the composition and the distribution of the poly-cyclic units which are thought to comprise the most important units in coals. This group[10-13] has recently contributed some x-ray scattering studies which have as their goal a better understanding of the poly-cyclic units. X-ray scattering studies are one-dimensional in nature and address distances in the average scattering unit of a condensed phase material.[14] Structural models of some poly-cyclic (PC) moieties thought to be found in coals have been developed in order to better interpret and understand the x-ray scattering data obtained from these coals. Our models are based on the findings of the NMR and other studies noted above. The structural PC models may be utilized in real space to predict distances between bonded C-C atom-pairs and between non-bonded C··C atom-pairs. In addition, the distance array calculated for each PC model may be Fourier transformed into reciprocal space and compared to the experimentally measured x-ray scattering intensity for a coal (or any other scattering unit).

Whether the analysis occurs in reciprocal space or in real space, the accuracy of the structural models is as important as the accuracy of the x-ray scattering experiments to developing an understanding of the average PC unit in the coal.

EXPERIMENTAL

This group has "built" three-dimensional structural models of several of the poly-cyclic (PC) compounds thought to occur in coals. These models incorporate the "best available" crystallographic data concerning the various C-C bond distances and the C··C·C bond angles as well as information about the planarity of each aromatic ring as well as the co-planarity of each entire PC unit. From the bond distance-bond angle-planarity information, an atom-coordinate map for each of the carbon atoms has been constructed. All of the bonded and non-bonded C··C atom-pair distances have been calculated. The distance array calculated for each PC model has been used to construct a simulated structure curve, in real space, by:

$$W_A(r) = 36\ el^2 \times \sum\{n_{JK}/r_{JK}^{0.5}\} \times \exp(-\gamma \times \Delta r_{JK}^2/r_{JK}^{0.5}). \qquad (1)$$

This real space simulation has been adapted from the Kurrita model for diffraction peaks[15] and is consistent with the shapes of the maxima and minima in the atom-pair correlation functions calculated from x-ray scattering measurements of several of the Argonne Premium Coals.[11-13] In eq. 1, 36 el^2 represents the scattering power of one C-C atom-pair, and n_{JK} represents the number of J-K atom-pairs found at the distance r_{JK} in the average short-range scattering unit of the coal, and $\Delta r_{JK} = r - r_{JK}$.

RESULTS AND DISCUSSION.

Analysis in Real Space. The atom-map and the three-dimensional atomic coordinates developed for naphthalene are presented in Table I. The distance/frequency arrays for naphthalene, anthracene, and phenanthrene are presented in Table II. Shown In Figure I are the simulated real-space structure curves calculated for benzene, naphthalene, anthracene, and naphthacene. Each of these models has been developed based on the first approximation that all of the bonded C-C atom-pair distances are 1.39 Å, that each of the C··C··C bond angles is 120° (i.e., $\phi = 2\pi/3 - \pi/2$ in Table II), and $\tau = 0$ (i.e., the PC rings are co-planar). Numerous other combinations of d, ϕ, and τ have been considered. The longest non-bonded C··C distance is marked by * in each $W_A(r)$. Differences in the longest non-bonded C··C distance and other differences) are clear from comparison of these simulated $W_A(r)$'s.

The simulated structure curve calculated from each model may be compared to the atom-pair correlation function (APCF). The APCF is experimentally determined and

provides a measure of the deviation from randomness of the atom-pairs in the scattering material. The APCF, g(r), is limited to describing a one-dimensional description (i.e., atom-pair distances) which characterize the structuring found in the average short-range structural unit of the subject material (i.e., the coal)and may be obtained from measuring the secondary coherent X rays scattered by the coal.

Correlation between the simulated structure curve calculated from each PCA model, $W_A(r)$, and the experimentally-based atom-pair correlation function, g(r), is initiated by calculating the difference function for each model:

$$\varepsilon_A(r) = W_A(r) - g(r). \quad (2)$$

The difference function is then used to calculate the structure correlation factor for each model by:

$$R_A = \Sigma[\varepsilon_A(r)]^2/\Sigma[g(r)]^2. \quad (3)$$

As with three-dimensional crystal structure analyses, the simulated structure considered to be best representation real-space structure results fram the model which minimizes R_A.

Shown in Table III is are the structure correlatian factars calculated for several PC models campared to the APCF obtained fram Pittsburgh # 8 coal, a high volatile bituminous coal. These comparisans show that g(r) correlates best with the W(r)'s calculated for the two C_{14} PC models> The R_A's praduced for anthracene and for phenanthrene are similar.

Inclusian of the alkyl moieties into the structural model improves the correlation between $W_A(r)$ and g(r) for both phenanthrene and for anthracene. Shown in Figure 2 is a comparison of the $W_{AN}(r)$ with the addition of faur alkyl moieties added to the C_{14} unit. This arrangement produces lower R_A's for bath the anthracene and the phenanthrene models, as seen in Table IV.

Correlatians in Reciprocal Space. The simulated structure curve, W(r), may be Fourier transformed to produce the simulated x-ray scattering intensity in reciprocal space by:

$$J(Q) = \{4\pi/Q\} \times \Sigma n_{JK} \times \int r^2 \times \{W_A(r) - \rho o\} \times \sin (Q \times r) \times \Delta r; \quad (4)$$

where ρ_o is the bulk atom density of the coal.

Defining i(Q) as the experimentally determined intensity in reciprocal space, the comparison between I(Q) and J(Q) may also be used to evaluate the validity of the PC model(s) being considered. Shawn in Figure 3 is the J(Q) calculated from the 4 alkyl-onthracene model compared to I(Q). The correlation factor for the comparison in reciprocal space is termed R*, where:

$$R^* = \Sigma\{i(Q) - J(Q)\}^2/\Sigma\{i(Q)\}^2 \quad (5).$$

Using the alkyl substituted anthracene as the PC model, R* = 0.039 when R* is evaluated from Q = 2.00 Å-1 to 15.00 Å-1. If the region < Q = 2.00 Å-1 is included in the calculation, R* increases dramatically to 0.768; indicating that the large peak in i(Q) centered at 1.7 Å-1 is not due to the average PC structure in the coal. Similar results have been obtained when an alkyl substituted phenanthrene model is used to generate J(Q). All other PCA models produce R* values which are much larger than the R*'s measured for the substituted C_{14} PC's.

CONCLUSIONS

Structural models and detailed atom maps are useful in determining the average PC unit in coals because their simulated structure curves may be directly campared to the results of wide angle x-ray scattering experiments used to examine the coals. However, the resulting statistical analysis does not, necessarily, produce unequivocal results.

REFERENCES

1. Solum, M. S., Pugmire, R. J., and Grant, D. M., *Energy Fuel, 1989 (3) 187.*
2. Muntean, J. V. and Stock, L. M., *Energy Fuel, 1991 (5) 768; 1993 (7) 704.*
3. Franz, J. A., Garcia, R., Lineman, J. C., Love, G. D., and Snape, C. E., *Energy Fuel, 1992 (6) 598.*
4. Codeine, K., Mariti, S., and Nomura, M., *Energy Fuel, 1996 (10) 672.*
5. Winans, R. E., *Am. Chem. Soc., Div. fuel Chem., 1994 (39) 27.*
6. Thiyagarajan, P. and Cody, G. D., *Am. Chem. Soc., Div. Fuel Chem.,* 1997 (42) 253.
7. Takanohashi, T., Iina, M., Kumagai, H., Sanada, Y., and Nakamura, K., "Coal Science". J. A. Pajares and J. M. D. Tascon, ed., Elsevier Science, Amsterdam,

TABLE II. ATOM-PAIR DISTANCE/FREQUENCY ARRAY FOR NAPHTHALENE, ANTHRACENE, AND PHENANTHRENE

DISTANCE (d_{JK})	FREQUENCY (n_{JK}) IN		
	NAPHTHALENE	ANTHRACENE	PHENANTHRENE
1.39 Å	11	17	17
2.47 Å	14	22	21
2.78 Å	6	8	10
3.68 Å	6	12	13
4.17 Å	4	8	10
4.82 Å	2	6	8
5.01 Å	2	4	6
5.56 Å		2	2
6.07 Å		4	2
6.37 Å		4	4
6.96 Å			1
7.23 Å		2	
7.36 Å		2	

TABLE III. STRUCTURE CORRELATION FACTORS BETWEEN SEVERAL PCA MODELS AND THE APCF FOR PITTSBURGH # 8 COAL.

Carbons	PC MODEL	R-VALUEA
C10	naphthalene	0.303
C14	anthracene	0.053
	phenanthrene	0.079
C16	pyrene	0.334
C18	naphthacene	0.750
	1,2-benzophenonthrene	0.553
	crysene	0.568
	tri-phenylene	0.396

[A] R has been calculated over the interval from r = 0.00 Å to r = 10.00 Å.

TABLE IV. EFFECTS OF ADDING FOUR ALKYLS TO THE C_{14} PC MODELS.

PC MODEL	4 ALKYS ADDED	R_A
Anthracene	no	0.053
	yes	0.046 to 0.037[A]
Phenanthrene	no	0.079
	yes	0.062 to 0.040[A]

[A] The actual value of the structural correlation factor depends upon the relative positions of the alkyls as added to the C_{14} unit.

1995, 55.
8. Stock, L.M. and Obeng, M., *ibid.*, p. 67.
9. Winans, R. E., Kim. Y., Hunt, J. E., and McBeth, R. L., *ibid.*, 87.
10. Zhan, Q., Zenobi, R., Buseck, P. R, and Teerman, S., *Energy Fuel, 1997* (11) 144.
11. Wertz, D. L.. and Bissell, M., *Adv. X-Ray Anal., 1994* (37) 491.
12. Wertz, D. L. and Bissell, M., *Fuel, 1995* (74) 1431.
13. Wertz, D. L. and Bissell, M, *Energy Fuel,* 1994 (8) 613.
14. Kruh, R. F.., *Chem. Rev.*, 1962 (62) 314.
15. Kurita, M., *Adv. x-Ray Anal., 1987* (31) 277.

TABLE I. ATOM MAP AND ATOM LOCATIONS FOR NAPHTHALENE

A. ATOM MAP.

TOP VIEW OF XY PLANE SIDE VIEW, XZ PLANE

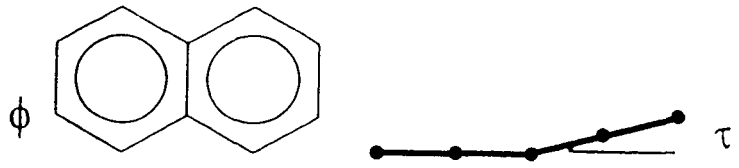

B. ATOM LOCATIONS.

CARBON		ATOM LOCATIONS	
NUMBER	X	Y	Z
1	0	0	0
2	0	d	0
3	d×cosϕ	d×[1+sinϕ]	0
4	2×d×cosϕ	d	0
5	2×d×cosϕ	0	0
6	d×cosϕ	-d×sinϕ	0
7	d×cosϕ×[2+cosτ]	-d×sinϕ	d×cosϕ×sinτ
8	2×d×cosϕ×[1+cosτ]	0	2×d×cosϕ×sinτ
9	2×d×cosϕ×[1+cosτ]	d	2×d×cosϕ×sinτ
10	d×cosϕ×[2+cosτ]	d×[1+sinϕ]	d×cosϕ×sinτ

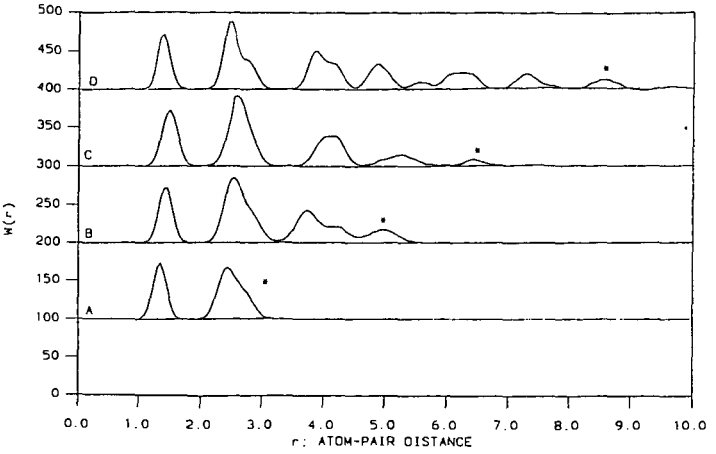

Figure 1. W(r)'s for benzene (A), naphthalene (B), anthracene (C), and naphthacene (D). The longest non-bonded C··C distance in each is marked by *.

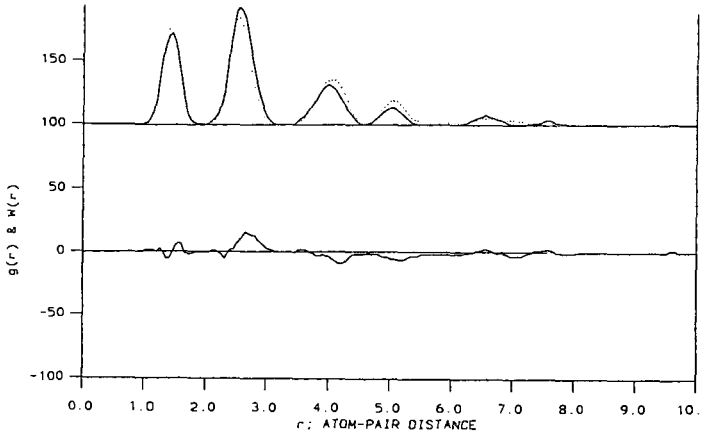

Figure 2. W(r) for the alkylated C_{14} PC {....} compared to the APCF {____}. The ε(r) for this comparison is shown below.

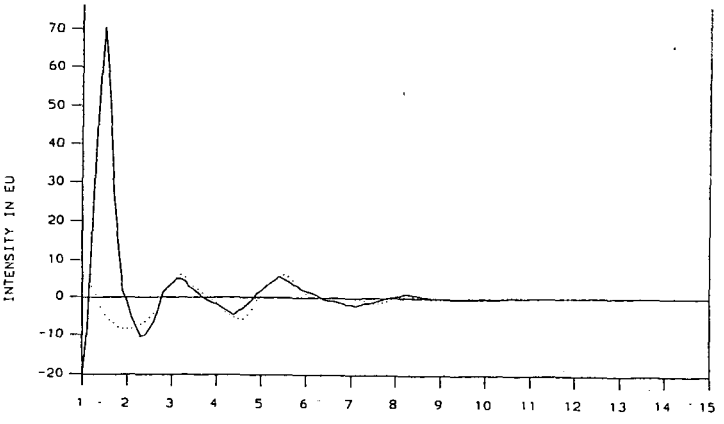

Figure 3. Comparison in reciprocal space of the simulated intensity for an alkylated C_{14} PC unit {....} and the experimentally measured intensity {____}.

EFFECTS OF TEMPERATURE AND PRESSURE ON THE STRUCTURE OF FGD SCRUBBER SLUDGE

S. P. Kelley[1], P. S. Valimbe[1], V. M. Malhotra[1], and D. D. Banerjee[2]
(1) Department of Physics, Southern Illinois University, Carbondale, IL 62901
(2) Illinois Clean Coal Institute, Carterville, IL 62918.

ABSTRACT

Approximately 20 million tons of flue gas desulfurization (FGD) residue are generated in the US every year. To find cost effective disposal approaches for FGD residue, we are attempting to fabricate composite materials from the sludges. We subjected the as- received scrubber sludge (CWLP, Springfield, Illinois) and the sludge which had been dried at 180°C to various formation pressures and temperatures to form 3.2 and 5.7 cm diameter cylinders. The chemical and physical structures of the pressurized materials were probed using scanning electron microscopy (SEM), transmission-Fourier transform infrared (FTIR), and differential scanning calorimetry (DSC) techniques. The formation temperature ($20°C < T < 220°C$) and pressure ($400 \text{ psi} < P < 5500 \text{ psi}$) were variables. The formation pressure did not affect the crystal growth habits of the materials. However, the formation temperature not only controlled the size of the crystallites in our materials, but it also influenced the chemical structure of the fabricated materials.

INTRODUCTION

In the past when electric power utilities shifted from oil to coal for electric power generation, it created environmental concerns related to the emission of SO_x and NO_x from the combustion of coal [1]. These gases are formed in combustion units due to oxidation of sulfur and nitrogen present in coal. To mitigate environmental concerns, various technologies have been developed including Flue Gas Desulfurization (FGD). FGD technology involves the use of scrubbers which utilize lime or limestone to capture the flue gasses. Unfortunately, though FGD technology is successful in reducing the emission of undesirable gases, it generates a large quantity of solid waste in the form of scrubber sludge. In fact, approximately 20 million tons of FGD residues are generated annually in the United States. The properties of these solid wastes strongly depend on the type of coal used in the combustion units as well as the desulfurization process employed [2]. In general, the scrubber sludge is believed to contain mostly gypsum ($CaSO_4.2H_2O$), calcium sulfate ($CaSO_4$), calcium sulfite ($CaSO_3$), calcite ($CaCO_3$), and in addition small quantities of fly ash and excess reagents [3,4]. Of the different types, wet scrubber units are the most commonly used for SO_2 removal from flue gases. The purity of gypsum obtained from a wet scrubber unit is believed to range from 95% to 99%.

The disposal of 20 million tons of scrubber sludge annually is in itself becoming a serious economic problem for coal utilities. Even though different usages of scrubber sludges have been proposed in road base construction [5,6], prefabricated products (gypsum boards) [7], the cement industry [5,7], plaster fabrication [7], and agriculture [7,8], their overall utilization is still very small. This is largely due to the changes in the sludges' properties from batch to batch and unit to unit as well as to market specifications and seasonal variations. Unfortunately, a major portion of the total amount of scrubber sludge generated continues to be dumped in landfills.

The implementation of the Clean Air Act of 1990 will require new utilization of scrubber sludges. Proposed applications of synthetic gypsum, produced by certain power plants, are the formation of plaster [7], formation of binder material, self leveling floor screeds, and fiber reinforced slabs from FGD sludge [9]. In addition, we have been exploring techniques of forming structural composite materials from both sulfate- and sulfite-rich FGD sludges. Before these technologies can be matured, we must understand how formation pressure and temperature affect the crystalline growth habits of the sludge and how these parameters affect the structure of the formed material. Therefore, we subjected a sulfate-rich scrubber sludge to various structural formation conditions and examined the formed materials with the help of SEM, DSC, and FTIR techniques.

EXPERIMENTAL TECHNIQUES

The present study is based on materials fabricated from a scrubber sludge generated by the City Water and Light Power plant (CWLP) in Springfield, Illinois. The scrubber sludge sample was obtained from the sample bank maintained by the Department of Mining Engineering at Southern Illinois University, Carbondale, Illinois. The as-received sample was in a thick slurry form, and

the sample was air dried at room temperature prior to fabricating materials from it. Our characterization studies showed this material to be largely $CaSO_4.2H_2O$ [10].

The cylindrical disks of the material were formed by hot pressing the CWLP scrubber sludge in dies of diameter 3.2 cm and 5.7 cm, respectively. The length of the cylinders varied from 2.5 cm to 7.5 cm. We used temperature ($20°C < T < 220°C$), pressure ($400 \text{ psi} < P < 5000 \text{ psi}$), and hot pressing time ($15 \text{ min.} < T < 120 \text{ min.}$) as variables in forming the materials. We fabricated our disks using two different methods. In the first, the air dried samples were used with water to form a slurry paste, which was subjected to the conditions mentioned above. In the second approach, the CWLP scrubber sludge was thermally treated in air at 180°C for two hours to convert the sludge into hemihydrate ($CaSO_4.0.5H_2O$) crystals. This white powdery material was then combined with water to form a slurry [11] which was subsequently used to form the cylinders as described above. The formation parameter summary and identification of the samples are listed in Table 1.

Table 1
The sample identity and formation conditions of cylindrical disks.

Sample Identity	Formation Conditions		
	Time (minutes)	Pressure (psi)	Temperature (°C)
CWLP A1	20	5,000	24
CWLP A2	20	4,000	24
CWLP A3	20	3,000	24
CWLP A4	20	2,000	24
CWLP B1	20	4,000	60
CWLP B2	20	4,000	100
CWLP B3	20	4,000	140
CWLP B4	20	4,000	180
SPK 31	90	2,500	94
SPK 32	90	2,500	125
SPK 29	90	2,500	200
SPK 33	90	500	160
SPK 34	90	1,500	160
SPK 35	90	4,500	160

The morphology of the crystallites formed in our cylinders was studied using a Hitachi S570 scanning electron microscope. Initially, we cut small pieces of the cylinder with the help of a diamond saw. However, our SEM results exhibited smooth surface textures of the cut material, clearly indicating that the sawing itself affected the crystallites. Therefore, the samples were prepared by breaking the cylinders and extracting small pieces of the material from the interior as well as from the exterior of the cylinders. The pieces were mounted on the SEM sample stubs, using carbon paint, and were placed in an oven at 60°C for 24 hours to allow their fixation on the stubs. The samples, thus mounted, were sputter coated with a 40 nm of Ag/Pd layer to avoid the problem of charging. The SEM study was carried out using an accelerating voltage of 20 kV.

The thermal behavior of the fabricated materials, i.e., CWLP Ax (x = 1,2,3 or 4), CWLP Bx (x = 1, 2, 3, or 4), and SPKxx (xx = 29, 31, 32, 33, 34, or 35) was recorded using a Perkin-Elmer DSC7 system [12, 13]. To record the DSC thermographs at $40°C < T < 300°C$, the samples were sealed in aluminum pans with a hole drilled in them so that gases or vapors could escape easily. The transmission-FTIR data were collected using a nujol mull technique. Thin films of nujol mull, containing the ground sample, were formed on the KBr windows. The FTIR spectra of the various samples were recorded at 4 cm^{-1} resolution using an IBM IR44 FTIR spectrometer.

RESULTS AND DISCUSSION

Microscopic Results: The CWLP Ax series was formed with a view to explore how pressure affects the crystal growth habit of sludge-derived hemihydrate powder at room temperature.

Figure 1 reproduces the microphotograph of CWLP A1 sample. The SEM pictures revealed that for all CWLP Ax series the crystals were mostly needle-shaped with thin needles ranging from 2.5 μm to 40 μm in length. However, most of the crystals were around 2.5 μm in length. On average the thickness of the needles was about 2.5 μm. A similar compact, needle-shaped crystal growth habit has been reported for hydrated calcium sulfate when hemihydrate crystals were exposed to water vapor [14]. We did not observe any effect of pressure on the growth habit of crystallites for CWLP Ax series.

The effect of temperature on the crystallization behavior of hemihydrate was studied by fabricating CWLP Bx series in which a hemihydrate-water slurry was hot pressed at 50°C < T < 200°C at a constant pressure of 4000 psi. Similar to the results of CWLP Ax series, CWLP B1 sample also showed small needle-shaped crystals of gypsum. This sample was fabricated at 60°C. As the fabrication temperature increased, the size of crystallites formed in the sample also increased. This can be clearly seen in Fig. 2 which depicts the SEM photograph of CWLP B4 sample grown at 180°C. SEM pictures of CWLP B2 fabricated at 100°C showed a few small parallelogram-shaped crystals (length ~ 18 μm, thickness ~ 3 μm) in addition to mostly needle-shaped crystals. The parallelogram-shaped crystals are a typical morphology for gypsum [10]. On increasing the formation temperature to 140°C and 180°C, we observed not only the increase in the size of crystals formed but interestingly also the cession of needle-shaped crystals. Large interlocked crystals over the range from 20 μm to 240 μm in length and of thicknesses varying from 5 μm to 50 μm were formed at 180°C. It appears from our results that while formation pressure has only a marginal effect on the crystal growth habit, the formation temperature drastically alters the crystal growth behavior of sludge-derived hemihydrate.

In the second set of experiments, we examined how pressure and temperature affected the crystal growth habits of as-received scrubber sludge, i.e., gypsum-water slurry. Unlike previously discussed results, where we converted the sludge into hemihydrate powder by heating the sludge at 180°C (CWLP Ax and CWLP Bx series), in the present set of experiments (SPKxx series) the sludge was only air dried at room temperature prior to forming the materials. Figure 3 shows SEM microphotograph of SPK31 sample, which clearly shows large crystals are formed ranging from 6 μm to 50 μm in length, while the thickness varied from 2 μm to 20 μm. A comparison of these dimensions with those of CWLP B2 led us to conclude that the starting phase of the hydrated calcium sulfate influences the size and morphology of the crystals formed at T < 140°C. On increasing the formation temperature to 125°C (SPK32 sample), a further increase in the dimensions of the crystals resulted. For SPK31 particle size ranged from 8 μm to more than 100 μm in lengths and thickness varied from 8 μm to 30 μm. However, an increase in temperature to 200°C revealed that crystals started to form which resembled needle-like shapes and the crystallites were compacted in the sample.

The SPK33, SPK34, and SPK35 samples were formed at a fixed temperature of 160°C using different pressures. A comparative analysis of SEM pictures of SPK33 and SPK 35 showed that while the surfaces of the crystallites in SPK35 (formed at 4500 psi) had considerable roughness and flaky-like appearance, this was not the case for SPK33 which was formed at a much lower pressure, i.e., 500 psi. Since both samples were fabricated by hot pressing the slurry at the same temperature for equal lengths of time, it was possible that the surface roughness observed for SPK35 sample was the consequence of higher pressure used. One possible explanation could be that these flaky structures were formed by escaping water molecules, thus leaving traces of "water channels". These traces were oriented in one particular direction, i.e., in the longitudinal direction of the crystallites. Since under our hot pressing conditions, the water vapors could only escape from the rim of our die, therefore, it was not surprising to observe oriented defects on the surface of the crystallites. The crystal dimensions were not affected by the pressure applied like for CWLP Ax series, and in general crystallite sizes varied from 10 μm to 90 μm in length and 4 μm to 30 μm in thickness.

Thermal and Infrared Results: It is well known [10,15,16] that gypsum undergoes a two step dehydration process at 110°C < T < 220°C. Therefore, DSC experiments could be used to identify the phases of the calcium sulfate formed in our materials. For example, Fig. 4 reproduces the observed DSC thermographs of SPK29 and SPK31 samples formed at 2500 psi pressure at 94°C and 200°C, respectively. Two endothermic peaks were observed for SPK31 sample at around 170°C and 195°C, while a single endothermic peak was seen for SPK29 sample at around 195°C. In our thermal characterization measurements on CWLP scrubber sludge [10], we observed two endothermic peaks centered at around 154°C and 189°C. The first endothermic peak was associated with $CaSO_4.2H_2O$ decomposing into $CaSO_4.0.5H_2O$ and the second endothermic peak with the dehydration of $CaSO_4.0.5H_2O$ into $CaSO_4$. The shift in the peak temperatures seen for SPK31 sample could be attributed to the compaction of the crystallites,

presenting additional mechanical barriers for water's desorption. Thus, shifts in the temperatures of endothermic peaks were produced. It is therefore argued that while SPK31 sample crystallized perhaps in gypsum phase, the crystallites formed in SPK29 sample were hemihydrate. All the samples fabricated in CWLP Ax and CWLP Bx series exhibited a two-step dehydration endothermic reaction. This result leads us to believe that the gypsum crystallites were present in all these fabricated samples. Whether hemihydrate phase was also present can not be answered from DSC measurements alone since the presence of both gypsum and hemihydrate phases in the sample will still generate two endothermic reactions. However, it is possible for us to argue that only hemihydrate phase was formed for SPK29, SPK33, SPK34, and SPK35 samples since we observed a single endothermic reaction at around 190°C.

Infrared spectroscopic technique [10,17] can be used to further verify and identify which calcium sulfate phases have formed in our fabricated cylinders. In water's stretching region, gypsum produces three vibrational modes at around 3550, 3490 (weak band), and 3400 cm^{-1}; while in the bending region, two distinct oscillators are observed at 1686 and 1623 cm^{-1}. For hemihydrate structure, two vibrational bands in the stretching region appear at around 3610 and 3555 cm^{-1}. A single vibrational mode is seen at around 1620 cm^{-1} for the hemihydrate in the bending region. If anhydrous calcium sulfate phase is present, then that phase will produce no water bands but still can be recognized from SO_4^{2-} ions' vibrations. We have summarized our FTIR results for CWLP Ax, CWLP Bx, and SPKxx series in Table 2. The identified phases are also listed in that table. The CWLP Ax and CWLP Bx (x = 1,2) cylinders were largely composed of gypsum crystallites with some hemihydrate crystallites also present. The CWLP Bx (x = 3, 4) cylinders on the other hand were formed from largely hemihydrate crystallites with some gypsum phase also present in them. It is interesting to note that if as-received, but air dried, CWLP scrubber sludge was used to fabricate the materials then the cylinders, depending upon formation temperature, either crystallized in gypsum or hemihydrate phase rather than in mixed phases like CWLP Ax and CWLP Bx series.

ACKNOWLEDGMENTS

This work was supported in part by Illinois Clean Coal Institute (Illinois Department of Commerce and Community Affairs).

REFERENCES:

1. Randolph, A. D.; Kelly, B. J.; Keough, B. "Calcium Sulfite and Calcium Sulfate Crystallization, Vol.1: Effect of Crystallization Type on Gypsum Size Distribution", *EPRI, Palo Alto, California, Research Project* 1031-3, Nov. 1986.
2. Puri, V.K.; Paul, B. C.; Mukherjee, J.; Hock, K. K.; Yu, Z. "Utilization Coal Refuse and FBC Fly Ash: Strength Aspects", *Procd. NMLRC Sympos, (Eds.) Y. P. Chugh and D. C. Davin*, pp 187-195, 1993.
3. Clarke, L. B. "Management of FGD residues: An International Overview", *Procd. 10th Pittsburgh Coal Conf., (Ed.) S-H Chiang*, pp. 561-566 , 1993.
4. Taulbee, D. N.; Graham, U.; Rathbone, R. F.; Robl, T. L. *Am. Chem. Soc. Prep., Div. Fuel Chem. 40(4), 858, 1995.*
5. Valimbe, P. S.; Malhotra, V. M.; Banerjee, D. D.; *Am. Chem. Soc. Prep., Div. Fuel Chem.*, **40(4)**, 776, 1995.
6. Goodrich-Mahoney, J. W. "Coal Combustion By-products Field Research Program at EPRI: An Overview", *EPRI (Environmental Division)*, 1994.
7. Luckevich, L. M. "Making and Marketing Flue Gas Desulfurization Gypsum", *Procd. 12th Inter. Sympos. on Coal Combustion By-Products Management and Use, Orlando, Florida*, **Vol. 2**, pp 67-1 to 67-7, 1997.
8. Chou, M.-I. M.; Bruinius, J. A.; Li, Y. C.; Rostam-Abadi, M.; Lytle, J. M. *Am. Chem. Soc. Prep., Div. Fuel Chem. 40(4), 896, 1995.*
9. Sclieper, H.; Duda, A.; Jager, R.; Kanig, M.; Kwasny-Echterhagen, R. "FGD Gypsum - A Raw Material for New Binder Systems" *Procd. 12th Inter. Sympos. on Coal Combustion By-Products Management and Use, Orlando, Florida*, **Vol. 2**, pp 48-1 to 48-13, 1997.
10. Valimbe, P. S.; Malhotra, V. M.; Banerjee, D. D.; *Am. Chem. Soc. Prep., Div. Fuel Chem.*, 1997 (this volume).
11. Lynch, W. M. *Am. Ceramic Soc. Bull.* **74**, 60, 1995.
12. Jasty, S.; Malhotra, V. M. *Phys. Rev. B* **45**, 1, 1992.
13. Jasty, S.; Malhotra, V. M.; Robinson, P. D. *J. Physics: Condens. Matter* **4**, 4769, 1992.
14. Gans, W.; Klocker, H.; Knacke, O. Z. Metallkd. **87**, 98, 1996.
15. Blaine, R. *American Laboratory*, **Sept. 1995**, pp 24-28.

16. Dunn, J. G.; Oliver, K.; Sills, I. *Thermochim. Acta* **155**, 93, 1989.
17. Bensted, J.; Prakash, S. *Nature* **219**, 60, 1968.

Table 2
The observed water bands for various samples fabricated from CWLP scrubber sludge and the possible crystallite phases. CWLP HP represents hemihydrate phase derived from the sludge by heating it at ambient pressure at 180°C.

Sample Name	Water Stretching Vibrations (cm^{-1})	Water Bending Band (cm^{-1})	Phase Identified
CWLP HP	3607, 3553, 3406	1622	Largely Hemihydrate
CWLP A4	3607, 3551, 3404	1685, 1622	Gypsum + Hemihydrate
CWLP A1	3608, 3553, 3404	1685, 1622	Gypsum + Hemihydrate
CWLP B1	3607, 3545, 3400	1686, 1620	Gypsum + Hemihydrate
CWLP B2	3607, 3553, 3404	1686, 1620	Gypsum + Hemihydrate
CWLP B3	3609, 3553, 3404	1685, 1620	Hemihydrate + Gypsum
CWLP B4	3607, 3553, 3404	1685, 1620	Hemihydrate + Gypsum
SPK 31	3543, 3493, 3400	1688, 1622	Gypsum
SPK 32	3545, 3493, 3400	1685, 1622	Gypsum
SPK 29	3609, 3555	1618	Hemihydrate
SPK 33	3611, 3555	1621	Hemihydrate
SPK 35	3611, 3555	1620	Hemihydrate

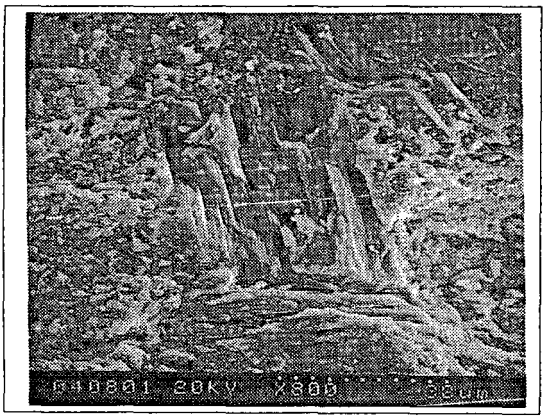

Figure 1. SEM microphotograph of sample fabricated from hemihydrate powder derived from CWLP scrubber sludge. The water slurry was pressed at 5000 psi pressure for 20 minutes at 24°C.

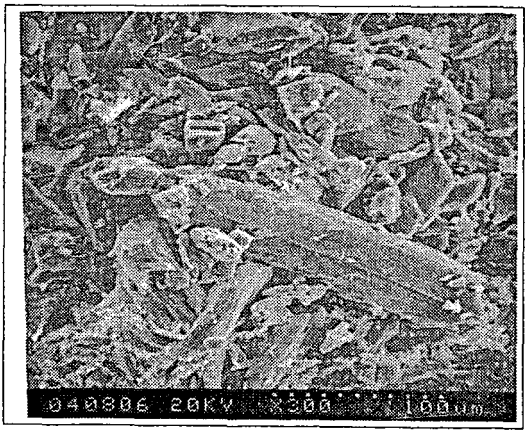

Figure 2. SEM microphotograph of sample fabricated from hemihydrate powder derived from CWLP scrubber sludge. The water slurry was pressed at 4000 psi pressure for 20 minutes at 180°C.

Figure 3. SEM microphotograph of sample fabricated from CWLP scrubber sludge. The water slurry was pressed at 2500 psi pressure for 90 minutes at 94°C.

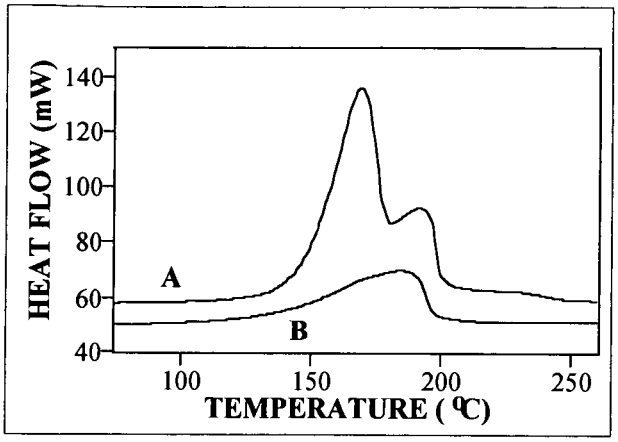

Figure 4. The observed DSC thermographs for (A) SPK31 sample formed at 94°C at 2500 psi pressure and (B) SPK29 sample fabricated at 200°C at 2500 psi pressure.